Efficient implementations of high-resolution wideband FFT-spectrometers and their application to an APEX Galactic Center line survey

Dissertation
zur
Erlangung des Doktorgrades (Dr. rer. nat.)
der
Mathematisch-Naturwissenschaftlichen Fakultät
der
Rheinischen Friedrich-Wilhelms-Universität Bonn

vorgelegt von
Stefan Hochgürtel
aus
Euskirchen

Bonn, 2013

Angefertigt mit Genehmigung der Mathematisch-Naturwissenschaftlichen Fakultät der Rheinischen Friedrich-Wilhelms-Universität Bonn

1. Gutachter: Prof. Dr. Karl M. Menten
2. Gutachter: Prof. Dr. Pavel Kroupa
Tag der Promotion: 13.05.2013
Erscheinungsjahr: 2013

Abstract

Spectroscopy has been a major technique in radioastronomy for decades and spectrometers are used in a wide range of radioastronomical applications. With more stable receivers that are wider in bandwidth, spectrometers are required that possess both wide bandwidth and high spectral resolution. The availability of analog-to-digital converters (ADCs) that sample a signal at rates of multiple GHz allowed the development of a novel type of spectrometer. The fast Fourier transform spectrometer (FFTS) digitizes a radio signal and calculates its power spectrum at high speed. The increased complexity of field-programmable gate arrays (FPGAs) provides the processing power necessary for such high-speed operation at a low price and with high flexibility. However, to fully utilize the speed and flexibility offered by FPGAs and to achieve a bandwidth of 2.5 GHz with up to 65536 channels, it is necessary to develop efficient algorithms that are optimized for FPGA-based implementation.

This thesis first explains the basic principles behind an FFTS. Then it describes the requirements of astronomical applications that utilize FFTSs and evaluates their requirements. Besides the main application of wideband spectroscopy, the demands of high resolution spectroscopy, of an incoherent pulsar search, and of a readout for microwave kinetic inductance detectors (MKIDs) are specified.

The thesis then presents efficient algorithms, that satisfy these requirements. After defining the components of an FFTS and their purpose, the technical requirements of each component are described, and algorithms or implementations are discussed with respect to their processing speed, hardware utilization, memory occupation, flexibility, or just simplicity. Concepts are developed to partition algorithms between the FPGA and the personal computer (PC) to create simple, hardware-efficient components inside the FPGA. To achieve both, high bandwidth and high spectral resolution, parallel and pipelined algorithms are combined. The hardware utilization and the flexibility of different such fast Fourier transform (FFT) architectures are compared, dependent on the significance of either bandwidth or resolution. Control mechanisms are developed and implemented to function in different time frames, dependent on the application. Two fully functional high-resolution wideband spectrometers, in which such algorithms are implemented, benefit from the optimization of the processing pipeline: the Array Fast Fourier Transform Spectrometer (AFFTS) and the eXtended-bandwidth Fast Fourier Transform Spectrometer (XFFTS).

Finally, an astronomical application of the aforementioned spectrometers is presented: two unbiased line surveys of molecular cloud positions near the center of our Galaxy with the First Light APEX Submillimeter Heterodyne receiver (FLASH) in the Atacama Pathfinder EXperiment (APEX) telescope. Containing hundreds of spectral lines, those surveys provide a large amount of information on the physical and chemical conditions of the observed objects and thus work for several years of analysis. We present the basic results that can be extracted from a first iteration with the data: line identification, selection of the best molecular tracers, and analysis of those tracers to obtain the physical properties in the studied regions. Unidentified lines and so far unaccessed information, and the possibility to add this data to unbiased surveys taken with other telescopes are a legacy to future astronomical research and thus demonstrate the benefits of the presented concepts.

Contents

Acronyms

AFFTS	Array Fast Fourier Transform Spectrometer
ALMA	Atacama Large Millimeter/submillimeter Array
APEX	Atacama Pathfinder EXperiment
ATLASGAL	APEX Telescope Large Area Survey of the Galaxy
C	C (programming language)
CDMS	Cologne Database for Molecular Spectroscopy
CHAMP	Carbon Heterodyne Array of the MPIfR
CLASS	GILDAS Continuum and Line Analysis Single-dish Software
CSO	Caltech Submillimeter Observatorium
DCM	Digital Clock Manager (component in Xilinx FPGAs)
DVB-T	Digital Video Broadcasting - Terrestrial
EBHIS	Effelsberg Bonn H-I Survey
FLASH	First Light APEX Submillimeter Heterodyne receiver
GC	Galactic Center
GREAT	German Receiver for Astronomy at Terahertz frequencies
GSM	Global System for Mobile Communications
IDELAY	Input Delay Element (component in Xilinx FPGAs)
IEEE	Institute of Electrical and Electronics Engineers
IODELAY	Input/Output Delay Element (component in Xilinx FPGAs)
IP	Internet Protocol
ISERDES	Input Serial-to-Parallel Logic Resource (component in Xilinx FPGAs)
IRAM	Institut de Radioastronomie Millimétrique
JCMT	James Clerk Maxwell Telescope
JPL	Jet Propulsion Laboratory
LAB	Leiden/Argentine/Bonn
LABOCA	Large APEX BOlometer CAmera
MMCM	Mixed-Mode Clock Manager (component in Xilinx FPGAs)
MPIfR	Max Planck Institut für Radioastronomie
NI	National Instruments
PCI	Peripheral Component Interconnect
PMCD	Phase-Matched Clock Divider (component in Xilinx FPGAs)

SgrA	Sagittarius A
SgrB2(N)	Sagittarius B2(North)
SOFIA	Stratospheric Observatory for Infrared Astronomy
SRON	Space Research Organization Netherlands
TCP	Transmission Control Protocol
UMTS	Universal Mobile Telecommunications System
VHDL	Very-high-speed integrated circuits HDL (hardware description language)
XFFTS	eXtended-bandwidth Fast Fourier Transform Spectrometer
Xilinx ISE	Xilinx Integrated Software Environment
AC	alternating current
ACF	autocorrelation function
ACS	autocorrelator spectrometer
ADC	analog-to-digital converter
AOS	acousto optical spectrometer
ASIC	application-specific integrated circuit
BRAM	block RAM (random-access memory)
CC	central cavity (R<1 pc around the GC)
CLB	configurable logic block
CMZ	central molecular zone (R<200 pc around the GC)
CND	circumnuclear disk (1.5 pc <R<4 pc around the GC)
CO	carbon monoxide
CPU	central processing unit
CTS	chirp transform spectrometer
DAC	digital-to-analog converter
DC	direct current
DDR	double data rate
DFT	discrete Fourier transform
DIF	decimation in frequency
DIT	decimation in time
DM	dispersion measure
DSP	digital signal processing
DSP slice	digital signal processing slice
ENBW	effective noise bandwidth
ENOB	effective number of bits
FDM	frequency division multiplexing
FFT	fast Fourier transform
FFTS	fast Fourier transform spectrometer
FM	frequency modulation
FPGA	field-programmable gate array

FWHM	full width at half maximum
GMC	giant molecular cloud
H I	hydrogen I (neutral atomic hydrogen)
H II	hydrogen II (ionized hydrogen)
HDL	hardware description language
IF	intermediate frequency
IP core	intellectual property core
ISM	interstellar medium
isotopologue	molecule containing isotopes
I/O	input/output
LO	local oscillator
LSB	lower sideband
LSR	local standard of rest (reference frame for relative velocities)
LTE	local thermodynamic equilibrium
LUT	lookup table
LVDS	low-voltage differential signaling
MACC	multiply-accumulate
MKID	microwave kinetic inductance detector
NaN	not a number (special value in numeric data types)
OH	hydroxyl (radical molecule)
PC	personal computer
PDF	probability density function
PDR	photodissociation region
pwv	precipitable water vapor
PSD	power spectral density
QN	quantum number
RAM	random-access memory
RF	radio frequency
RFI	radio frequency interference
RMS	root-mean-square
SINAD	signal-to-noise and distortion ratio
SMBH	supermassive black hole
SNR	supernova remnant
SSB	single sideband
S/N	signal-to-noise ratio
USB	upper sideband
WASP	wideband analog autocorrelation spectrometer
WOLA	weighted overlap-add
WLAN	wireless local area network

dB	decibel (logarithmic unit of power-ratio)
Hz	Hertz (unit of frequency)
kHz	kiloHertz (unit of frequency, 10^3 Hz)
MHz	MegaHertz (unit of frequency, 10^6 Hz)
GHz	GigaHertz (unit of frequency, 10^9 Hz)
pc	parsec (unit of length, $\sim 3.086 \cdot 10^3$ m)
kpc	kiloparsec (unit of length, 10^3 pc)
arcsec	arcsecond (unit of arc, $1'' = 1^\circ/3600$)
arcmin	arcminute (unit of arc, $1' = 1^\circ/60$)

List of Figures

List of Tables

Chapter 1

Introduction

Spectroscopy has been a major technique in radioastronomy for decades. In 1963, hydroxyl (OH) was discovered in the interstellar medium (ISM) in a 100 kHz spectrum measured at 1667 MHz sky frequency, using an autocorrelator spectrometer (ACS) [100]. This was the first detection of an interstellar molecule at radio wavelengths [52]. Many absorption and emission lines of more complex molecules are located at sub-mm wavelengths [11, 60]. There are several facilities and instruments that allow observations at those wavelengths, such as the CSO, the JCMT, the Herschel Space Observatory, or the Atacama Large Millimeter/submillimeter Array (ALMA). This thesis will focus on the following three:

- Front-ends at the Institut de Radioastronomie Millimétrique (IRAM) 30-m telescope cover sky frequencies from 83 to 358 GHz [42].
- The Atacama Pathfinder EXperiment (APEX) 12-m telescope is sensitive to sub-mm radiation from $\sim$ 200 GHz to $\sim$ 1500 GHz [55, 33, 4].
- The airborne Stratospheric Observatory for Infrared Astronomy (SOFIA) opens the atmospheric windows that are blocked for ground-based telescopes [90]. The windows between 1250 GHz and 2500 GHz can be observed by the German Receiver for Astronomy at Terahertz frequencies (GREAT) [38, 31], which is installed at SOFIA.

These facilities alone cover frequencies from 83 to 2500 GHz, which allows to make unbiased line surveys, that do not focus on a particular spectral line, to study the properties of galactic and extragalactic sources. To link studies of galactic and extragalactic sources, observations of the center of our Galaxy are of particular importance. The complex kinematics in this region results in a mixture of wide emission lines from the inner disk and narrow absorption lines from gas in the line of sight.

With more stable receivers that are wider in bandwidth, the successful analysis of such unbiased line surveys requires spectrometers that possess both wide bandwidth and high spectral resolution.

- The first spectrometers in radio astronomy were analog filter banks just consisting of a set of analog bandpass filters.

- The widely used autocorrelator spectrometers (ACSs) digitize a radio signal to 1 or 2 bits and calculate the autocorrelation function (ACF) [99]. Due to the limited number of quantization levels, this task is simple, but also limits the dynamic range of ACSs. After integration, an ACS calculates a power spectrum under much weaker timing constraints using the Wiener-Khinchin theorem [55]. The digital ACS at the APEX telescope divides a bandwidth of 1 GHz into 1024 spectral channels ($\sim$ 1 ch/MHz) [48]. Analog correlators reach higher bandwidths by shifting the ACF to analog circuits. This way, wideband analog autocorrelation spectrometers (WASPs) can achieve a bandwidth of 4 GHz. They are, however, limited to 128 spectral channels [44].

- The acousto optical spectrometer (AOS) is an analog spectrometer type that is optimized for high bandwidth. Based on the incoming radio signal, it creates acoustic waves in a crystal, which is used to diffract a laser to produce a spectrum. Therefore, an AOS requires a mechanically and thermally stable environment. State-of-the-art AOSs achieve bandwidths of up to 3 GHz, with a resolution limited to $\sim$ 1 ch/MHz [78].

- The chirp transform spectrometer (CTS) is also an analog spectrometer type. It uses sonic waves on the surface of crystals and calculates spectra by analyzing the velocity dispersion of those waves [5, Ch. 1.2.5.2.3]. Since it is optimized for high resolution, state-of-the-art instruments have a good spectral resolution of $\sim$ 20 ch/MHz, but only over a narrow bandwidth of 200 MHz [96].

- The availability of analog-to-digital converters (ADCs) that sample a signal at rates of multiple GHz allowed the development of a novel type of spectrometer. The fast Fourier transform spectrometer (FFTS) digitizes a radio signal and calculates its power spectrum at high speed. Differing from an ACS, a fast Fourier transform (FFT) first calculates an amplitude spectrum. Only after squaring the spectrum, integration over time finally reduces the data rate. Recently, state-of-the-art FFTSs have evolved over a period of just seven years from 50 MHz bandwidth divided into 1024 spectral channels [92] over 1 GHz with 16384 channels [9] and 1.8 GHz with 8192 channels [54] to 2.5 GHz with up to 65536 channels [52, Fig. 1]. So FFTSs offer both, wide bandwidth and high spectral resolution.

Besides fast ADCs, this development also required hardware to process the digitized data at high speed. The increased complexity of field-programmable gate arrays (FPGAs) now provides the processing power necessary for such high-speed operation at a low price and with high flexibility. Therefore, the above examples use FPGAs to process data and calculate an FFT. However, to fully utilize the speed and flexibility offered by FPGAs and to achieve the aforementioned specifications, it is necessary to develop efficient algorithms that are optimized for FPGA-based implementation.

This thesis first explains the basic principles behind an FFTS. Then it describes the requirements of astronomical applications that utilize FFTSs. The thesis then presents efficient algorithms, that satisfy these requirements. Different applications, as well as different components of the FFTS, may require optimization of processing speed, hardware utilization, memory occupation, flexibility, or

just simplicity. High-speed data sampling requires to carefully adjust the parameters of interleaved ADCs or the delay on data wires, using limited resources for signal analysis. Pipelined and parallel implementations of digital signal processing (DSP) algorithms, such as the FFT, are discussed with respect to hardware utilization and memory occupation. The impact of simplifications is examined with respect to common operating conditions to reduce complexity of certain components of the processing pipeline. General considerations and interfaces allow the flexibility to use the algorithms in various applications. Two fully functional high-resolution wideband spectrometers, in which such algorithms are implemented, benefit from the optimization of the processing pipeline. Finally, an astronomical application of the aforementioned spectrometers is presented: two unbiased line surveys of molecular cloud positions near the center of our Galaxy with the First Light APEX Submillimeter Heterodyne receiver (FLASH) in the APEX telescope. Containing hundreds of spectral lines, those surveys provide a large amount of information on the physical and chemical conditions of the observed objects and thus work for several years of analysis. We present the basic results that can be extracted from a first iteration with the data: line identification, selection of the best molecular tracers, and analysis of those tracers to obtain the physical properties in the studied regions. Unidentified lines and so far unaccessed information, and the possibility to add this data to unbiased surveys taken with other telescopes are a legacy to future astronomical research and thus demonstrate the benefits of the presented concepts.

Chapter 2

Basic principles

2.1 FPGA

A field-programmable gate array (FPGA) is a semiconductor device based on configurable logic blocks (CLBs) that are arranged in a matrix and connected via programmable interconnects [104]. State-of-the-art FPGAs contain components with a wide range of complexity:

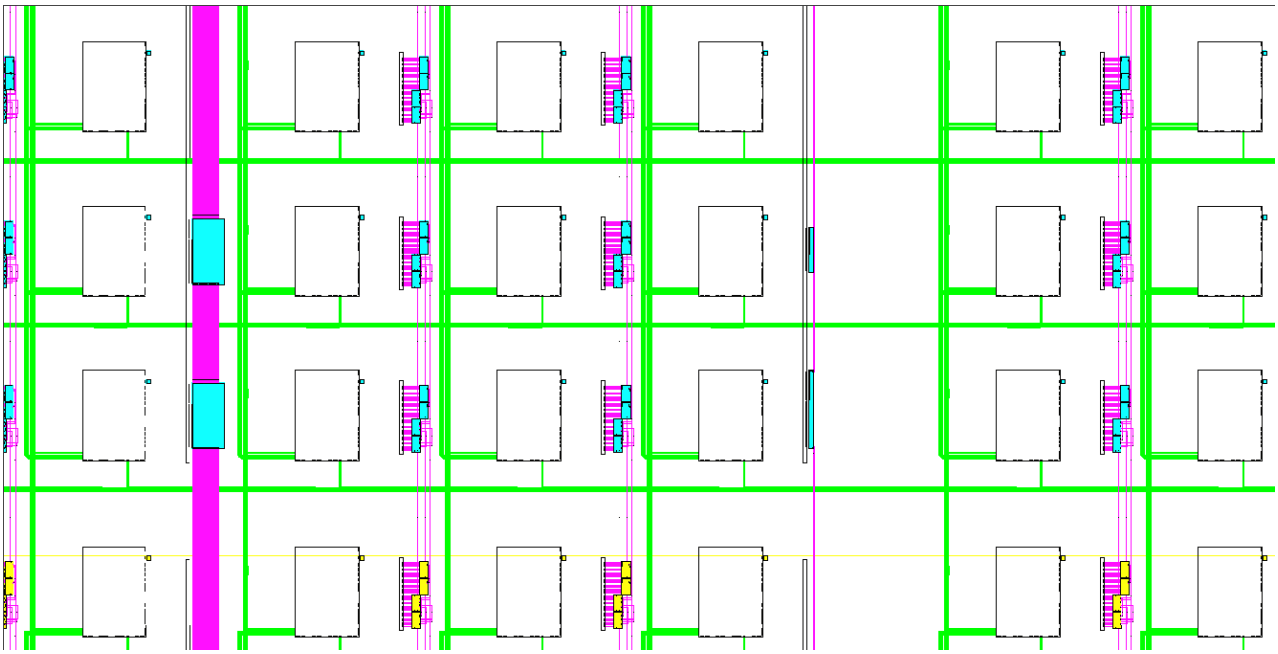

Figure 2.1: section of a Virtex4 FPGA with used (yellow) and unused (cyan) CLBs, DSP slices and BRAMs, connected by short distance (magenta) and long distance (green) interconnect wires and interconnect matrices (white).

- Buffers transform impedance or voltage between circuits.
- Tri-states access a wire bidirectionally to create a bus.
- Flip-flops store one bit if triggered, ready for immediate reading.
- Lookup tables (LUTs) implement arbitrary boolean function.
- Clock-management circuits stabilize, shift, multiply or divide incoming clock signals.
- Memory of various size and speed stores or buffers data for different purposes.
- I/O transceivers connect external circuits and allow high speed data transfer.
- Digital signal processing slices (DSP slices) implement standard functions such as multiply-accumulate (MACC) or multiplying.
- Central processing units (CPUs) allow implementation of complex algorithms in high-level languages.

The interconnect wires allow to connect all of these components according to a hardware description that configures the FPGA to perform a particular task (see figure 2.1).

A hardware description is usually written in a hardware description language (HDL). The most common ones are Very-high-speed integrated circuits HDL (VHDL) and Verilog. They allow low-level programming, describing each component and connection manually, or high-level programming, using mathematical formulas, functions, loops, generics and registers. A combination of these is possible, as well as compilation from higher-level languages such as C++. Either way, HDL code needs to be synthesized in multiple steps: Xilinx Integrated Software Environment (Xilinx ISE) divides the process into synthesis, translation, mapping and place & route [108].

- Synthesis transforms high-level constructs into low-level ones: formulas and functions into logical nets, loops into lists, generics into actual values and assignments into flip-flops or memory.
- Translation adds constraints on the synthesized design, such as the location of certain I/O or length restrictions to certain wires.
- Mapping identifies the components used on a particular FPGA.
- Finally, place & route decides what instance of a component and what wires are used on the FPGA to meet all requirements of the hardware description and the constraints on the hardware design.

Since an FPGA can be configured repeatedly with different hardware descriptions, it bridges the gap between classic hardware, such as an application-specific integrated circuit (ASIC), and classic software, such as C code, compiled for a central processing unit (CPU) or digital signal processing (DSP) chip. Classic hardware is usually optimized for a particular task and designed to represent the fastest solution for this task. Its development is expensive and hence it is only cost-efficient for widespread tasks that don't change significantly. Classic software is highly flexible. Changes are easy and almost every application may be implemented with reasonable effort, but a software implementation is usually slower than a specialized hardware solution. Although FPGAs reach neither the speed of specialized hardware nor the flexibility of software, they may be optimized on a low level, allow a wide range of applications and have the cost advantage of a mass product. Thus they are a viable alternative where a software solution is too slow and specialized hardware is too expensive or too inflexible.

2.2 DFT

An N-point discrete Fourier transform (DFT) calculates N frequency channels $\hat{a}_k$ out of N time-discrete samples a_j:

$$\hat{a}_k = \sum_{j=0}^{N-1} e^{-2\pi i \frac{j \cdot k}{N}} \cdot a_j \tag{2.1}$$

Since a DFT yields complex channels, one can distinguish the phase $\Phi(\hat{a}_k)$ of a channel from its amplitude $|\hat{a}_k|$ or its power $|\hat{a}_k|^2$. One should also distinguish between the (normalized) spectrum and the spectral density, as these two differ in scaling factors [36]. The power spectrum $\hat{a}_{k,\mathrm{PS}}$ scales single input frequencies correctly to $U^2 \propto P$ in units of V^2 or W, whereas the power spectral density (PSD) $\hat{a}_{k,\mathrm{PSD}}$ scales noise correctly to energy $\frac{P}{f} = E$ in units of $\mathrm{W\,Hz^{-1}}$ or $\mathrm{W\,s}$. The same applies to the amplitude spectrum $\hat{a}_{k,\mathrm{AS}}$ and the amplitude spectral density $\hat{a}_{k,\mathrm{ASD}}$, which are just the square root of their power equivalents. For a DFT of length N with input sampled at frequency f_S, the scaling factors are

$$\begin{aligned}
\hat{a}_{k,\mathrm{PS}} &= \frac{|\hat{a}_k|^2}{N^2} \\
\hat{a}_{k,\mathrm{AS}} &= \frac{|\hat{a}_k|}{N} \\
\hat{a}_{k,\mathrm{PSD}} &= \frac{|\hat{a}_k|^2}{N \cdot f_\mathrm{S}} \\
\hat{a}_{k,\mathrm{ASD}} &= \frac{|\hat{a}_k|}{\sqrt{N \cdot f_\mathrm{S}}}
\end{aligned} \tag{2.2}$$

The relationship between power spectrum and PSD is described by the effective noise bandwidth (ENBW):

$$\hat{a}_{k,\mathrm{PS}} = \hat{a}_{k,\mathrm{PSD}} \cdot ENBW \tag{2.3}$$

In the above case, the ENBW obviously equals the frequency resolution of the DFT:

$$ENBW = \frac{f_\mathrm{S}}{N} \tag{2.4}$$

In the presence of a window (chapter 2.4), the ENBW is still proportional to the resolution [36].

One basic property of the DFT is its linearity. Assume two sets of samples a_j, b_j and their spectra $\hat{a}_k$, $\hat{b}_k$. It is obvious that taking a DFT of the sum of samples $c_j = a_j + b_j$ yields the sum of their respective spectra:

$$\hat{c}_k = \sum_{j=0}^{N-1} e^{-2\pi i \frac{j \cdot k}{N}} \cdot (a_j + b_j) = \hat{a}_k + \hat{b}_k \tag{2.5}$$

The same is true for a constant multiple $c \in \mathbb{C}$ of the samples $c_j = c \cdot a_j$. It yields the same multiple of the spectrum:

$$\hat{c}_k = \sum_{j=0}^{N-1} e^{-2\pi i \frac{j \cdot k}{N}} \cdot c \cdot a_j = c \cdot \hat{a}_k \tag{2.6}$$

Assuming a periodic signal, a shift by $z \in \mathbb{Z}$ samples $c_j = a_{j+z \bmod N}$ yields a rotation of each spectral channel:

$$\hat{c}_k = \sum_{j=0}^{N-1} e^{-2\pi i \frac{j \cdot k}{N}} \cdot a_{j+z \bmod N} = \sum_{j=0}^{N-1} e^{-2\pi i \frac{(j-z) \cdot k}{N}} \cdot a_j = e^{+2\pi i \frac{z \cdot k}{N}} \cdot \hat{a}_k \tag{2.7}$$

A complex conjugation of samples $c_j = \overline{a_j}$ yields a spectrum that is mirrored and complex conjugated:

$$\hat{c}_k = \sum_{j=0}^{N-1} e^{-2\pi i \frac{j \cdot k}{N}} \cdot \overline{a_j} = \overline{\sum_{j=0}^{N-1} e^{-2\pi i \frac{j \cdot (N-k)}{N}} \cdot a_j} = \overline{\hat{a}_{N-k}} \tag{2.8}$$

The product of samples $c_j = a_j \cdot b_j$ yields a convolution of their spectra [93, Ch. 7.4]:

$$\hat{c}_k = \sum_{j=0}^{N-1} e^{-2\pi i \frac{j \cdot k}{N}} \cdot a_j \cdot b_j = \frac{1}{N} \sum_{l=0}^{N-1} \hat{a}_l \cdot \hat{b}_{k-l \bmod N} \tag{2.9}$$

Another important property of the DFT is given by Parseval's theorem [13, Ch. 8.12]. It can be proved by defining $c_j = a_j \cdot \overline{a_j}$ and using (2.8) and (2.9):

$$\sum_{j=0}^{N-1} |a_j|^2 = \hat{c}_0 = \frac{1}{N} \sum_{k=0}^{N-1} |\hat{a}_k|^2 \tag{2.10}$$

The theorem poses that the overall energy of noise, as well as the average power of individual frequencies are conserved by a DFT:

$$\begin{aligned} \sum_{j=0}^{N-1} \frac{|a_j|^2}{f_\mathrm{S}} &= \sum_{k=0}^{N-1} \hat{a}_{k,\mathrm{PSD}} \\ \frac{1}{N} \sum_{j=0}^{N-1} |a_j|^2 &= \sum_{k=0}^{N-1} \hat{a}_{k,\mathrm{PS}} \end{aligned} \tag{2.11}$$

DFT of a phasor Assume a_j is a phasor of frequency f, sampled with frequency f_S:

$$a_j = e^{2\pi i \frac{f}{f_\mathrm{S}} \cdot j + i\varphi} \tag{2.12}$$

According to the Nyquist-Shannon sampling theorem, f must not exceed half the sampling rate in order to reconstruct the input from the samples [93, Ch. 4.2]. For $0 < f < \frac{f_\mathrm{S}}{2}$, a phasor of frequency $f' = f - f_\mathrm{S}$ would yield the same samples and will not be distinguishable from that in (2.12). The effect is called aliasing and is reflected in the periodicity of the DFT spectrum:

$$\hat{a}_{k+N} = \sum_{j=0}^{N-1} e^{-2\pi i \frac{j \cdot (k+N)}{N}} \cdot a_j = \hat{a}_k \tag{2.13}$$

The following formulas describe how an N-point DFT responds to a single tone of frequency f. To simplify them, we define the theoretical channel of this frequency k_f and its distance $\delta_{f,k}$ to an actual channel k:

$$\begin{aligned} k_f &:= \frac{f}{f_\mathrm{S}} \cdot N \\ \delta_{f,k} &:= k - k_f = k - \frac{f}{f_\mathrm{S}} \cdot N \end{aligned} \tag{2.14}$$

To make the upcoming mathematical transformation easier to follow, it is helpful to recall some basic trigonometry, such as the sum and double-angle equations, and the basic relationships between trigonometric functions and the complex exponential function:

$$\begin{aligned} \cos(x+y) &= \cos(x)\cdot\cos(y) - \sin(x)\cdot\sin(y) \\ \sin(x+y) &= \sin(x)\cdot\cos(y) + \cos(x)\cdot\sin(y) \end{aligned} \tag{2.15}$$

$$\begin{aligned} \cos(2x) &= \cos(x+x) = \cos^2(x) - \sin^2(x) \\ &= 1 - 2\cdot\sin^2(x) = 2\cdot\cos^2(x) - 1 \end{aligned} \tag{2.16}$$

$$\sin(2x) = \sin(x+x) = 2\cdot\sin(x)\cdot\cos(x)$$

$$e^{+i\cdot x} = \cos(x) + i\cdot\sin(x) \tag{2.17}$$

$$e^{+i\cdot x} + e^{-i\cdot x} = 2\cdot\cos(x) \tag{2.18}$$

$$e^{+i\cdot x} - e^{-i\cdot x} = 2i\cdot\sin(x) \tag{2.19}$$

Now feeding a DFT with (2.12) yields the following spectrum:

$$\begin{aligned} \hat{a}_k &= e^{+i\varphi}\cdot\sum_{j=0}^{N-1} e^{-2\pi i\cdot\frac{k-k_f}{N}\cdot j} \\ &= e^{+i\varphi}\cdot\frac{e^{-2\pi i\cdot\left(k-k_f\right)}-1}{e^{-2\pi i\cdot\frac{k-k_f}{N}}-1} \\ &= e^{-\pi i\cdot\left(k-k_f\right)\cdot\frac{N-1}{N}+i\varphi}\cdot\frac{\sin\left(\pi\left(k-k_f\right)\right)}{\sin\left(\pi\frac{k-k_f}{N}\right)} \end{aligned} \tag{2.20}$$

$$|\hat{a}_k|^2 = \frac{\sin^2\left(\pi\left(k-k_f\right)\right)}{\sin^2\left(\pi\frac{k-k_f}{N}\right)} \tag{2.21}$$

For frequencies $k_f = z$, which exactly match a spectral channel $z \in \mathbb{Z}$, (2.20) can be simplified, since all channels $k \neq z \bmod N$ show no spectral response:

$$\hat{a}_k = e^{-\pi i\cdot(k-z)\cdot\frac{N-1}{N}+i\varphi}\cdot\frac{0}{\sin\left(\pi\frac{k-z}{N}\right)} = 0 \tag{2.22}$$

The channel $k = z \bmod N$ that does match shows a non-zero response, which can be calculated by the original sum-formula in (2.20):

$$\hat{a}_k = e^{+i\varphi}\cdot\sum_{j=0}^{N-1} e^{-2\pi i\cdot 0} = e^{+i\varphi}\cdot N \tag{2.23}$$

As expected, the spectrum shows a single peak, at the respective channel (see figure 2.2). The other case is described in chapter 2.4 in more detail.

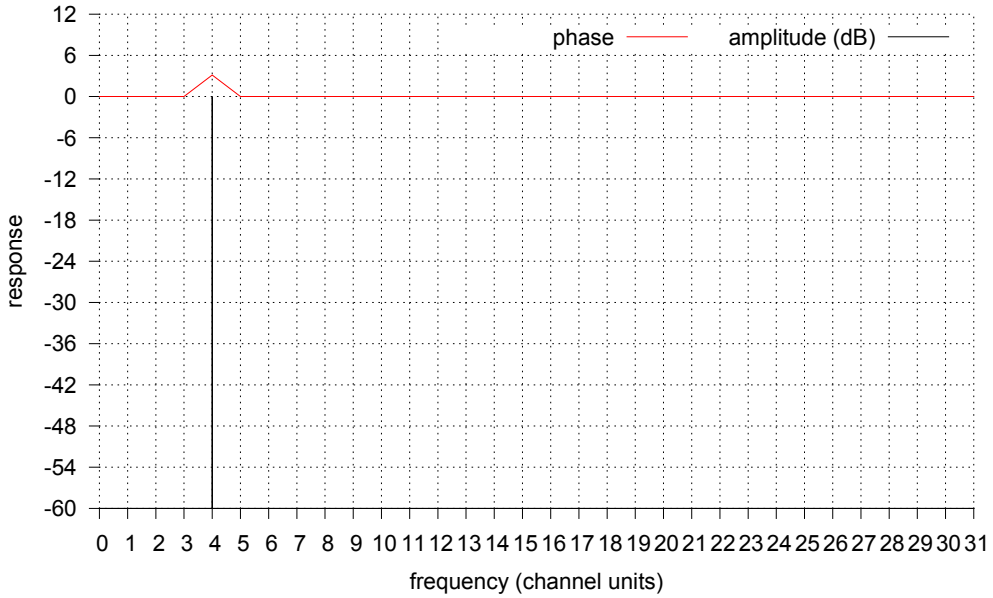

Figure 2.2: DFT spectrum with $N = 32$ channels. Input is a phasor with phase $\varphi = \pi$ and frequency $k_f = 4$ exactly. The amplitude spectrum is plotted in dB ($20 \lg \frac{|\hat{a}_k|}{N}$, black) and the phase in radians ($\Phi(\hat{a}_k)$, red).

DFT of a cosine wave Now assume a real cosine wave a'_j of frequency f. To make use of the results outlined in the preceding paragraph, the cosine wave can be defined as the mean of two phasors a_j and $\overline{a_j}$ that oscillate in opposite directions:

$$a'_j = \frac{a_j + \overline{a_j}}{2} = \cos\left(2\pi \frac{f}{f_S} \cdot j + \varphi\right) \tag{2.24}$$

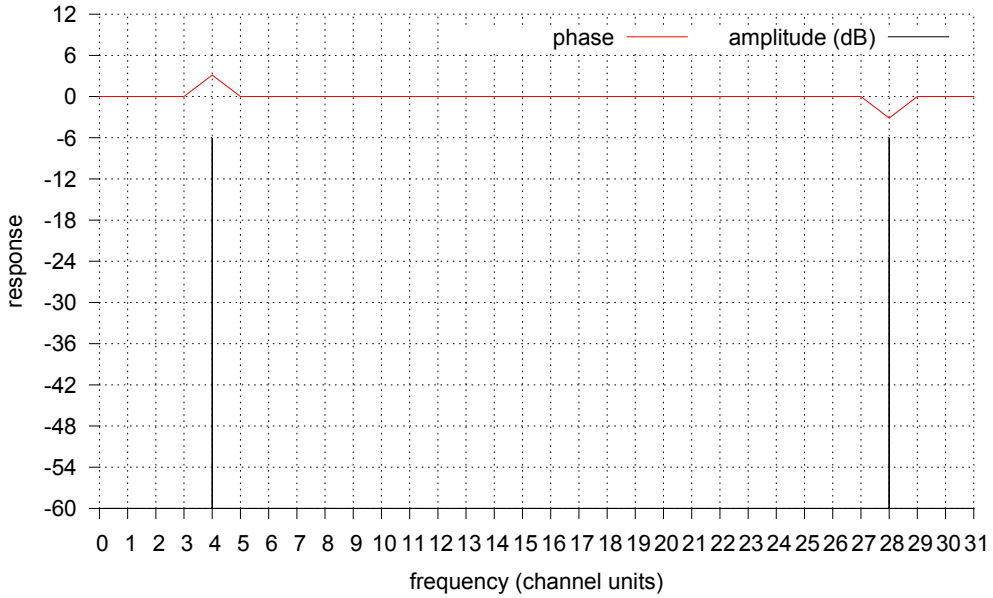

Figure 2.3: DFT spectrum with $N = 32$ channels. Input is a cosine with phase $\varphi = \pi$ that exactly matches channel $k = 4$. The amplitude spectrum is plotted in dB ($20 \lg \frac{|\hat{a}_k|}{N}$, black) and the phase in radians ($\Phi(\hat{a}_k)$, red).

Since $\overline{a_j}$ equals a_j with f and φ negated, using (2.5) and (2.20), yields the following spectrum:

$$\begin{aligned}
\hat{a}'_k &= \frac{1}{2} e^{-\pi i \cdot (k-k_f) \cdot \frac{N-1}{N} + i\varphi} \cdot \frac{\sin(\pi(k-k_f))}{\sin\left(\pi \frac{k-k_f}{N}\right)} + \frac{1}{2} e^{-\pi i \cdot (k+k_f) \cdot \frac{N-1}{N} - i\varphi} \cdot \frac{\sin(\pi(k+k_f))}{\sin\left(\pi \frac{k+k_f}{N}\right)} \\
&= \frac{1}{2} e^{+\pi i \cdot \frac{k}{N}} \cdot \sin(\pi k_f) \cdot \left(\frac{e^{+\pi i \cdot k_f \cdot \frac{N-1}{N} + i\varphi}}{\sin\left(\pi \frac{k-k_f}{N}\right)} + \frac{e^{-\pi i \cdot k_f \cdot \frac{N-1}{N} - i\varphi}}{\sin\left(\pi \frac{k+k_f}{N}\right)} \right)
\end{aligned} \tag{2.25}$$

$$\begin{aligned}
|\hat{a}'_k|^2 &= \hat{a}'_k \cdot \overline{\hat{a}'_k} \\
&= \frac{\sin^2(\pi k_f)}{4} \cdot \left(\frac{e^{+\pi i \cdot k_f \cdot \frac{N-1}{N} + i\varphi}}{\sin\left(\pi \frac{k-k_f}{N}\right)} + \frac{e^{-\pi i \cdot k_f \cdot \frac{N-1}{N} - i\varphi}}{\sin\left(\pi \frac{k+k_f}{N}\right)} \right) \cdot \left(\frac{e^{-\pi i \cdot k_f \cdot \frac{N-1}{N} - i\varphi}}{\sin\left(\pi \frac{k-k_f}{N}\right)} + \frac{e^{+\pi i \cdot k_f \cdot \frac{N-1}{N} + i\varphi}}{\sin\left(\pi \frac{k+k_f}{N}\right)} \right) \\
&= \frac{\sin^2(\pi k_f)}{4} \cdot \left(\frac{1}{\sin^2\left(\pi \frac{k-k_f}{N}\right)} + \frac{2 \cdot \cos\left(2\pi k_f \cdot \frac{N-1}{N} + 2\varphi\right)}{\sin\left(\pi \frac{k-k_f}{N}\right) \cdot \sin\left(\pi \frac{k+k_f}{N}\right)} + \frac{1}{\sin^2\left(\pi \frac{k+k_f}{N}\right)} \right)
\end{aligned} \tag{2.26}$$

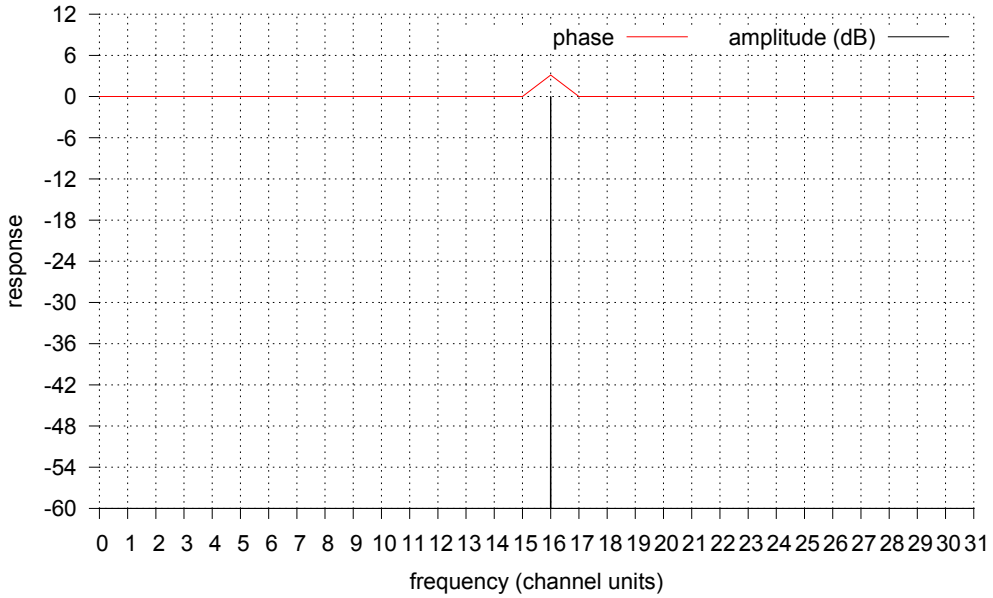

Figure 2.4: DFT spectrum with $N = 32$ channels. Input is a cosine with phase $\varphi = \pi$ that exactly matches channel $k = 16$. The amplitude Spectrum is plotted in dB ($20 \lg \frac{|\hat{a}_k|}{N}$, black) and the phase in radians ($\Phi(\hat{a}_k)$, red).

Again, this simplifies for frequencies $k_f = z$ that exactly match a spectral channel z. All channels $k \neq \pm z \bmod N$ show no spectral response:

$$\hat{a}'_k = \frac{1}{2} e^{+\pi i \cdot \frac{k}{N}} \cdot 0 \cdot \left(\frac{e^{+\pi i \cdot z \cdot \frac{N-1}{N} + i\varphi}}{\sin\left(\pi \frac{k-z}{N}\right)} + \frac{e^{-\pi i \cdot z \cdot \frac{N-1}{N} - i\varphi}}{\sin\left(\pi \frac{k+z}{N}\right)} \right) = 0 \tag{2.27}$$

The matching channels $k = \pm z \bmod N$ show a non-zero response (see figure 2.3), which can be calculated the same way as in (2.25):

$$\hat{a}'_k = e^{\pm i\varphi} \cdot \frac{N}{2} \tag{2.28}$$

In case $k = z \bmod N = -z \bmod N$, which is true for $k = z = 0 \bmod N$ or $k = z = \frac{N}{2} \bmod N$, both responses are added (see figure 2.4):

$$\hat{a}'_k = e^{+i\varphi} \cdot \frac{N}{2} + e^{-i\varphi} \cdot \frac{N}{2} = \cos(\varphi) \cdot N \tag{2.29}$$

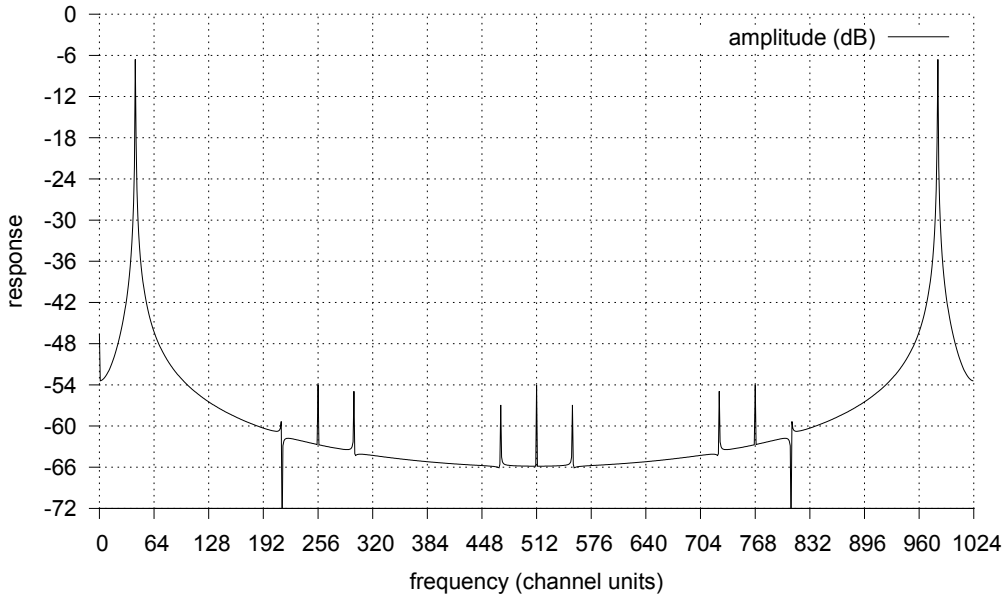

Figure 2.5: Response of a cosine with $k_f = 42.2$ in a DFT spectrum with $N = 1024$ channels, which is sampled 4 times interleaved. The first ADC has a 1 % offset error ($O_0 = 0.01$), the second has 1 % gain error ($G_1 = 1.01$) and the third has 1 % phase error ($P_2 = 0.01$). Y-axis shows the amplitude spectrum in dB ($20 \lg \frac{|\hat{a}_k|}{N}$).

2.3 Interleaving

When using M interleaved analog-to-digital converters (ADCs) to sample a signal, their offset, gain and phase may differ. ADC m therefore changes the original input sample $a_{M \cdot n+m}$ by offset O_m, gain G_m and phase P_m:

$$\begin{aligned} a'_{M \cdot n+m} &= a_{M \cdot n+m+P_m} \\ a''_{M \cdot n+m} &= G_m \cdot a'_{M \cdot n+m} \\ a'''_{M \cdot n+m} &= O_m + a''_{M \cdot n+m} \end{aligned} \tag{2.30}$$

Compared to an ideal ADC with $O = 0$, $G = 1$ and $P = 0$, this yields a spectral error and therefore altered spectra $\hat{a}'_k$, $\hat{a}''_k$ and $\hat{a}'''_k$ (figure 2.5).

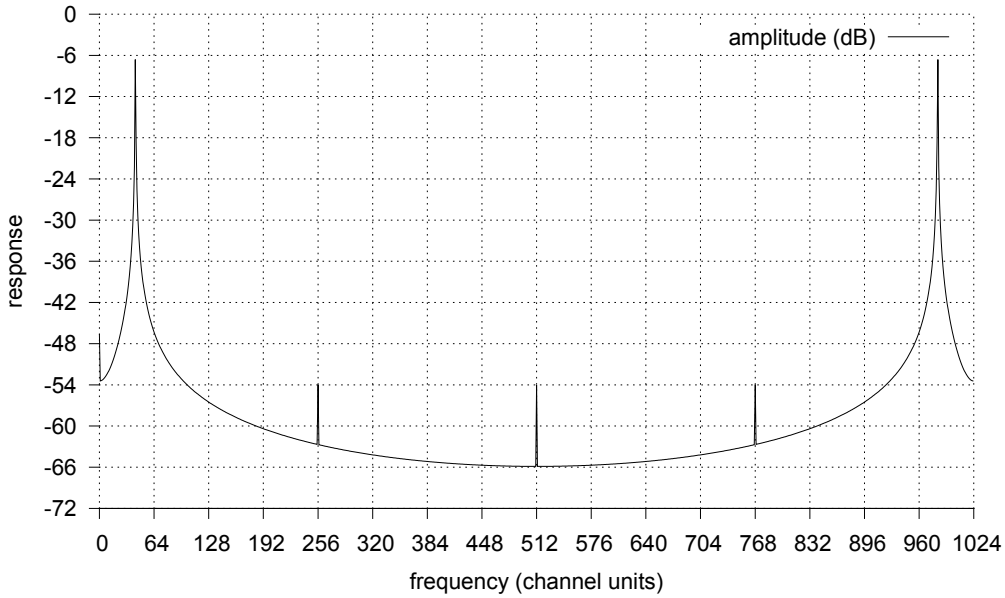

Figure 2.6: Response of a cosine with $k_f = 42.2$ in a DFT spectrum with $N = 1024$ channels, which is sampled 4 times interleaved. One ADC has a 1 % offset error. Y-axis shows the amplitude spectrum in dB ($20 \lg \frac{|\hat{a}_k|}{N}$).

Offset error To separate the offset error, one can assume the M samples O_m repeating themselves N times to create $M \cdot N$ samples $O'_{M \cdot n+m} = O_m$ and form a spectrum $\hat{O}'_k$ with the same size as $\hat{a}'''_k$ from the M channels of $\hat{O}_p$:

$$\begin{aligned} \hat{O}'_{N \cdot p+q} &= \sum_{m=0}^{M-1} \sum_{n=0}^{N-1} e^{-2\pi i \frac{(M \cdot n+m) \cdot (N \cdot p+q)}{M \cdot N}} \cdot O_m \\ &= \sum_{m=0}^{M-1} e^{-2\pi i \frac{m \cdot (N \cdot p+q)}{M \cdot N}} \cdot O_m \cdot \sum_{n=0}^{N-1} e^{-2\pi i \frac{n \cdot q}{N}} \end{aligned} \tag{2.31}$$

Dependent on $q = 0$, $\hat{O}_{N \cdot p+q}$ exists or not:

$$\begin{aligned} q \neq 0 : \hat{O}'_{N \cdot p+q} &= \sum_{m=0}^{M-1} e^{-2\pi i \frac{m \cdot (N \cdot p+q)}{M \cdot N}} \cdot O_m \cdot 0 = 0 \\ q = 0 : \hat{O}'_{N \cdot p+0} &= \sum_{m=0}^{M-1} e^{-2\pi i \frac{m \cdot p}{M}} \cdot O_m \cdot N = N \cdot \hat{O}_p \end{aligned} \tag{2.32}$$

Now offset error can be separated easily using (2.30) and (2.5), but is only present in M channels on fixed positions multiple of N:

$$\hat{a}'''_{N \cdot p+0} = \hat{a}''_{N \cdot p+0} + N \cdot \hat{O}_p \tag{2.33}$$

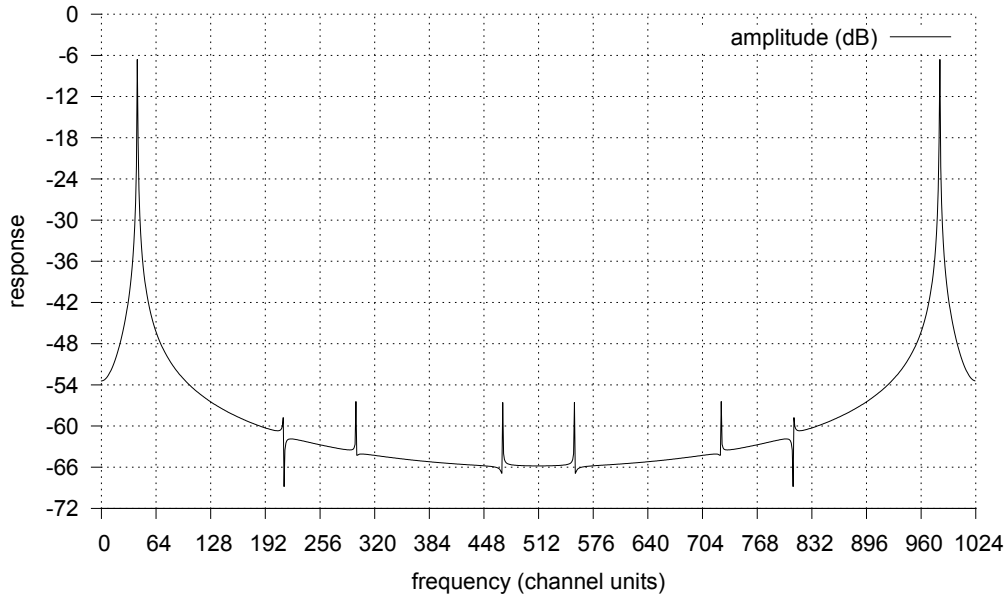

Figure 2.7: Response of a cosine with $k_f = 42.2$ in a DFT spectrum with $N = 1024$ channels, which is sampled 4 times interleaved. One ADC has a 1 % gain error. Y-axis shows the amplitude spectrum in dB ($20 \lg \frac{|\hat{a}_k|}{N}$).

All other channels are not changed by offset error: $\hat{a}'''_k = \hat{a}''_k$ (figure 2.6).

Gain error Gain error can be separated as well with an extended spectrum of G_m like in (2.31) and (2.32), using (2.30) with convolution (2.9):

$$\begin{aligned} \hat{a}''_k &= \frac{1}{MN} \sum_{l=0}^{M \cdot N - 1} \hat{G}'_l \cdot \hat{a}'_{k-l \bmod (M \cdot N)} \\ &= \frac{1}{M} \sum_{p=0}^{M-1} \hat{G}_p \cdot \hat{a}'_{k-N \cdot p \bmod (M \cdot N)} \end{aligned} \tag{2.34}$$

So gain error affects all channels, but only M channels with fixed distances multiple of N influence each other. Since real input samples yield a spectrum that is complex-conjugate-mirrored (compare (2.81)), gain error adds $M - 1$ attenuated mirror-images to a spectrum (figure 2.7).

Phase error Since phase error shifts the moment a sample is taken, usually by a fraction of the sampling-frequency, it can only be specified with further assumptions about the input-signal between the samples usually taken.

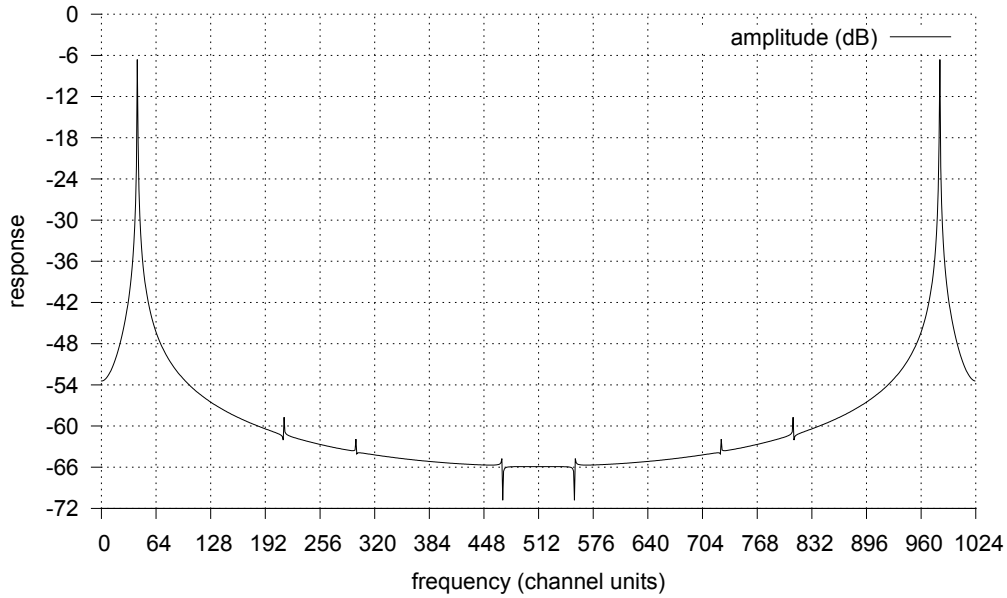

Figure 2.8: Response of a cosine with $k_f = 42.2$ in a DFT spectrum with $N = 1024$ channels, which is sampled 4 times interleaved. One ADC has a 1 % phase error. Y-axis shows the amplitude spectrum in dB ($20 \lg \frac{|\hat{a}_k|}{N}$, black).

One possibility is to assume linear behavior between two samples. With $0 \leq P_m \leq 1$ this can be written as

$$a'_{M \cdot n+m} = (1 - P_m) \cdot a_{M \cdot n+m} + P_m \cdot a_{M \cdot n+m+1} \tag{2.35}$$

Using (2.5), (2.9) and (2.7), this yields the following spectrum:

$$\begin{aligned} \hat{a}'_k &= \frac{1}{M} \sum_{p=0}^{M-1} \left(1 - \hat{P}_p\right) \cdot \hat{a}'_{k-N \cdot p \bmod (M \cdot N)} + \frac{1}{M} \sum_{p=0}^{M-1} \hat{P}_p \cdot e^{+2\pi i \frac{k}{M \cdot N}} \cdot \hat{a}'_{k-N \cdot p \bmod (M \cdot N)} \\ &= \frac{1}{M} \sum_{p=0}^{M-1} \left(1 - \hat{P}_p \cdot \left(1 - e^{+2\pi i \frac{k}{M \cdot N}}\right)\right) \cdot \hat{a}_{k-N \cdot p \bmod (M \cdot N)} \end{aligned} \tag{2.36}$$

Another possibility is to assume a common input. A phasor yields samples, phase error changes by a repeating complex factor:

$$\begin{aligned} a_{M \cdot n+m} &= e^{+2\pi i \frac{f}{f_S} \cdot (M \cdot n+m)+i\varphi} \\ \Rightarrow a'_{M \cdot n+m} &= e^{+2\pi i \frac{f}{f_S} \cdot (M \cdot n+m+P_m)+i\varphi} \\ &= e^{+2\pi i \frac{f}{f_S} \cdot P_m} \cdot a_{M \cdot n+m} \end{aligned} \tag{2.37}$$

Defining $Q_m = e^{+2\pi i \frac{f}{f_S} \cdot P_m}$, calculating the according spectrum $\hat{Q}_p$, and using the same method as for gain (2.34) yields the spectral error:

$$\hat{a}'_k = \frac{1}{M} \sum_{p=0}^{M-1} \hat{Q}_p \cdot \hat{a}_{k-N \cdot p \bmod (M \cdot N)} \tag{2.38}$$

A cosine yields a similar result, since the cosine, sampled with phase error, can be written as a sum of M regular cosines at frequencies with constant distances [58]:

$$\begin{aligned} a_{M \cdot n+m} &= \cos\left(2\pi \frac{f}{f_S} \cdot (M \cdot n + m) + \varphi\right) \\ \Rightarrow a'_{M \cdot n+m} &= \cos\left(2\pi \frac{f}{f_S} \cdot (M \cdot n + m + P_m) + \varphi\right) \\ &= \sum_{p=0}^{M-1} A_p \cdot \cos\left(2\pi \left(\frac{f}{f_S} + \frac{p}{M}\right) \cdot (M \cdot n + m) + \varphi_p\right) \end{aligned} \tag{2.39}$$

So with usual input, we can expect phase error to affect the spectrum in a similar way gain error does: M channels with fixed distances multiple of N influence each other. With real input samples, this adds $M - 1$ attenuated mirror-images to a spectrum (figure 2.8).

2.4 Windowing

Chapter 2.2 provides formulas that show how an N-point DFT responds to a single tone of frequency f that matches no channel k exactly. So the frequency's channel k_f is a fractional number, which means $\delta_{f,k}$ is never zero:

$$\begin{aligned} k_f &\neq k, \quad \forall_k \\ \delta_{f,k} &\neq 0, \quad \forall_k \end{aligned} \tag{2.40}$$

As (2.20)–(2.26) indicate, an input of that kind leaks into each channel $0 \leq k < N$ and a channel k leaks sensitivity for nearby frequencies ($k_f \approx k$) to distant ones. The response diagram in figure 2.9 displays this leakage effect, as well as the aliasing effect, described in (2.13). Leakage is a result of the limited amount of samples the DFT processes, which equals a rectangular window over an infinite amount of samples: N samples inside the window are multiplied by one, all others by zero.

One method to reduce leakage is to multiply the input samples a_j with a window w_j other than a rectangular one. This represents a convolution between the original spectrum $\hat{a}_k$ and the spectrum of the window $\hat{w}_k$ (compare (2.9)) and allows to recover some leakage from other channels:

$$\begin{aligned} b_j &= w_j \cdot a_j \\ \Rightarrow \hat{b}_k &= \frac{1}{N} \sum_{l=0}^{N-1} \hat{w}_l \cdot \hat{a}_{k-l \bmod N} \end{aligned} \tag{2.41}$$

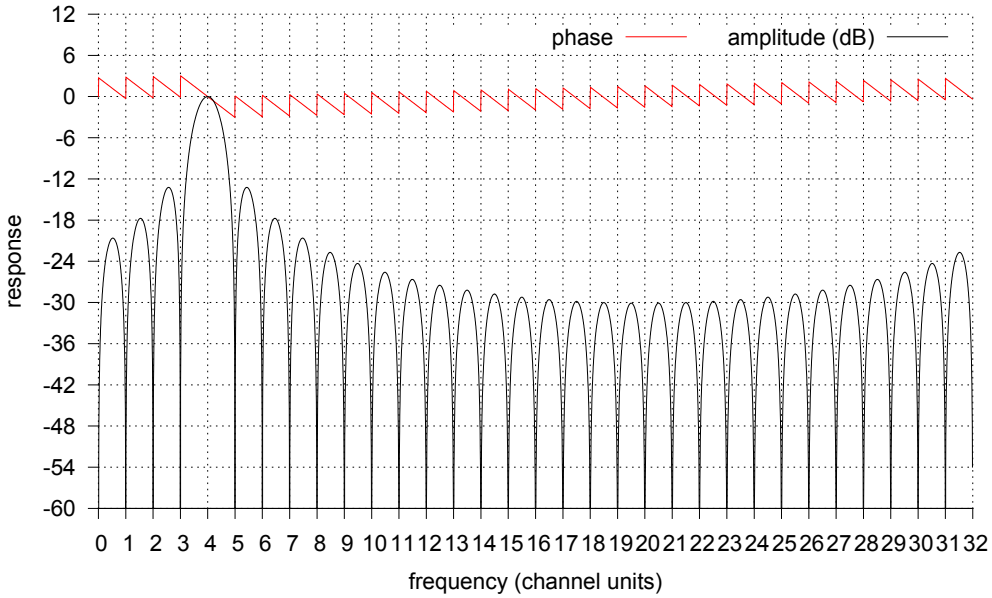

Figure 2.9: Response of phasors in channel $k = 4$ of a DFT spectrum with $N = 32$ channels. X-axis runs over input frequencies f of phasors and is scaled to k_f. Y-axis shows the amplitude spectrum in dB ($20 \lg \frac{|\hat{a}_k|}{N}$, black) and the phase in radians ($\Phi(\hat{a}_k)$, red).

Leakage is usually measured by the response of a channel $\hat{b}_k$ to phasors with frequencies f around the channel's frequency, which is plotted in a response diagram. The focus lies on properties of the response diagram for the channel's amplitude or power. Using samples a_j of a phasor as in (2.12) and (2.20) with (2.14) and (2.41) yields the following:

$$\begin{aligned} \hat{b}_k &= \frac{1}{N} \sum_{l=0}^{N-1} \hat{w}_l \cdot e^{-\pi i \cdot \left(\delta_{f,k} - l\right) \cdot \frac{N-1}{N} + i\varphi} \cdot \frac{\sin\left(\pi\left(\delta_{f,k} - l\right)\right)}{\sin\left(\pi \frac{\delta_{f,k} - l}{N}\right)} \\ &= e^{-\pi i \cdot \delta_{f,k} \cdot \frac{N-1}{N} + i\varphi} \cdot \sin\left(\pi \delta_{f,k}\right) \cdot \frac{1}{N} \sum_{l=0}^{N-1} \hat{w}_l \cdot \frac{e^{-\pi i \cdot \frac{l}{N}}}{\sin\left(\pi \frac{\delta_{f,k} - l}{N}\right)} \end{aligned} \tag{2.42}$$

$$\left|\hat{b}_k\right|^2 = \frac{\sin^2\left(\pi \delta_{f,k}\right)}{N^2} \cdot \left| \sum_{l=0}^{N-1} \hat{w}_l \cdot \frac{e^{-\pi i \cdot \frac{l}{N}}}{\sin\left(\pi \frac{\delta_{f,k} - l}{N}\right)} \right|^2 \tag{2.43}$$

Of course the phase $\Phi\left(\hat{b}_k\right)$ of the response $\hat{b}_k$ can be extracted as well as its amplitude or its power. To simplify the handling of upcoming equations, we separate the phase into the part from the input φ and the rest $\beta_{w,f,k}$, dependent on the window w_j and on $\delta_{f,k}$, but independent of φ:

$$\begin{aligned} \beta_{w,f,k} &= -\pi \cdot \delta_{f,k} \cdot \frac{N-1}{N} + \Phi\left(\sum_{l=0}^{N-1} \hat{w}_l \cdot \frac{e^{-\pi i \cdot \frac{l}{N}}}{\sin\left(\pi \frac{\delta_{f,k}-l}{N}\right)}\right) \\ \Rightarrow \hat{b}_k &= e^{+i\varphi + i\beta_{w,f,k}} \cdot \left|\hat{b}_k\right| \end{aligned} \tag{2.44}$$

To simplify the calculation of $\hat{b}_k$, one can assume that $\delta_{f,k}$ is sufficiently well approximated by a binary fixed-point number:

$$\delta_{f,k} = \frac{z}{M}, \quad z \in \mathbb{Z} \tag{2.45}$$

Now using M to be a power of two and feeding an $M \cdot N$-point DFT with a window w_j of size N which is filled up with zeros, yields channels $\hat{c}_k$, similar to $\hat{b}_k$:

$$\begin{aligned} c_j &= \begin{cases} w_j, & 0 \le j < N \\ 0, & N \le j < M \cdot N \end{cases} \\ \Rightarrow \hat{c}_k &= \sum_{j=0}^{N-1} e^{-2\pi i \frac{j \cdot k}{M \cdot N}} \cdot w_j \end{aligned} \tag{2.46}$$

Combining (2.45) and (2.46) with the definition in (2.20), now easily yields $\hat{b}_k$:

$$\begin{aligned} \hat{b}_k &= e^{+i\varphi} \cdot \sum_{j=0}^{N-1} e^{-2\pi i \cdot \frac{\delta_{f,k}}{N} \cdot j} \cdot w_j \\ &= e^{+i\varphi} \cdot \sum_{j=0}^{N-1} e^{-2\pi i \frac{z}{M \cdot N} \cdot j} \cdot w_j = e^{+i\varphi} \cdot \hat{c}_z \end{aligned} \tag{2.47}$$

Leakage of a cosine wave As (2.21) shows for a rectangular window and (2.43) shows in general, the response power of phasors only depends on $\delta_{f,k}$. It is in particular independent of the phasor's phase φ and the channel k. Unfortunately, (2.26) indicates that this does not hold for a single sine or cosine wave: In this case leakage depends on phase φ and is different for each channel k. To analyze a windowed cosine-input a'_j with frequency f, it is defined as the mean of two phasors a_j, $\overline{a_j}$, the same way as in (2.24). This yields a similar definition for b'_j, since a window is real $w_j \in \mathbb{R}$:

$$b'_j = \frac{b_j + \overline{b_j}}{2} = \cos(2\pi \frac{f}{f_\mathrm{S}} \cdot j + \varphi) \cdot w_j \tag{2.48}$$

Using (2.5) and (2.8) and combining both with (2.44), allows to calculate the response of $\hat{b}'_k$, dependent on the response of the phasors:

$$\hat{b}'_k = \frac{\hat{b}_k + \overline{\hat{b}_{N-k}}}{2} = \frac{1}{2} e^{+i\varphi + i\beta_{w,f,k}} \cdot \left|\hat{b}_k\right| + \frac{1}{2} e^{-i\varphi - i\beta_{w,f,N-k}} \cdot \left|\hat{b}_{N-k}\right| \tag{2.49}$$

$$\left|\hat{b}'_k\right|^2 = \hat{b}'_k \cdot \overline{\hat{b}'_k} = \frac{1}{4} \cdot \left(\left|\hat{b}_k\right|^2 + 2 \cdot \cos\left(2\varphi + \beta_{w,f,k} + \beta_{w,f,N-k}\right) \cdot \left|\hat{b}_k\right| \cdot \left|\hat{b}_{N-k}\right| + \left|\hat{b}_{N-k}\right|^2 \right) \tag{2.50}$$

For a given window w_j, input-frequency f, and channel k, one can now use properties of the cosine and the binomial theorems to define the average, the minimum, and the maximum of the response-power over all input phases φ:

$$\varnothing_\varphi \left(\left|\hat{b}'_k\right|^2 \right) = \frac{1}{4} \cdot \left(\left|\hat{b}_k\right|^2 + 0 \cdot \left|\hat{b}_k\right| \cdot \left|\hat{b}_{N-k}\right| + \left|\hat{b}_{N-k}\right|^2 \right) = \frac{\left|\hat{b}_k\right|^2 + \left|\hat{b}_{N-k}\right|^2}{4} \tag{2.51}$$

$$\max_\varphi \left(\left|\hat{b}'_k\right|^2 \right) = \frac{1}{4} \cdot \left(\left|\hat{b}_k\right|^2 + 2 \cdot \left|\hat{b}_k\right| \cdot \left|\hat{b}_{N-k}\right| + \left|\hat{b}_{N-k}\right|^2 \right) = \frac{\left(\left|\hat{b}_k\right| + \left|\hat{b}_{N-k}\right| \right)^2}{4} \tag{2.52}$$

$$\min_\varphi \left(\left|\hat{b}'_k\right|^2 \right) = \frac{1}{4} \cdot \left(\left|\hat{b}_k\right|^2 - 2 \cdot \left|\hat{b}_k\right| \cdot \left|\hat{b}_{N-k}\right| + \left|\hat{b}_{N-k}\right|^2 \right) = \frac{\left(\left|\hat{b}_k\right| - \left|\hat{b}_{N-k}\right| \right)^2}{4} \tag{2.53}$$

Since $\hat{b}_{N-k}$ is the same spectrum as $\hat{b}_k$ shifted dependent on k, the response power of cosines can be estimated easily from the response power of the phasors. As previously shown in figure 2.9, response power drops quite rapidly with increasing distance between k and k_f, even with a rectangular window. This has two effects, which can both be seen in figure 2.10. First, the closer $N - k$ is to k, the greater the span between minimum and maximum values, since the absolute values of $\hat{b}_{N-k}$ and $\hat{b}_k$ differ less. Therefore this span is highest for the DC-channel $k = 0$ and the Nyquist channel $k = \frac{N}{2}$, and lowest for the channel $k = \frac{N}{4}$ exactly between them. Secondly, the average response-power differs less between different channels k than the minimum or the maximum response power. This is because the powers of $\hat{b}_k$ and $\hat{b}_{N-k}$ in (2.51) differ more than their amplitudes in (2.52) and (2.53).

Measuring leakage Depending on the needs, leakage may be measured by various properties of a response diagram. Since a window w_j and its spectrum $\hat{w}_k$ may vary with N, we define $\vec{w}_N$ as a window w_j of size N. Two common properties of such a window are the main lobe's width and the side lobes' roll-off [66, Ch. 6]. The width of the main lobe indicates the separation from the neighboring channel. A narrow main lobe highly attenuates frequencies between the channels. A wide main lobe results in more response to frequencies closer to the neighboring channel. The roll-off of the side lobes indicates the separation from far-away channels. A flat roll-off indicates a uniformly low response to a wide range of frequencies, whereas a steep roll-off indicates a strong

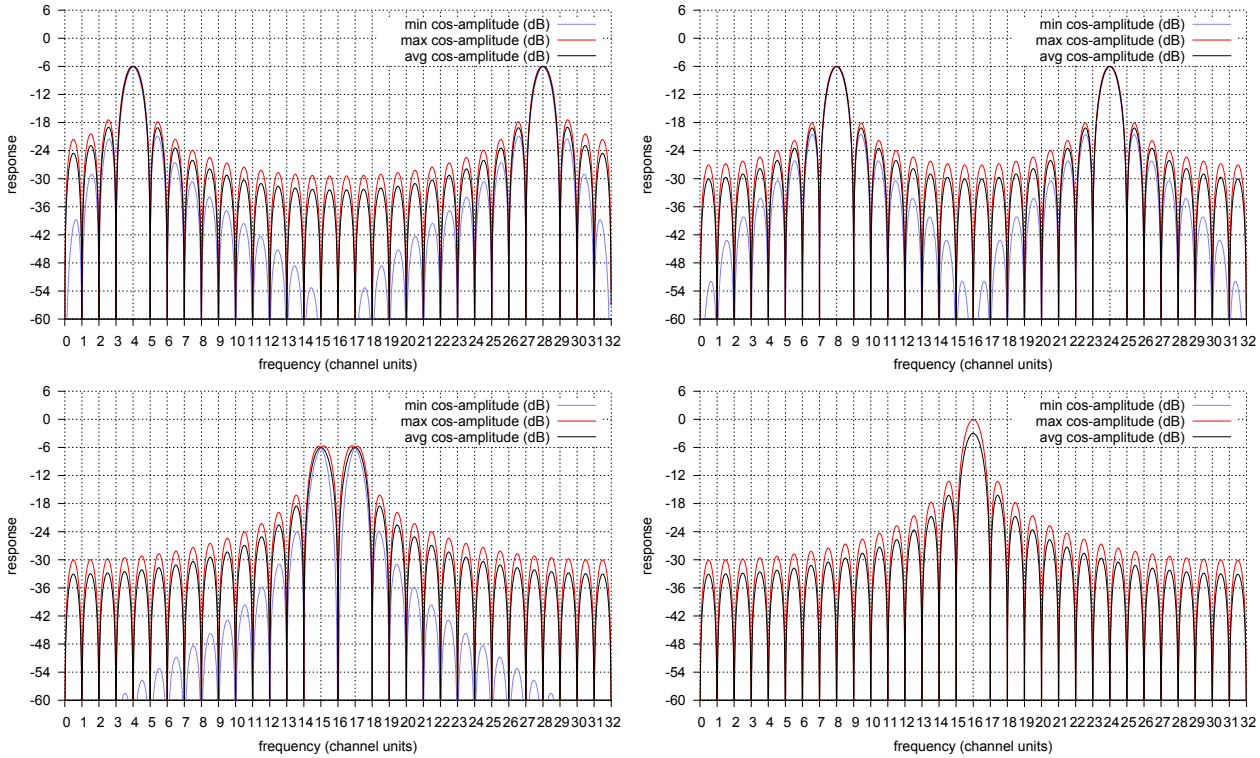

Figure 2.10: Response of cosines in channels $k = 4$, $k = 8$, $k = 15$ and $k = 16$ of a DFT spectrum with $N = 32$ channels. X-axis runs over input frequencies f of cosines and is scaled to k_f. The cosines phases $\varphi(f)$ are chosen for average (black), maximum (red) and minimum (blue) response. Y-axis shows the amplitude spectra in dB ($20 \lg \frac{|\hat{a}_k|}{N}$).

dependency between response and channel distance $\delta_{f,k}$. Another very common property is the $NENBW$ of a window [36]. It is the normalized quotient of the incoherent power gain PG_{I} and the coherent power gain PG_{C}, and evaluates the noise power accumulated in a bin (PG_{I}) relative to the signal power in the center of the bin (PG_{C}):

$$\begin{aligned} PG_{\mathrm{I}}(\vec{w}_N) &= \sum_{j=0}^{N-1} w_j^2 = \frac{1}{N} \sum_{k=0}^{N-1} |\hat{w}_k|^2 \\ PG_{\mathrm{C}}(\vec{w}_N) &= \left| \sum_{j=0}^{N-1} w_j \right|^2 = |\hat{w}_0|^2 \\ NENBW(\vec{w}_N) &= N \cdot \frac{PG_{\mathrm{I}}(\vec{w}_N)}{PG_{\mathrm{C}}(\vec{w}_N)} \end{aligned} \tag{2.54}$$

Furthermore the normalized equivalent noise bandwidth $NENBW$ is a window-specific factor between DFT resolution and the ENBW:

$$ENBW\left(\vec{w}_N\right) = NENBW\left(\vec{w}_N\right) \cdot \frac{f_\mathrm{S}}{N} \tag{2.55}$$

It is obvious that $NENBW\left(\vec{w}_N\right) \geq 1$. Consistent with (2.4), a rectangular window $w_j = 1$ yields $NENBW\left(\vec{w}_N\right) = 1$. Processing gain PG, the gain in signal-to-noise ratio (S/N) of the whole windowed DFT, and processing loss PL, the loss in S/N compared to an unwindowed DFT of the same length, are closely related to the $NENBW$:

$$\begin{aligned} PG\left(\vec{w}_N\right) &= \frac{N}{NENBW\left(\vec{w}_N\right)} \\ PL\left(\vec{w}_N\right) &= \frac{1}{NENBW\left(\vec{w}_N\right)} \end{aligned} \tag{2.56}$$

Relevant literature describes other properties correlated to the aforementioned properties. For instance, the width of the main lobe correlates with the minimum resolution bandwidth. It measures the range of frequencies that respond with at least half the power of the central one (3 dB-bandwidth $BW_{3\mathrm{dB}}$) or with half the amplitude (6 dB-bandwidth $BW_{6\mathrm{dB}}$). Both are used as indicators for the minimum distance over which equally powered frequencies can be distinguished, though only the latter qualifies for that purpose [35]. Scalloping loss also correlates with the main lobe's width. It measures the response to a frequency half way between two channels relative to the central response, and thereby quantifies worst case attenuation of a single frequency. For simple windows, it indicates the main lobe's flatness as well. However, there are common windows whose response power in the center of a bin is even lower than it is half way between two channels. One way to compensate this drawback is to measure the flatness of a window's main lobe. This can be performed by relating the minimum and maximum response power to all frequencies between the center of a bin and the point half way to the next bin [36]. Using (2.43), scalloping loss can be calculated by the power channel $\hat{b}_k$ responds with to a phasor of frequency $k_f = k - \frac{1}{2}$, divided by PG_C:

$$\begin{aligned} \left|\hat{b}_k\right|^2 &= \frac{1}{N^2} \cdot \left| \sum_{l=0}^{N-1} \hat{w}_l \cdot \frac{e^{-\pi i \cdot \frac{l}{N}}}{\sin\left(\pi\left(\frac{1}{2N} - \frac{l}{N}\right)\right)} \right|^2 \\ SL\left(\vec{w}_N\right) &= \frac{1}{\left|\hat{w}_0\right|^2} \cdot \left| \sum_{k=0}^{N-1} \hat{w}_k \cdot \frac{e^{-\pi i \cdot \frac{k}{N}}}{N \cdot \sin\left(\pi\left(\frac{1}{2N} - \frac{k}{N}\right)\right)} \right|^2 \end{aligned} \tag{2.57}$$

Aside from the side lobe level, the worst case processing loss $WCPL$ is considered the most important indicator of the quality of a window [35]. It combines the effect of scalloping loss and processing loss:

$$\begin{aligned} WCPL\left(\vec{w}_N\right) &= PL\left(\vec{w}_N\right) \cdot SL\left(\vec{w}_N\right) \\ &= \frac{\left| \sum_{k=0}^{N-1} \hat{w}_k \cdot \frac{e^{-\pi i \cdot \frac{k}{N}}}{N \cdot \sin\left(\pi\left(\frac{1}{2N} - \frac{k}{N}\right)\right)} \right|^2}{\sum_{k=0}^{N-1} \left|\hat{w}_k\right|^2} \end{aligned} \tag{2.58}$$

As (2.57) and (2.58) indicate, properties of a window's response may vary with N. Therefore, to find the universal properties of the windows, it is necessary to define them more generally than merely by their responses. Since leakage drops with increasing distance $\delta_{f,k}$, windowing usually recovers energy from nearby channels. Although there are lots of window types, most common windows w_j are therefore a combination of carefully weighted cosines with not more than a small number K of oscillations [35]:

$$w_j = \sum_{k=0}^{K} c_k \cdot (-1)^k \cdot \cos\left(2\pi \frac{k}{N} \cdot j\right) \tag{2.59}$$

Using (2.5) and (2.28), this yields a window spectrum $\hat{w}_k$ that only differs from zero in $2K+1$ points (compare (2.41)):

$$\begin{array}{rll} \hat{w}_0 & = c_0 \cdot N & \\ \hat{w}_k = \hat{w}_{N-k} & = c_k \cdot \frac{N}{2} \cdot (-1)^k & , \ 0 < k \leq K \\ \hat{w}_k = \hat{w}_{N-k} & = 0 & , \ K < k \leq \frac{N}{2} \end{array} \tag{2.60}$$

Therefore, windows such as those described in (2.60) affect the aforementioned properties in the following way: as can be expected, the normalized equivalent noise bandwidth is a universal property, independent of N. Incoherent and coherent power gain are not, but could be easily normalized by dividing them by their respective values for an unwindowed DFT $PG_{\mathrm{I}}(\mathrm{rect}_N) = N$, $PG_{\mathrm{C}}(\mathrm{rect}_N) = N^2$:

$$\begin{aligned} PG_{\mathrm{I}}(\vec{w}_N) &= N\left(c_0^2 + \frac{1}{2}\sum_{k=1}^{K} c_k^2\right) \\ PG_{\mathrm{C}}(\vec{w}_N) &= N^2 c_0^2 \\ NENBW(\vec{w}) &= 1 + \frac{1}{2c_0^2}\sum_{k=1}^{K} c_k^2 \end{aligned} \tag{2.61}$$

The scalloping loss equation can be rewritten to depend on c_k:

$$SL(\vec{w}_N) = \frac{1}{c_0^2} \cdot \left(\sum_{k=0}^{K} c_k \cdot \frac{(-1)^k}{2N} \cdot \left(\frac{e^{-\pi i \cdot \frac{k}{N}}}{\sin\left(\pi\left(\frac{1}{2N} - \frac{k}{N}\right)\right)} + \frac{e^{\pi i \cdot \frac{k}{N}}}{\sin\left(\pi\left(\frac{1}{2N} + \frac{k}{N}\right)\right)}\right)\right)^2 \tag{2.62}$$

To find a universal value independent of N, it is not sufficient to divide it by $SL(\mathrm{rect})$. Instead, it needs to be approximated by increasing N to infinity. This is now possible, assuming $k \leq K << N$:

$$\begin{aligned} SL(\vec{w}) = \lim_{N\to\infty} SL(\vec{w}_N) &= \frac{1}{c_0^2} \cdot \left(\sum_{k=0}^{K} c_k \cdot (-1)^k \cdot \left(\frac{1}{\pi(1-2k)} + \frac{1}{\pi(1+2k)}\right)\right)^2 \\ &= \frac{1}{c_0^2} \cdot \frac{4}{\pi^2} \cdot \left(\sum_{k=0}^{K} c_k \cdot \frac{(-1)^k}{1-4k^2}\right)^2 \end{aligned} \tag{2.63}$$

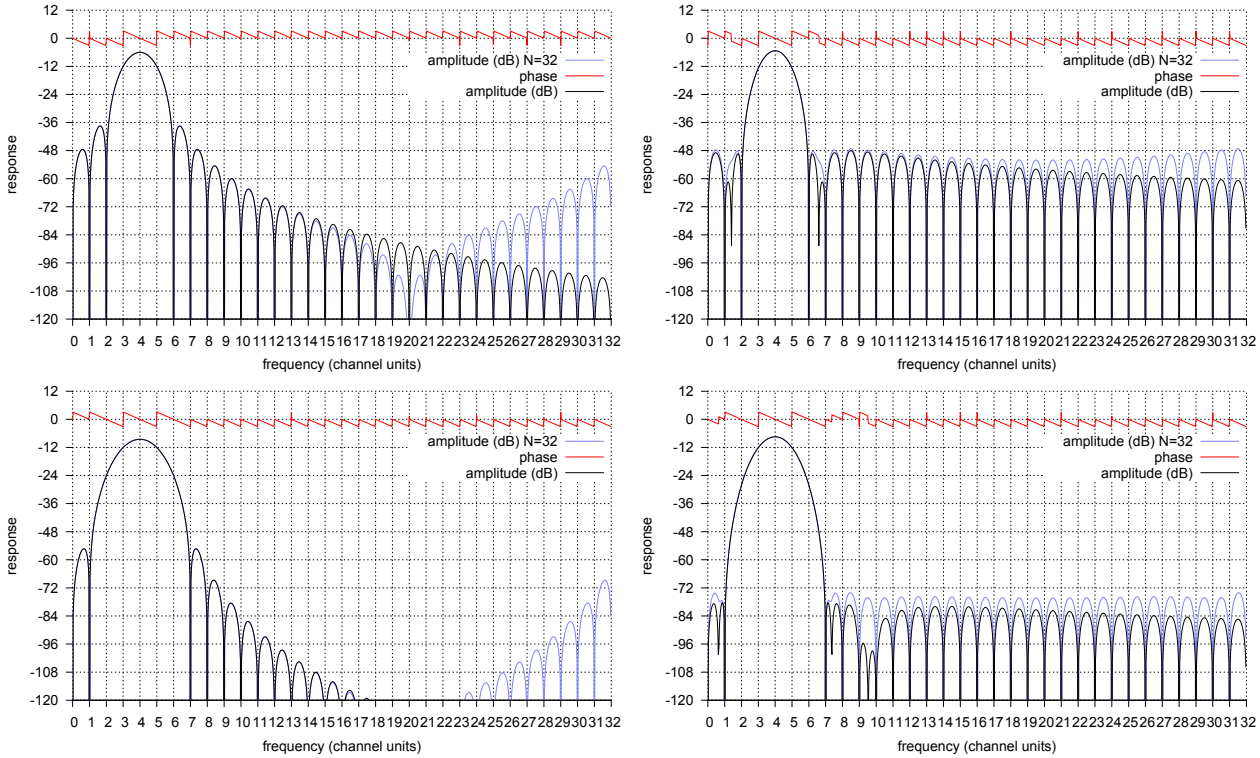

Figure 2.11: Response of phasors in channel $k = 4$, preprocessed with different windows: Hanning window (upper left), Hamming window (upper right), 3-term Nuttall window (lower left) and minimum 3-term Blackman-Harris window (lower right). Each plot shows amplitude in dB (black) and phase (red) of a DFT spectrum with $N = 32768$ channels and amplitude in dB (blue) of a DFT spectrum with $N = 32$ channels.

The same conclusion is obviously achieved for worst case processing loss $WCPL$, using (2.58) with (2.61) and (2.63). It is, however, important to consider the differences between the universal values and the ones for small N. The normalized side lobe level (relative to the main lobe's level) is affected by N in two ways. First, (2.23) shows that the average level decreases with N, since the absolute main lobe level rises proportionally to N, whereas (2.21) suggests that the absolute level far from the main lobe does not. Secondly, figure 2.9 shows how the phase shifts not only by 2π per bin, but by an additional 2π over the whole spectrum. Windows made of cosines try to return leaked energy to neighboring bins by adding or subtracting their responses (compare (2.41)). If the DFT introduces too much phase shift between neighboring channels, this may fail. To illustrate the effect, the upcoming examples show the response of two DFTs with different N. So to find an universal value for the level of the strongest side lobe, N needs to run to infinity as well.

Table 2.1: Cosine parameters of different windows: Hanning window, Hamming window, 3-term Nuttall window and minimum 3-term Blackman-Harris window.

	$\mathbf{c_0}$	$\mathbf{c_1}$	$\mathbf{c_2}$
Rectangle	1		
Hanning	0.5	0.5	
Hamming	0.54	0.46	
Nuttall3	0.375	0.5	0.125
Blackman-Harris	~ 0.42323	~ 0.49755	~ 0.07922

Table 2.2: Properties of different windows: Hanning window, Hamming window, 3-term Nuttall window and minimum 3-term Blackman-Harris window.

	NENBW	SL	$\mathbf{BW_{6dB}}$	max side lobe	roll-off/octave
Rectangle	$1.00 \equiv 0.00\,\text{dB}$	$-3.92\,\text{dB}$	1.21 bins	$-13.3\,\text{dB}$	$\frac{1}{2} \equiv -6\,\text{dB}$
Hanning	$1.50 \equiv 1.76\,\text{dB}$	$-1.42\,\text{dB}$	2.00 bins	$-31.5\,\text{dB}$	$\frac{1}{8} \equiv -18\,\text{dB}$
Hamming	$\sim 1.36 \equiv 1.34\,\text{dB}$	$-1.75\,\text{dB}$	1.81 bins	$-43.2\,\text{dB}$	$-6\,\text{dB}$
Nuttall3	$1.9\overline{4} \equiv 2.89\,\text{dB}$	$-0.86\,\text{dB}$	2.58 bins	$-46.7\,\text{dB}$	$\frac{1}{32} \equiv -30\,\text{dB}$
Blackman-Harris	$\sim 1.69 \equiv 2.29\,\text{dB}$	$-1.15\,\text{dB}$	2.27 bins	$-70.8\,\text{dB}$	$-6\,\text{dB}$

Examples for windows Some very common windows are made of less than 2 cosines. Their parameters are listed in table 2.1. Using (2.61) and (2.63) with these parameters easily yields $NENBW$, SL and their quotient $WCPL$. Table 2.2 lists them, along with other common properties from literature [35, 36, 77, 74]. The most simple window is the Rectangle window (figure 2.9). Therefore, it is easy to process. Although it performs badly in most applications, it accumulates less noise than any other window, since $NENBW\,(\text{rect}) = 1$, and it has the most narrow main-lobe. In case a channel exactly matches, these properties may improve signal to noise ratio as well as frequency resolution. So a rectangular window should be considered for an input that is aligned with the DFT. The Hanning and the Hamming windows (figure 2.11) are made of one cosine ($K = 1$), which gives them a parameter to optimize: the weight of this cosine. The former one weighs it with 0.50, the latter one with 0.46 (compare (2.1)). The Hanning window uses this to optimize the side lobes' roll-off rate, by adjusting the window borders to 0 [77]. The Hamming window minimizes the highest side lobe by reducing the response to a frequency $f_{0,\text{Hamming}}$ in the first side lobe to zero:

$$\begin{aligned} \delta_{k,f_{0,\text{Hamming}}} &= \frac{3}{2} \cdot \sqrt{3} \approx 2.598 \\ \Rightarrow \hat{b}_k &= 0 \end{aligned} \tag{2.64}$$

Therefore, frequencies near $f_{0,\mathrm{Hamming}}$ are attenuated as well and the maximum level of the side lobe decreases. A further advantage of the Hanning window besides leakage properties, is the possibility of calculating it easily by convoluting spectra [35]. The 3-term Nuttall window [77] and the Minimum 3-term Blackman-Harris window [35, 77] are both plotted in figure 2.11. They are made of two cosines ($K = 2$), which gives them two degrees of freedom to optimize the response. Nuttall uses both to increase side lobe roll-off. Harris uses each one to reduce the response to some side lobe frequency $f_{0,\mathrm{Bl-H}}$ to zero:

$$\begin{aligned} \delta_{k,f_{0,\mathrm{Bl.Harris}}} &\approx 3.4 \\ \vee\, \delta_{k,f_{0,\mathrm{Bl.Harris}}} &\approx 5.5 \\ \Rightarrow \hat{b}_k &= 0 \end{aligned} \tag{2.65}$$

Of course one can trade these optimizations off as well, using one degree of freedom to increase roll-off and one to lower the maximum side lobe, which the Blackman window does.

One can observe that a narrow main lobe comes with a high average side lobe level, and vice versa. Furthermore, the width of the main lobe depends on K for windows made of cosines. For main lobes of comparable width, i.e. the same value of K, the rate of asymptotic roll-off competes against the level of the first side lobe, as well as against the flatness of the main lobe: A flat roll-off allows to optimize the other properties.

2.5 WOLA

The weighted overlap-add (WOLA) is a method to increase effective spectral-resolution by reducing leakage of a following DFT with real input. To perform M-fold WOLA for an N-point DFT, $M \cdot N$ real input samples a_j are first multiplied by a window function w_j of same size:

$$b_j = a_j \cdot w_j \tag{2.66}$$

If these $M \cdot N$ weighted input samples b_j are divided into M frames m, each with N consecutive samples n, so that $j = m \cdot N + n$, the frames can be overlapped so that one sample of each frame corresponds. The corresponding samples of each segment are added:

$$c_n = \sum_{m=0}^{M-1} b_{m \cdot N + n} \tag{2.67}$$

The N sums c_n may form the input samples of a following N-point DFT resulting in N channels $\hat{c}_q$:

$$\hat{c}_q = \sum_{n=0}^{N-1} e^{-2\pi i \frac{n \cdot q}{N}} \cdot c_n \tag{2.68}$$

The same weighted input samples b_j could be used for an $M \cdot N$-point DFT as well and would result in $M \cdot N$ channels $\hat{b}_k$:

$$\hat{b}_k = \sum_{j=0}^{M \cdot N - 1} e^{-2\pi i \frac{j \cdot k}{M \cdot N}} \cdot b_j \tag{2.69}$$

Combining (2.69) with (2.67) and (2.68), and using $e^{-2\pi i \frac{(m \cdot N) \cdot q}{N}} = 1$ with $m, q \in \mathbb{N}$, shows that spectrum $\hat{b}_k$ implies spectrum $\hat{c}_q$:

$$\begin{aligned}
\hat{c}_q &= \sum_{n=0}^{N-1} e^{-2\pi i \frac{n \cdot q}{N}} \cdot c_n \\
&= \sum_{n=0}^{N-1} e^{-2\pi i \frac{(m \cdot N + n) \cdot q}{N}} \cdot \sum_{m=0}^{M-1} b_{m \cdot N + n} \\
&= \sum_{n=0}^{N-1} \sum_{m=0}^{M-1} e^{-2\pi i \frac{(m \cdot N + n) \cdot q}{N}} \cdot b_{m \cdot N + n} \\
&= \sum_{j=0}^{M \cdot N - 1} e^{-2\pi i \frac{j \cdot q}{N}} \cdot b_j = \sum_{j=0}^{M \cdot N - 1} e^{-2\pi i \frac{j \cdot M \cdot q}{M \cdot N}} \cdot b_j = \hat{b}_{M \cdot q}
\end{aligned} \tag{2.70}$$

So M-fold WOLA with an N-point DFT yields channels with equivalent spectral disjunction as a windowed $M \cdot N$-point DFT, since each channel $\hat{c}_q$ equals channel $\hat{b}_{M \cdot q}$. However, there are some differences between these two: First, channels $\hat{b}_k$ that are not multiples of M are lost when using WOLA with a smaller DFT. To avoid losing their spectral information as well, the WOLA window has to be chosen carefully, so that frequencies that are present in the lost channels, leak into a kept one. Therefore, a window is required, whose main lobe is approximately M times as wide as usually desired and preferably flat over M bins. Secondly, the length of the DFT may define the time resolution if samples are processed continuously. Assuming this, an $M \cdot N$-point DFT yields a spectrum every $M \cdot N$ time samples, whereas an N-point DFT preceded by M-fold WOLA yields one every N time samples. Thirdly, overlap processing may increase S/N, although the same samples are used multiple time and are therefore statistically dependent [101]. To utilize this, it is again required to chose the WOLA window carefully. A basic parameter for doing so is the overlap coefficient OC [101, 35], which measures the correlation between two windowed noise-sequences of N samples that overlap by a fraction of r:

$$OC\left(r, \vec{w}_N\right) = \frac{\sum_{j=0}^{rN-1} w_j \cdot w_{j+(1-r) \cdot N}}{\sum_{j=0}^{N-1} w_j^2} \tag{2.71}$$

Of course, non-overlapping segments do not correlate at all ($OC\left(r \leq 0, \vec{w}_N\right) = 0$) and completely overlapping ones fully correlate ($OC\left(1, \vec{w}_N\right) = 1$). For a rectangular window $w_j = 1$, overlap

coefficients of other fractions $0 < r < 1$ are linear ($OC\left(r, \mathrm{rect}\right) = r$). For other windows OC is a rather complex function of r. Now assume continuous processing and averaging of the resulting power-spectra. The number of averaged spectra as well as the amount of overlap affect the variance of noise in the final spectrum [101] and therefore incoherent processing gain and S/N. To isolate the influence of overlap alone, one can assume $S \cdot M \cdot N$ samples and compare the noise-variance in the two cases mentioned above: First, the average of $K_{S,1} = S$ spectra from an $M \cdot N$-point DFT without overlap, and second, the average of $K_{S,M} = S \cdot M - (M-1)$ spectra using M-fold WOLA with an N-point DFT. For infinite S, the ratio of both noise-variances [101, 35] yields the incoherent overlap power gain OPG_{I}. It measures the amount, by which incoherent power is gained by the overlap in M-fold WOLA processing:

$$\begin{aligned} OPG_{\mathrm{I}}\left(M, \vec{w}_N\right) &= \lim_{S\to\infty} \frac{K_{S,1}}{K_{S,M}} \cdot \left(1 + 2 \sum_{j=1}^{K_{S,M}-1} \frac{K_{S,M} - j}{K_{S,M}} \cdot OC^2\left(\frac{M-j}{M}, \vec{w}_N\right)\right) \\ &= \frac{1}{M} \cdot \left(1 + 2 \sum_{j=1}^{M-1} OC^2\left(\frac{j}{M}, \vec{w}_N\right)\right) \end{aligned} \tag{2.72}$$

A rectangular window poorly profits from overlap, since noise variance will not fall to less than $\frac{2}{3}$ of its original level:

$$\begin{aligned} OPG_{\mathrm{I}}\left(M, \mathrm{rect}\right) &= \frac{1}{M} \cdot \left(1 + 2 \sum_{j=1}^{M-1} \left(\frac{j}{M}\right)^2\right) \\ &= \frac{2M^2 + 1}{3M^2} \end{aligned} \tag{2.73}$$

A window, however, whose overlap coefficients almost disappear ($OC\left(\frac{j}{M}\right) \approx 0$), could reduce noise by almost $\frac{1}{M}$. Other indicators evaluate a window by assessing the equality of each sample or find a trade-off between signal gain and the additional computation effort [36].

Since WOLA affects incoherent power gain as well as frequency resolution, some window properties have to be reconsidered. When comparing WOLA processing ($\hat{c}_q$) to a not overlapping DFT, one should distinguish the $M \cdot N$-point DFT ($\hat{b}_k$) from an N-point DFT. The former has the same window size as WOLA processing, but different frequency-resolution, for the latter it is the other way around. Unless stated otherwise, the properties of the windows $\vec{w}_{M\cdot N}$ and $\vec{w}_N$ are assumed to be sufficiently equal to each other and to a universal property. However, this is not necessarily true for small N. Since a coherent signal stays constant when averaging spectra, PG_{C} will not change by overlap processing, whereas PG_{I} multiplies by OPG_{I}. Compared to an N-point DFT without

Table 2.3: Cosine parameters of National Instruments Flat Top window.

	$\mathbf{c_0}$	$\mathbf{c_1}$	$\mathbf{c_2}$	$\mathbf{c_3}$	$\mathbf{c_4}$
NI Flat Top	0.215578948	0.416631580	0.277263158	0.083578947	0.006947368

WOLA, both experience additional gain. Assuming cosine windows (2.59), this yields factors that neutralize each other in the universal value $NENBW$:

$$\begin{aligned} PG_{\mathrm{C}}\left(M, \vec{w}_{M\cdot N}\right) &= PG_{\mathrm{C}}\left(\vec{w}_{M\cdot N}\right) \\ &= PG_{\mathrm{C}}\left(\vec{w}_{N}\right) \cdot M^2 \\ PG_{\mathrm{I}}\left(M, \vec{w}_{M\cdot N}\right) &= PG_{\mathrm{I}}\left(\vec{w}_{M\cdot N}\right) \cdot OPG_{\mathrm{I}}\left(M, \vec{w}_{M\cdot N}\right) \\ &= PG_{\mathrm{I}}\left(\vec{w}_{N}\right) \cdot M \cdot OPG_{\mathrm{I}}\left(M, \vec{w}_{M\cdot N}\right) \\ NENBW\left(M, \vec{w}_{M\cdot N}\right) &= NENBW\left(\vec{w}_{M\cdot N}\right) \cdot OPG_{\mathrm{I}}\left(M, \vec{w}_{M\cdot N}\right) \\ &= NENBW\left(\vec{w}\right) \cdot OPG_{\mathrm{I}}\left(M, \vec{w}_{M\cdot N}\right) \end{aligned} \tag{2.74}$$

3 dB-bandwidth and 6 dB-bandwidth are both defined by a certain amplitude that is not changed by WOLA. However, the actual bandwidth, measured in bins, changes, since the width of each bin increases by the factor of M. Therefore, the bandwidth in bins drops accordingly:

$$\begin{aligned} BW_X\left(M, \vec{w}_{M\cdot N}\right) &= BW_X\left(\vec{w}_{M\cdot N}\right) \cdot \frac{N \text{ bins}}{f_S} \cdot \frac{f_{\mathrm{S}}}{M \cdot N \text{ bins}} \\ &= BW_X\left(\vec{w}_{M\cdot N}\right) \cdot \frac{1}{M} \end{aligned} \tag{2.75}$$

Scalloping loss is measured half way between channels of an $M \cdot N$-point DFT. So, measured in bins, it is M times closer to a channel $\hat{c}_q$ than it is to $\hat{b}_k = \hat{b}_{M\cdot q}$:

$$q_f = \frac{f}{f_{\mathrm{S}}} \cdot N = \frac{k_f}{M} = \frac{k}{M} - \frac{1}{2M} = q - \frac{1}{2M} \tag{2.76}$$

The correct scalloping loss in presence of WOLA would be the response at $k_f = k - \frac{M}{2}$ instead of $k_f = k - \frac{1}{2}$ and can therefore not be calculated from the usual SL. However, overlapping the windows presented in chapter 2.4, would provide quite poor scalloping loss anyway. Actually, the response of cosine-windows would be 0 for even $M > 2 \cdot K$. Neither the side lobes' roll-off nor its highest level change at all, since both are defined independent of noise and of the width of a bin. The distance of the first side lobe scaled in bins, however, drops, and may yield side lobes at frequencies that are closer than the neighboring bin.

As discussed, WOLA requires windows with a wide and flat main lobe and with good overlap behavior. So called Flat Top windows are designed for the former, but usually perform good at the latter as well [36]. In their software (i.e. LabVIEW or MatLAB), National Instruments (NI)

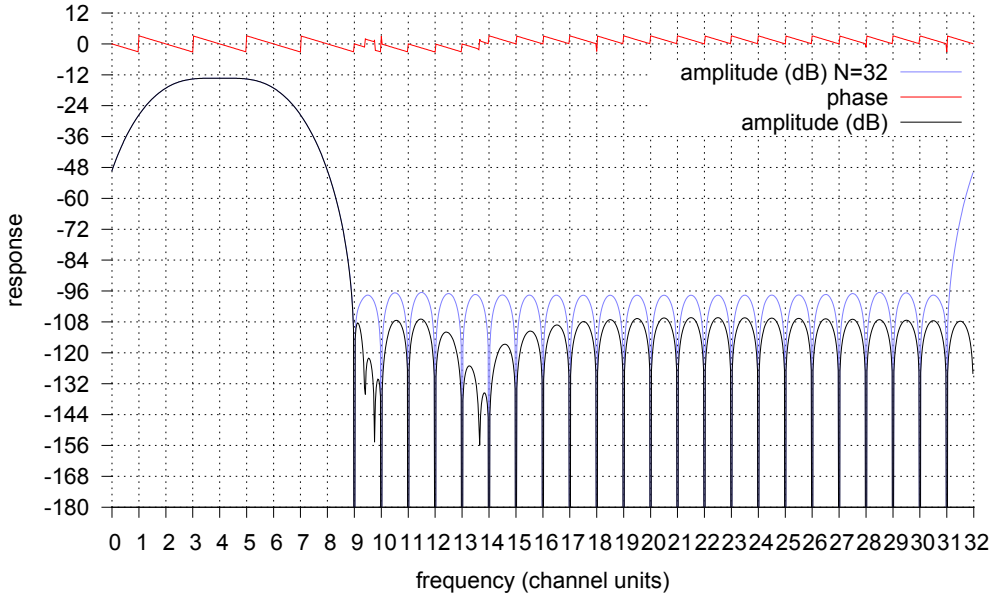

Figure 2.12: Response of phasors in channel $k = 4$, preprocessed with a National Instruments Flat Top window. It plots amplitude in dB (black) and phase (red) of a DFT spectrum with $N = 32768$ channels and amplitude in dB (blue) of a DFT spectrum with $N = 32$ channels.

Table 2.4: Properties of National Instruments Flat Top window.

	NENBW	SL	$\mathrm{BW_{6dB}}$	max side lobe	roll-off/octave
NI Flat Top	$\sim 3.77 \equiv 5.76\,\mathrm{dB}$	$-0.01\,\mathrm{dB}$	$4.58\,\mathrm{bins}$	$-93.0\,\mathrm{dB}$	$-6\,\mathrm{dB}$

Table 2.5: Incoherent overlap power gain of different windows, when using 2-fold, 4-fold or 8-fold WOLA: Hanning window, Hamming window, 3-term Nuttall window, minimum 3-term Blackman-Harris window and National Instruments Flat Top window.

	$\mathrm{OPG_I}(2)$	$\mathrm{OPG_I}(4)$	$\mathrm{OPG_I}(8)$
Rectangle	$0.75 \equiv -1.25\,\mathrm{dB}$	$\sim 0.69 \equiv -1.63\,\mathrm{dB}$	$\sim 0.67 \equiv -1.73\,\mathrm{dB}$
Hanning	$\sim 0.53 \equiv -2.78\,\mathrm{dB}$	$\sim 0.48 \equiv -3.18\,\mathrm{dB}$	$\sim 0.48 \equiv -3.18\,\mathrm{dB}$
Hamming	$\sim 0.55 \equiv -2.56\,\mathrm{dB}$	$\sim 0.53 \equiv -2.78\,\mathrm{dB}$	$\sim 0.53 \equiv -2.78\,\mathrm{dB}$
Nuttall3	$\sim 0.50 \equiv -2.99\,\mathrm{dB}$	$\sim 0.37 \equiv -4.33\,\mathrm{dB}$	$\sim 0.37 \equiv -4.34\,\mathrm{dB}$
Blackman-Harris	$\sim 0.51 \equiv -2.93\,\mathrm{dB}$	$\sim 0.42 \equiv -3.78\,\mathrm{dB}$	$\sim 0.42 \equiv -3.79\,\mathrm{dB}$
NI Flat Top	$\sim 0.50 \equiv -3.01\,\mathrm{dB}$	$\sim 0.25 \equiv -6.00\,\mathrm{dB}$	$\sim 0.22 \equiv -6.63\,\mathrm{dB}$

provides such a Flat Top window (figure 2.12) made of five cosines, as shown in table 2.3 [74, 75]. Again, (2.61) and (2.63) yield $NENBW$, SL and $WCPL$ (table 2.4). More properties are documented by NI [75]. Besides its excellent side lobe level and scalloping loss, this Flat Top window performs badly, when not using WOLA, since the wide main lobe would lower frequency resolution and acquire a lot of noise. Using 4-fold WOLA, both frequency resolution ($\frac{1}{4}BW_{6\mathrm{dB}}$) and noise bandwidth ($NENBW \cdot OPG_{\mathrm{I}}(4)$) outperform an unwindowed DFT. The overview of $OPG_{\mathrm{I}}(M)$ in table 2.5 (compare (2.72)) illustrates this effect and compares the windows presented in chapter 2.4. Remember the optimal value $OPG_{\mathrm{I}}(M) = \frac{1}{M}$ and note that common windows almost achieve this optimal value for 2-fold WOLA, but only the Flat Top window does for $M > 2$. However, its excellent scalloping loss drops to $-3.83\,\mathrm{dB}$ for 4-fold WOLA (the response to $k_f = k - 2$). An even wider or flatter main lobe may prevent this.

2.6 Split FFTs

The fast Fourier transform (FFT) is an algorithm that is used to calculate an N-point DFT efficiently by recursively splitting the DFT into multiple smaller ones [17]. Therefore, its size N is a power of two in common implementations.

An $M \cdot N$-point FFT calculates $M \cdot N$ spectral channels $\hat{a}_k$ out of $M \cdot N$ input samples a_j, where M and N are powers of two:

$$\hat{a}_k = \sum_{j=0}^{M \cdot N - 1} e^{-2\pi i \frac{j \cdot k}{M \cdot N}} \cdot a_j \tag{2.77}$$

The input can be split into N groups n of M consecutive samples m, so that $j = M \cdot n + m$. In the same way, the output is split into M groups p of N consecutive channels q, with $k = N \cdot p + q$. Applying this to (2.77) results in a double sum that can be simplified, since $e^{-2\pi i \cdot n \cdot p} = 1$, with $n, p \in \mathbb{N}$:

$$\begin{aligned}
\hat{a}_{N \cdot p + q} &= \sum_{m=0}^{M-1} \sum_{n=0}^{N-1} e^{-2\pi i \frac{(M \cdot n + m) \cdot (N \cdot p + q)}{M \cdot N}} \cdot a_{M \cdot n + m} \\
&= \sum_{m=0}^{M-1} e^{-2\pi i \frac{m \cdot (N \cdot p + q)}{M \cdot N}} \cdot \sum_{n=0}^{N-1} e^{-2\pi i \frac{n \cdot q}{N}} \cdot a_{M \cdot n + m} \\
&= \sum_{m=0}^{M-1} e^{-2\pi i \frac{m \cdot p}{M}} \cdot e^{-2\pi i \frac{m \cdot q}{M \cdot N}} \cdot \sum_{n=0}^{N-1} e^{-2\pi i \frac{n \cdot q}{N}} \cdot a_{M \cdot n + m}
\end{aligned} \tag{2.78}$$

The inner sums can be computed as M single N-point FFTs, fed with undersampled data:

$$a'_{m,q} = \sum_{n=0}^{N-1} e^{-2\pi i \frac{n \cdot q}{N}} \cdot a_{M \cdot n + m} \tag{2.79}$$

Thereby, M spectra a'_m are calculated and time-shifted to each other by the original sampling rate, each one with a fraction $\frac{1}{M}$ of the original bandwidth.

If their channels $a'_{m,q}$ are multiplied by the correct power of $e^{-2\pi i}$, a set of N different M-point FFTs remains to be computed. These complex factors are called twiddle factors, since a multiplication with $e^{-2\pi i \cdot x}$, with $x \in \mathbb{R}$, equals a clockwise rotation (twiddle) by x full turns. The correct twiddle here depends on time-shift (FFT number $0 \leq m < M$) and channel $0 \leq q < N$:

$$\begin{aligned} a''_{m,q} &= e^{-2\pi i \frac{m \cdot q}{M \cdot N}} \cdot a'_{m,q} \\ \hat{a}_{N \cdot p + q} &= \sum_{m=0}^{M-1} e^{-2\pi i \frac{m \cdot p}{M}} \cdot a''_{m,q} \end{aligned} \tag{2.80}$$

2.7 Use of imaginary input

Using (2.8) yields, a complex FFT fed with real input samples produces a spectrum whose second half is the complex conjugate of its first half:

$$\begin{aligned} a_j &= \overline{a_j} \\ \Rightarrow \hat{a}_k &= \overline{\hat{a}_{N-k}} \end{aligned} \tag{2.81}$$

A method to prevent a waste of computational resources is to alternately feed real samples $a_j \in \mathbb{R}$ into real and imaginary input of a half-sized FFT [13, Ch. 10.10]:

$$\tilde{a}_k = \sum_{j=0}^{\frac{N}{2}-1} e^{-2\pi i \frac{j \cdot k}{\frac{N}{2}}} \cdot (a_{2j} + i \cdot a_{2j+1}) \tag{2.82}$$

These intermediate channels form corresponding pairs $\tilde{a}_k$ and $\tilde{a}_{\frac{N}{2}-k}$. Note that $\tilde{a}_0 = \tilde{a}_{\frac{N}{2}-0}$ corresponds with itself, as well as $\tilde{a}_{\frac{N}{4}} = \tilde{a}_{\frac{N}{2}-\frac{N}{4}}$. Complex conjugating $\tilde{a}_{\frac{N}{2}-k}$ yields twiddles equal to (2.82).

$$\begin{aligned} \overline{\tilde{a}_{\frac{N}{2}-k}} &= \sum_{j=0}^{\frac{N}{2}-1} e^{+2\pi i \frac{j \cdot (\frac{N}{2}-k)}{\frac{N}{2}}} \cdot (a_{2j} - i \cdot a_{2j+1}) \\ &= \sum_{j=0}^{\frac{N}{2}-1} e^{-2\pi i \frac{j \cdot k}{\frac{N}{2}}} \cdot (a_{2j} - i \cdot a_{2j+1}) \end{aligned} \tag{2.83}$$

By adding and subtracting $\tilde{a}_k$ and $\overline{\tilde{a}_{\frac{N}{2}-k}}$ two independent half-sized FFTs can be calculated:

$$\begin{aligned} a'_{0,k} &= \frac{\overline{\tilde{a}_{\frac{N}{2}-k}} + \tilde{a}_k}{2} = \sum_{j=0}^{\frac{N}{2}-1} e^{-2\pi i \frac{j \cdot k}{\frac{N}{2}}} \cdot a_{2j} \\ a'_{1,k} &= i \cdot \frac{\overline{\tilde{a}_{\frac{N}{2}-k}} - \tilde{a}_k}{2} = \sum_{j=0}^{\frac{N}{2}-1} e^{-2\pi i \frac{j \cdot k}{\frac{N}{2}}} \cdot a_{2j+1} \end{aligned} \tag{2.84}$$

A twiddle-multiplication and an addition yield the final spectral channels.

$$a'_{0,k} + e^{-2\pi i \frac{k}{N}} \cdot a'_{1,k} = \sum_{j=0}^{\frac{N}{2}-1} e^{-2\pi i \frac{2j \cdot k}{N}} \cdot a_{2j} + \sum_{j=0}^{\frac{N}{2}-1} e^{-2\pi i \frac{(2j+1) \cdot k}{N}} \cdot a_{2j+1} = \hat{a}_k \tag{2.85}$$

Since the two half-sized FFTs use real inputs as well and therefore $a'_{x,k} = \overline{a'_{x,\frac{N}{2}-k}}$, the same channels $a'_{0,k}$, $a'_{1,k}$ that yield $\hat{a}_k$ also yield $\hat{a}_{\frac{N}{2}-k}$.

$$\overline{a'_{0,k}} - e^{+2\pi i \frac{k}{N}} \cdot \overline{a'_{1,k}} = a'_{0,\frac{N}{2}-k} + e^{-2\pi i \frac{\frac{N}{2}-k}{N}} \cdot a'_{1,\frac{N}{2}-k} = \hat{a}_{\frac{N}{2}-k} \tag{2.86}$$

One should note that the middle channel $\hat{a}_{\frac{N}{2}}$ is lost this way, since it has no analogon in the first half of the original spectrum and is not calculated by a half-sized FFT.

2.8 Integration

Integration of spectra means averaging their PSD over time. Assuming a signal coherent to the FFT, which recurs each FFT frame, this has no effect, of course, since all spectra would be the same. For astronomical applications, however, consider white Gaussian noise a relevant part of the signal. Mathematically it is a stationary random process X with a Gaussian probability density function (PDF) $p_X(x)$ and with statistically independent samples x_j taken from it [85, Ch. 4.1]:

$$p_X(x) = \frac{1}{\sigma\sqrt{2\pi}} \cdot e^{-\frac{x^2}{2\sigma^2}} \tag{2.87}$$

To evaluate the random process X, define the expected value $\mathrm{E}\{X\}$, which allows to calculate its mean μ_X and its variance σ_X^2, which is the square of its standard deviation σ_X or its root-mean-square (RMS):

$$\begin{aligned} \mathrm{E}\{X\} &= \int_{-\infty}^{+\infty} x \cdot p_X(x)\,\mathrm{d}x \approx \frac{1}{N}\sum_{j=0}^{N-1} x_j \\ \mu_X &= \mathrm{E}\{X\} \\ \sigma_X^2 &= \mathrm{E}\left\{(X-\mu_X)^2\right\} \\ &= \mathrm{E}\left\{X^2\right\} - \mathrm{E}^2\{X\} \end{aligned} \tag{2.88}$$

The mean of the noise from (2.87) is $\mu_X = 0$ and its variance is $\sigma_X^2 = \sigma^2$.

However, after passing spectral filters of bandwidth Δf, a square law detector, and a time smoothing filter over time τ, X is transformed to Z with related but different properties. Its mean μ_Z equals the average noise power introduced by X, and its variance σ_Z^2 actually measures spectral noise over time. Relating the standard deviation of the noise σ_Z to its average level $\mu_Z = T_{\text{sys}}$ now yields the radiometer formula [85, Ch. 4.2]:

$$\sigma_Z = \frac{T_{\text{sys}}}{\sqrt{\Delta f \cdot \tau}} \tag{2.89}$$

In a fast Fourier transform spectrometer (FFTS), which samples at rate f_{S}, this means that an N-point FFT filters a channel of bandwidth $\Delta f = \frac{f_{\text{S}}}{N}$, a square unit calculates the power spectrum, and the integration of N_{I} spectra smoothes the spectra over time $\tau = \frac{N \cdot N_{\text{I}}}{f_{\text{S}}}$. Using (2.89) yields that S/N on spectral channels increases with the square-root of integrations:

$$\frac{\mu_Z}{\sigma_Z} = \sqrt{N_{\text{I}}} \tag{2.90}$$

Assuming a signal combined from coherent and incoherent components, however, requires to find properties of μ_Z and σ_Z independently. Therefore compare N_{I} random variables Z_i', describing the noise on single spectra. Assuming the variables are independent, the mean μ_Z and the variance σ_Z^2 of their linear combination $Z = \sum_{i=0}^{N_{\text{I}}-1} Z_i' \cdot c_i$ can be calculated by a linear combination of the original means and variances [71, Ch. 5.7]:

$$\begin{aligned} \mu_Z &= \sum_{i=0}^{N_{\text{I}}-1} \mu_{Z_i'} \cdot c_i \\ \sigma_Z^2 &= \sum_{i=0}^{N_{\text{I}}-1} \sigma_{Z_i'}^2 \cdot c_i^2 \end{aligned} \tag{2.91}$$

Now assuming the same mean $\mu_{Z_i'} = \mu_{Z'}$, variance $\sigma_{Z_i'}^2 = \sigma_{Z'}^2$ and weight $c_i = 1$ for all Z_i' yields the desired result:

$$\begin{aligned} \mu_Z &= \sum_{i=0}^{N_{\text{I}}-1} \mu_{Z'} = N_{\text{I}} \cdot \mu_{Z'} \\ \sigma_Z^2 &= \sum_{i=0}^{N_{\text{I}}-1} \sigma_{Z'}^2 = N_{\text{I}} \cdot \sigma_{Z'}^2 \end{aligned} \tag{2.92}$$

Noise X produces signal power μ_Z that rises linearly with N_{I}, the same way a coherent signal does. Signal power dispersion σ_Z, however, only rises with $\sqrt{N_{\text{I}}}$.

Chapter 3

Astronomical applications

Spectrometers are used in a wide range of radioastronomical applications. Analyzing spectral lines may yield information about chemical composition, speed, temperature or pressure of an object. The higher the observed frequency and the more extreme the properties of the object, the wider these lines in frequency. Aside from the width of the lines, their frequency shift, shape and fine structure provides information as well. Other applications deal with objects that vary over time and provide information in that variation. Since the interstellar medium (ISM) is responsible for dispersion of the signal, a spectrometer is necessary to compensate for the frequency-dependent delay, and access the information in the variation. Many applications try to find very weak signals, which may not be detectable until they are subjected to spectral analysis. Last but not least spectrometers allow more efficient readout of information, by using frequency division multiplexing (FDM) to transmit data, e.g. over a single wire that connects multiple microwave kinetic inductance detectors (MKIDs).

Depending on the actual application a spectrometer must satisfy requirements with respect to different criteria. The previous examples suggest bandwidth, spectral resolution, time resolution, and sensitivity to be important. To define their significance to common tasks, this chapter specifies the requirements of wideband spectroscopy, high resolution spectroscopy, pulsar search, and the readout of MKIDs [18] according to these criteria.

3.1 Wideband spectroscopy

Chapter 1 mentioned telescopes and receivers with sky frequencies up to 2500 GHz and tuning ranges exceeding 100 GHz. A limited band of the received radio frequency (RF) signal is mixed down to a fixed intermediate frequency (IF). Table 3.1 lists the IF bandwidths along with the aforementioned instrument properties to illustrate the capabilities of current IF processors. They currently provide instantaneous bandwidth of up to 8 GHz, which may be processed by multiple spectrometers with smaller bandwidth. A survey over the full tuning range therefore requires combination of multiple spectra, measured by different instances of hardware, at different frequencies, or at different points of time. All may yield slight variations in spectra to be joined. Different hardware or

Table 3.1: Sky frequencies of current sub-mm radio telescopes along with the tuning range of their receivers and the bandwidth of their IF processors: CHAMP+ [48, 16, 55] and FLASH [39, 25, 52] at APEX 12 m telescope [33, 4], GREAT [38, 31] at SOFIA [90], IRAM 30 m telescope [42] and ALMA [2, 103].

	sky freq. (GHz)	**tuning range (GHz)**	**IF bandw. (GHz)**
CHAMP+ at APEX 12 m telescope	$620 - 950$	< 170	14×2.8
FLASH at APEX 12 m telescope	$272 - 495$	< 110	4×4
GREAT on SOFIA	$1250 - 2500$	$7 - 142$	2×2.5
IRAM 30 m telescope	$83 - 358$	< 75	$1.5; 4; 8$
ALMA	$31 - 950$	< 163	$4 \times 4; 2 \times 8$

different frequency tunings may cause variations due to production tolerances of analog components or limited accuracy when synchronizing digital components. Spectra from different points of time may vary due to environmental changes in the astronomical source itself, in the interstellar medium, in the atmosphere, or in the condition of an instrument. A common cause for variations is the temperature of the telescope, the front-end (receiver), or the back-end (spectrometer). Due to the limited accuracy of the atmospheric calibration process, the weather dominates variations between spectra. To join two spectra with adjacent frequencies properly, often requires an overlapping frequency range. To be able to compare and adjust the spectra with low statistical uncertainty, the overlap must contain a reasonable amount of stable, reliable data. Since spectral lines are the main object of spectroscopic research, their properties are not completely known, which implies an uncertainty in the spectral range of the line. Joining two spectra properly is therefore complicated if most of their overlap range is filled with spectral lines. Thus, the astronomical requirements on bandwidth can be specified by the expected width of spectral lines.

The velocity range of wide spectral lines that are measured in the Galactic Center (GC) may easily exceed $\Delta v = 100\,\mathrm{km\,s^{-1}}$ [46, 83]. To demonstrate how this affects signal bandwidth, let us transform velocity Δv to frequency Δf, at a given sky frequency f_{sky}:

$$\frac{\Delta f}{f_{\mathrm{sky}}} = \frac{\Delta v}{c}, \quad c = 299792.458\,\mathrm{km\,s^{-1}} \approx 3 \cdot 10^5\,\mathrm{km\,s^{-1}} \tag{3.1}$$

Thus, using (3.1) yields lines that span a frequency range of $\Delta f = 100\,\mathrm{MHz}$ at $f_{\mathrm{sky}} \approx 300\,\mathrm{GHz}$ (FLASH-345) and $\Delta f > 800\,\mathrm{MHz}$ at $f_{\mathrm{sky}} \approx 2500\,\mathrm{GHz}$ (GREAT). This suggests overlap of several $100\,\mathrm{MHz}$ to $1\,\mathrm{GHz}$, dependent on f_{sky}. Assuming a fixed absolute overlap between two spectra for a given input signal, the relative amount of overlap decreases with increasing spectrometer bandwidth. Observations at high sky frequencies therefore require a spectrometer bandwidth of multiple GHz.

However, the goal for wideband spectrometers is to maximize the fraction of the IF bandwidth that is covered by one spectrometer. This reduces variations over multiple instances of hardware

and may save space and money, since the number of spectrometers decreases, and so does the complexity of the IF processor. Thus, current maximum IF bandwidths of 4 GHz or 8 GHz demand a spectrometer bandwidth of multiple GHz.

Until now, we have not mentioned the fact that in addition to wide spectral lines, wideband spectroscopy has to adequately resolve very narrow spectral lines as well. An example relevant to Galactic Center (GC) observations is broad emission from molecular clouds in the GC that may be more than 10 km s^{-1} broad, partly absorbed by ISM in the same line of sight [83] with superimposed narrow lines. Self-absorption [70] or different velocity components in one source [83] may result in similar features. To detect and analyze them, high bandwidth has to be combined with high spectral resolution. Even narrower lines below 0.2 km s^{-1} (200 kHz at 300 GHz sky frequency) can appear without underlying broad lines, such as emission from very cold objects, e.g. prestellar cores [79, 15]. Observing the hyperfine lines of these objects at sky frequencies from table 3.1 requires spectral resolution of order 100 kHz per channel at sub-mm frequencies and 10-100 times smaller values in the radio regime (see chapter 3.2).

Using the same instruments for line surveys for all kinds of sources demands high bandwidth of at least multiple GHz, as well as high resolution below 100 kHz. Finally, the fact that observation time is a limited resource demands high sensitivity to minimize the duration of each measurement, but without missing a weak signal. The spectrometer should not add a significant amount of noise to the signal. Thus, wideband spectroscopy is a challenging task for spectrometers with respect to bandwidth as well as resolution and sensitivity.

3.2 High resolution spectroscopy

In contrast to the Atacama Pathfinder EXperiment (APEX) telescope, the Effelsberg telescope observes at sky frequencies up to 96 GHz. In fact most receivers operate at much lower frequencies, some even below 1 GHz [22]. Of course wide lines of $\Delta v = 100\,\mathrm{km\,s^{-1}}$ would only span $\Delta f = 333\,\mathrm{kHz}$ at $f_{\mathrm{sky}} \approx 1\,\mathrm{GHz}$. So the spectral resolution that dissolves the most narrow lines in sub-mm wideband spectroscopy is just sufficient for the widest lines to expect at those sky frequencies.

The first detection of hydroxyl (OH) at 1667 MHz, mentioned in chapter 1 used a spectrum with 7.5 kHz spectral resolution, which equals ~ 133 ch/MHz [100]. Starting in 2008, the Effelsberg Bonn H-I Survey (EBHIS) maps the sky at frequencies in the 21 cm line of atomic hydrogen at ~ 1420 MHz [49]. Referring to the Leiden/Argentine/Bonn (LAB) survey, the most narrow spectral lines are just below 4 km s^{-1} wide [47]. It therefore demands velocity resolution of ~ 1 km s^{-1}, which equals a frequency resolution of ~ 5 kHz. Other applications such as Zeeman effect measurements demand even higher spectral resolution below 0.1 km s^{-1} [97].

Extrapolating the spectral resolution from the OH detection or from EBHIS yields at least $2^{17} = 131.072$ channels per GHz. To cover a receiver bandwidth of several GHz with these resolutions, would require a huge amount of spectral channels. Although this seems reasonable for an unbiased survey with no focus on a specific spectral line, the mentioned applications allow much smaller

bandwidth. Not more than 100 kHz were sufficient for the OH detection in 1963 [100]. Essentially EBHIS requires a band that is just wide enough to cover all the velocity components of the hydrogen I (H I) line. Again referring to the LAB survey most of these are distributed over 850 km s^{-1}, which equals a bandwidth of ~ 4 MHz. With an extended bandwidth of 100 MHz, the survey still covers a limited band with a demand for 2^{14} channels, but it qualifies as an unbiased survey. So two different approaches satisfy the forecited demands in spectral resolution: The first is to increase the amount of spectral channels, the second is to reduce bandwidth by zooming to the frequencies of interest. Of course compromises of both are possible as well.

Another characteristic of sky frequencies up to several GHz is the massive presence of radio frequency interference (RFI) from terrestrial sources. A well known example is frequency modulation (FM) radio around 100 MHz. More recently the Global System for Mobile Communications (GSM), wireless local area networks (WLANs), the Universal Mobile Telecommunications System (UMTS), Digital Video Broadcasting - Terrestrial (DVB-T), and many others started transmitting additionally, mostly in bands from 900 MHz to 2400 MHz. Further, there is RFI from all kind of electronic devices that radiate unintentionally. Dependent on its source, it may be limited to narrow bands as well as broadband, and it may be constant as well as varying in frequency or amplitude. It may also seem constant, since it varies much faster than the time resolution of the observation. Using its differences from astronomical signals allows to mitigate RFI if the instruments, including the spectrometer, are able to detect these. Strong narrowband RFI therefore requires a proper channel separation to blank it, and sufficient dynamic range to prevent some kind of overflow or clipping. To mitigate broadband RFI of short duration, it should only affect single spectra. For EBHIS a time resolution of 500 ms was found to be sufficient [26].

3.3 Pulsar search

Besides a black hole and a white dwarf, a neutron star is a final state of a star. It mainly consists of pure neutrons, packed more dense than an atomic nucleus. What we observe as pulsars is commonly accepted to be highly magnetized rotating neutron stars. Given its enormous magnetic field, a pulsar emits radiation only along its magnetic axis. Combined with fast rotation around an independent axis, we detect pulses, comparable to a lighthouse, when a magnetic pole of the pulsar is directed to the observer [53, Ch. 1.1]. Defining the required time resolution, the pulse period as well as the pulse width of the pulsar are of course crucial for its detection. The same importance has dispersion, the frequency dependent delay added by the ISM. It demands proper spectral resolution to extract the original pulse from the broader and therefore weaker continuum pulse, received from the telescope. The similar effect of scattering finally demands observation at high sky frequencies [53, Ch. 1.3].

To estimate timing constraints, it is obvious to concentrate on the faster millisecond pulsars. With a lower physical limit at $P_{\mathrm{lim}} \approx 0.5$ ms, the fastest pulse period found so far is $P = 1.56$ ms. Since the average pulse width at 400 MHz of $W \approx P \cdot 4.8\,\%$, and most millisecond pulsars have periods above 2 ms [53, Ch. 1.2], most pulses can be expected to be more than 100 µs wide. Therefore, a time resolution slightly faster than 100 µs is sufficient to detect the majority of pulses properly.

The ISM adds different signal delays to a frequency f and a reference frequency f_{sky}. The difference Δt of those signal delays can be calculated from the dispersion constant k_{DM} and a dispersion measure (DM) [63, Ch. 5.2]:

$$\Delta t = k_{DM} \cdot \left(f_{\mathrm{sky}}^{-2} - f^{-2}\right) \cdot DM, \;\; k_{DM} \approx 4.15 \cdot 10^6 \,\mathrm{MHz}^2\,\mathrm{pc}^{-1}\,\mathrm{cm}^3\,\mathrm{ms} \tag{3.2}$$

The DM quantifies the effect for each pulsar and defines the integrated column density of electrons between the observer and the pulsar. Using $f_{\mathrm{sky}} \gg \Delta f = f - f_{\mathrm{sky}}$ with (3.2), displays a positive effect of high observation frequency [63, Ch. 5.2]:

$$\Delta t = k_{DM} \cdot 2 \cdot \frac{\Delta f}{f_{\mathrm{sky}}^3} \cdot DM, \;\; k_{DM} \approx 4.15 \cdot 10^6 \,\mathrm{MHz}^2\,\mathrm{pc}^{-1}\,\mathrm{cm}^3\,\mathrm{ms} \tag{3.3}$$

Estimating a frequency resolution, now requires to assume maximum and minimum values for DM, Δt and f_{sky}. To prevent dispersion from smearing the pulse, it is sufficient if the delay Δt over a spectral channel of width Δf is significantly shorter than the pulse itself. Thus, the previous considerations about the maximum time resolution yield $\Delta t > 100\,\mu\mathrm{s}$. From statistics about galactic pulsars a maximum DM can be derived with $DM < 1000\,\mathrm{pc\,cm}^{-3}$ [56, Ch. 2]. Now assuming $f_{\mathrm{sky}} > 1\,\mathrm{GHz}$, (3.3) yields that a frequency resolution that is limited by $\Delta f > \frac{100\,\mu\mathrm{s\,MHz}}{8.3\,\mathrm{ms}} \approx 0.012\,\mathrm{MHz}$ would be sufficient. Since each parameter has been individually limited by its worst case, the resolution, required in actual applications, is orders of magnitude lower. Ignoring pulsars with high DM, as in the GC region, allows to increase Δf by a factor of ~ 10, ignoring millisecond pulsars by a factor of ~ 100. Of course the constraint rapidly eases with rising sky frequency, which is anyway demanded by scattering: $f_{\mathrm{sky}} = 18.95\,\mathrm{GHz}$ allows to increase Δf by a factor of ~ 6800 [21].

According to the pulsar radiometer equation, higher bandwidth used in pulsar searches reduces the noise so that the observing time is reduced. Applied from (2.89) the equation derives the minimum detectable signal S_{min} from a minimum signal-to-noise ratio (S/N) and the noise variance. Aside from the integration time Δt, it additionally depends on the antenna gain G, a correction factor β, the pulse width W, and the pulse period P [63, Ch. A1.4]. The total bandwidth Δf_{tot}, (2.89) refers to, can be derived from the number of polarizations n_{p}, the number of spectral channels n_{ch}, and the spectral resolution Δf:

$$\begin{aligned} S_{\mathrm{min}} &= \beta \frac{(S/N_{\mathrm{min}})\,\sigma}{G} \cdot \frac{W}{P} \\ &= \beta \frac{(S/N_{\mathrm{min}})\,T_{\mathrm{sys}}}{G\sqrt{n_{\mathrm{p}} \cdot n_{\mathrm{ch}} \cdot \Delta f \cdot \Delta t}} \cdot \sqrt{\frac{W}{P - W}} \end{aligned} \tag{3.4}$$

However, operating at radio sky frequencies, the bandwidth is limited to several GHz.

Finally, consider a technical limit for the data transmission rate R. Aside from the bit-length b of one spectral channel R depends on Δf_{tot}, Δf, and Δt:

$$R = \frac{n_{\mathrm{p}} \cdot n_{\mathrm{ch}} \cdot b}{\Delta t} = \frac{\Delta f_{\mathrm{tot}} \cdot b}{\Delta f \cdot \Delta t} \tag{3.5}$$

Assuming a bit-length $b = 32\,\text{bit}$, a total bandwidth $\Delta f_{\text{tot}} = 1\,\text{GHz}$ and the aforementioned values of $\Delta t > 100\,\mu\text{s}$ and $\Delta f > 0.012\,\text{MHz}$, (3.5) yields a data rate $R < \sim 27\,\text{Gbit}\,\text{s}^{-1}$. Although R increases with total bandwidth, it decreases with eased constraints on DM, Δt or f_{sky}. According to the factors that were discussed for Δf, actual applications can be expected between the capabilities of Fast Ethernet ($R_{\max} = 100\,\text{Mbit}\,\text{s}^{-1}$) and Gigabit Ethernet ($R_{\max} = 1\,\text{Gbit}\,\text{s}^{-1}$).

3.4 MKID readout

Unlike heterodyne receivers that are used for spectroscopy, a bolometer receives broadband continuum radiation without distinguishing between frequencies in its band [85, Ch. 4.3]. A rather new concept for incoherent detectors is the microwave kinetic inductance detector (MKID) receiver [18]. It is made of multiple superconductive MKIDs, which change their properties dependent on received radiation, as figure 3.1 shows. These properties can be read out by generating an artificial signal, feeding it into the circuit, and measuring how the MKID affects amplitude and phase near its resonance frequency. Producing MKIDs with different resonance frequencies and connecting them by a feedline allows to read out all of them simultaneously, using frequency division multiplexing (FDM). Although the astronomical signal is not analyzed spectrally, this setup requires a spectrometer to analyze the artificial signal. This procedure allows to connect 1000s of MKIDs by one cable [113] and build arrays with many 10.000 pixels, such as the A-MKID camera [1].

The resonance width of an MKID mainly defines the spectral resolution the readout requires. It should be able to generate and measure a frequency close enough to the resonance frequency of each MKID. Research indicates, an MKID spans 10-100 kHz in frequency [7, 68], demanding a spectral resolution that is slightly better.

Comparable to pulsar search, the spectrometer bandwidth affects S/N of an MKID receiver. With a given minimum spacing between resonance frequencies [68], the bandwidth of a spectrometer limits the number of MKIDs. The same way the number of polarizations or channels lowers the detection limit in (3.4), S/N of an MKID receiver is increased by integration over multiple MKIDs, rising with the square-root of their number.

Similarly, the number of MKIDs could affect the demands on dynamic range of the readout. The crest-factor $CF\,(a_j)$ is defined as the ratio between the maximum amplitude and the amplitude spectral density of a time-domain signal a_j:

$$CF\,(a_j) = \frac{\max\,(a_j)}{\sqrt{\frac{1}{N}\sum_{j=0}^{N-1} a_j^2}} \tag{3.6}$$

Assuming the worst case of phase relations between tones, CF may as well rise with the square-root of their number. On the other hand it can be limited to a fixed value for an arbitrary number of equidistant tones [12]. Since an MKID readout probably won't meet this condition, a crest-factor between those extremes should be expected, demanding higher dynamic range for a higher number of MKIDs.

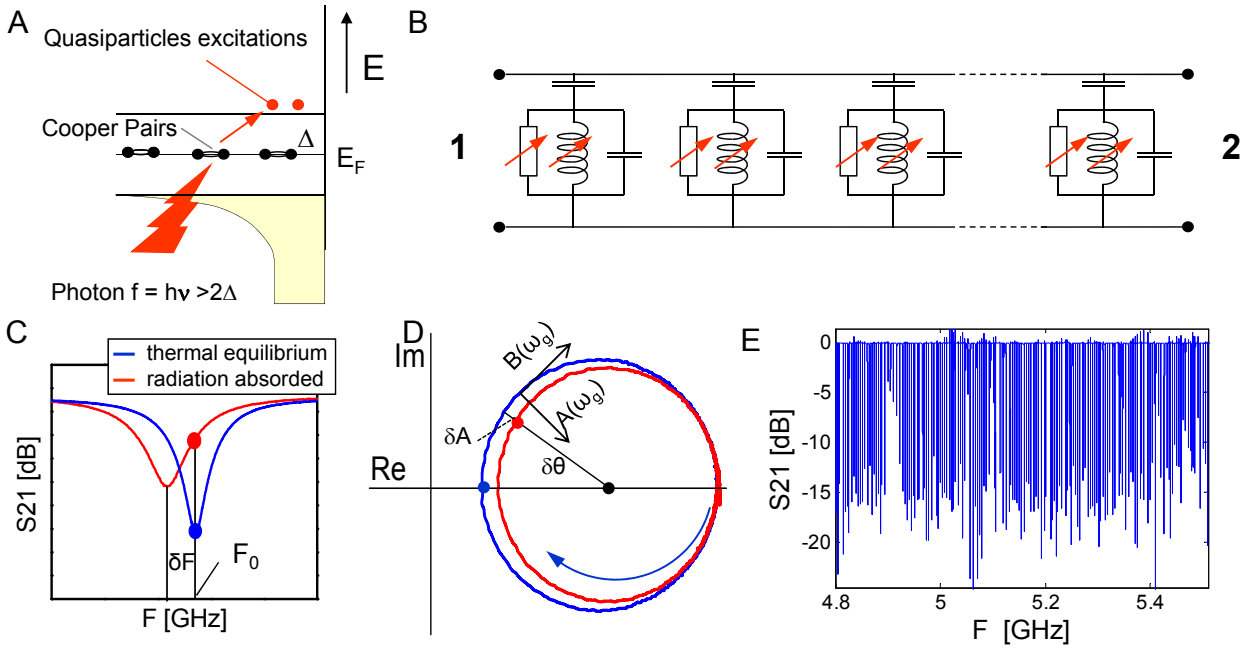

Figure 3.1: Operation principle of MKIDs [8, Fig. 1]. "**A**: Photons break Cooper pairs in a superconductor creating quasiparticles. **B**: By making the superconductor part of a resonance circuit it is possible to read out changes in the complex surface impedance of the superconductor due to radiation absorption as a change in microwave transmission. Frequency division multiplexing can be achieved by coupling many resonators to one feedline. **C**: Measured transmission from contact 1 to 2 in B for one [MKID] resonator. The [deeper] blue line represents the equilibrium situation and the [flatter] red line after photon absorption. **D**: The same data as in C but in the complex plane, showing that either δA or $\delta\theta$ using a readout tone at F_0 can be used to measure the amount of absorbed radiation. The arrow indicates the direction of increasing frequency, $B(\omega_g)$ and $A(\omega_g)$ represent the direction tangent and normal to the resonance circle. **E**: 175 resonators with $Q = 2 \cdot 10^4$ and $\delta F_0 = 4 \pm 2$ MHz." [8, Fig. 1].

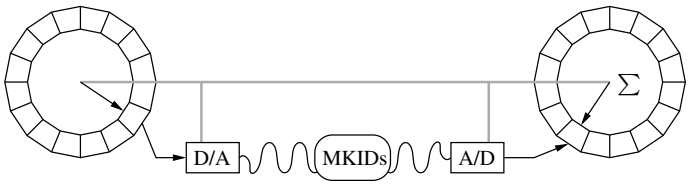

Figure 3.2: Two ring buffers that are synchronized to each other and to the clocked circuits of an MKID readout between them.

In theory it is sufficient to generate one tone per MKID to read out its properties. In contrast to usual spectroscopy the phase of the altered signal is vital, but could be lost, when integrating spectra over time. To prevent cancellation of a random frequency, phase has to be extracted before integration to compensate a shift from one fast Fourier transform (FFT) spectrum to another. Of course leakage effects on amplitude, described in chapter 2.4, should be minimized as well. Another approach prevents leakage at all by synchronizing the spectrometer and the signal generator carefully: each tone in the generated signal needs to match a channel in the FFT exactly. Since the former approach requires high mathematical and algorithmic effort just to limit leakage, the latter is chosen for the A-MKID readout. Assuming signals that produce no leakage allows integration in the time domain. As shown in figure 3.2, the part of the processing pipeline that needs to operate at full sampling rate f_S is reduced to two ring buffers. In any case, technical and algorithmic effort must be considered to achieve proper synchronization between those ring buffers and other time discrete components in between, such as a digital-to-analog converter (DAC), an analog-to-digital converter (ADC), clock dividers and counters. To ensure a fixed phase relation between all these components, first of all, a common clock reference is required. Secondly, a reset in any of these components must either ensure that the previous phase relation of the reset component is restored, or the resulting time shift must be detected, measured and compensated. With an unknown signal from the receiver included the latter is close to impossible. Therefore any reset with unknown timing should be avoided during measurements.

Chapter 4

FFTS optimization

Exploring the technical requirements outlined in chapter 3, requires a closer look at the design of a fast Fourier transform spectrometer (FFTS). The processing chain, outlined in figure 4.1, starts with an analog-to-digital converter (ADC), that samples the input signal. The digitized signal is transferred from the ADC to a field-programmable gate array (FPGA), which basically calculates the frequency spectrum. The processing chain ends with a controller that collects all data for transfer to a personal computer (PC). Both, the controller on board and the PC, possibly analyze the data and adjust settings of the spectrometer accordingly.

Figure 4.1: Processing chain of an FFTS board. The arrows indicate the data flow. Control is performed the opposite direction.

Figure 4.2: Custom-built AFFTS board with a $3\,\mathrm{GS\,s^{-1}}$ ADC, a Virtex-4 SX-55 FPGA for FFT and a Spartan-3 1000 FPGA for controlling.

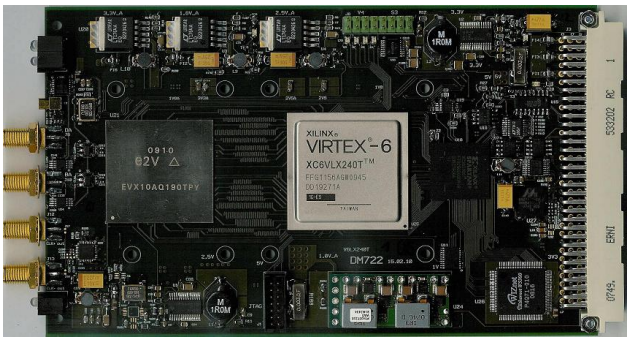

Figure 4.3: Custom-built XFFTS board with a $5\,\mathrm{GS\,s^{-1}}$ ADC, a Virtex-6 LX-240T FPGA for FFT and a Spartan-3 1000 FPGA for controlling.

During the time of this thesis, two custom-built FFTS boards were developed. The Array Fast Fourier Transform Spectrometer (AFFTS), shown in figure 4.2, and the eXtended-bandwidth Fast Fourier Transform Spectrometer (XFFTS), shown in figure 4.3.

The ADC on an FFTS is intended to sample at high speed f_S to allow an instantaneous bandwidth up to the Nyquist frequency $\frac{f_\mathrm{S}}{2} > 1\,\mathrm{GHz}$ (compare (2.13)). Note this may differ from the analog input bandwidth, which defines the maximum frequency the ADC is reasonably sensitive to. With respect to dynamic range and signal-to-noise ratio (S/N), the quantization resolution, measured in bits per sample, is another basic property. It limits the more relevant effective number of bits (ENOB), defined as the theoretical resolution of a perfect ADC that provides the same signal-to-noise and distortion ratio (SINAD) as the real ADC, when digitizing a sine signal [50, 51]:

$$ENOB = \frac{SINAD}{20\lg(2)\ \mathrm{dB}} - \log_2\sqrt{\frac{3}{2}} \approx \frac{SINAD - 1.76\,\mathrm{dB}}{6.02\,\mathrm{dB}} \tag{4.1}$$

The AFFTS uses a $3\,\mathrm{GS\,s^{-1}}$ ADC from National Semiconductor (now Texas Instruments) with 8 bit resolution, an analog input bandwidth of 3 GHz and an ENOB of 7 [76]. The XFFTS uses a $5\,\mathrm{GS\,s^{-1}}$ ADC with 10 bit resolution from e2v semiconductor. Its analog input bandwidth is 3.2 GHz and its ENOB is up to 7.9 bit at full speed [20]. Thus, both FFTSs are equipped with one of the highest-performance ADCs available at the time to satisfy the demands of wideband spectroscopy on bandwidth and sensitivity from chapter 3.1. Data is transferred to the FPGA via four low-voltage differential signaling (LVDS) buses, each running at a quarter of the sampling rate. The Xilinx Virtex-4 SX55 FPGA on the AFFTS therefore receives up to $750\,\mathrm{Mbit\,s^{-1}}$ per wire. The Xilinx Virtex-6 LX240T FPGA on the XFFTS even receives up to $1250\,\mathrm{Mbit\,s^{-1}}$ per wire. The data goes along with a clock, running at half this data rate.

Aside from a fast Fourier transform (FFT) the main FPGA may perform further signal processing that requires high speed:

- Receive, align and demultiplex digitized data from the ADC at high speed.
- Measure interleaving errors between multiple ADCs and perform a proper calibration.
- Provide statistical properties of the input signal.
- Preprocess the data by filters, by a window or by weighted overlap-add (WOLA).
- Perform an FFT.
- Square complex channels to calculate the power spectrum or the power spectral density (PSD).
- Integrate spectra to increase S/N and reduce the data rate.
- Convert the data format, e.g. from integer to floating point.
- Reorder spectral channels and combine them with further data about the operating conditions.

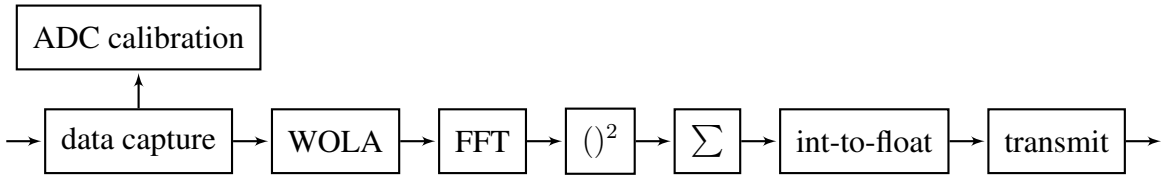

Figure 4.4: Steps of the processing pipeline inside the main FPGA of the AFFTS and the XFFTS.

- Transmit data with respect to external triggers or settings, like blank/sync signals, a reset signal or a counter value.

Figure 4.4 shows the tasks that are performed by the processing pipeline of the main FPGA on the AFFTS and the XFFTS.

Control of the spectrometer can be shared between an on-board controller and a PC. Basic operations of the spectrometer are more easily and more reliably performed on board. The PC may perform tasks of the spectrometer that are not time-critical, but computationally complex and feed back the results by adjusting settings of the spectrometer.

Both aforementioned FFTSs are equipped with a Xilinx Spartan-3 1000 FPGA that controls all the components on the FFTS board. Its tasks possibly define operating conditions of the spectrometer and limits to astronomical applications. Some of those tasks affect the main FPGA or the PC, and thus the algorithms presented in chapter 4:

- Establish communication with a PC via Transmission Control Protocol (TCP), Internet Protocol (IP) and Ethernet. The communication chip on the AFFTS allows to continuously transfer 20 Mbit s^{-1} of data, the one on the XFFTS allows almost 100 Mbit s^{-1}.

- Configure the main FPGA according to a hardware description, that is received from the PC. This feature allows multiple configurations for different applications. It, however, requires to carefully weigh between optimization and generalization of the algorithms that are implemented on the main FPGA to achieve high performance as well as high flexibility.

- Provide control clocks and control data for the main FPGA. A 50 MHz clock is used for communication between the FPGAs. Write accesses to 256 control registers are forwarded to the main FPGA.

- Initiate and control the data transmission from the main FPGA to the PC. The final data is sent in portions of 32 bit, including 1024 B of status information.

Figure 4.4 gives an overview of the processing pipeline inside the main FPGA to guide through the discussion of the implemented algorithms. However, the implementation is not limited to the main FPGA, but may be partly shifted to the on-board controller or the PC. It requires considering the demands of the different astronomical applications named in chapter 3. These demands translate to technical or algorithmic criteria, named in chapter 1: processing speed, hardware utilization,

memory occupation, flexibility, or just simplicity. Additionally, the technical restrictions of the aforementioned hardware must be considered.

4.1 Data capture

State-of-the-art FPGAs achieve clock rates of several 100 MHz. Table 4.1 shows some maximum ratings for the main FPGAs on the AFFTS and the XFFTS, as well as their counterparts with maximum speed grade. However, note that those numbers define maximum ratings for the listed components of the FPGA, based on the propagation delay inside the component. The overall performance of a complete design is decreased by propagation delay on wires between those components. A speed-optimized intellectual property core (IP core) that implements a pipelined FFT with certain parameters for a certain FPGA already limits performance about 100 MHz below the FPGA's maximum [110, Performance and Resource Usage]. Connecting multiple of those with other components to a complex design, increases the delay on wires and reduces the performance Xilinx Integrated Software Environment (Xilinx ISE) may achieve. Thus, expect a clock-rate below 200 MHz from a complex spectrometer design that needs to be balanced between high-speed optimization and flexibility.

However, chapter 4 mentions ADCs that sample data at rates up to 5 GHz and transmit them at 1.25 Gbit s^{-1} per wire, along with a clock of half that speed. With FPGAs that operate below 200 MHz, each input data line needs to be split up into some parallel data streams with reduced speed. The input clock from the ADC needs to be divided accordingly and a proper alignment between the clock and each data line needs to be established to receive valid data (see figure 4.5). Virtex-4 and Virtex-6 FPGAs both provide circuits to divide a clock, to demultiplex data from one

Table 4.1: Maximum performance and switching characteristics of Xilinx FPGAs. Input data is received via a low-voltage differential signaling (LVDS) bus operating in double data rate (DDR) mode. Dedicated digital signal processing slice (DSP slice) and block RAM (BRAM) components may limit the internal clock rate below f_{max}. Ratings of the Virtex-4 are for the AFFTS (-10) and for maximum speed grade (-12) [106]. Ratings of the Virtex-6 are for the XFFTS (-1) and for maximum speed grade (-3) [112].

	DDR LVDS receiver (Mbit/s)	**BRAM/DSP slice f_{max} (MHz)**	**global clock f_{max} (MHz)**
Xilinx Virtex-4 -10	800	400	400
Xilinx Virtex-4 -12	1000	500	500
Xilinx Virtex-6 -1	1100	450	700
Xilinx Virtex-6 -3	1400	600	800

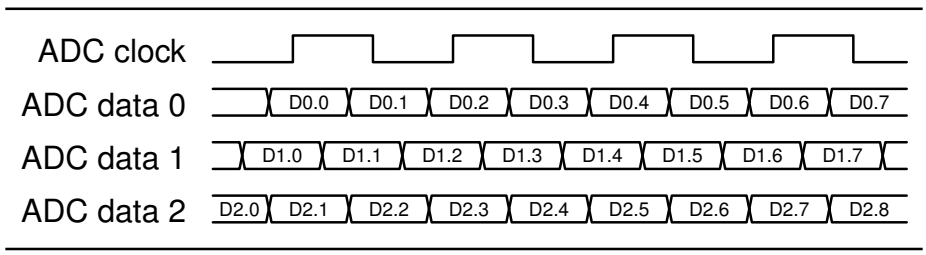

Figure 4.5: Alignment between a DDR clock and multiple data lines. The data lines need to be shifted to be aligned to the common clock and to each other.

line to multiple parallel streams, and to delay any input independently (IDELAY, IODELAY) [105, 107, 111]:

- The clocking resources of a Virtex-4 FPGA include Phase-Matched Clock Dividers (PMCDs) and Digital Clock Managers (DCMs) to divide a global clock. In a Virtex-6 FPGA, these components are combined by the advanced Mixed-Mode Clock Managers (MMCMs). However, DCMs and MMCMs provide no reset function with predictable timing, which results in a slightly different propagation delay of the input circuits after any initialization [105, 111].
- The input/output (I/O) resources include Input Serial-to-Parallel Logic Resources (ISERDESs) that allow to demultiplex a DDR signal by a factor of 4, 6, 8, or 10 [105, 107].
- The Input Delay Element (IDELAY) of a Virtex-4 FPGA may delay an input in 64 steps of 75 ps. The Input/Output Delay Element (IODELAY) of a Virtex-6 FPGA may delay any signal in 32 steps of 78 ps. The Virtex-4 IDELAY, however, requires dedicated control logic, which makes it inefficient to control many delays independently.

The task of aligning a data line to the clock of course requires to detect a proper alignment. In theory, it is possible to detect a misalignment in presence of an astronomical input signal, since its spectrum would be affected. This, however, requires assumptions about the properties of an unknown signal. These assumptions may affect multiple data lines, e.g. multiple bits of one data value. Since this would not allow to evaluate each data line individually, the algorithmic and mathematical effort of the alignment process would multiply. Thus, it is more reliable to use a defined test signal the ADC provides, to detect whether each data line is sampled at a valid point in time. Checking the signal integrity inside the FPGA for each delay setting and each data line, results in the matrix shown in figure 4.6, which can be analyzed outside the FPGA to calculate proper delay settings. In doing so, consider a safety margin, since clock jitter as well as changes in temperature or other environmental conditions could alter the range of proper delays. From stability tests with the AFFTS and the XFFTS, a minimum range of 3 to 4 valid delay steps was found to be sufficient, which equals $\sim 250\,\text{ps}$. The AFFTS data rate of $750\,\text{Mbit}\,\text{s}^{-1}$ easily allows to keep this margin for each data line with just one delay setting for all of them. As figure 4.6 shows for an XFFTS, a safety margin above 3 can only be found with individual delays for each data line.

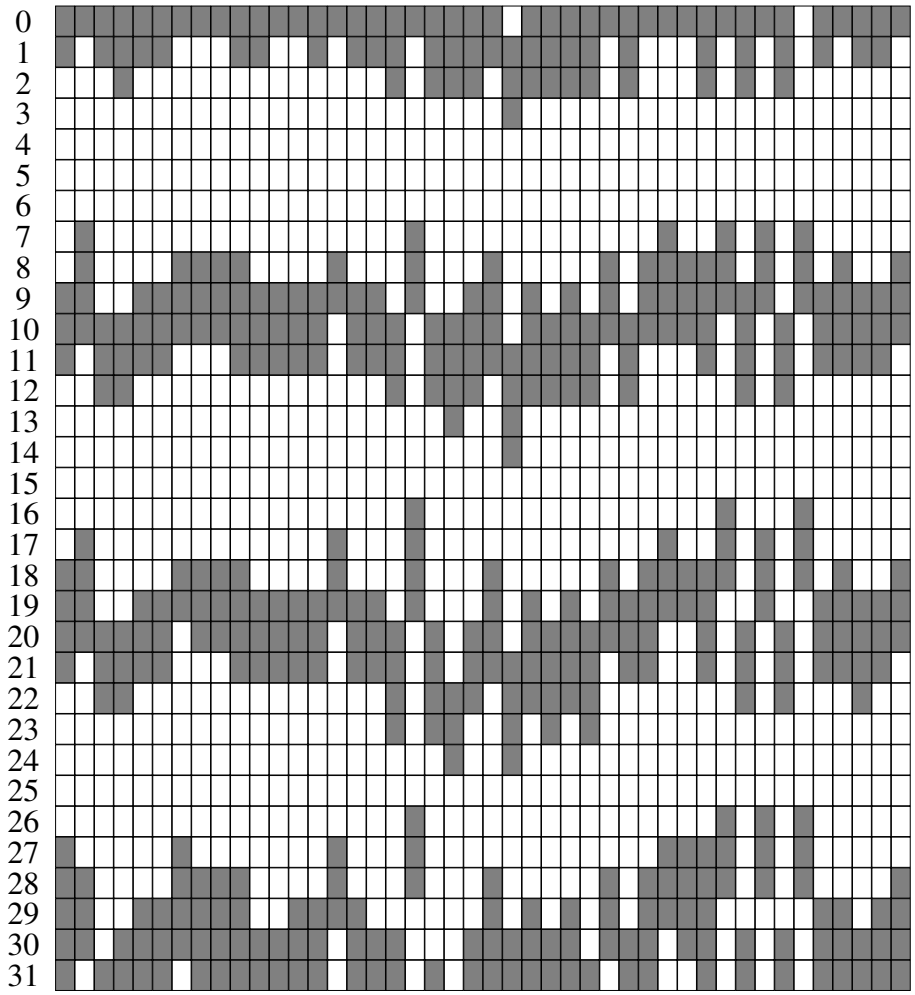

Figure 4.6: Delay settings that lead to valid (□) or invalid (■) data on the input data lines of an XFFTS. Each column represents a data line. Each row represents a delay setting, labeled in multiples of a delay step of 78 ps. With a data rate of 1250 Mbit s^{-1} two bits differ by 800 ps, which equals ~ 10.3 delay steps.

Figure 4.5 shows how a data line may be shifted by a substantial amount of a bit cycle, i.e. the time difference of two bits on a data line. Therefore it might be insufficient to individually align each data line to the clock, but they have to be aligned with each other as well. The matrix in figure 4.6, however, indicates that the shift is limited to an amount that allows proper alignment between the data lines, just using the matrix itself. Assuming that the shift roughly follows a standard deviation and is limited to half a bit cycle, offers an algorithm to do so. A central delay setting for each bit cycle can be defined by the setting with the most data lines that receive valid data. Using these central settings as anchors allows assigning each range of valid settings of any data line to a certain central delay setting. Thus, using individual delay settings from ranges that are assigned to the same central setting, results in proper alignment between the data lines. Now, the total valid range of a central setting can be defined as the minimum of all individual ranges that are assigned to this central setting. Thus, the central setting with the highest total valid range is the best choice to guarantee a maximum lower limit among safety margins. The actual delay settings for each data line can be provided by the median of the according range of delay settings that is assigned to the chosen central setting. The successful implementation of this algorithm for AFFTS and XFFTS allows to limit hardware requirements: the FPGA only needs to check the validity of each individual data line, but not the alignment to each other. Additionally, it successfully extends the data rate specifications of a Xilinx Virtex-6 FPGA with speed grade -1 that are listed in table 4.1.

4.2 ADC calibration

Chapter 2.3 describes how different amplitude offset, power gain or phase alignment among the channels of a time-interleaved ADC affects the spectrum of a signal the ADC samples. To limit the effects on the spectrum, time-interleaved ADCs require a calibration procedure. Therefore, the ADC083000 ADC on the AFFTS offers an automated internal calibration, and the EV10AQ190A ADC on the XFFTS offers registers to manually adjust the offset, gain and phase of its channels to one of 1024 settings [76, 20]. The offset can be adjusted in steps of $\sim 8\,\%$ of the least significant bit, the gain allows adjustment in steps of $\sim 0.02\,\%$ of the average amplitude, and the phase can be shifted in steps of $\sim 30\,\text{fs}$.

Post-processing techniques exist to analyze and alter the digitized signal with no feedback to the ADC. These, however, either require assumptions about the input signal, such as a band limitation, or a significant amount of FPGA resources, e.g. for advanced filter banks [62, 98]. The approach chosen here uses a well-known test signal for calibration and analyzes the output of each interleaved channel to adjust the interleaving of the ADC accordingly [27]. To allow proper analysis of a test signal, its analyzed properties must not change after sampled by one channel of an interleaved ADC. Especially mean, variance, standard deviation, and average absolute amplitude of a reasonable amount of the samples from any channel must converge to the corresponding properties of the signal itself. To achieve this, the test signal should be asynchronous to the sampling clock of the ADC. White noise obviously meets this condition, a single tone yields converging properties, if its frequency is chosen

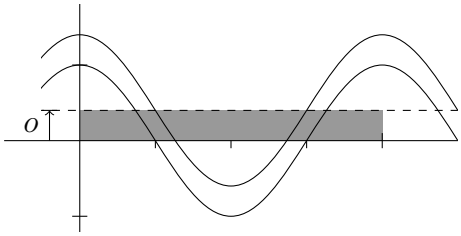

Figure 4.7: The area (grey) below the mean of a cosine wave is obviously proportional to the cosine's offset o.

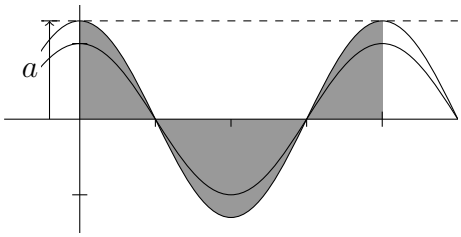

Figure 4.8: The area (grey) below a cosine wave with no offset is proportional to its peak amplitude a and to its standard deviation and therefore to its gain.

properly, and a synchronized signal, such as in the microwave kinetic inductance detectors (MKIDs) readout, may be significantly altered by the sampling process of a channel.

To limit the complexity of the spectrometer's analog input chain and the FPGA resources for the signal analysis, a single tone frequency was chosen as a simple and well determined test signal. Therefore an independent calibration oscillator with a frequency $f_{\mathrm{T}} = 32.768\,\mathrm{MHz}$, which is intentionally no fraction of the sampling frequency $f_{\mathrm{S}} = 5000\,\mathrm{MHz}$, is connected to an unused analog input of the ADC on the XFFTS.

Figure 4.7 displays the accumulated values of the samples of each channel, which is proportional to the mean of the samples. The offset error can easily be derived from the mean of the samples by subtracting the original mean of the signal, which usually equals zero [27].

The standard deviation, or root-mean-square (RMS), of the signal's samples defines its average amplitude, which is proportional to its gain [27]. The gain error can be derived by comparing the standard deviation from each channel to a reference, e.g. the average over all channels. Calculating the standard deviation requires to square each sample in the FPGA before accumulation. However,

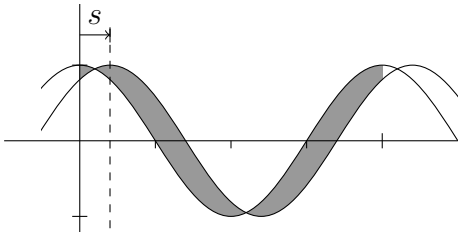

Figure 4.9: The area (grey) between two time-shifted cosine waves with same offset and gain depends on their shift s, which depends on the phase errors.

using (2.16) yields that the amplitude of a cosine wave with no offset is proportional to the integral of its absolute value that is visualized in figure 4.8:

$$\sqrt{\int_0^{2\pi} (a \cdot \cos(x))^2 \, \mathrm{d}x} = \frac{\sqrt{\pi}}{4} \cdot \int_0^{2\pi} |a \cdot \cos(x)| \, \mathrm{d}x \tag{4.2}$$

Assuming the offset error is already eliminated, the test signal allows to calculate the gain error from the accumulated absolute values. Therefore, the square operation can be replaced by a simpler absolute value operation, which requires no FPGA multipliers.

To measure the phase error P_m, assume both, offset and gain error, to be eliminated. Consecutive ADC channels $m-1$, m now can be considered to sample time-shifted versions of the test signal. The relative shift s_m of the test signal between the channels can be calculated from the difference $P'_m = P_m - P_{m-1}$ between their phase errors in units of a sample, the sampling rate, and the frequency of the test signal:

$$s_m = 2\pi \frac{f_\mathrm{T}}{f_\mathrm{S}} \cdot (1 + P'_m) \tag{4.3}$$

Applied to the cosine test signal, figure 4.9 illustrates how the shift s_m affects the area S_m between the signals. The absolute differences between the sample values of both channels, the FPGA easily calculates, accumulate to this area. To calculate S_m for a cosine wave use (2.15) and (2.16):

$$\begin{aligned} S_m &= \int_0^{2\pi} |\cos(x) - \cos(x - s_m)| \, \mathrm{d}x = \left|2 \sin\left(\frac{s_m}{2}\right)\right| \cdot \int_0^{2\pi} \left|\sin\left(x - \frac{s_m}{2}\right)\right| \, \mathrm{d}x = \left|8 \sin\left(\frac{s_m}{2}\right)\right| \\ &\approx 4 s_m, \; s_m \ll \pi \end{aligned} \tag{4.4}$$

To recover P'_m from S_m easily, consider the linear approximation for small shifts $S_m \approx 4s_m$. With $f_\mathrm{T} = 32.768\,\mathrm{MHz}$ and $f_\mathrm{S} = 5000\,\mathrm{MHz}$ the absolute approximation error Δt is below the resolution of the phase adjustment of $\sim 30\,\mathrm{fs}$:

$$\begin{aligned} \Delta s &= \frac{S_m}{4} - s_m = 2\sin\left(\pi\frac{f_\mathrm{T}}{f_\mathrm{S}}\right) - 2\pi\frac{f_\mathrm{T}}{f_\mathrm{S}} \approx -2.909 \cdot 10^{-6} \\ \Rightarrow \Delta t &= \frac{\Delta s}{2\pi f_\mathrm{T}} \approx -14.13\,\mathrm{fs} \end{aligned} \tag{4.5}$$

Therefore, find $P'_m \approx \frac{S_m}{4} \cdot \frac{f_\mathrm{S}}{2\pi f_\mathrm{T}} - 1$. To actually find the individual phase errors P_m, calculate $P''_m := \sum_{j=1}^{m} P'_j = P_m - P_0$. Since the phase errors are not measured independently, but with respect to each other, a value must be picked for the first phase error P_0, such as the average of all P''_m or just $P_0 = 0$.

In total, the suggested calibration procedure just requires FPGA resources to accumulate three values for each ADC channel: its samples, their absolute values, and the absolute differences to the previous sample. Further operations, such as scaling to the stepsize of the ADC's calibration registers, can be performed after sent to a PC.

4.3 Windowing and WOLA

The first step of signal processing related to spectral analysis is to apply a window function and WOLA. With respect to chapter 4.1 expect P parallel data streams of input samples. Additionally, expect to output Q samples per data stream to an FFT and collect a total of $P \cdot Q \cdot R$ samples for R-fold WOLA processing on FFT frames that contain $P \cdot Q$ samples.

To perform R-fold WOLA, it is convenient to store the samples from previous frames in $R - 1$ buffers. Including samples from the current frame, this allows to read samples from R frames simultaneously. One way to address those buffers is to write them circularly. This limits write access to one buffer at a time. However, read and write access require additional control logic to define the first buffer and multiplexing to order the frames correctly. Regarding the buffers as delay elements instead, allows to arrange them linearly [94]. Current samples are always written to the same buffer unit and each sample that is going to be overwritten is copied to the following buffer.

To choose any window with full flexibility requires to store $P \cdot Q \cdot R$ window values w_j. Since most windows are symmetric, it is safe to assume $w_j = w_{PQR-j}$, which allows to save almost half of the window memory [69]. It appears obvious to just store the first half $0 \leq j < \frac{PQR}{2}$ of a symmetric window and use it in reverse order to simulate the second half $\frac{PQR}{2} \leq j < PQR$. In fact $w_{\frac{PQR}{2}}$ is not stored this way and the second half of the window is shifted by one value, such as if $w_j = w_{PQR-1-j}$. Figure 4.10 displays the effect to the spectrum for a National Instruments Flat Top window with $PQR = 32768$ values, such as used for a 8192-point FFT and 4-fold WOLA. The effect to the spectrum and to all window parameters from chapter 2.5 is negligible with even falling significance for longer windows. Usual windows for wideband spectroscopy modes are $PQR = 65536$ values

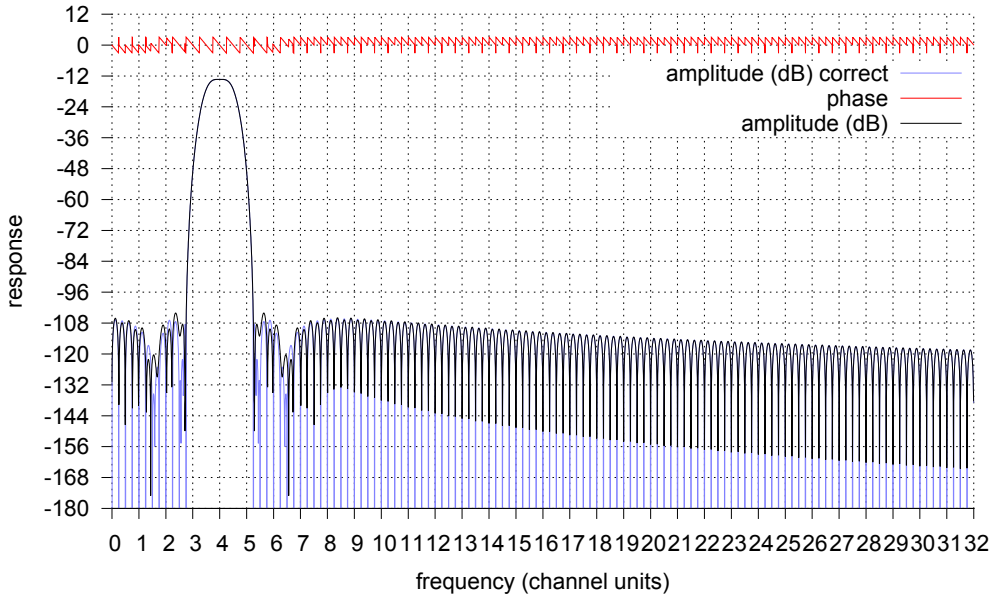

Figure 4.10: Response of phasors in channel $k = 4$, preprocessed with a National Instruments Flat Top window that is mirrored incorrectly. It plots amplitude in dB (black) and phase (red) for a window with $PQR = 32768$ values, scaled for $R = 4$-fold WOLA. It is compared to the amplitude in dB (blue) for the correct window.

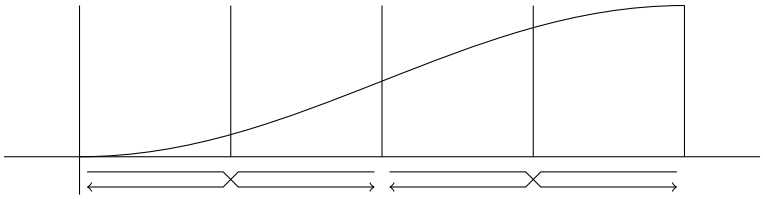

Figure 4.11: First half of a window distributed to $R = 4$ memory blocks. The arrows indicate the order of read access to each block.

long for the AFFTS and $PQR = 262144$ for the XFFTS. Therefore, the WOLA implementation can be simplified by accepting an incorrectly mirrored window without significant loss of performance.

To read the window values properly, it is convenient again to store them in R independent memory blocks. If each block $0 \leq r < R$ stores window values w_j in the range $rPQ \leq j < rPQ + PQ - 1$, any block must provide one set of P window values at a time. Access to the unmirrored first half of the window starts with the first values of an even block and finishes with the last values of the following uneven block. The mirrored second half of the window can be accessed in reverse order, starting at the end of an uneven block and finishing with the beginning of the previous even block. Thus, addressing the window memory blocks requires counters that alternately count up and down, with differing direction between even and odd blocks, such as shown in figure 4.11.

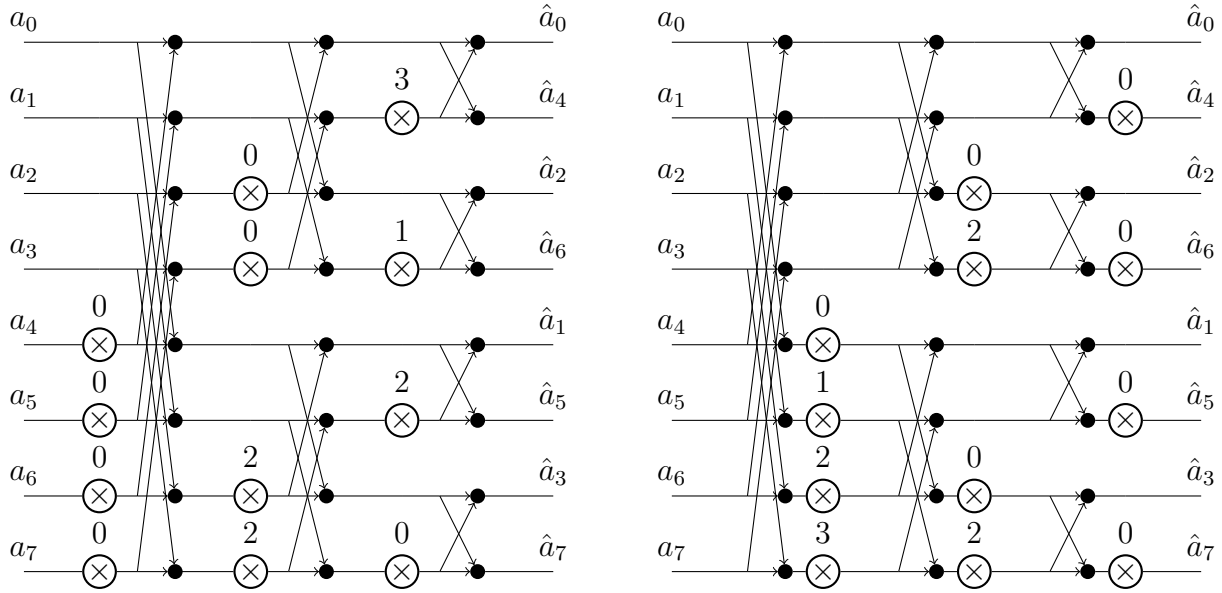

Figure 4.12: Structure of a radix-2 DIT FFT (left) and a radix-2 DIF FFT (right) with $P = 8$ points. The butterfly operations are displayed by arrows to filled circles. The complex multipliers are represented by crossed circles that are labeled with the exponent p of the twiddle factor $e^{-2\pi i \frac{p}{P}}$.

4.4 FFT architecture

Motivated by the sampling rate that is required by the wideband applications from chapter 3.1 and the FPGA clock rates mentioned in chapter 4.1, ADC data is demultiplexed. Thus, we obtain P parallel data streams, each one containing undersampled data with offsets of one sample to the adjoining streams. If a P-point FFT is insufficient for the desired spectral resolution, input samples have to be collected over Q clock cycles to calculate a $P \cdot Q$-point FFT. Since the structure of an FFT usually demands P and Q to be powers of 2, we assume this unless otherwise stated.

Parallel FFT To perform an FFT on P samples that arrive simultaneously from parallel data streams, a parallel FFT is required. Its basic element combines a complex twiddle multiplier and a butterfly unit with the size of the radix. Thus, the butterfly unit of a common radix-2 implementation is a 2-point FFT, which just calculates the sum and the difference of its inputs. Basically, a parallel FFT can be built by using (2.79) and (2.80) repeatedly until the remaining FFTs are the size of the radix itself. Choosing $N = 2$ results in a decimation in frequency (DIF) radix-2 FFT, which performs a twiddle multiplication before each butterfly. Choosing $M = 2$ yields a decimation in time (DIT) radix-2 FFT with a multiplier behind the butterflies. Both results in $\log_2(P)$ steps with $\frac{P}{2}$ parallel butterflies, such as shown in figure 4.12. Observe that non-trivial multiplications are concentrated at early steps for DIF and at later steps for DIT. Assuming the datawidth increases

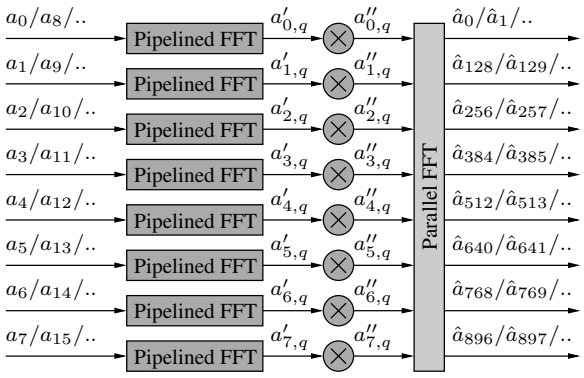

Figure 4.13: 8 pipelined 128-point FFTs followed by a parallel 8-point FFT form a combined 1024-point FFT (8x128).

with each operation, a DIF implementation is preferable, since it may safe hardware resources in the FPGA.

Pipelined FFT Performing an FFT on Q consecutive samples requires a pipelined FFT. It can be built from the same basic units as a parallel FFT, but organized linearly and supplemented with a buffer to store intermediate results [86]. A radix-2 pipelined Q-point FFT therefore utilizes $\log_2(Q)$ butterfly units. Such implementations are available as speed-optimized IP cores that are delivered with Xilinx ISE [110]. The input or output order of a parallel FFT can be changed at no cost, since it just requires to route wires differently during synthesis. A pipelined FFT, however, requires additional memory to change the order naturally given by an FFT, such as shown in figure 4.12. Common pipelined FFTs therefore output data in bit-reversed order if the input is in natural order [110, Bit and Digit Reversal]. Proper indexing of the FFT output just requires to reverse the bits of an increasing counter. However, the order itself must be taken into account for further processing steps after a pipelined FFT.

An input of both, Q consecutive samples, received on P parallel data streams, requires to combine both, parallel and pipelined FFTs.

4.4.1 Combining parallel and pipelined FFTs

The way an FFT is split up (chapter 2.6) suggests feeding each parallel data stream into a pipelined N-point FFT ($N = Q$) to calculate the inner sums $a'_{m,q}$. After twiddle multiplication, a parallel M-point FFT can be used to calculate $M = P$ spectral channels in any clock cycle [45]. Altogether, this creates a combined FFT (figure 4.13) that operates sequentially on parallel data streams [40]. In applications that require high frequency resolution, an FFT may exceed the capabilities of a single FPGA. Therefore, it may be desirable to split it into independent parts. Expecting the pipelined

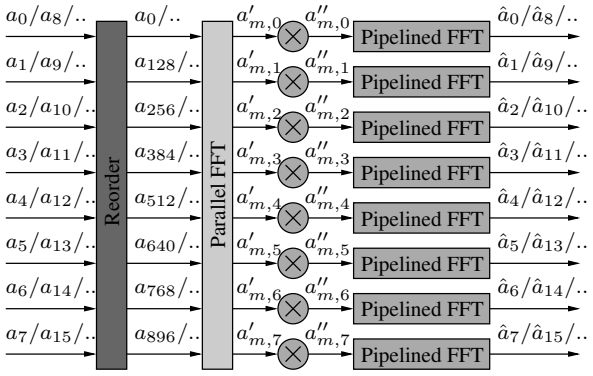

Figure 4.14: Rearranging the input, allows parallel FFT first and splitting data streams afterward. A parallel 8-point FFT followed by 8 pipelined 128-point FFTs form a splitting 1024-point FFT (8x128).

FFTs to be the largest part of a combined FFT, separating them from each other would have the highest impact on resource consumption. In a combined FFT, data from all parallel streams has to be set against each other at the end. Therefore, separating the pipelined FFTs to different, parallel FPGAs, requires a high speed bus between them with a consistent and synchronous delay [45]. Since current Xilinx FPGAs lack synchronization circuits naturally (chapter 4.1), implementing such a bus would require lots of manual effort. Therefore, independent data streams at the end of a combined FFT would simplify parallelization over several FPGAs.

A splitting FFT (figure 4.14) achieves this by moving the parallel N-point FFT ($N = P$) to the beginning [40]. Since each FFT in (2.79) needs undersampled input, the data has to be rearranged first, dependent on the size of the complete FFT: The parallel FFT at the front requests $M = Q$ consecutive samples at each input, skipping the next $M \cdot N - M$ samples, which are needed at its other inputs in parallel. Chapter 4.4.2 describes a memory module for $M \cdot N$ samples, followed by a two-dimensional shift register, implementing the rearrange efficiently. Behind the parallel FFT, the data streams become independent of each other. Each one is multiplied by twiddle factors and the resulting $a''_{m,q}$ are fed into pipelined M-point FFTs to calculate the Nth part of the complete spectrum. So a splitting FFT combines a rearrange unit, a parallel FFT and multiple pipelined FFTs, such that data streams become independent after parallel FFT and can therefore be split into multiple partitions at the end.

Note that its width P and its length Q affect hardware utilization of a combined or splitting FFT differently [40]. Further note the difference in memory utilization $\mathrm{Mem}\,(P, Q)$ and computation logic $\mathrm{Logic}\,(P, Q)$ that can be counted in butterfly units for the pipelined and parallel FFTs and in complex multipliers for twiddle multiplication. Rearranging before a splitting FFT is excluded from this consideration. Doubling P will double the number of pipelined FFTs and therefore all hardware utilized by them. The same is approximately true for twiddle multipliers, noting that all twiddles of the first multiplier equal 1 (compare (2.80)). The parallel FFT grows with P as $\mathrm{O}(P \cdot \log P)$. Doubling Q on the other hand only affects the pipelined FFTs and the memory to store twiddles.

In summary a combined or splitting FFT's use of FPGA logic grows stronger with its width P than with its length Q [40]:

$$\begin{aligned} \mathrm{Logic}(P,Q) &= \mathrm{O}\left(P \cdot \log P \cdot \log Q\right) \\ \mathrm{Mem}\left(P,Q\right) &= \mathrm{O}\left(P \cdot Q\right) \end{aligned} \tag{4.6}$$

4.4.2 Matrix Rearrange

As described in chapter 4.4, a set of $P \cdot Q$ high-speed input samples can be expected in P parallel data streams over Q clock cycles. So initially a sample a_j is available at cycle q_j on data stream p_j:

$$\begin{aligned} p_j &= j \bmod P \\ q_j &= \left\lfloor \frac{j}{P} \right\rfloor \\ j &= q_j \cdot P + p_j \end{aligned} \tag{4.7}$$

The P samples available at cycle q form a vector A_q:

$$A_q = (a_{P \cdot q}, a_{P \cdot q+1}, \ldots, a_{P \cdot q+P-1}) \tag{4.8}$$

To keep overview, r counts full frames of Q vectors A_q, that form the input of an FFT:

$$r = \left\lfloor \frac{q}{Q} \right\rfloor \tag{4.9}$$

This arrangement fits for a combined FFT. A splitting FFT however requires consecutive samples on each data stream. So sample a_j shall be at cycle $\hat{q}_j$ on data stream $\hat{p}_j$:

$$\begin{aligned} \hat{p}_j &= \left\lfloor \frac{j}{Q} \right\rfloor \\ \hat{q}_j &= j \bmod Q \\ j &= \hat{p}_j \cdot Q + \hat{q}_j \end{aligned} \tag{4.10}$$

Combining equations (4.7) and (4.10), we can calculate the origin p, q of a sample a_j that is needed on output data stream $\hat{p}$ at a given cycle $\hat{q}$:

$$\begin{aligned} p &= (\hat{p}_j \cdot Q + \hat{q}_j) \bmod P \\ q &= \left\lfloor \frac{\hat{p}_j \cdot Q + \hat{q}_j}{P} \right\rfloor \end{aligned} \tag{4.11}$$

Our application demands the FFT size $P \cdot Q$ as big as possible to increase spectral resolution. Additionally, the number of parallel data streams P shall be small to reduce hardware usage. Therefore,

Figure 4.15: Matrix rearrange of $Q = 128$ vectors A_q, each with $P = 8$ samples a_j. First, a buffer repeatedly groups P vectors. Secondly, a matrix rearranges the P^2 samples of each group.

assume $P \leq Q$. Since the structure of an FFT demands P and Q to be powers of 2, this yields Q to be a multiple of P, which eases (4.11):

$$\begin{aligned} p &= \hat{q}_j \bmod P \\ q &= \hat{p}_j \cdot \frac{Q}{P} + \left\lfloor \frac{\hat{q}_j}{P} \right\rfloor \end{aligned} \tag{4.12}$$

So all samples needed at cycle $\hat{q}$ origin from the same input data stream $p = \hat{q} \bmod P$. Using BRAM only would therefore require to read P values at once, that have been written in P cycles. In principle BRAM is capable of doing so by defining the data port used for reading P times the data width of the one used for writing [109]. However, a real-time application requires a new set of P samples to be stored, replacing the current ones when they are read. So another data port for writing would be needed as well with P times the original ones' data width. For most values of P and Q, this problem iterates, each step multiplying port width by P. Therefore, some kind of additional rearrangement, which precedes or succeeds the BRAM, is necessary. A way to do so is a full sized 2-port memory, followed by a smaller register matrix.

Vector buffer The first step of the matrix rearrange algorithm uses a BRAM buffer to presort a frame of Q vectors A_q. Each A_q is written in cycle q as it arrives [80]. The final output at one cycle $\hat{q}$ requires P samples, whose indices differ by Q. These are distributed over P vectors, whose indices differ by $\frac{Q}{P}$. Therefore groups of P vectors that are read from the buffer consecutively, shall have this property. A way to do so, is to read vector $A_{R(q')}$ in cycle q':

$$R\left(q'\right) = \left(q' \bmod P\right) \cdot \frac{Q}{P} + \left\lfloor \frac{q' \bmod Q}{P} \right\rfloor \tag{4.13}$$

It still takes P cycles to read these vectors, each containing one sample that is needed in a current cycle q', but $P - 1$ samples that are not. However note, the samples in each vector are consecutive,

as they are needed in consecutive cycles of a certain output data stream. To summarize, $R(q')$ offers a sequence to read groups of P vectors consecutively, whose P^2 samples are needed consecutively as well. So the remaining problem for a second step would be to rearrange subsets of P^2 samples from the original $P \cdot Q$ ones (figure 4.15).

A continuous flow of data, however, requires to consider an addressing scheme. Assume the buffer to store a full frame of Q vectors, reading the first vector of a frame just after its last one is written:

$$\begin{aligned} q' &= q - Q \\ \Rightarrow r' &= r - 1 \end{aligned} \tag{4.14}$$

As soon as the buffer is filled, each new vector needs to be written to the buffer address that is just read. Otherwise, data would be overwritten and therefore lost. Although a slightly smaller buffer is imaginable, it would require to reduce the offset between write and read. This would complicate the addressing, but may even save no hardware if the buffer is implemented in BRAM. So using (4.14), a vector A_q from the second frame of input data ($r = 1$) is written, when vector A_{q-Q} is read from buffer address $R(q)$. Therefore, A_q should be written to the same address. To read a vector $A_{R(q')+Q}$ from this second frame obviously requires to access the buffer address $R^2(q')$. Iterating this concept yields to read from address $R^{r'+1}(q')$ in cycle q', which equals the designated write address $R^r(q)$ in cycle q. Despite its complicated formula, it is easy to implement $R(q)$ in hardware if q is represented by an unsigned integer q_{bin} with $\log_2 Q$ bits. Note the implicit modulo operation $q_{\text{bin}} = q \bmod Q$, which is negligible, since the addressed buffer is limited accordingly. Now $R(q_{\text{bin}})$ equals a circular right shift $\hookrightarrow$ by $\log_2 P$ bits. The iterated function $R^r(q)$ therefore requires a circular barrel shift:

$$\begin{aligned} R^r(q_{\text{bin}}) &= q_{\text{bin}} \hookrightarrow (r \log_2 P) \\ &= q_{\text{bin}} \hookrightarrow (r \log_2 P \bmod \log_2 Q) \end{aligned} \tag{4.15}$$

Sample matrix As figure 4.15 displays, the matrix rearrange algorithm requires a second step to rearrange P^2 samples in P associated vectors $A_{R(q')}$. Storing these vectors as columns of a $P \times P$ matrix, ordered as they are read from the vector buffer, yields a promising result: Samples that are needed simultaneously are located in the same row. Reading a set of output samples from the matrix obviously deallocates one of its rows, which can be filled with the next vector that is read from the buffer. Arranging a group of P vectors in columns and in rows alternately therefore yields the final arrangement of the samples.

Still there are options to implement this matrix. The preceding description suggests to store the next vector to the row or column that is just read. If addressed memory can be used, this method is probably the easiest way to access the data. Using BRAM may actually require this method, since it has a limited number of access ports. For the same reason the use of BRAM may be ineffective or even impossible for certain P. Using flip-flops instead, allows simultaneous access to each sample, but requires additional logic to address them. To read any of P rows and any of P columns requires P multiplexers with $2P$ inputs each. To write accordingly, each matrix location requires a write-enable

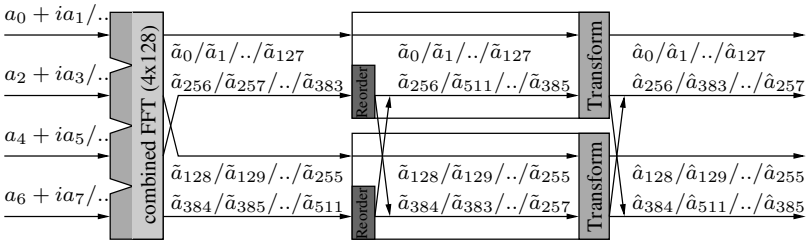

Figure 4.16: A combined 512-point FFT (4x128 points) that uses its imaginary inputs. Channel transformation results in the first half of a 1024-point FFT. The second half is obsolete.

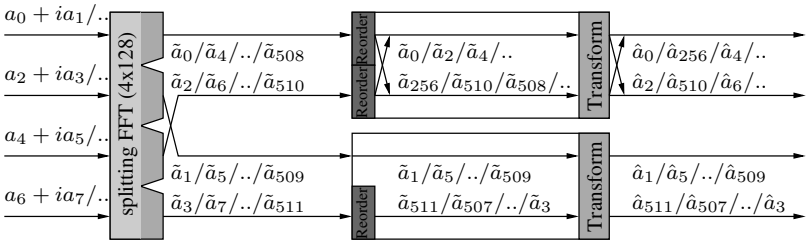

Figure 4.17: A splitting 512-point FFT (4x128 points) that uses its imaginary inputs. Channel transformation results in the first half of a 1024-point FFT. The second half is obsolete. Pairs of data streams are still independent at the end.

switch and a multiplexer with 2 inputs, which depend on its row and on its column. Additionally, lots of interconnect is required to connect each input and each output to $2P$ possible matrix locations. A method that is more suited to flip-flops is to implement the matrix as a two-dimensional shift register. When the vectors $A_{R(q')}$ are arranged in columns, it is always read from the first row $p = 0$ and written to the last one $p = P - 1$. At the same time, the content of each row p is shifted one position ahead to row $p - 1$. When the vectors are arranged in rows, the same actions apply to the columns accordingly. Each P cycles the direction of the shift changes. This implementation just requires P multiplexers with 2 inputs each, since only one row and one column need to be considered. Although each matrix location is constantly shifted, it requires less logic than the first method: Each location still has two possible sources, but requires no write-enable switch, since it is accessed constantly. Additionally, the amount of interconnect decreases, since only neighboring matrix locations are connected.

Finally note, the matrix rearrange grows with P as $O(P^2)$, exceeding the complexity of the splitting FFT itself. This increases the need to keep P small for splitting FFTs.

4.4.3 Use of imaginary input

Chapter 2.7 asserts the waste of resources when feeding a complex FFT with real input by calculating each data content twice, and describes a way to avoid it. Using the imaginary inputs of a combined or

splitting FFT for half the real input samples has another positive effect, since its width can be reduced to $\frac{P}{2}$ (figures 4.16, 4.17). Pairs of intermediate channels $\tilde{a}$ from the FFT output are transformed to the final channels $\hat{a}$, as in (2.84), (2.85) and (2.86). This transformation requires to re-sort the data, calculate four complex sums and a complex multiplication. So its hardware costs are just slightly higher than doubling the FFT length Q by one stage in pipelined FFTs. Using imaginary inputs is therefore similar to halving P and doubling Q. According to (4.6), this yields a more efficient use of the FPGA logic. Remember from (2.81), that spectral resolution is preserved, although the number of computed channels is halved.

Locate channel pairs First, note that in terms of chapter 2.7, an FFT of size $P \cdot Q = \frac{N}{2}$ is implemented. Remember from that chapter, that all intermediate channels form corresponding pairs, except $\tilde{a}_0$ and $\tilde{a}_{\frac{P \cdot Q}{2}}$, which correspond to themselves. To simplify re-sorting, assume these two are corresponding to each other as well. This yields corresponding channels $\tilde{a}_k$ and $\tilde{a}_{k'}$ and the issue of self-correspondence becomes a special case of the actual computation:

$$k \longleftrightarrow k' = \begin{cases} \frac{P \cdot Q}{2}, & k = 0 \\ 0, & k = \frac{P \cdot Q}{2} \\ P \cdot Q - k, & \text{else} \end{cases} \tag{4.16}$$

Secondly, the initial arrangement of the channels has to be defined. A combined FFT yields the same arrangement as (4.10) and a splitting FFT yields the same as (4.7). A general approach is to introduce the smallest distance S between the indices of values in the same stream. This yields that a value $\tilde{a}_k$ is located in stream p at cycle q the following way:

$$\begin{aligned} p_k &= \left\lfloor \frac{k}{Q \cdot S} \right\rfloor \cdot S + k \bmod S \\ q_k &= \left\lfloor \frac{k}{S} \right\rfloor \bmod Q \\ k_{p,q} &= q \cdot S + \left\lfloor \frac{p}{S} \right\rfloor \cdot Q \cdot S + (p \bmod S) \\ &= q \cdot S + p \cdot Q + (p \bmod S) \cdot (1 - Q) \end{aligned} \tag{4.17}$$

$S = 1$ yields the output arrangement of a combined FFT and $S = P$ the one of a splitting FFT. Mixtures of combined and splitting FFTs may yield arrangements with $1 < S < P$. Now define corresponding stream pairs p, p' similar to corresponding channels $k \longleftrightarrow k'$:

$$p' = \begin{cases} \frac{P}{2}, & p = 0 \\ 0, & p = \frac{P}{2} \\ P - p, & \text{else} \end{cases} \tag{4.18}$$

Note that $p'' = p \neq p'$ and therefore both streams form a real pair if there are at least two. Also note that p and p' are from different halves of the streams: $p < \frac{P}{2} \Leftrightarrow p' \geq \frac{P}{2}$.

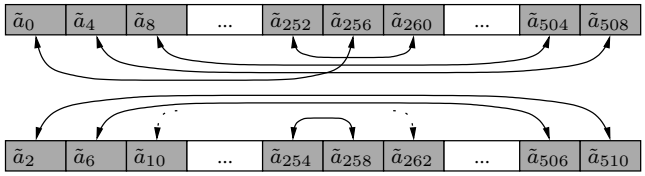

Figure 4.18: Channels correspond with others in the same stream if $S = P$ and $p \bmod S = 0$. Indices arise from streams $p = 0$ and $p' = \frac{P}{2} = 2$ of a splitting 512-point FFT ($S = 4, P = 4, Q = 128$).

First, consider the $\frac{P}{S}$ streams with $p \bmod S = 0$. All P streams of a combined FFT meet this criterion and one stream of a splitting FFT does. We will see that combining the channels from a stream pair p, p' is not sufficient if $p \bmod S = 0$. Therefore define streams p^*, secondary corresponding to p:

$$\begin{aligned} &p \bmod S = 0 \\ &\quad \Rightarrow p^* = P - S - p \end{aligned} \tag{4.19}$$

It is obvious that $p^* \bmod S = 0$ and $p^{**} = p$ as well. However p^*, p form no real pair if $S = P$, whereas p and p' are defined to differ, although there's only one stream $p \bmod S = 0$. This case obviously occurs at the first stream $p = 0$ of any splitting FFT, but also at a "combined" FFT with only one pipeline ($S = P = 1$), where no p' exists at all:

$$\begin{aligned} &p \bmod S = 0 \wedge S = P \\ \Rightarrow &p = 0 \wedge p^* = 0 \wedge p' = \frac{P}{2} \end{aligned} \tag{4.20}$$

Using (4.16) and (4.17) with (4.20) yields all channels corresponding with others in the same stream:

$$\begin{aligned} 0 = \quad & k_{p,0} \quad \longleftrightarrow \quad k_{p,\frac{Q}{2}} \quad = \tfrac{Q}{2} \cdot P \\ q \cdot P = \quad & k_{p,q} \quad \longleftrightarrow \quad k_{p^*,Q-q} \quad = Q \cdot P - q \cdot P \quad , 0 < q < \tfrac{Q}{2} \\ q \cdot P + \tfrac{P}{2} = \quad & k_{p',q} \quad \longleftrightarrow \quad k_{p',Q-1-q} \quad = Q \cdot P - q \cdot P - \tfrac{P}{2} \quad , 0 \leq q < \tfrac{Q}{2} \end{aligned} \tag{4.21}$$

Figure 4.18 displays this correspondence graphically. Remember that p' may not exist.

The usual case in a combined FFT yields p' and p^* that differ from p, but are multiples of S:

$$\begin{aligned} &p \bmod S = 0 \wedge S < P \\ \Rightarrow &p^* \bmod S = 0 \wedge p' \bmod S = 0 \end{aligned} \tag{4.22}$$

Now using (4.16) and (4.17) with (4.22) yields the first channel from p corresponding with one from p' and the rest with ones from p^*:

$$\begin{aligned} p \cdot Q = \quad & k_{p,0} \quad \longleftrightarrow \quad k_{p',0} \quad = p' \cdot Q \\ q \cdot S + p \cdot Q = \quad & k_{p,q} \quad \longleftrightarrow \quad k_{p^*,Q-q} \quad = P \cdot Q - q \cdot S - p \cdot Q \quad , 0 < q < Q \end{aligned} \tag{4.23}$$

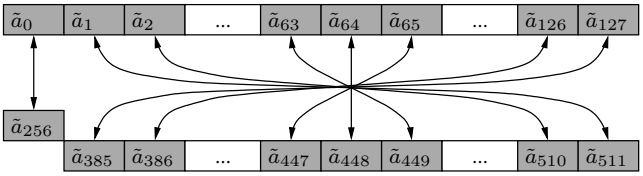

Figure 4.19: Channels from each stream correspond with others in two further streams if $S < P$ and $p \bmod S = 0$. Indices arise from streams $p = 0$, $p' = \frac{P}{2} = 2$ and $p^* = P - 1 = 3$ of a combined 512-point FFT ($S = 1, P = 4, Q = 128$).

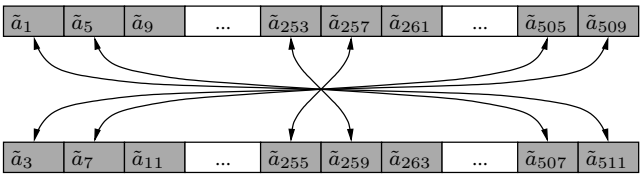

Figure 4.20: Channels of two corresponding streams correspond with each other if $p \bmod S > 0$. Indices arise from streams $p = 1$ and $p' = P - 1 = 3$ of a splitting 512-point FFT ($S = 4, P = 4, Q = 128$).

Figure 4.19 displays this correspondence graphically. To prevent a channel pair from being considered twice, one may ignore the second half of streams $p \geq \frac{P}{2}$:

$$\begin{aligned} & p \bmod S = 0 \wedge S < P \wedge p < \frac{P}{2} \\ \Rightarrow & p' \geq \frac{P}{2} \wedge p^* \geq \frac{P}{2} \end{aligned} \tag{4.24}$$

One could assume that channel pairs are missed this way, since (4.23) only considers parts of each p' and p^*. But (4.24) proves that each channel pair is distributed to a stream from the first half and to a stream from the second half. Therefore each pair is considered by the channels from the first half of streams $p < \frac{P}{2}$. Looking more closely and combining (4.18) and (4.19) with (4.24) yields that each channel p' secondarily corresponds to a channel p'^* and vice versa:

$$\begin{aligned} p'^* &= p - S \bmod \frac{P}{2} \\ p^{*\prime} &= p + S \bmod \frac{P}{2} \end{aligned} \tag{4.25}$$

Although $p'' = p$ and $p^{**} = p$ is always true, $p'^* = p^{*\prime} = p$ only is if $S = \frac{P}{2}$. Therefore, note that all streams $p \bmod S = 0$ correspond to each other in some way and therefore have to exchange data. Since the parallel FFT at the end of a combined FFT already does so, that is no disadvantage.

Luckily, there is only one channel $p \bmod S = 0$ in a splitting FFT that is represented by the special case in (4.20). The usual case in a splitting FFT, however, misses a secondary correspondent stream p^*:

$$\begin{aligned} & p \bmod S > 0 \\ \Rightarrow & p' \bmod S = S - (p \bmod S) > 0 \wedge 1 < S \leq P \end{aligned} \tag{4.26}$$

Using imaginary inputs of a splitting FFT therefore still allows independent pairs of data streams at its end (compare chapter 4.4.1). Figure 4.17 displays that. Now using (4.16) and (4.17) with (4.26) yields each channel from p correspond with one from p'. Since channel $\tilde{a}_0$ is handled in (4.21) or (4.23), there is no case distinction here:

$$k_{p,q} \quad \longleftrightarrow \quad k_{p',Q-1-q} \quad = P \cdot Q - k_{p,q} \quad 0 \leq q < Q \tag{4.27}$$

Figure 4.20 displays this correspondence graphically.

Join channel pairs To transform a pair of intermediate channels into final channels, the pair has to be joined: Channels from each stream need to be buffered and resequenced, such that corresponding channels appear simultaneously. In the usual cases (4.22) and (4.26), corresponding channels are located in different streams. Obviously, some kind of resequencing within each stream is sufficient to output corresponding channels simultaneously. In case (4.20) however, corresponding channels share the same stream. A valid method to join these channels is to output them consecutively and delay one of them. Doing so with two streams $p = 0$ and $p' = \frac{P}{2}$, allows to transform a channel pair from each stream alternately. Before considering methods to resequence streams, remember from chapter 4.4, a pipelined FFT may output channels in bit-reversed order. Therefore distinguish between cycles q and time t to allow cycles not incrementing with time naturally, and define the input order by q_t as a bidirectional function of time t. Streams with natural input order $q_t = t$ will be considered if necessary, but consider bit-reversed order $q_t = \text{BITREV}\,(t)$ as the usual input order of each stream.

One general approach to resequence a stream is to buffer a complete frame of Q channels and read them in a valid output order (compare the vector buffer from chapter 4.4.2) [80]. A channel $k_{p,q}$ from the next frame is allocated to the address $R\,(q)$ that is read at that cycle q. Of course the allocation has to change from one frame to another if the input order q_t differs from the output order $R\,(q_t) \neq q_t$. Ideally, just two allocations alternate ($R^2\,(q_t) = q_t$). However, note that $Q!$ ways exist to allocate Q values to Q addresses. The approach works for any input order, but in case (4.20) applies, others than a bit-reversed input order may yield lots of different allocations or odd ones. Note that two corresponding streams contain Q channel pairs and a subset of more than Q of these $2Q$ channels contains at least one corresponding pair. So it would be sufficient to buffer just $\frac{Q}{2}$ channels per stream to access at least one channel pair. This is true for any input order, but some of them require cycles, when a channel is not buffered, but instantly joined with its correspondent. This requires an extended concept for allocation that allows missing allocations and changes twice

a frame. An implementation therefore requires additional case differentiations to chose the source of a channel as well as the correct allocation scheme. This is particularly true for a bit-reversed input order. Therefore, the first approach is chosen to elaborate on, although the second one would consume less memory. It may however be worth to reconsider if memory is the critical resource in a spectrometer design. According to (4.6), this urge rises with spectral resolution.

Case (4.20) requires two independent allocation schemes R_p for stream $p = 0$ and $R_{p'}$ for stream $p' = \frac{P}{2}$. To output the corresponding channels of a stream consecutively, R has to meet the following condition:

$$k_{p,R(q_{2t})} \longleftrightarrow k_{p,R(q_{2t+1})} \tag{4.28}$$

A bit-reversed input order now yields consecutive channels with fixed distance:

$$q_{2t+1} = \text{BITREV}\,(2t+1) = \text{BITREV}\,(2t) + \frac{Q}{2} = q_{2t} + \frac{Q}{2} \tag{4.29}$$

Using (4.28) and (4.29) with (4.21) yields a passable allocation scheme for R_p:

$$R_p\,(q) = \begin{cases} q, & q = 0 \\ q, & 0 < q < \frac{Q}{2} \\ q, & q = \frac{Q}{2} \\ \frac{3Q}{2} - q, & \frac{Q}{2} < q < Q \end{cases} \tag{4.30}$$

The same is true for $R_{p'}$:

$$R_{p'}\,(q) = \begin{cases} q, & 0 \leq q < \frac{Q}{2} \\ \frac{3Q}{2} - 1 - q, & \frac{Q}{2} \leq q < Q \end{cases} \tag{4.31}$$

Note that $R_p^2\,(q) = R_{p'}^2\,(q) = q$ and, therefore, none of them iterates to further allocations. A natural input order still allows $R_p^2\,(q) = q$, but requires a more sophisticated allocation scheme R_p. Assuring all conditions, when iterating from $R_p\,(0) = 0$ yields

$$R_p\,(q) = \begin{cases} q, & q = 0 \\ \frac{Q}{2}, & q = 1 \\ \frac{Q}{2} - q, & 1 < q < \frac{Q}{2}, \quad q \text{ even} \\ \frac{Q}{2} - 1 + q, & 1 < q < \frac{Q}{2}, \quad q \text{ uneven} \\ 1 - \frac{Q}{2} + q, & \frac{Q}{2} \leq q < Q, \quad q \text{ even} \\ \frac{3Q}{2} - q, & \frac{Q}{2} \leq q < Q, \quad q \text{ uneven} \end{cases} \tag{4.32}$$

In contrast to that a natural order allows a quite simple $R_{p'}$:

$$R_{p'}\,(q) = \begin{cases} q, & q \text{ even} \\ Q - q, & q \text{ uneven} \end{cases} \tag{4.33}$$

Cases (4.22) and (4.26) require to resequence the channels of the corresponding streams p and p' with respect to each other. Therefore the allocation scheme R_p may be freely chosen and $R_{p^*} = R_{p'}$ needs to be adjusted to that choice. So let $R_p(q) = q$. This implies (4.28) becoming obsolete, since corresponding channels shall appear the same cycle q:

$$k_{p,R_p(q)} \longleftrightarrow \begin{cases} k_{p',R_{p'}(q)}, & q = 0 \\ k_{p^*,R_{p^*}(q)}, & q > 0 \end{cases} \tag{4.34}$$

Therefore, the allocation scheme is independent of the input order q_t. Using (4.34) with (4.23) yields simple allocation schemes for case (4.22):

$$\begin{aligned} R_p(q) &= q \\ R_{p^*}(q) = R_{p'}(q) &= Q - q \bmod Q \end{aligned} \tag{4.35}$$

Case (4.26) finally requires to modify (4.34), since there is only one corresponding stream:

$$k_{p,R_p(q)} \longleftrightarrow k_{p',R_{p'}(q)} \tag{4.36}$$

Now using (4.36) with (4.27) yields

$$\begin{aligned} R_p(q) &= q \\ R_{p'}(q) &= Q - 1 - q \end{aligned} \tag{4.37}$$

Transform channel pairs Remember from chapter 2.7 that the actual transformation of $\tilde{a}_k$ and $\tilde{a}_{k'}$ is a quite easy task that can be implemented in three steps. Still the special case $k = 0, k' = \frac{N}{4}$ must be considered in each step, since $\tilde{a}_0$ and $\tilde{a}_{\frac{N}{4}}$ in fact don't correspond to each other, but to themselves.

First use (2.84) to add and subtract the intermediate channels $\tilde{a}_k, \tilde{a}_{k'}$ and calculate a'. Separating real parts $\Re$ from imaginary parts $\Im$ and excluding $k = 0$, yields four values x that represent all parts of $a'_{*,k}$ as well as $a'_{*,k'}$:

$$\begin{aligned} x_{1,k} &= \Re(\tilde{a}_{k'}) + \Re(\tilde{a}_k) = \Re\left(2 \cdot a'_{0,k}\right) = \Re\left(2 \cdot a'_{0,k'}\right) \\ x_{2,k} &= \Im(\tilde{a}_{k'}) + \Im(\tilde{a}_k) = \Re\left(2 \cdot a'_{1,k}\right) = \Re\left(2 \cdot a'_{1,k'}\right) \\ x_{3,k} &= \Re(\tilde{a}_{k'}) - \Re(\tilde{a}_k) = \Im\left(2 \cdot a'_{1,k}\right) = -\Im\left(2 \cdot a'_{1,k'}\right) \\ x_{4,k} &= \Im(\tilde{a}_{k'}) - \Im(\tilde{a}_k) = -\Im\left(2 \cdot a'_{0,k}\right) = \Im\left(2 \cdot a'_{0,k'}\right) \end{aligned} \tag{4.38}$$

Of course there's no such relation between $a'_{*,0}$ and $a'_{*,\frac{N}{4}}$ which would result in eight values x instead of four. Luckily, the imaginary parts of $a'_{*,0}$ and $a'_{*,\frac{N}{4}}$ equal zero. Therefore four values x are sufficient as well to store a' if $k = 0$:

$$\begin{aligned} x_{1,0} &= 2 \cdot \Re(\tilde{a}_0) = 2 \cdot a'_{0,0} \\ x_{2,0} &= 2 \cdot \Im(\tilde{a}_0) = 2 \cdot a'_{1,0} \\ x_{3,0} &= 2 \cdot \Re\left(\tilde{a}_{\frac{N}{4}}\right) = 2 \cdot a'_{0,\frac{N}{4}} \\ x_{4,0} &= 2 \cdot \Im\left(\tilde{a}_{\frac{N}{4}}\right) = 2 \cdot a'_{1,\frac{N}{4}} \end{aligned} \tag{4.39}$$

Second step is the twiddle multiplication in (2.85):

$$\begin{aligned} y_{2,k} &= \Re\left((x_{2,k} + ix_{3,k}) \cdot e^{-2\pi i \frac{k}{N}}\right) \\ &= \Re\left(2 \cdot a'_{1,k} \cdot e^{-2\pi i \frac{k}{N}}\right) = \quad \Re\left(2 \cdot a'_{1,k'} \cdot e^{+2\pi i \frac{k}{N}}\right) \\ y_{3,k} &= \Im\left((x_{2,k} + ix_{3,k}) \cdot e^{-2\pi i \frac{k}{N}}\right) \\ &= \Im\left(2 \cdot a'_{1,k} \cdot e^{-2\pi i \frac{k}{N}}\right) = -\Im\left(2 \cdot a'_{1,k'} \cdot e^{+2\pi i \frac{k}{N}}\right) \end{aligned} \tag{4.40}$$

Using $\Re(i \cdot \overline{z}) = \Im(z)$ and $\Im(i \cdot \overline{z}) = \Re(z)$ with (4.40) yields an equivalent implementation, in case it's easier to provide twiddles running counter clockwise:

$$\begin{aligned} y_{2,k} &= \Im\left((x_{3,k} + ix_{2,k}) \cdot e^{+2\pi i \frac{k}{N}}\right) \\ y_{3,k} &= \Re\left((x_{3,k} + ix_{2,k}) \cdot e^{+2\pi i \frac{k}{N}}\right) \end{aligned} \tag{4.41}$$

The case $k = 0$ and $k' = \frac{N}{4}$ just require twiddles 1 and $-i$, which can be implemented without an actual complex multiplication. Since the twiddle provided in that case equals 1 anyway, multiplication requires no special treatment, which yields x_2 and x_3 just delayed to y_2 and y_3:

$$\begin{aligned} y_{2,0} &= x_{2,0} = 2 \cdot a'_{1,0} \cdot 1 \\ y_{3,0} &= x_{3,0} = 2 \cdot a'_{0,\frac{N}{4}} \end{aligned} \tag{4.42}$$

Of course x_1 and x_4 must always be delayed, according to the twiddle multiplication, before they are set against y_2 and y_3.

This provides all terms to calculate the sums and differences in (2.85) and (2.86) as a third and final step:

$$\begin{aligned} \Re(\hat{a}_k) &= \frac{x_{1,k} + y_{2,k}}{2} = \quad \Re\left(a'_{0,k}\right) + \Re\left(a'_{1,k} \cdot e^{-2\pi i \frac{k}{N}}\right) \\ \Im(\hat{a}_k) &= \frac{y_{3,k} - x_{4,k}}{2} = \quad \Im\left(a'_{0,k}\right) + \Im\left(a'_{1,k} \cdot e^{-2\pi i \frac{k}{N}}\right) \\ \Re(\hat{a}_{k'}) &= \frac{x_{1,k} - y_{2,k}}{2} = \quad \Re\left(a'_{0,k}\right) - \Re\left(a'_{1,k} \cdot e^{-2\pi i \frac{k}{N}}\right) \\ \Im(\hat{a}_{k'}) &= \frac{y_{3,k} + x_{4,k}}{2} = -\Im\left(a'_{0,k}\right) + \Im\left(a'_{1,k} \cdot e^{-2\pi i \frac{k}{N}}\right) \end{aligned} \tag{4.43}$$

This is also true for $k = 0$, but requires special processing again:

$$\begin{aligned} \Re(\hat{a}_0) &= \frac{x_{1,0} + y_{2,0}}{2} = a'_{0,0} + a'_{1,0} \\ \Im(\hat{a}_0) &= 0 \\ \Re\left(\hat{a}_{\frac{N}{4}}\right) &= \frac{y_{3,0}}{2} = \quad a'_{0,\frac{N}{4}} \\ \Im\left(\hat{a}_{\frac{N}{4}}\right) &= \frac{-x_{4,0}}{2} = -a'_{1,\frac{N}{4}} \end{aligned} \tag{4.44}$$

However, note that the final step to calculate $\Re(\hat{a}_k)$ does not differ if $k = 0$.

4.5 Complex square

A power builder extracts the absolute power $|\hat{a_k}|^2$ of each channel from its value in the complex plane that is calculated by the FFT. This requires a complex square operation:

$$|\hat{a_k}|^2 = \Re(\hat{a}_k)^2 + \Im(\hat{a}_k)^2 \tag{4.45}$$

This simple operation usually requires two multiplications and a sum, which can be performed by two DSP slices of a Virtex-4 or Virtex-6 FPGA. The bit width b of those multipliers is, however, limited, so that the number of DSP slices increases if the multiplicands exceed 18 bit. Although Xilinx ISE is capable of splitting long values x, y and distributing the multiplication to multiple multipliers, a square operation allows optimization, since the multiplicands are equal. The multiplication of two split values $x = x_{\mathrm{lo}} + x_{\mathrm{hi}} \cdot 2^b$, $y = y_{\mathrm{lo}} + y_{\mathrm{hi}} \cdot 2^b$ requires 4 multiplications and the sum of the products.

$$x \cdot y = x_{\mathrm{lo}} \cdot y_{\mathrm{lo}} + x_{\mathrm{lo}} \cdot y_{\mathrm{hi}} \cdot 2^b + x_{\mathrm{hi}} \cdot y_{\mathrm{lo}} \cdot 2^b + x_{\mathrm{hi}} \cdot y_{\mathrm{hi}} \cdot 2^{2b} \tag{4.46}$$

Squaring one of these just requires 3 multiplications and the sum:

$$x^2 = x_{\mathrm{lo}}^2 + x_{\mathrm{lo}} \cdot x_{\mathrm{hi}} \cdot 2^{b+1} + x_{\mathrm{hi}}^2 \cdot 2^{2b} \tag{4.47}$$

Additionally, the last product's order of magnitude exceeds the maximum value of the first product. Thus, their bits do not interfere and summing those two actually requires no logic.

Finally, evaluate the output bit width b_{o} of the complete complex square operation from the input bit width b_{i}. The absolute maximum value of a two's complement number with b_{i} bit is $2^{b_{\mathrm{i}}-1}$. With this restriction on the components of a complex number, its maximum square amplitude is limited to $2 \cdot \left(2^{b_{\mathrm{i}}-1}\right)^2 = 2^{2b_{\mathrm{i}}-1}$. Since the result is always positive $b_{\mathrm{o}} = 2b_{\mathrm{i}}$ is always sufficient to prevent overflow.

4.6 Integration

Integration of power spectra has two desirable effects: First, it increases S/N, such as stated in chapter 2.8. Secondly, it reduces the data rate to allow transmission to an on-board controller or to a PC. However, it also manifests in increased bit width of the integrated channels.

Since both, WOLA and the FFT, perform a kind of integration already, these components require increasing bit width as well. Starting with an ADC resolution of A bit, a sample a_j is limited to $|a_j| \leq 2^{A-1}$. Performing an N-point FFT that uses its imaginary inputs sums up $2N$ samples, and performing R-fold WOLA sums up R weighted samples. A window different from a rectangle of

course reduces the signal amplitude. To compensate for that, the WOLA implementation of the AFFTS and the XFFTS multiplies each sample by 2. Depending on the signal and the window, the total gain may be up to a maximum of $4RN$. With a white noise signal and a window that gains incoherent power to $R \cdot 50\,\%$, using (2.92) allows to assume the total gain to the standard deviation of the noise only $\sqrt{2RN}$. Therefore, the power in a spectral channel $\hat{a}_k$ is limited to $\max\left(|\hat{a}_k|^2\right) = 2^{2A-2} \cdot 16R^2N^2$ and can be expected at an average $\mathrm{E}\left\{|\hat{a}_k|^2\right\} \leq 2^{2A-2} \cdot 2RN$ for white noise.

According to (2.92), further integration of N_I spectra over time $\tau = \frac{2N \cdot N_\mathrm{I}}{f_\mathrm{S}}$ increases the expectation value linearly, such as the limit:

$$\begin{aligned} \max_\Sigma\left(|\hat{a}_k|^2\right) &= \max\left(|\hat{a}_k|^2\right) \cdot N_\mathrm{I} = 2^{2A-2} \cdot 8R^2 N f_\mathrm{S} \cdot \tau \\ \mathrm{E}_\Sigma\left\{|\hat{a}_k|^2\right\} &= \mathrm{E}\left\{|\hat{a}_k|^2\right\} \cdot N_\mathrm{I} = 2^{2A-2} \cdot R f_\mathrm{S} \cdot \tau \end{aligned} \tag{4.48}$$

With Parameters that match for the XFFTS and for the requirements of wideband spectroscopy from chapter 3.1, we yield:

$$\begin{aligned} f_\mathrm{S} &= 5\,\mathrm{GHz} \approx 2^{32.2}\,\mathrm{Hz} \\ A &= 10,\ R = 4,\ N = 2^{15} \\ \Rightarrow \max_\Sigma\left(|\hat{a}_k|^2\right) &\approx \tau \cdot 2^{72.2}\,\mathrm{Hz} \\ \mathrm{E}_\Sigma\left\{|\hat{a}_k|^2\right\} &\approx \tau \cdot 2^{52.2}\,\mathrm{Hz} \end{aligned} \tag{4.49}$$

Such parameters for the AFFTS yield:

$$\begin{aligned} f_\mathrm{S} &= 3\,\mathrm{GHz} \approx 2^{31.5}\,\mathrm{Hz} \\ A &= 8,\ R = 4,\ N = 2^{13} \\ \Rightarrow \max_\Sigma\left(|\hat{a}_k|^2\right) &\approx \tau \cdot 2^{65.5}\,\mathrm{Hz} \\ \mathrm{E}_\Sigma\left\{|\hat{a}_k|^2\right\} &\approx \tau \cdot 2^{47.5}\,\mathrm{Hz} \end{aligned} \tag{4.50}$$

With these parameters an integration buffer with $b_\Sigma = 64\,\mathrm{bit}$ for the AFFTS and a $b_\Sigma = 72\,\mathrm{bit}$ buffer for the XFFTS are sufficient to allow almost a second of integration under worst case conditions and probably more than a day on pure white noise.

Integration of a coherent time domain signal, such as performed in MKIDs readout, requires different considerations, since no window, no WOLA, no FFT and no complex square is present. Therefore the maximum integrated value is $\max_\Sigma\left(|a_j|\right) = 2^{A-1} \cdot \frac{f_\mathrm{S}}{2N} \cdot \tau$ and can be expected as the relevant limit with regard to the coherent signal. The aforementioned XFFTS parameters now yield $\max_\Sigma\left(|a_j|\right) = \tau \cdot 2^{25.2}\,\mathrm{Hz}$, which suggests a buffer with $b_\Sigma = 32\,\mathrm{bit}$.

Anyway, an overflow must be detected to discard the affected spectra and either adjust the input signal, the integration time, or the bit width of the buffer. Integration of positive integer values, however, allows to detect an overflow easily if the bit width b_Σ of the integration buffer exceeds the bit width b_a of a single value by at least one bit. The complex square to calculate power spectra

guarantees positive values by construction. Although the MKID does not calculate the power, the maximum value of the repeating coherent signal can be expected to be positive and allows overflow detection representative for all values. Positive values imply that the buffer value can not decrease over time. Therefore, the most significant bit switching from 1 to 0 during integration implies an overflow. Conversely, the overflow implies limits for the proper previous buffer value $a_{\Sigma,\mathrm{old}}$ and for the overflown new buffer value $a_{\Sigma,\mathrm{new}}$:

$$\begin{aligned} 2^{b_\Sigma} - 2^{b_\mathrm{a}} \leq a_{\Sigma,\mathrm{old}} \leq 2^{b_\Sigma} - 1 \\ 2^{b_\Sigma} \leq a_{\Sigma,\mathrm{new}} \leq 2^{b_\Sigma} - 1 + 2^{b_\mathrm{a}} \end{aligned} \tag{4.51}$$

Using the restriction to the single values $b_\mathrm{a} \leq b_\Sigma - 1$ with (4.51) yields:

$$\begin{aligned} 2^{b_\Sigma - 1} \leq a_{\Sigma,\mathrm{old}} \leq 2^{b_\Sigma} - 1 \\ 2^{b_\Sigma} \leq a_{\Sigma,\mathrm{new}} \leq 3 \cdot 2^{b_\Sigma - 1} - 1 \end{aligned} \tag{4.52}$$

These limits imply the most significant bit to be 1 before the overflow and 0 after the overflow, which proves sufficiency of this method to detect an overflow.

After an integration cycle is finished, the resulting spectrum must be read before the next integration cycle overwrites the data. Assuming data transfer to the PC requires a significant time, a second buffer is required. On the one hand, the overwriting can be delayed by switching to a parallel integration unit, which allows to switch between integration cycles without a pause. On the other hand, a subsequent output buffer backups the data for transmission. This reduces the amount of control logic and multiplexing for integration and data transmission. Additionally, it allows to convert or reorder data during the copy process and store the final format that is ready for transmission.

4.7 Float conversion

With respect to integration bit widths up to $b_\Sigma = 72$ bit that are found in chapter 4.6, float conversion may significantly reduce the bit width of the channels with a limited loss of precision. Thus, the data rate of the transmission to the PC may decrease, as well as the memory requirements of I/O buffers in the main FPGA, the on-board controller, or the PC. The Institute of Electrical and Electronics Engineers (IEEE) standard 754-2008 for floating-point arithmetic defines formats for floating-point numbers with fixed lengths that are powers of 2 [41]. Its widely used 32 bit single precision float format suggests an interface for transmission that is based on 32 bit words. Additionally it allows immediate further processing in the PC.

A single precision float, such as shown in figure 4.21, may represent a wide range of values from 0 over $\pm 2^{-149}$ up to almost $\pm 2^{128}$, $\pm\infty$, and not a number (NaN). However, integration just outputs positive integers up to 2^{72} and 0, which allows a simplified float converter. The sign bit can be fixed to $S = 0$ and subnormal or special values other than 0 can be excluded. Basically the conversion requires to find the leading 1 in the integer value, shift the value accordingly and store the biased position as exponent. To limit the time integration must stop to read

Figure 4.21: Fields of a 32 bit single precision float from IEEE standard 754-2008. The most significant bit stores the sign S. The next 8 bit store the exponent E that is biased by 127. The 23 least significant bits store the fraction of the mantissa M as an integer. An exponent $1 \leq E \leq 254$ indicates a normalized value $v = (-1)^S \cdot 2^{E-127} \cdot (1 + M \cdot 2^{-23})$, an exponent $E = 0$ indicates a subnormal value $v = (-1)^S \cdot 2^{-149} \cdot M$ and $E = 255$ indicates special values.

To avoid multiplexing of up to 72 integer bits simultaneously, the leading 1 can be found in multiple steps, similar to a binary search. Each search step can be followed by a part of the shift to narrow the bits to search in the next step and to limit the multiplexing to a fraction of the total bit width. The float converter of the AFFTS and the XFFTS uses two such steps, starting with a search for the leading Byte. However, the number of instances should be limited, since it still requires a lot of interconnect to multiplex the bits of the integer.

4.8 Data transmission

To prepare data transmission, the integration must be finished, the integrated spectrum is copied to an output buffer, simultaneously ordered by channel number, and possibly converted to floating-point. To integrate without pause would require as many independent float converters and output buffers as there are data streams for integration to copy them simultaneously. To limit the number of float converters to one, the AFFTS and the XFFTS usually copy data from parallel streams consecutively to one single output buffer. Integration may restart when the integration buffer for the last stream starts to be copied. After the output buffer is filled with spectral data and control data, such as measurements for ADC calibration, actual start of transmission can be notified to the Spartan-3 onboard controller that forwards the data to a Fast Ethernet interface, or to an optional Gigabit Ethernet controller inside the main FPGA. Depending on the application, different events can be the initial trigger to prepare data transmission.

Common spectroscopy usually requires to synchronize data acquisition of the spectrometer and therefore integration to other instruments in the telescope. Therefore each instrument receives a

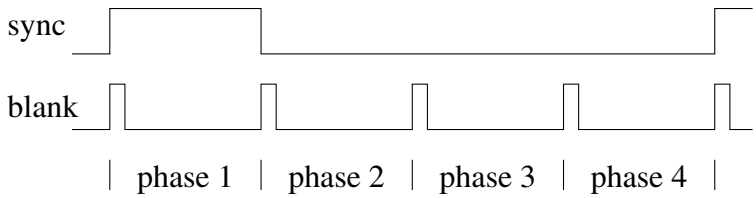

Figure 4.22: Time series of blank/sync signals during a 4-phase measurement.

reference signal, such as blank/sync, which is shown in figure 4.22. Sync indicates the first phase of the measurement, such as on source, or off source. Blank indicates a period of invalid data at the beginning of each phase, when settings are altered and instruments may be unstable. Usual settings for the duration of a blank period or a phase are in the order of milliseconds or seconds. The basic time slot to control integration of the spectrometer is defined by the time to acquire the samples of one FFT frame. Since $2N$ real samples at a rate f_{S} yield N complex channels over a bandwidth $f_{\mathrm{BW}} = \frac{f_{\mathrm{S}}}{2}$, the integration time resolution equals the reciprocal spectral resolution $\frac{N}{f_{\mathrm{BW}}}$. Chapter 3.1 demands a spectral resolution of 100 kHz, which yields a maximum delay of 10 µs to finish an ongoing integration at the beginning of the blank period. To prevent glitches in internal counters, and with regard to the limited accuracy of the blank signal, the same delay is accepted when integration restarts at the end of the blank period. However, the delay must be considered relevant, when using very high spectral resolution. Since the blank signal jitters with respect to the integration process, integration time slightly varies. Therefore an integration counter and a time stamp are added to each spectrum.

Chapter 3.3 demands integration times of $\sim 100\,\mu s$. Thus, the accuracy of the blank signal and the varying integration time become significant. Of course there still exists a basic time slot for integration, which depends on the spectral resolution. However, independent of the time resolution of the spectra, pulsar search requires continuous observation without phase switching over much longer periods to achieve the required sensitivity. Therefore, a constant delay of several microseconds is acceptable in combination with a time stamp to measure the delay. A single blank impulse can therefore be used to indicate the start of observation of one single measurement phase. To guarantee constant integration time during the phase, the integration counter can be used as a transmission trigger when it reaches a programmed maximum. Another blank impulse ends the phase and aborts the last integration.

The concept was successfully implemented into the XFFTS and into a modified AFFTS. Figure 4.23 displays the successful observation of a known pulsar with a period of ~ 343 ms over 15 min, using the XFFTS [21]. The respective FPGA core for the AFFTS recently led to successful detection of a millisecond pulsar at the Effelsberg 100- m telescope, which demonstrates the applicability of the procedure [6].

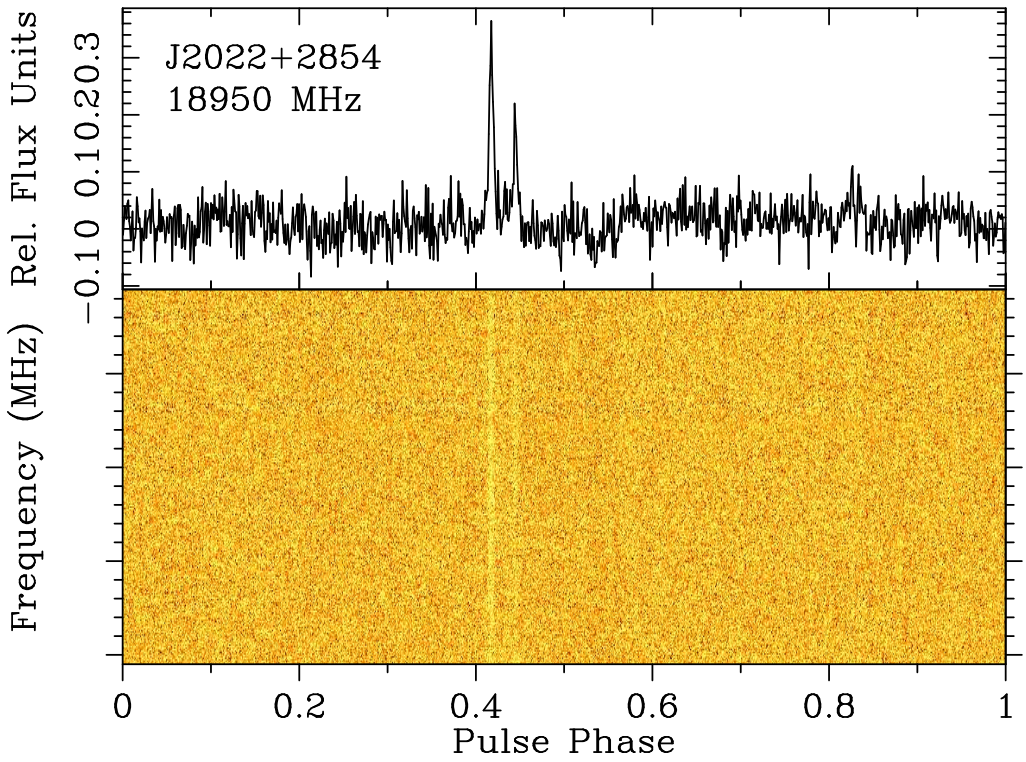

Figure 4.23: "15 minute test observation of PSR B2020+28 at a frequency of 18.95 GHz using the XFFTS system. The top panel displays the integrated profile, and the bottom panel shows phase folded subbands across the 2 GHz bandpass." [21, Fig. 1]

Chapter 5

An APEX Galactic Center line survey using the XFFTS

The Array Fast Fourier Transform Spectrometer (AFFTS) [54] and the eXtended-bandwidth Fast Fourier Transform Spectrometer (XFFTS) [52] implement the algorithms presented in chapter 4. Astronomical results using the XFFTS and the First Light APEX Submillimeter Heterodyne receiver (FLASH) at the Atacama Pathfinder EXperiment (APEX) telescope are presented here to prove the applicability and demonstrate the efficency of these algorithms. The complex molecular abundances of the Galactic Center (GC) regions, here studied by unbiased line surveys, highlight the benefits for wideband spectroscopy as the main application of these spectrometers.

5.1 Sources

Figure 5.1 shows a radio continuum map that gives an overview of the GC. Filled with giant molecular clouds (GMCs), a region within a range of ± 200 pc in longitude centered on the GC is called the central molecular zone (CMZ). Some of these GMCs a few parsec around the central compact radio source SgrA* form the Sagittarius A (SgrA) complex, shown in figure 5.1. Aside from SgrA* it contains the H II region SgrA-West and the supernova remnant (SNR) SgrA-East [72, Ch. 2.2]. SgrA* is most likely a supermassive black hole (SMBH), located at the very center of the Milky Way. Centered on its position, SgrA-West is shaped like a minispiral with three arms of ionized gas. It builds the central cavity (CC), an area of low density within the central parsec of the Galaxy, surrounded by a dense circumnuclear disk (CND). This CND is made of molecular gas, orbiting SgrA* at distances between 1.5 pc and ~ 4 pc [28, Ch. I.B]. As the name suggests, the projection of SgrA-East is centered slightly east of the SgrA*, but stretches out over the whole SgrA complex. However, note that this is only true for the projection in the sky [72, Ch. 2.2].

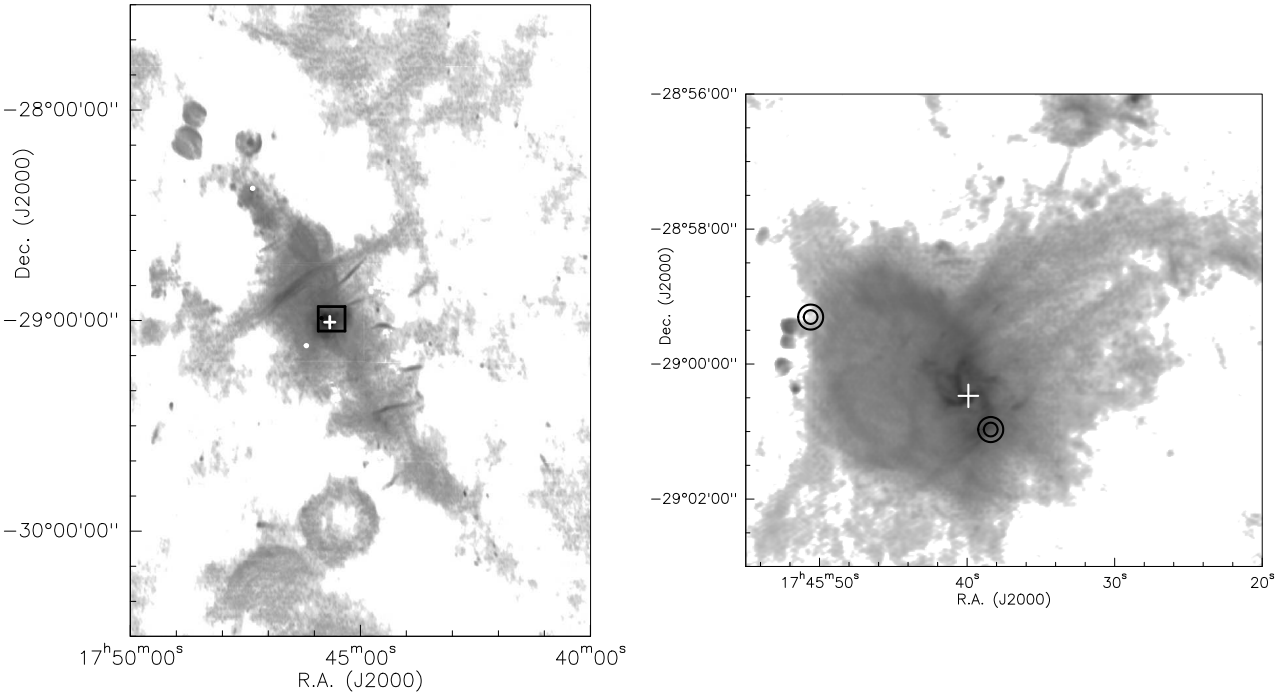

Figure 5.1: Radio continuum maps of the GC. The left image shows the CMZ at $\lambda = 90\,\mathrm{cm}$ [59] in a frame that spans $375\,\mathrm{pc} \times 450\,\mathrm{pc}$. The right image is zoomed from the black frame in the left one and spans $22\,\mathrm{pc} \times 17\,\mathrm{pc}$. It displays the SgrA complex at $\lambda = 6\,\mathrm{cm}$ [114]. A white cross marks the position of SgrA* in the center of the Galaxy. The small white circles mark the pointing source SgrB2(N), $\sim 120\,\mathrm{pc}$ north-east of the center, and the reference position SgrA*$(+400, -400)$, $\sim 23.5\,\mathrm{pc}$ south-east of it. The black circles mark the actual line survey positions SgrA*$(-20, -30)$, $\sim 1.5\,\mathrm{pc}$ south-west of the center, and SgrA*$(+140, +70)$, $\sim 6.5\,\mathrm{pc}$ north-east of it. The circles' diameters equal the beam size of the telescope at minimum and maximum sky frequencies. It ranges from $\sim 23''$ at 270 GHz to $\sim 12''$ at 497 GHz [33].

To convert between the projected distance d in the GC and the angular difference α in observing positions, the distance R_0 to the GC is required:

$$d = 2\pi R_0 \cdot \frac{\alpha[\text{arcsec}]}{360 \cdot 3600} \tag{5.1}$$

Assuming $R_0 = 8.5\,\text{kpc}$, yields that a parsec in the GC equals $\sim 24''$ [28, Ch. V.E].

Two positions in the SgrA complex were selected to perform unbiased line surveys. Both have a history of unbiased surveys at other frequencies.

- SgrA*$(-20, -30)$ is located $\sim 1.5\,\text{pc}$ south-west of SgrA*, at the inner edge of the CND. Ionized by the central cluster of stars around SgrA*, it is a photodissociation region (PDR), and therefore contains rather simple molecules. The Institut de Radioastronomie Millimétrique (IRAM) 30 m telescope observed the slightly different position SgrA*$(-30, -30)$ in another survey from 86 GHz to 116 GHz [23, Ch. 7.2]. This position was chosen, since it was found to be the peak in carbon monoxide (CO) emission in the southern CND [83].

- Except for a few arcseconds, SgrA*$(+140, +70)$ equals the position of the denser peak in the GMC M-0.02-0.07. Also known as the $50\,\text{km}\,\text{s}^{-1}$ cloud, it has been well studied over the last 30 years [14, Ch. 2]. It is located in projection $\sim 6.5\,\text{pc}$ north-east of SgrA*, at the edge of SgrA-East. The expanding SNR, interacting with the GMC, produces shocks and triggers star formation. The observed position shows a peak in the SiO emission, which is known as a shock tracer [65, Fig. 3]. For these reasons, it was selected as one of the positions that were observed in the aforementioned IRAM survey [23, Ch. 7.2].

Since the sources are extended, the observations were done in position switching mode with a reference position that is well outside the SgrA complex: SgrA*$(+400, -400)$ is located $\sim 23.5\,\text{pc}$ from SgrA*, and single position observations on this reference position confirmed that it is not contaminated by emission from the SgrA complex. Pointing scans have been performed on the continuum emission of Sagittarius B2(North) (SgrB2(N)), located $\sim 2700''$ from SgrA*. Note that the main beam of the APEX telescope has a full width at half maximum (FWHM) of $\sim 23''$ at the lowest $f_{\text{sky}} = 270\,\text{GHz}$ and $\sim 12''$ at the highest $f_{\text{sky}} = 497\,\text{GHz}$ of FLASH [33].

The coordinates of the survey refer to the positions of SgrA* and SgrB2(N). An offset position (α, δ) is derived from its reference (α_0, δ_0) and the offset $(\alpha_{\text{off}}, \delta_{\text{off}})$:

$$\begin{aligned} \alpha &= \alpha_0 + \frac{\alpha_{\text{off}}[\text{arcsec}]}{\cos(\delta_0) \cdot 15''/\,\text{s}} \\ \delta &= \delta_0 + \delta_{\text{off}}[\text{arcsec}] \end{aligned} \tag{5.2}$$

This yields the coordinates in table 5.1.

Table 5.1: Coordinates of the relevant sources (SgrA* and SgrB2(N)) and offset positions. All coordinates refer to epoch J2000.

	Right Ascension α	**Declination** δ
SgrA*	$17^{\mathrm{h}}\,45^{\mathrm{m}}\,39\overset{\mathrm{s}}{.}92$	$-29^{\circ}\,00'\,28\overset{''}{.}19$
SgrA*$(-20,-30)$	$17^{\mathrm{h}}\,45^{\mathrm{m}}\,38\overset{\mathrm{s}}{.}40$	$-29^{\circ}\,00'\,58\overset{''}{.}19$
SgrA*$(+140,+70)$	$17^{\mathrm{h}}\,45^{\mathrm{m}}\,50\overset{\mathrm{s}}{.}60$	$-28^{\circ}\,59'\,18\overset{''}{.}19$
SgrA*$(+400,-400)$	$17^{\mathrm{h}}\,46^{\mathrm{m}}\,10\overset{\mathrm{s}}{.}42$	$-29^{\circ}\,07'\,08\overset{''}{.}19$
SgrB2(N)	$17^{\mathrm{h}}\,47^{\mathrm{m}}\,19\overset{\mathrm{s}}{.}90$	$-28^{\circ}\,22'\,17\overset{''}{.}78$

5.2 Setup

Instruments A spectral line survey of these GC sources has been performed, using eight XFFTS boards that are installed at the APEX telescope and linked to the FLASH+ receiver.

Consisting of two receivers, FLASH offers two independent tuning ranges: FLASH-345 covers frequencies from 270 GHz to 379 GHz and FLASH-460 covers frequencies from 383 GHz to 497 GHz. Despite great efforts, the option to tune FLASH-460 higher than 500 GHz was not stable during the measurements of the survey. Each receiver has its own independently tunable local oscillator (LO), defining the sky frequency, and its own intermediate frequency (IF) chain. Figure 5.2 illustrates one chain, where two single sideband (SSB) mixers provide a lower sideband (LSB) and an upper sideband (USB) at IFs from 4 to 8 GHz. Those are split into 4 parts of 2.5 GHz bandwidth to feed four XFFTSs with partly overlapping bands. The XFFTSs at FLASH-460 provide 32768 channels each, whereas those at FLASH-345 provide 65536 channels. The increased spectral resolution allows lines being narrower in frequency units at lower sky frequencies as expected from (3.1). So FLASH simultaneously provides two receivers with independent sky frequencies, four sidebands, each of 4 GHz bandwidth and centered 6 GHz up and down from the associated LO frequency, and eight XFFTSs spectra with different spectral resolution, adapted for each receiver's tuning range.

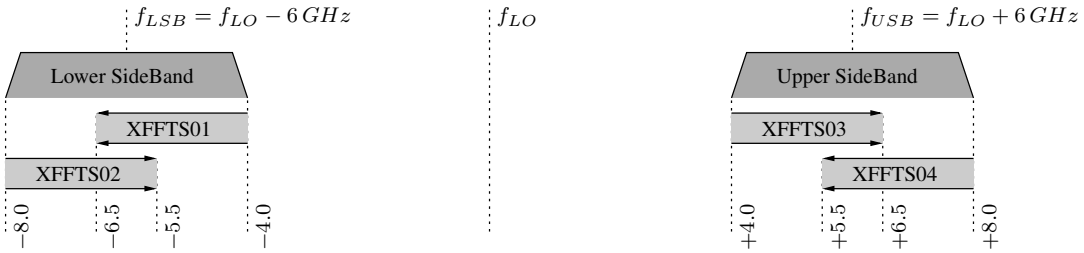

Figure 5.2: IF chain for one LO of FLASH at the APEX telescope: Each 4 GHz wide sideband is covered by two XFFTSs. Each XFFTS covers 2.5 GHz bandwidth, which includes 1 GHz overlap in the middle of each sideband.

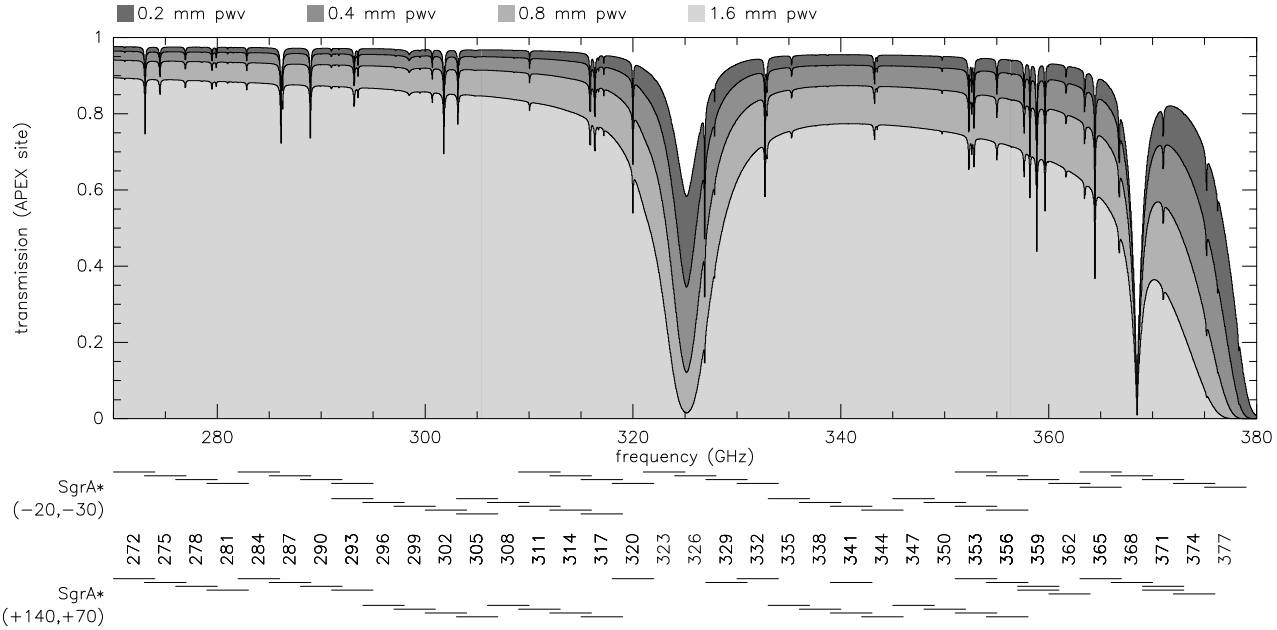

Figure 5.3: Transmission over the band of FLASH-345 under different weather conditions at APEX site: Excellent (0.2 mm pwv), good (0.4 mm pwv), common (0.8 mm pwv) and bad (1.6 mm pwv) weather. The frequency tunings of two line surveys are marked. At excellent weather (0.16 mm pwv), SgrA*$(-20, -30)$ was observed using 22 tunings. At common weather (0.76 mm pwv), SgrA*$(+140, +70)$ was observed using 19 tunings.

Frequency tunings The atmospheric water vapor absorbs part of the signal coming from any astronomical source. Dependent on the weather conditions and the frequency, this absorption is more or less severe. Figure 5.3 displays this atmospheric absorption for different amounts of precipitable water vapor (pwv) for FLASH-345 and figure 5.4 does so for FLASH-460. The pwv measures the accumulated water in a column above the site, which equals the amount of precipitation if all atmospheric water would condensate. Since the location of the APEX telescope is very dry, the average pwv at the site is below 1 mm pwv. Under good weather conditions humidity falls below 0.5 mm pwv about 25% of the time and very rarely even below 0.1 mm pwv [4]. The setup of a line survey now requires to cover a large fraction of the tuning range of the receiver, but possibly spare atmospheric lines. First, it saves observation time to skip opaque frequencies. Secondly, the sideband separation is limited to about 15 dB: if one sideband would cover atmospheric lines, noise would increase in the other sideband, too.

To cover the complete tuning range, the IF chain that is presented in figure 5.2 requires multiple frequency tunings to fill the gap of 8 GHz between the LSB and the USB. Theoretically three tunings that are shifted by 4 GHz relative to each other would cover a frequency range of 24 GHz without gaps. However, the demands that chapter 3.1 makes on overlap, suggest to cover the same frequency range by four tunings that are shifted by 3 GHz to each other. This leads to 1 GHz overlap between

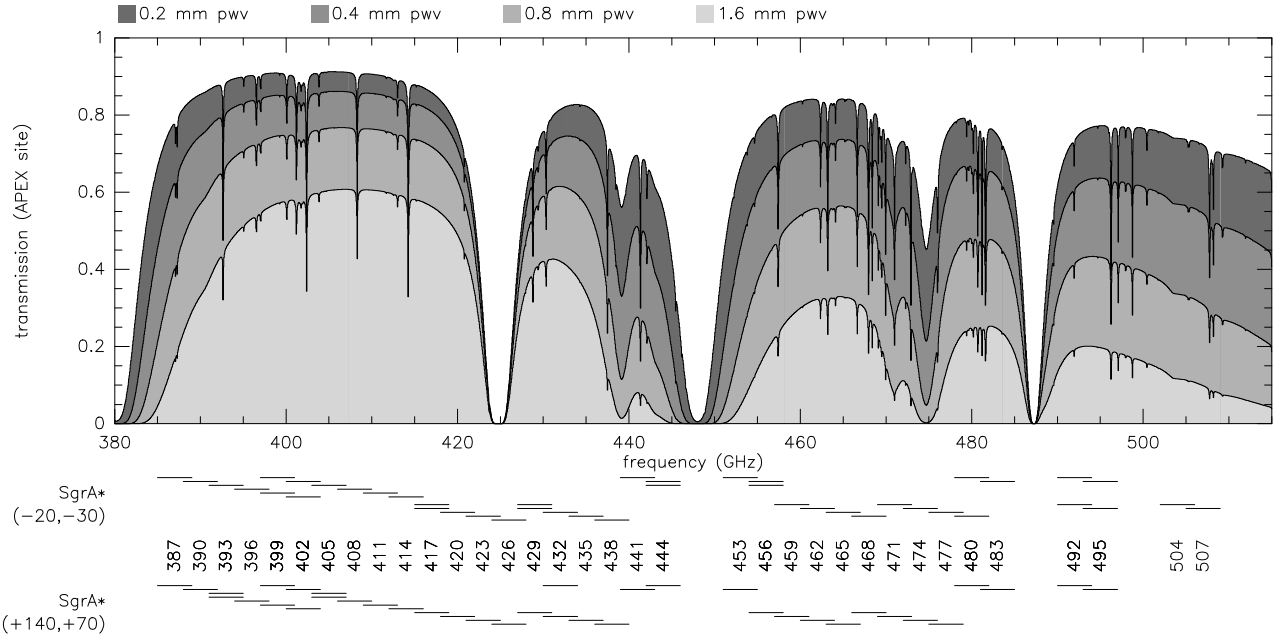

Figure 5.4: Transmission over the band of FLASH-460 under different weather conditions at APEX site: Excellent (0.2 mm pwv), good (0.4 mm pwv), common (0.8 mm pwv) and bad (1.6 mm pwv) weather. The frequency tunings of two line surveys are marked. At excellent weather (0.16 mm pwv), SgrA*$(-20, -30)$ was observed using 22 tunings. At common weather (0.76 mm pwv), SgrA*$(+140, +70)$ was observed using 19 tunings.

any pair of adjacent spectra. The GC survey therefore uses tunings, where sky frequencies change in steps of 3 GHz, running from $f_{\mathrm{LSB}} = 272$ GHz to $f_{\mathrm{USB}} = 377$ GHz for FLASH-345 and from $f_{\mathrm{LSB}} = 387$ GHz to $f_{\mathrm{USB}} = 495$ GHz for FLASH-460. The used tunings were selected according to the weather conditions. Figure 5.3 and figure 5.4 display all tunings used in the surveys near SgrA* that were performed end of June 2012. Each tuning frequency was measured on the source for 480 s, interrupted by off-position measurement of the same total duration each 20 s, calibration scans twice per tuning, and pointing scans at least once every hour, dependent on weather conditions.

The nights from 21st to 23rd of June had constantly excellent weather between 0.06 mm and 0.30 mm pwv and an average of 0.16 mm. During these nights SgrA*$(-20, -30)$ was surveyed using 22 tunings. Four tunings were planned for FLASH-460 to cover its band from 497 GHz up to 515 GHz. After two of these tunings were found unstable, the remaining ones were changed and used to repeat two other tunings ($f_{\mathrm{LSB}} = 417$ GHz, $f_{\mathrm{LSB}} = 444$ GHz) under even better weather conditions. Two atmospheric lines were intentionally spared, leaving gaps of 5 GHz width at 448.5 GHz and 487.5 GHz. The line at 424.5 GHz is 24 GHz away from another strong atmospheric line at 448.5 GHz. Unfortunately, 24 GHz is twice the frequency offset of the sidebands. Thus, only one of the lines could be spared if the frequencies around 436.5 GHz should be covered. Since the respective atmospheric line is wider, the observations around 448.5 GHz were spared. Since both receivers

measure simultaneously, both their tuning ranges are covered by the same number of tunings. According to the smaller bandwidth of FLASH-345, some of its frequencies are covered by multiple scans. Using different tunings, a frequency may therefore be covered using the LSB as well as the USB. This allows to compensate negative effects in one sideband from an atmospheric line in the other: One tuning may cover an atmospheric line to close gaps in the survey and the other is not affected by the line. The survey of SgrA*$(-20, -30)$ therefore compensates the atmospheric line around 325 GHz by two tunings for 311, 314, and 317 GHz. Two tunings at 355 GHz compensate the deep narrow atmospheric line at 368 GHz. Covering 365 GHz twice compensates the end of the tuning range at 277 GHz on the edge of the wide atmospheric line around 380 GHz.

From 24th to 26th of June, 19 tunings were used to survey SgrA*$(+140, +70)$, while weather conditions decreased from good 0.29 mm to poor 1.38 mm pwv with an average of 0.76 mm still being better than usual. With the experience from the first survey, the tunings higher than 497 GHz were skipped. The remaining 18 tunings were slightly changed according to the atmospheric line around 448.5 GHz, which widens with increasing humidity. A 19th scan was started to improve signal-to-noise ratio (S/N) by repeating tunings. The reduced number of tunings decreases the ability to compensate atmospheric lines by double scans. At the same time bad weather increases atmospheric absorption around 325 GHz and 380 GHz to a degree that suggests to spare these frequencies. This FLASH-345 survey therefore contains a 5 GHz gap at 324.5 GHz and ends at 376 GHz.

5.3 Data reduction

Using the GILDAS Continuum and Line Analysis Single-dish Software (CLASS) package in version Jul12b, several reduction steps need to be performed [29].

As first step bad channels in each individual subscan need to be eliminated, using **draw kill** to blank a single channel and **draw fill** to replace it by an interpolation from its neighbors. The channels at the edges of each spectrum were just blanked, since no proper interpolation can be assured there. Each edge of a 2500 MHz spectrum was cut by $\sim$10 MHz for FLASH-345 and by $\sim$5 MHz for FLASH-460. This avoids frequencies that may be attenuated by filters in the IF chain, or by the analog input circuits of the XFFTS, which filter direct current (DC) and low frequency alternating current (AC). Additionally a few known channels in the middle of the spectra, that are affected by radio frequency interference (RFI) from the telescope cabin, were blanked and interpolated.

The next step is to manually recognize spectral lines, atmospheric, and astronomical ones. Defining a local standard of rest (LSR) velocity v_{LSR} for each source, allows to calculate and store the rest frequency of each spectral line. Of course atmospheric lines are not affected by the velocity of astronomical sources, so they must be handled separately. Thus, atmospheric lines were derived from calibration scans without using v_{LSR}. Found by previous observations of the same sources, $v_{\mathrm{LSR}} = -75\,\mathrm{km\,s^{-1}}$ was defined for SgrA*$(-20, -30)$, and $v_{\mathrm{LSR}} = 50\,\mathrm{km\,s^{-1}}$ for SgrA*$(+140, +70)$, the 50 km s^{-1} cloud [83, 14] (compare figure 5.5). The velocity of each subscan was changed accordingly, using **modify velocity**. To increase S/N for better recognition, subscans of the same tuning and the same XFFTS were averaged, using **average /new**, as well as smoothed

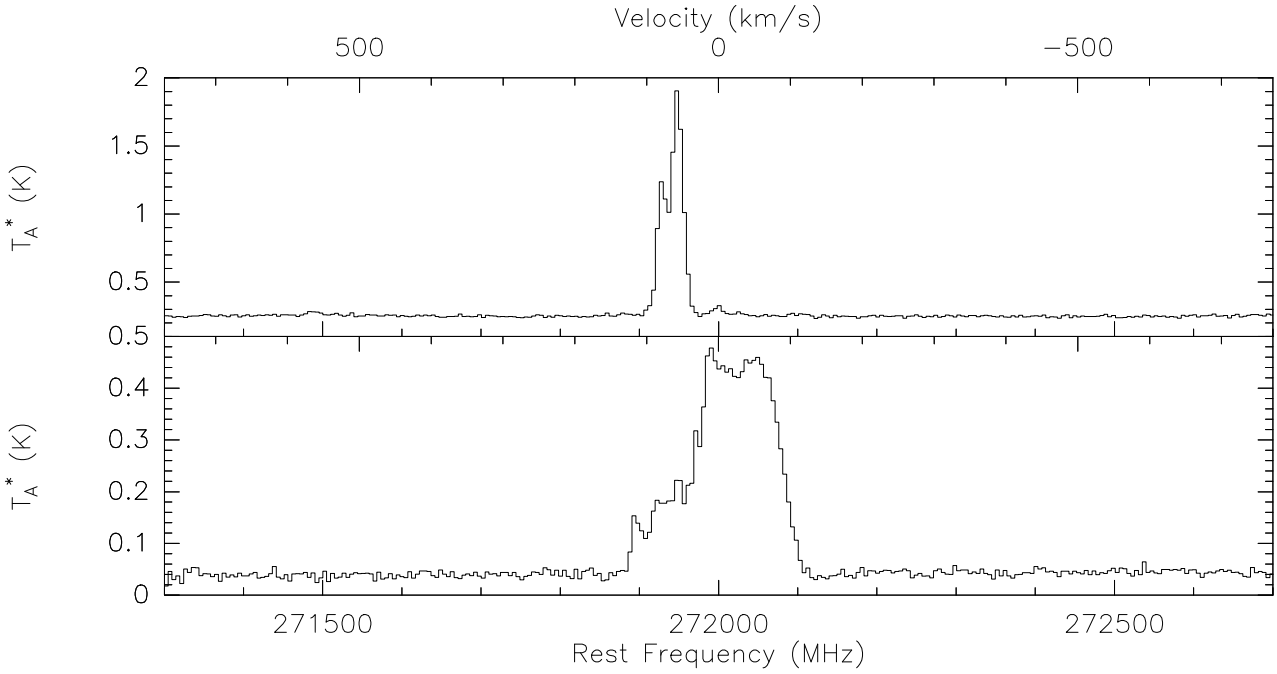

Figure 5.5: Comparison of a spectral line from HNC with a rest frequency of 271981 MHz, measured at SgrA*$(-20, -30)$ (bottom) and at SgrA*$(+140, +70)$ (top). The spectra are scaled to sky frequency and need to be shifted to compensate for the velocity of each source. It is assumed $v_{\rm LSR} = -75\,{\rm km\,s^{-1}}$ for SgrA*$(-20, -30)$, and $v_{\rm LSR} = 50\,{\rm km\,s^{-1}}$ for SgrA*$(+140, +70)$. To move each line to its rest frequency, the spectrum is shifted by $-v_{\rm LSR}$. Also note that the lines from SgrA*$(-20, -30)$ are wider and with lower peak intensity than those from SgrA*$(+140, +70)$.

by a factor of 128, using **smooth box**. The final velocity resolution was between $3.9\,{\rm km\,s^{-1}}$ at the highest frequencies of FLASH-345 and $7.6\,{\rm km\,s^{-1}}$ at the lowest frequencies of FLASH-460, which is still good for finding wide lines in the GC.

Defining the quality of each spectrum, using **tag**, allows to exclude bad ones from further reduction steps. Spectra with a noisy or curved baseline were therefore manually classified from **Good** to **Awful**. To evaluate them, subscans of the same tuning and the same XFFTS were averaged once more. Keeping all channels this time without smoothing, each average was stored to one spectrum afterwards.

Now masking the spectral lines, using **set window**, allows to subtract a baseline from each spectrum, using **base**. Proper masking ensures the absence of spectral lines in the velocity range that is used to determine the baseline fit. Experience from previous observations again, as well as a careful examination of the spectra of this survey led to maximum velocity ranges v_δ for each type of spectral lines and for each source. The atmospheric lines in both sources were masked over a range of $v_\delta = [-120, +120]\,{\rm km\,s^{-1}}$, astronomical lines in SgrA*$(-20, -30)$ were masked

over $v_\delta = [-90, +90]\,\mathrm{km\,s^{-1}}$ and astronomical lines in SgrA*$(+140, +70)$ were masked over $v_\delta = [-30, +30]\,\mathrm{km\,s^{-1}}$.

Figures 5.6 and 5.7 show the results of these reduction steps. Spectra of the same source and the same receiver were composed by aligning their sky frequencies, using **set align frequency composite**, before **average /new /resample /nocheck line**. The results were smoothed again to velocity resolutions between $3.9\,\mathrm{km\,s^{-1}}$ and $7.6\,\mathrm{km\,s^{-1}}$.

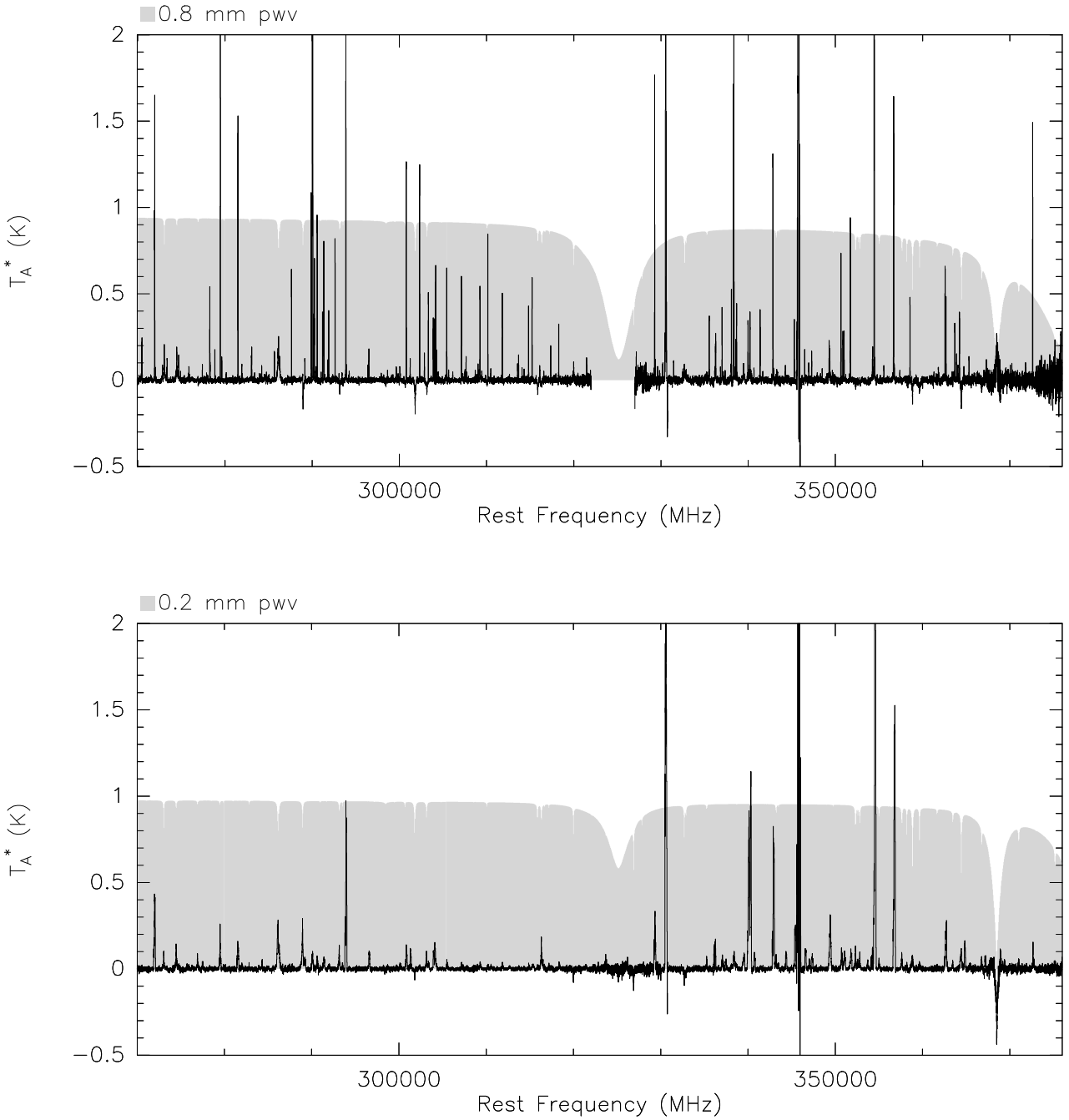

Figure 5.6: Reduced survey of SgrA*$(-20, -30)$ (bottom) and SgrA*$(+140, +70)$ (top), composing all subscans in the tuning range of FLASH-345. A second level baseline is subtracted from each spectrum and bad spectra are excluded. The result is smoothed to velocity resolutions between 3.9 km s^{-1} and 5.4 km s^{-1}. The grey background displays the atmospheric transmission for the average pwv of each survey.

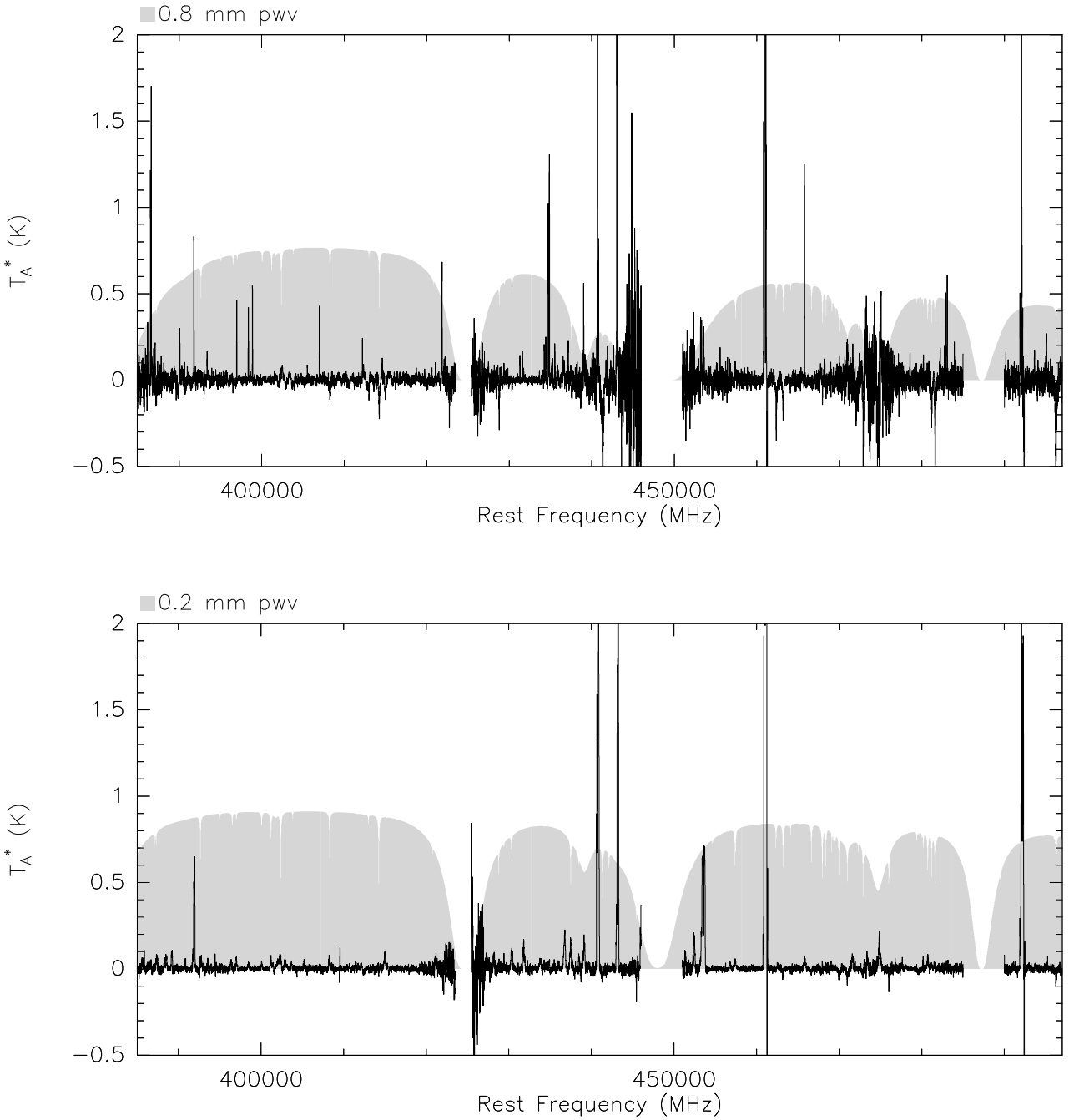

Figure 5.7: Reduced survey of SgrA*$(-20, -30)$ (bottom) and SgrA*$(+140, +70)$ (top), composing all subscans in the tuning range of FLASH-460. A second level baseline is subtracted from each spectrum and bad spectra are excluded. The result is smoothed to velocity resolutions between 5.8 km s^{-1} and 7.6 km s^{-1}. The grey background displays the atmospheric transmission for the average pwv of each survey.

5.4 Line identification

Identifying the spectral lines that were recognized before, requires a catalog of transitions. Searching this catalog for candidates around the rest frequency of each recognized line may create a large amount of candidates, which require manual analysis to exclude or identify them. Overhead in any of the initial lists, the catalog of transitions or the recognized lines, multiplies into the amount of candidates. Therefore, it is efficient to minimize both initial lists before their alignment to simplify the analysis of the candidates. A way to minimize the number of recognized lines is to look for duplicates, which easily emerge in segments of the survey, where multiple scans overlap, so a line is recognized in each scan individually. Defining a maximum offset allows to separate most duplicates automatically. Minimizing the size of the catalog requires to choose search parameters carefully. A too restricted search may exclude likely transitions, which must be added manually if they're found to be relevant.

Splatalogue [91, 73, 81] provided an initial catalog of ~3800 transitions, when limited to entries in the Cologne Database for Molecular Spectroscopy (CDMS) [73] with an intensity $I > -5$ and an energy level $E_L < 100\,\mathrm{K}$. The following additional ~3000 transitions were added in the process of line identification:

- Species that only appear with transitions on hyperfine structure.
- Transitions with higher energy levels $100\,\mathrm{K} < E_L < 1000\,\mathrm{K}$ or isotopes of selected species with strong lines in the spectra.
- Species from surveys of other sources on similar frequencies [87], which are missing in the CDMS [73], but present in the Jet Propulsion Laboratory (JPL) database [81].
- Recombination lines: Hα, Hβ.

To identify lines, their candidates were manually tagged as "identified" or "unprobable", or a whole line was canceled if it seemed to be another line's velocity component, or just noise. This process was iterated, starting with strong lines and preferring candidates with low-energy transitions. Further steps used statistics of identified species and checked the presence of all transitions of a species. Known abundances in the GC [102] allowed an additional check for molecules containing isotopes (isotopologues). The result of this process is presented in figures 5.8.1-5.8.49. Some strong lines create mirror images, due to limited sideband suppression (compare chapter 5.2), which is labeled accordingly. Multiple transitions of the same species are grouped if they relate to only one line in the spectrum.

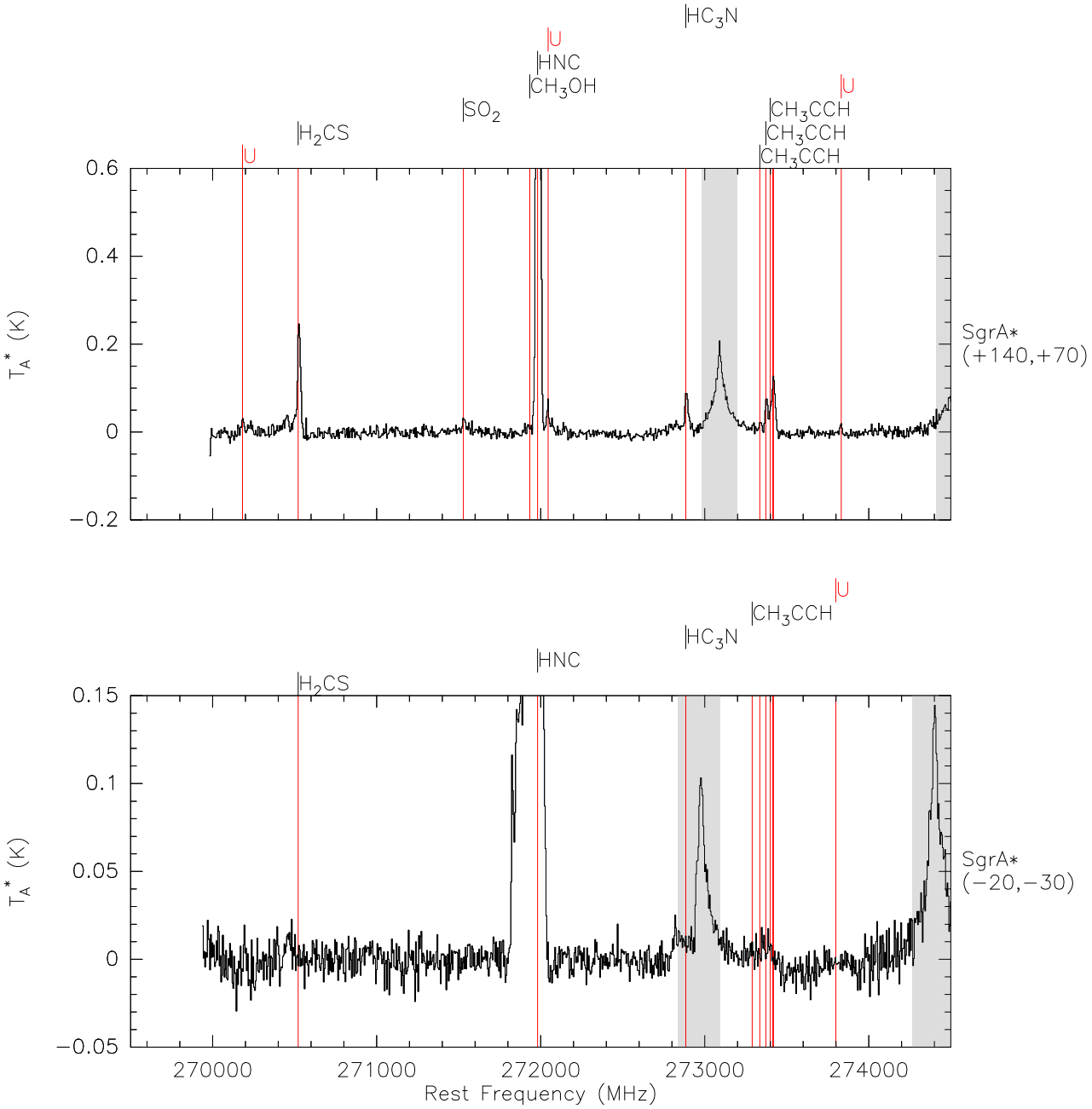

Figure 5.8.1: Reduced survey of SgrA*$(-20, -30)$ (bottom) and SgrA*$(+140, +70)$ (top), composing all subscans from 269500 MHz to 274500 MHz. Astronomical lines are marked by a vertical line that is labeled on top of each spectrum. The area 120 km s^{-1} around atmospheric lines in calibration scans is highlighted in grey. Lines that are "mirrored" from the other sideband are labeled accordingly.

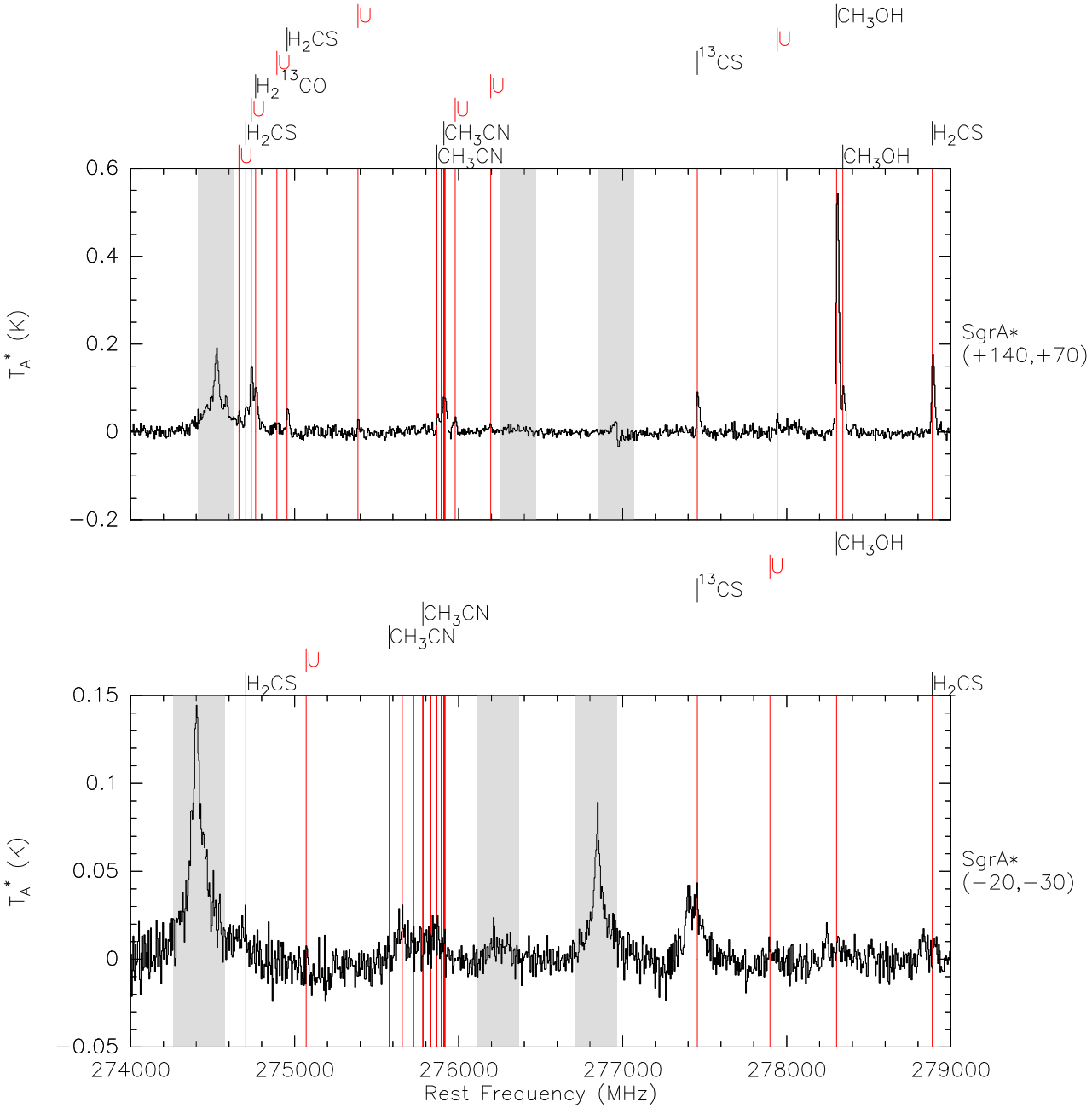

Figure 5.8.2: Reduced survey of SgrA*$(-20, -30)$ (bottom) and SgrA*$(+140, +70)$ (top), composing all subscans from 274000 MHz to 279000 MHz. Astronomical lines are marked by a vertical line that is labeled on top of each spectrum. The area 120 km s^{-1} around atmospheric lines in calibration scans is highlighted in grey. Lines that are "mirrored" from the other sideband are labeled accordingly.

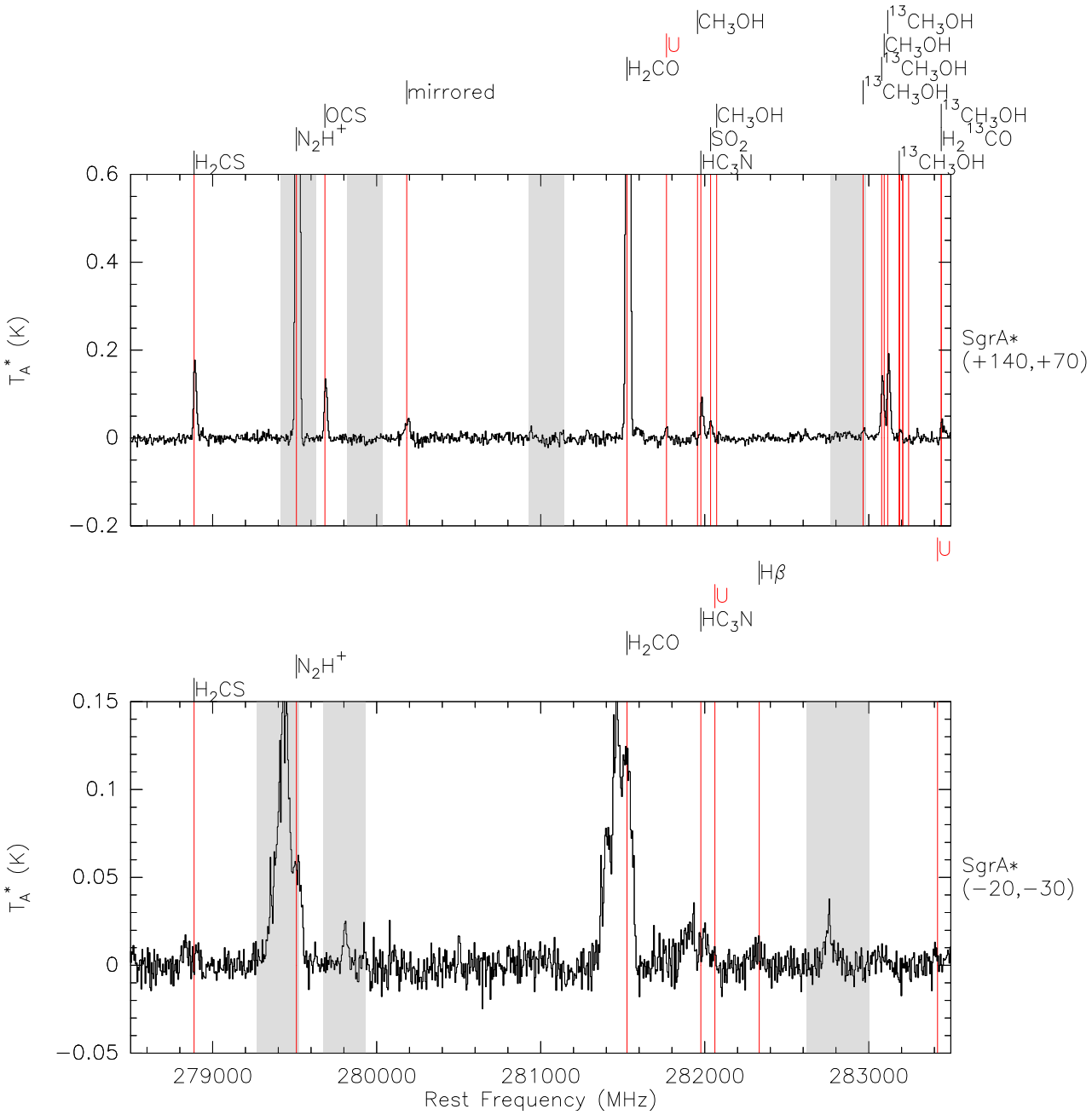

Figure 5.8.3: Reduced survey of SgrA*$(-20, -30)$ (bottom) and SgrA*$(+140, +70)$ (top), composing all subscans from 278500 MHz to 283500 MHz. Astronomical lines are marked by a vertical line that is labeled on top of each spectrum. The area 120 km s^{-1} around atmospheric lines in calibration scans is highlighted in grey. Lines that are "mirrored" from the other sideband are labeled accordingly.

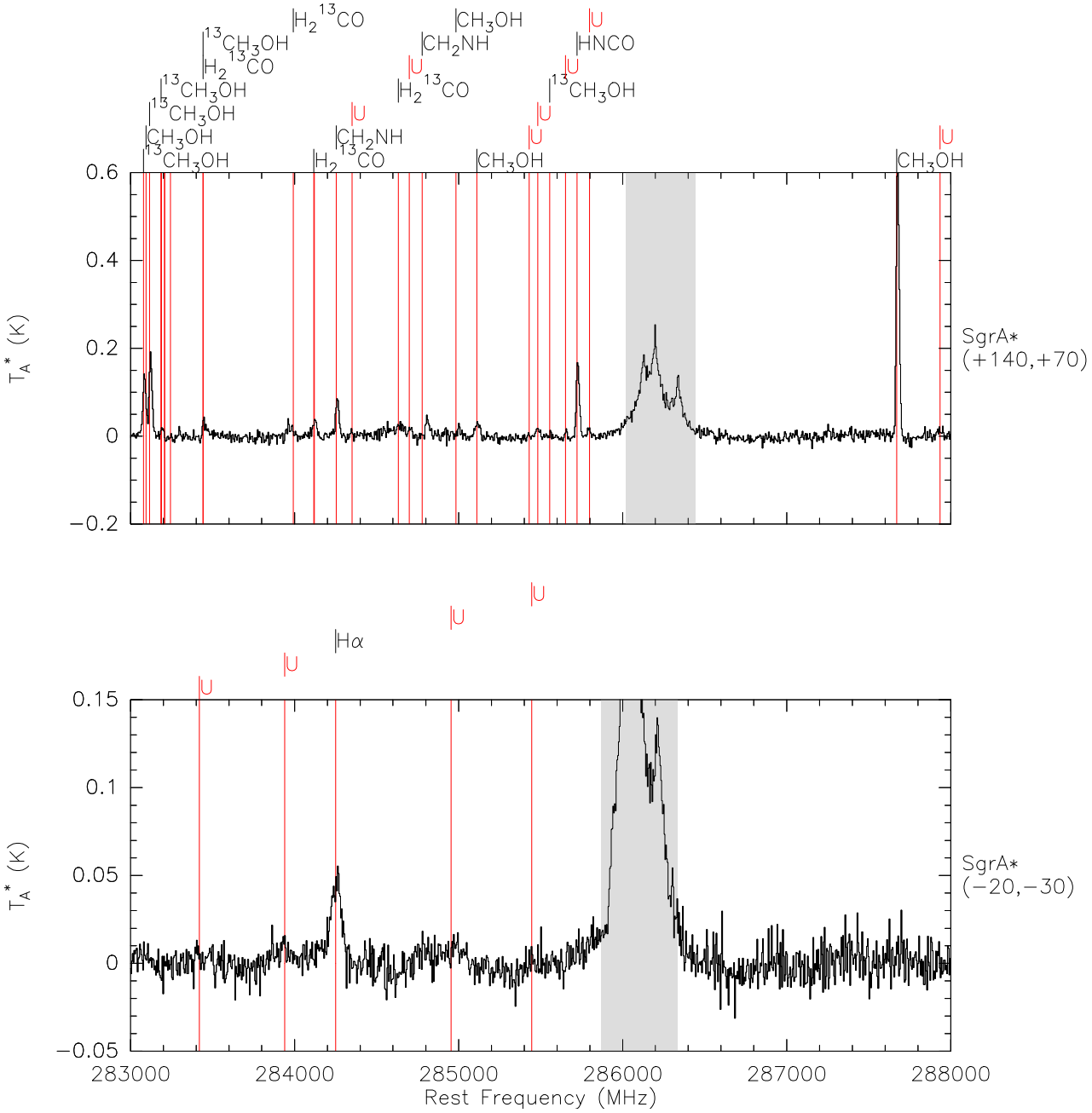

Figure 5.8.4: Reduced survey of SgrA*$(-20, -30)$ (bottom) and SgrA*$(+140, +70)$ (top), composing all subscans from 283000 MHz to 288000 MHz. Astronomical lines are marked by a vertical line that is labeled on top of each spectrum. The area 120 km s^{-1} around atmospheric lines in calibration scans is highlighted in grey. Lines that are "mirrored" from the other sideband are labeled accordingly.

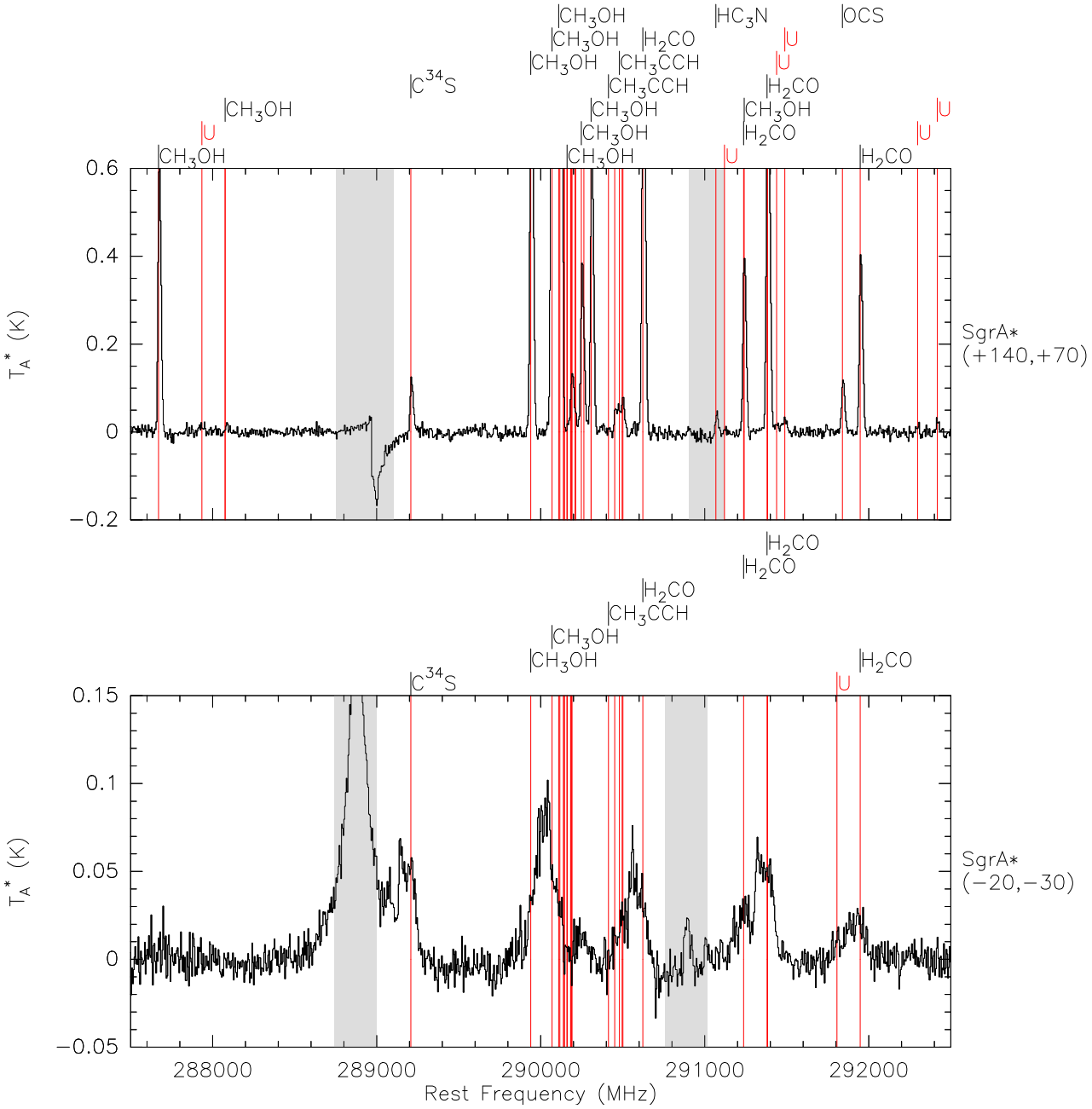

Figure 5.8.5: Reduced survey of SgrA*$(-20, -30)$ (bottom) and SgrA*$(+140, +70)$ (top), composing all subscans from 287500 MHz to 292500 MHz. Astronomical lines are marked by a vertical line that is labeled on top of each spectrum. The area 120 km s^{-1} around atmospheric lines in calibration scans is highlighted in grey. Lines that are "mirrored" from the other sideband are labeled accordingly.

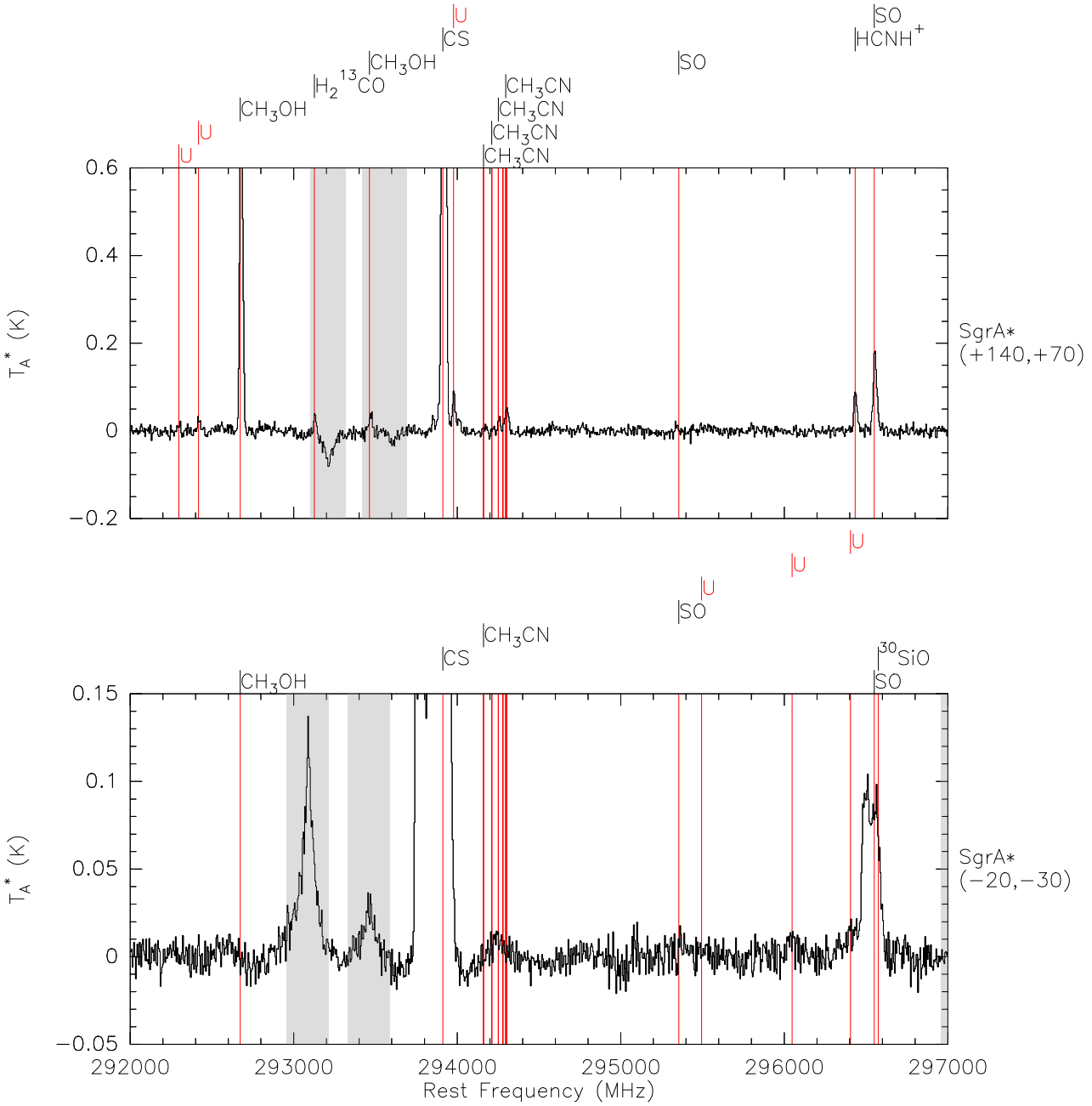

Figure 5.8.6: Reduced survey of SgrA*$(-20, -30)$ (bottom) and SgrA*$(+140, +70)$ (top), composing all subscans from 292000 MHz to 297000 MHz. Astronomical lines are marked by a vertical line that is labeled on top of each spectrum. The area 120 km s^{-1} around atmospheric lines in calibration scans is highlighted in grey. Lines that are "mirrored" from the other sideband are labeled accordingly.

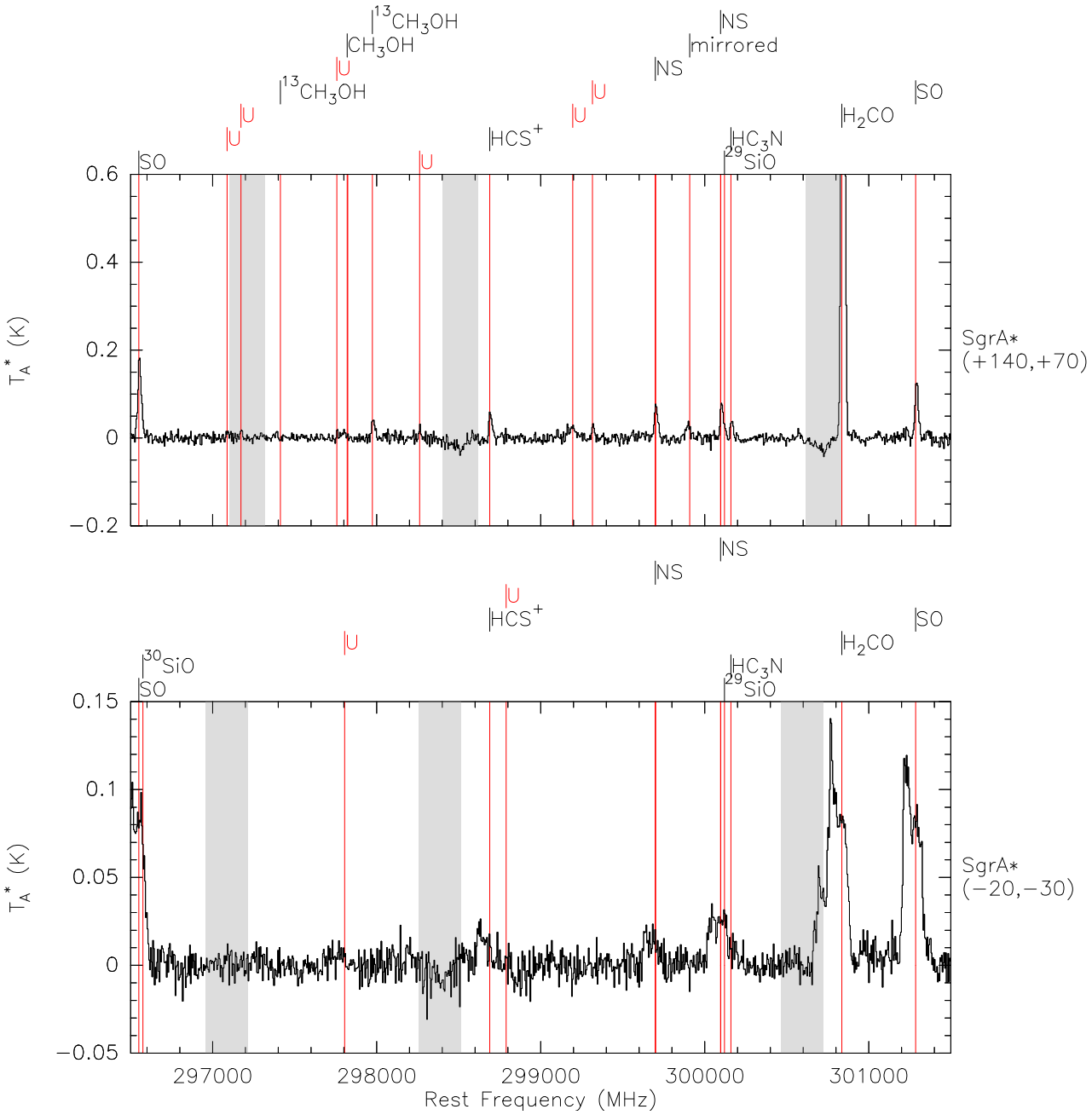

Figure 5.8.7: Reduced survey of SgrA*$(-20, -30)$ (bottom) and SgrA*$(+140, +70)$ (top), composing all subscans from 296500 MHz to 301500 MHz. Astronomical lines are marked by a vertical line that is labeled on top of each spectrum. The area 120 km s^{-1} around atmospheric lines in calibration scans is highlighted in grey. Lines that are "mirrored" from the other sideband are labeled accordingly.

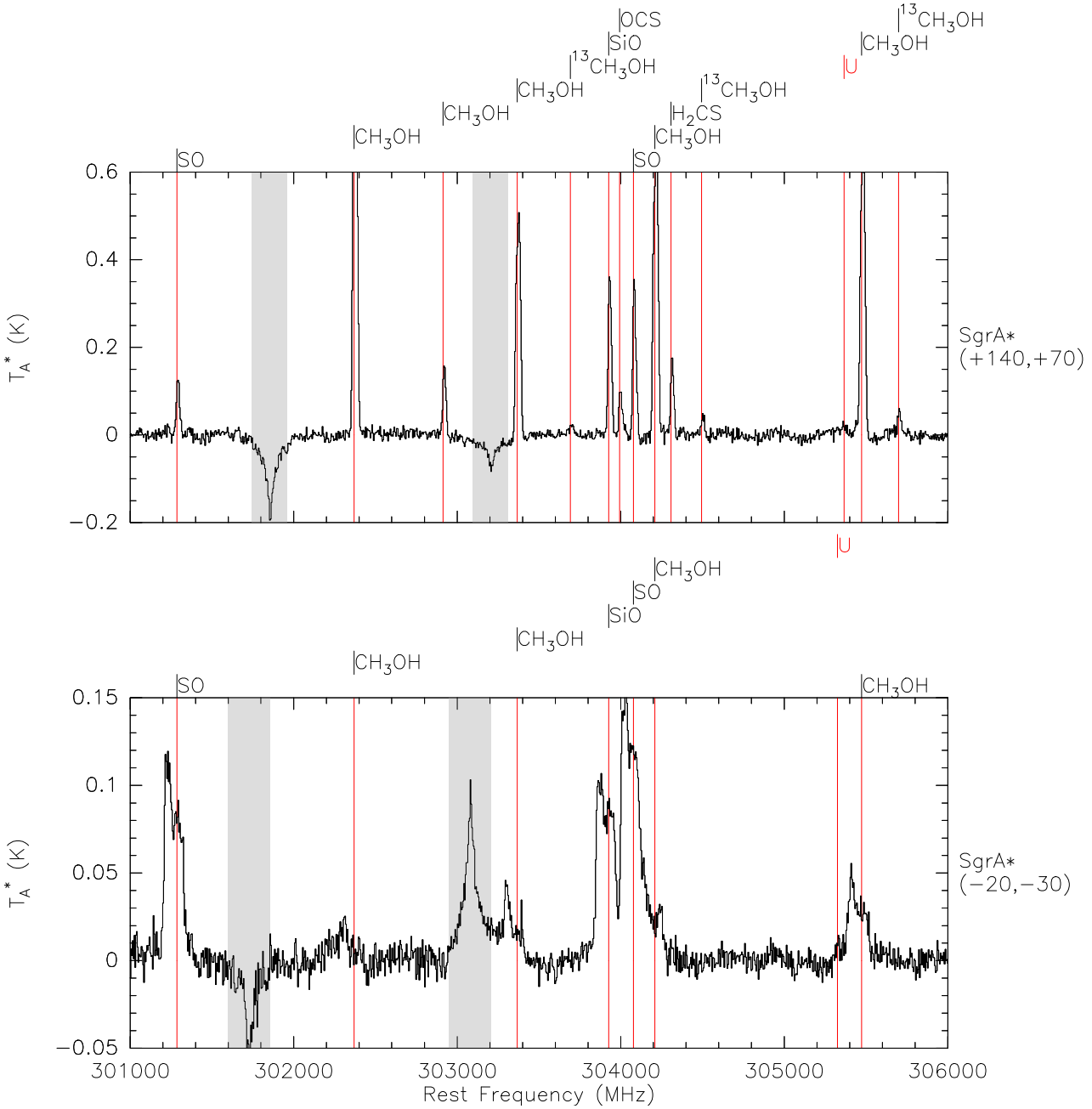

Figure 5.8.8: Reduced survey of SgrA*$(-20, -30)$ (bottom) and SgrA*$(+140, +70)$ (top), composing all subscans from 301000 MHz to 306000 MHz. Astronomical lines are marked by a vertical line that is labeled on top of each spectrum. The area 120 km s^{-1} around atmospheric lines in calibration scans is highlighted in grey. Lines that are "mirrored" from the other sideband are labeled accordingly.

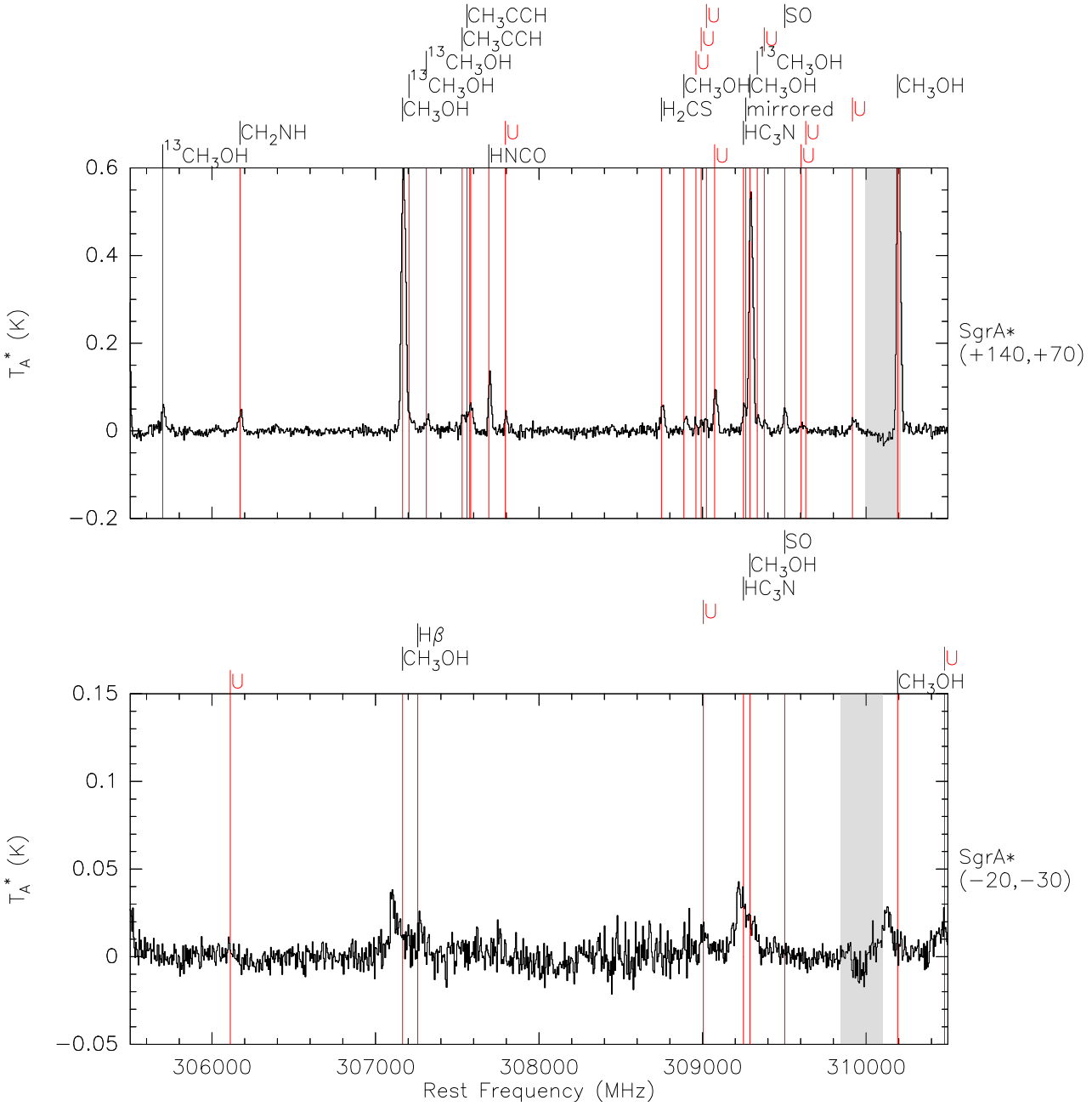

Figure 5.8.9: Reduced survey of SgrA*$(-20, -30)$ (bottom) and SgrA*$(+140, +70)$ (top), composing all subscans from 305500 MHz to 310500 MHz. Astronomical lines are marked by a vertical line that is labeled on top of each spectrum. The area 120 km s^{-1} around atmospheric lines in calibration scans is highlighted in grey. Lines that are "mirrored" from the other sideband are labeled accordingly.

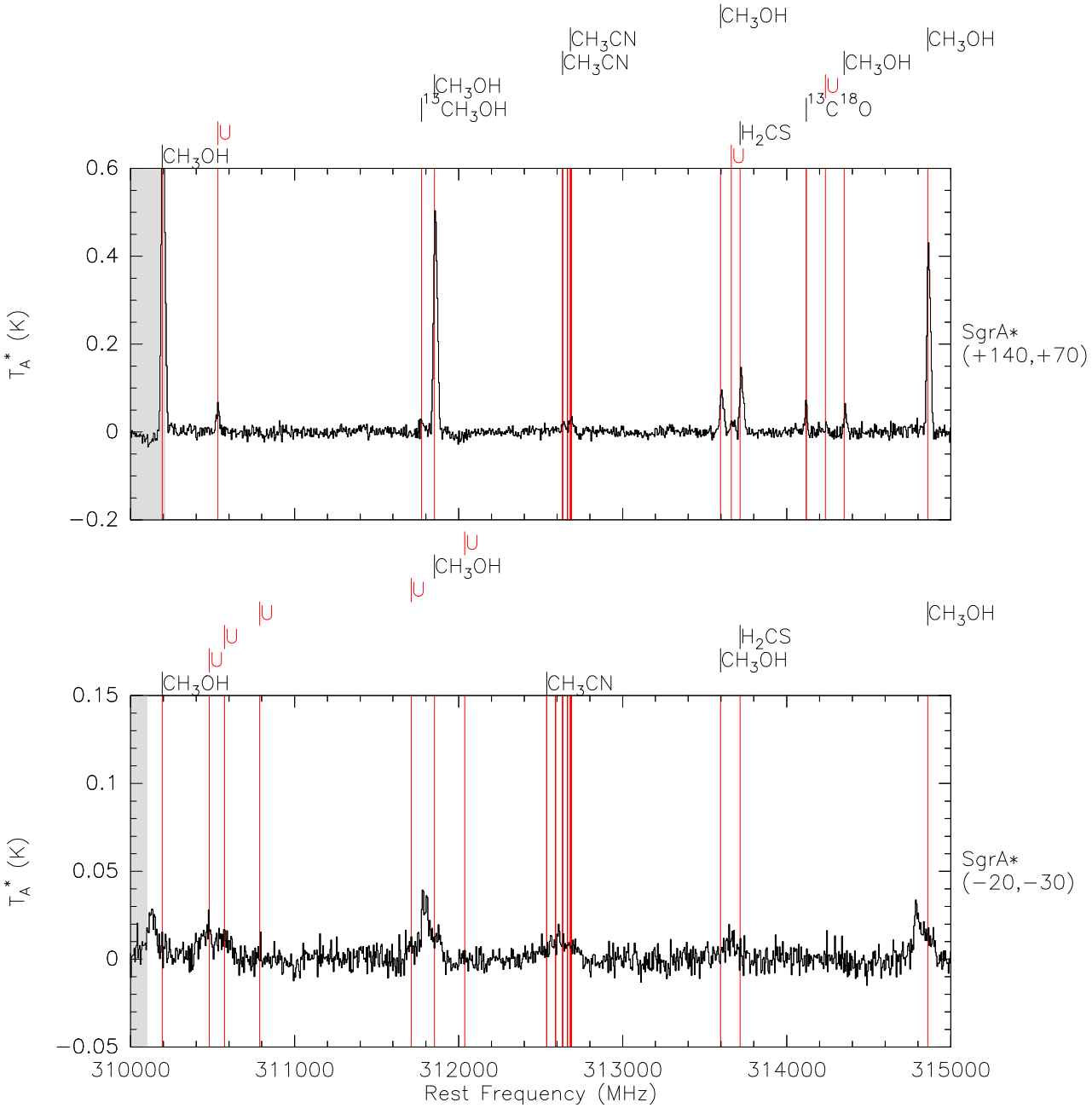

Figure 5.8.10: Reduced survey of SgrA*$(-20, -30)$ (bottom) and SgrA*$(+140, +70)$ (top), composing all subscans from 310000 MHz to 315000 MHz. Astronomical lines are marked by a vertical line that is labeled on top of each spectrum. The area 120 km s^{-1} around atmospheric lines in calibration scans is highlighted in grey. Lines that are "mirrored" from the other sideband are labeled accordingly.

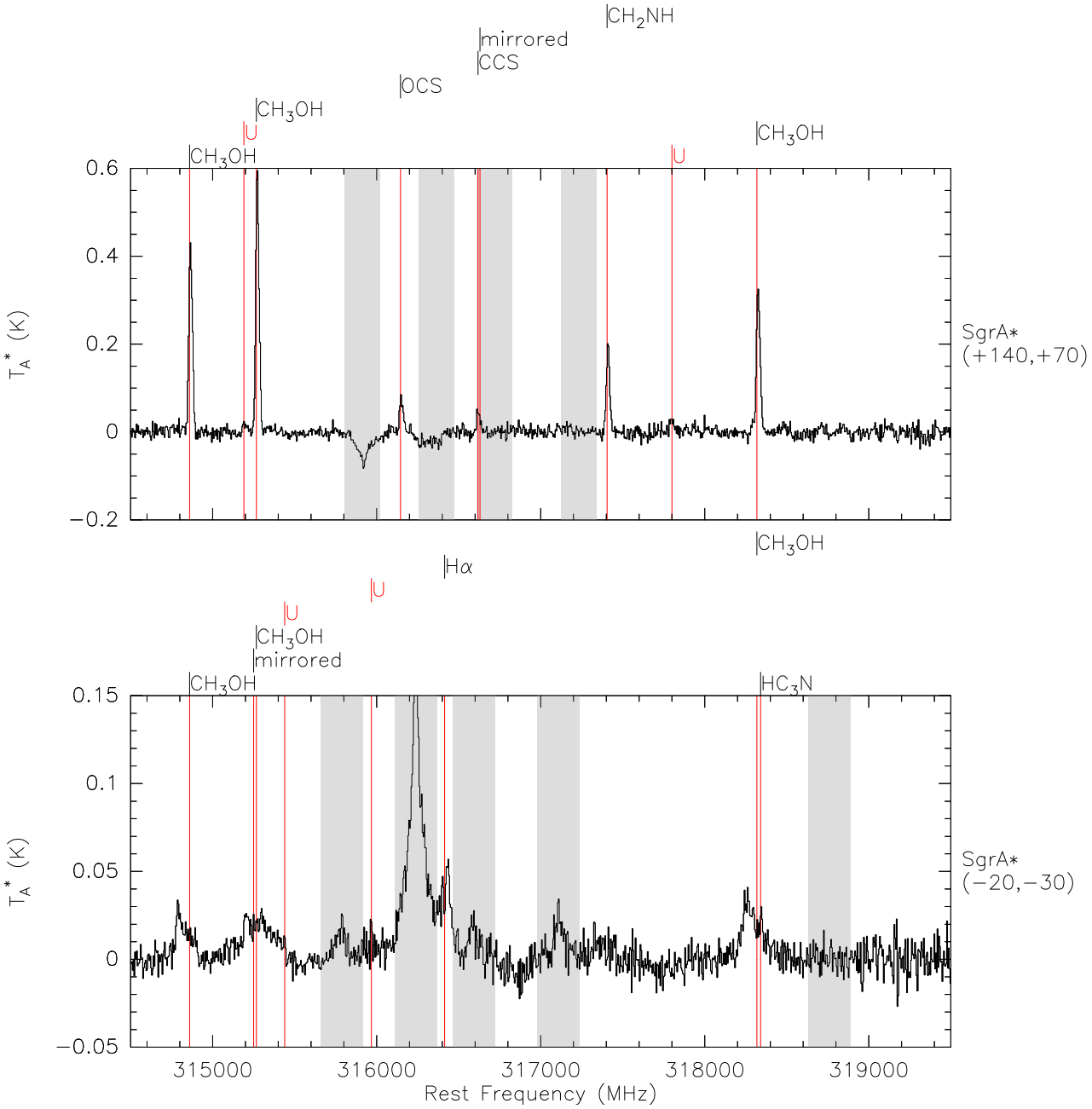

Figure 5.8.11: Reduced survey of SgrA*$(-20,-30)$ (bottom) and SgrA*$(+140,+70)$ (top), composing all subscans from 314500 MHz to 319500 MHz. Astronomical lines are marked by a vertical line that is labeled on top of each spectrum. The area 120 km s^{-1} around atmospheric lines in calibration scans is highlighted in grey. Lines that are "mirrored" from the other sideband are labeled accordingly.

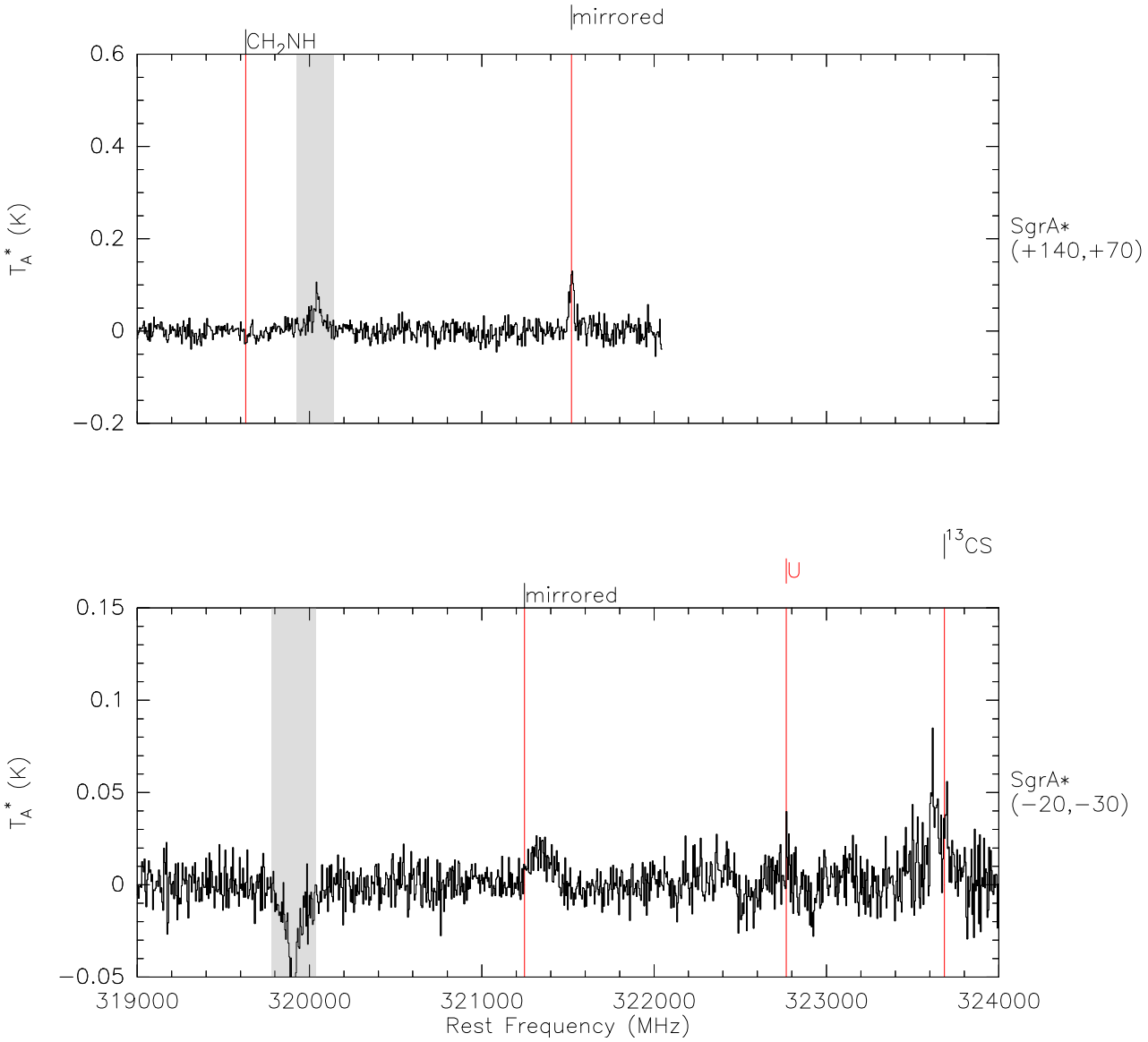

Figure 5.8.12: Reduced survey of SgrA*$(-20, -30)$ (bottom) and SgrA*$(+140, +70)$ (top), composing all subscans from 319000 MHz to 324000 MHz. Astronomical lines are marked by a vertical line that is labeled on top of each spectrum. The area 120 km s^{-1} around atmospheric lines in calibration scans is highlighted in grey. Lines that are "mirrored" from the other sideband are labeled accordingly.

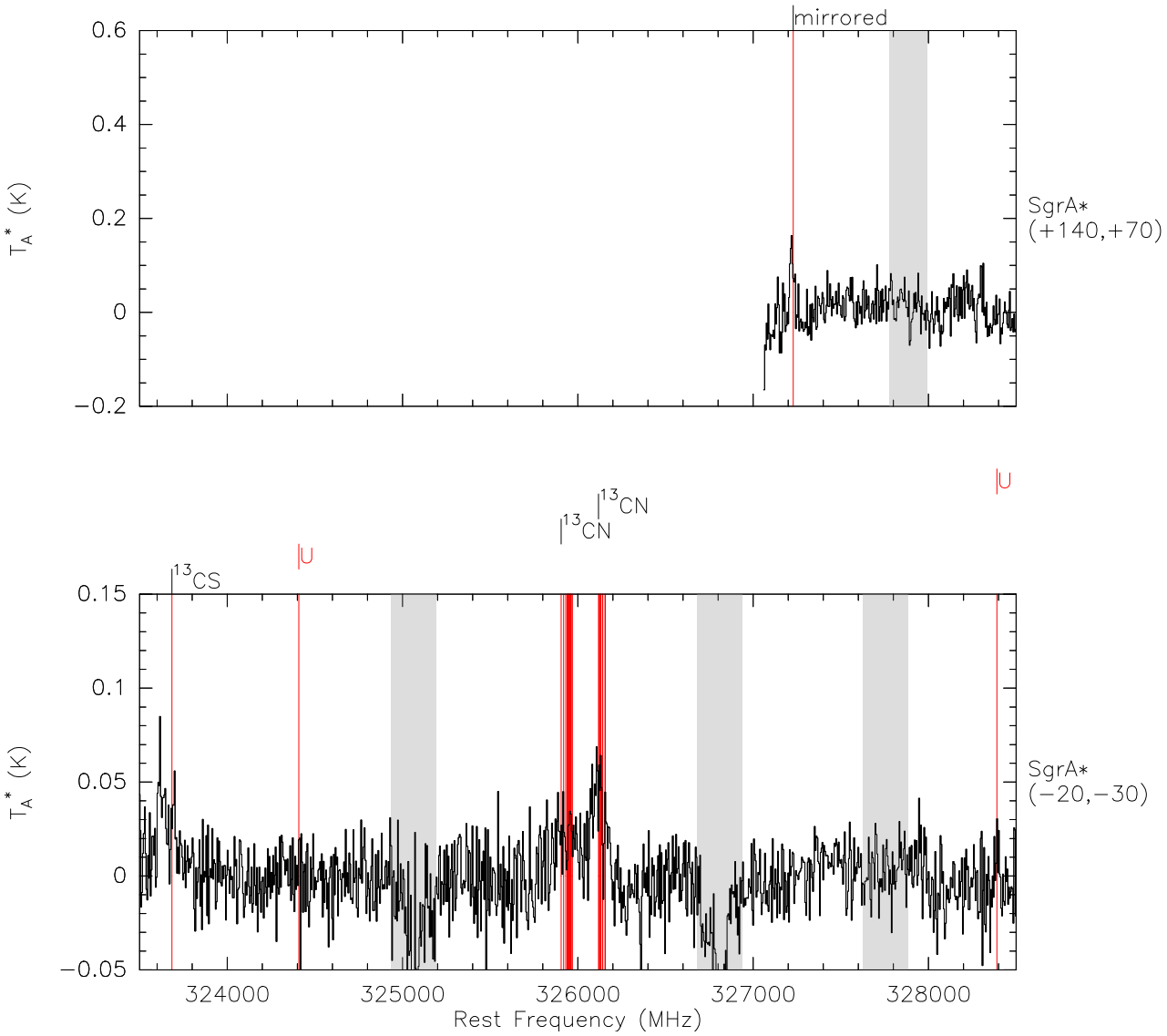

Figure 5.8.13: Reduced survey of SgrA*$(-20, -30)$ (bottom) and SgrA*$(+140, +70)$ (top), composing all subscans from 323500 MHz to 328500 MHz. Astronomical lines are marked by a vertical line that is labeled on top of each spectrum. The area 120 km s^{-1} around atmospheric lines in calibration scans is highlighted in grey. Lines that are "mirrored" from the other sideband are labeled accordingly.

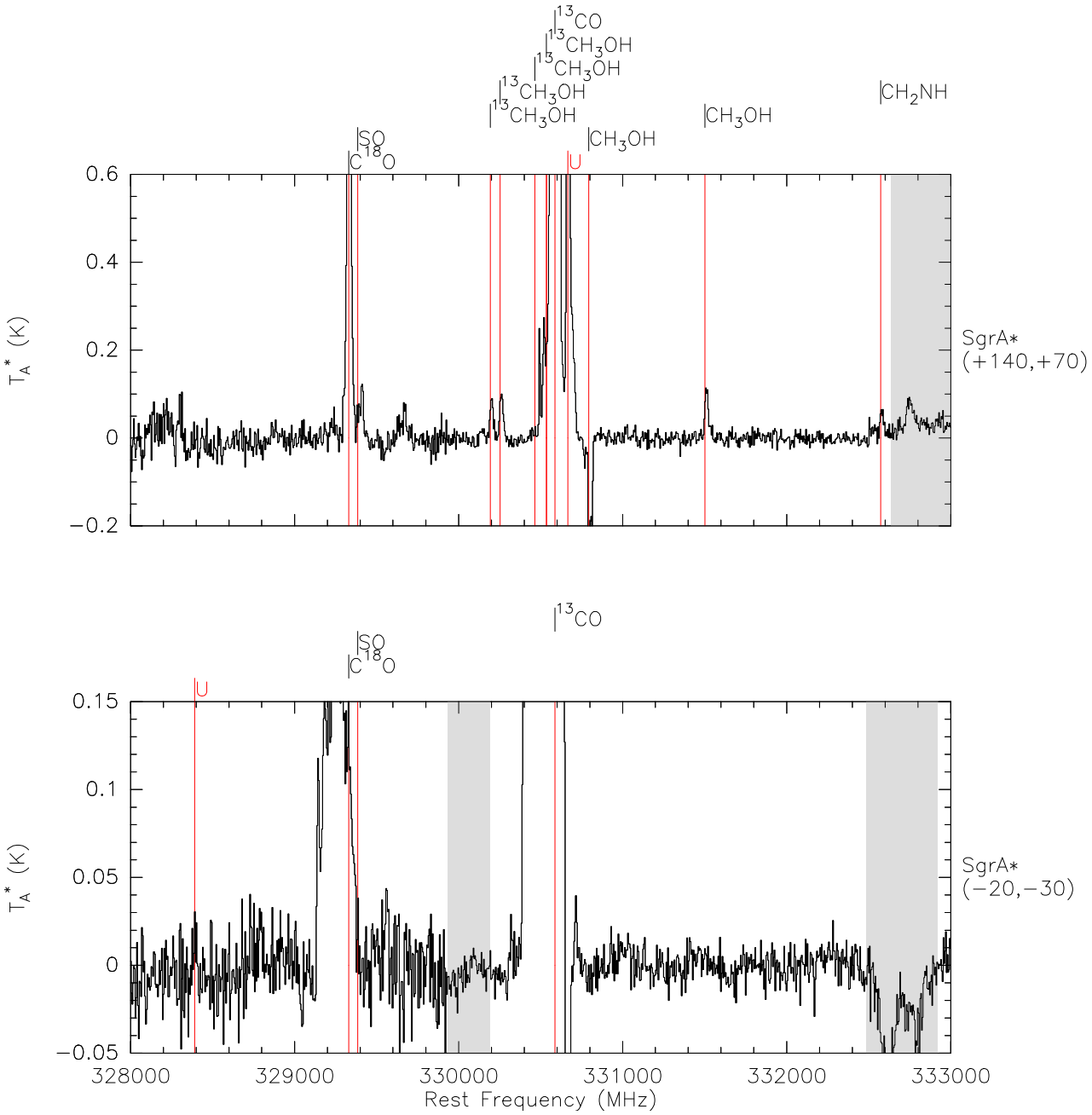

Figure 5.8.14: Reduced survey of SgrA*$(-20, -30)$ (bottom) and SgrA*$(+140, +70)$ (top), composing all subscans from 328000 MHz to 333000 MHz. Astronomical lines are marked by a vertical line that is labeled on top of each spectrum. The area 120 km s^{-1} around atmospheric lines in calibration scans is highlighted in grey. Lines that are "mirrored" from the other sideband are labeled accordingly.

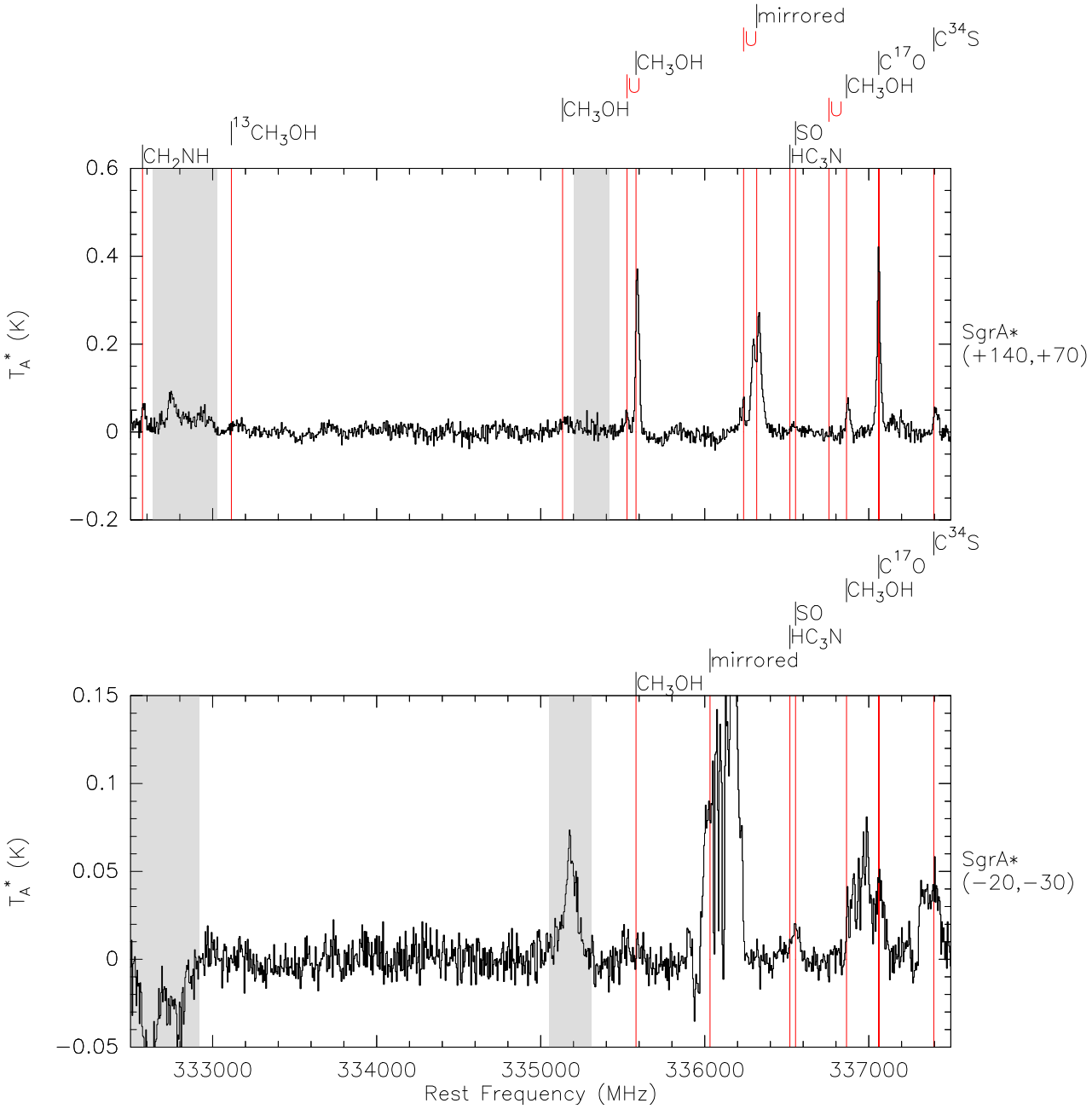

Figure 5.8.15: Reduced survey of SgrA*$(-20,-30)$ (bottom) and SgrA*$(+140,+70)$ (top), composing all subscans from 332500 MHz to 337500 MHz. Astronomical lines are marked by a vertical line that is labeled on top of each spectrum. The area 120 km s^{-1} around atmospheric lines in calibration scans is highlighted in grey. Lines that are "mirrored" from the other sideband are labeled accordingly.

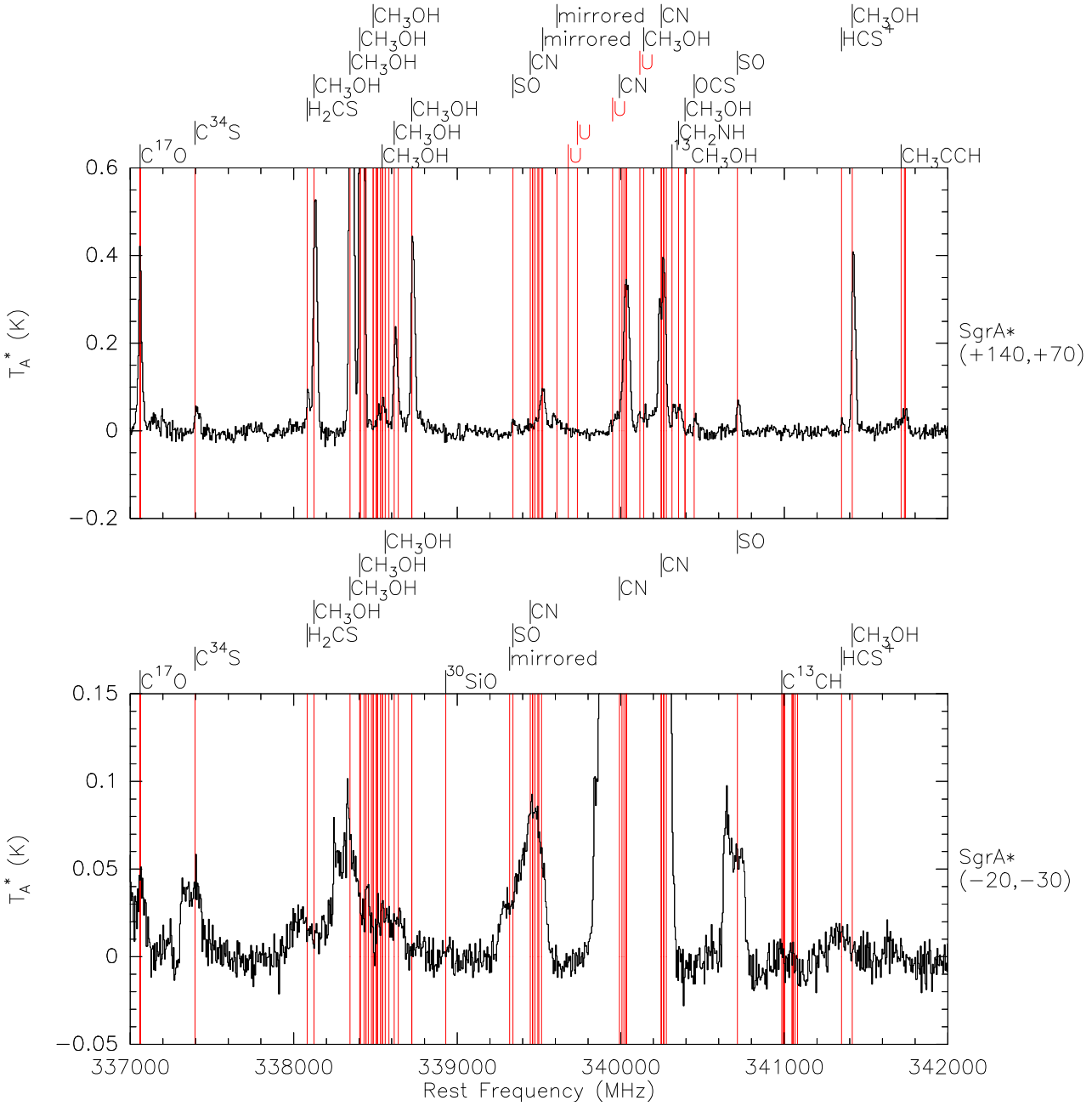

Figure 5.8.16: Reduced survey of SgrA*$(-20,-30)$ (bottom) and SgrA*$(+140,+70)$ (top), composing all subscans from 337000 MHz to 342000 MHz. Astronomical lines are marked by a vertical line that is labeled on top of each spectrum. The area 120 km s^{-1} around atmospheric lines in calibration scans is highlighted in grey. Lines that are "mirrored" from the other sideband are labeled accordingly.

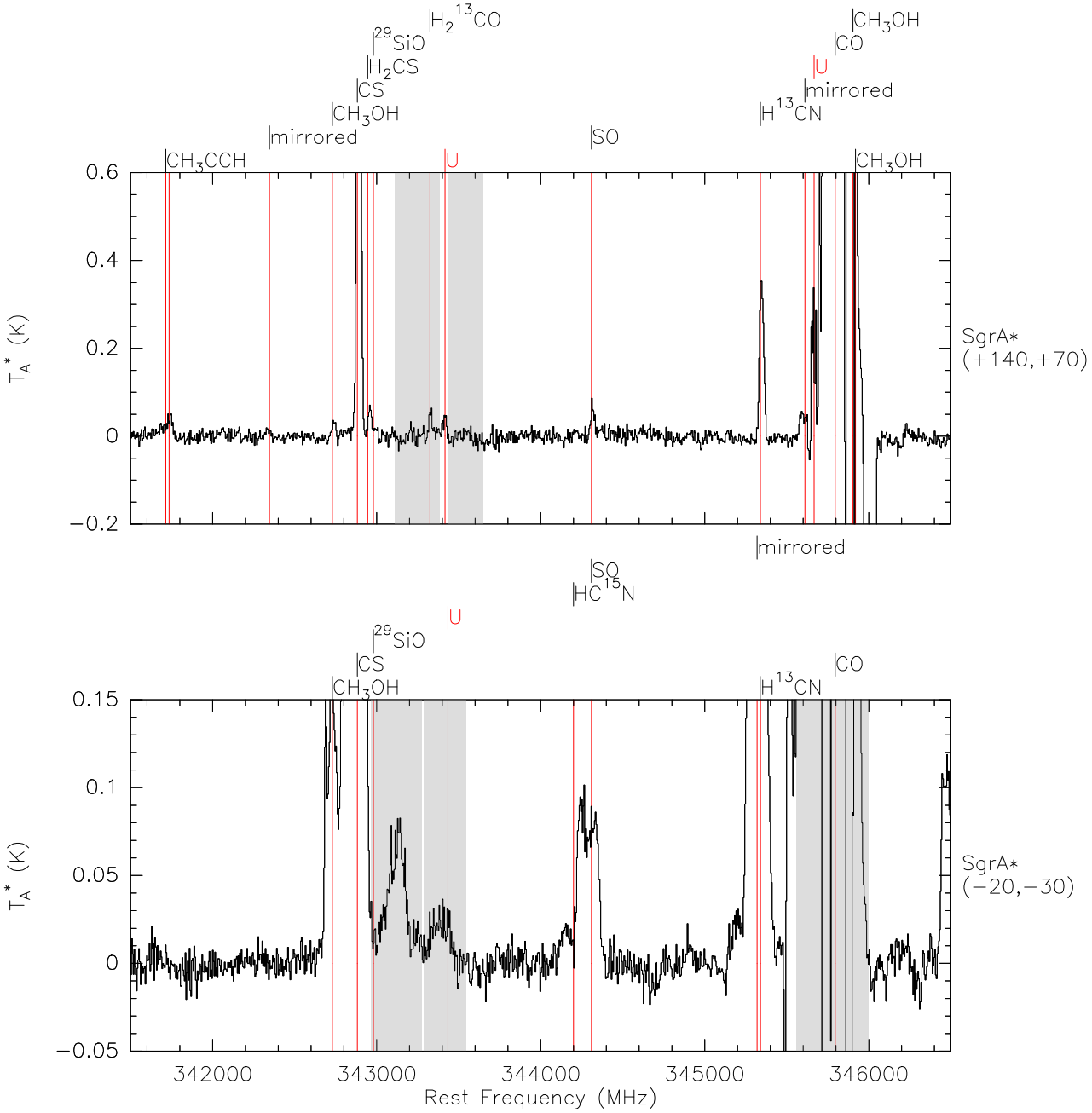

Figure 5.8.17: Reduced survey of SgrA*$(-20, -30)$ (bottom) and SgrA*$(+140, +70)$ (top), composing all subscans from 341500 MHz to 346500 MHz. Astronomical lines are marked by a vertical line that is labeled on top of each spectrum. The area 120 km s^{-1} around atmospheric lines in calibration scans is highlighted in grey. Lines that are "mirrored" from the other sideband are labeled accordingly.

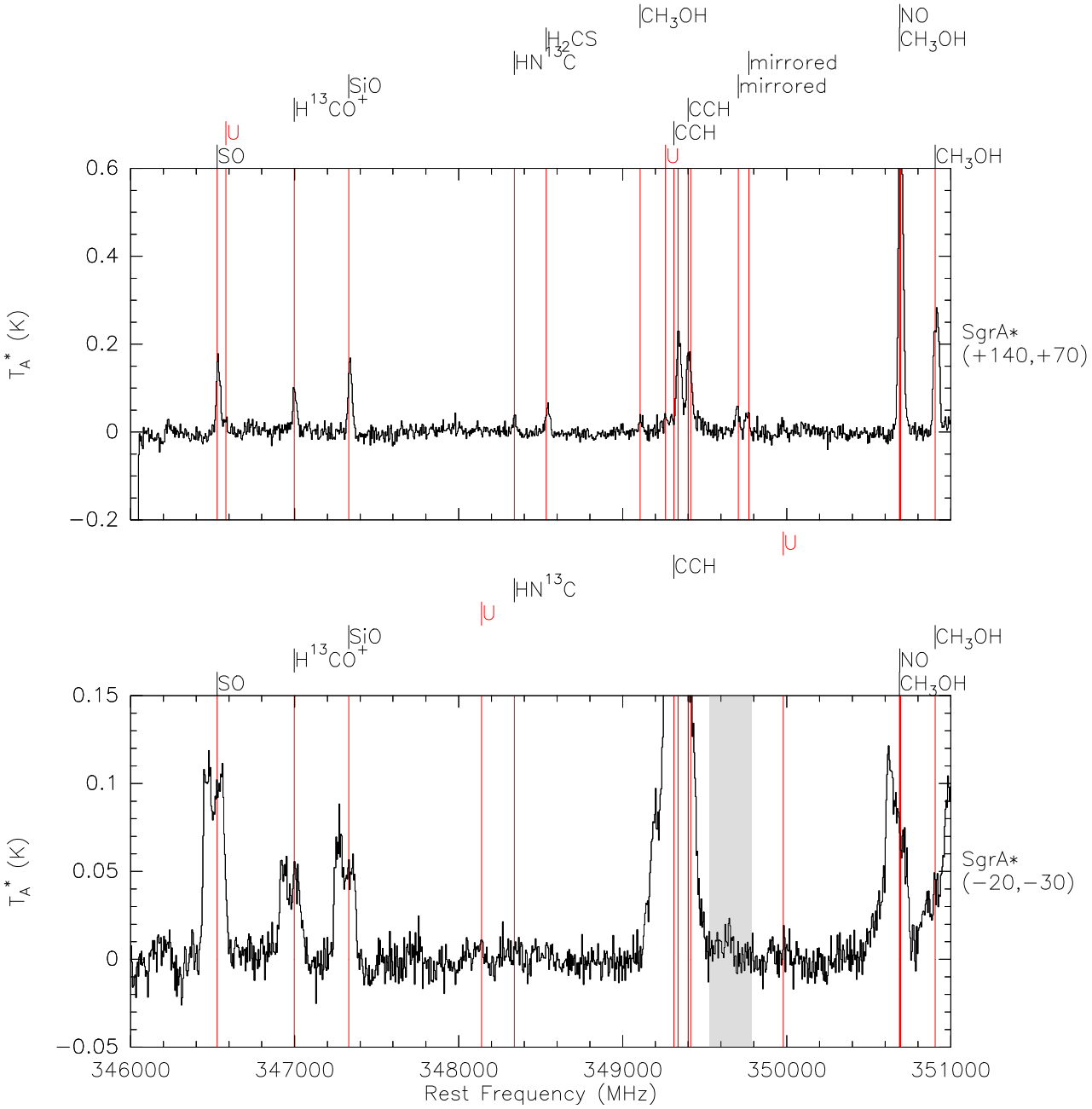

Figure 5.8.18: Reduced survey of SgrA*$(-20, -30)$ (bottom) and SgrA*$(+140, +70)$ (top), composing all subscans from 346000 MHz to 351000 MHz. Astronomical lines are marked by a vertical line that is labeled on top of each spectrum. The area 120 km s^{-1} around atmospheric lines in calibration scans is highlighted in grey. Lines that are "mirrored" from the other sideband are labeled accordingly.

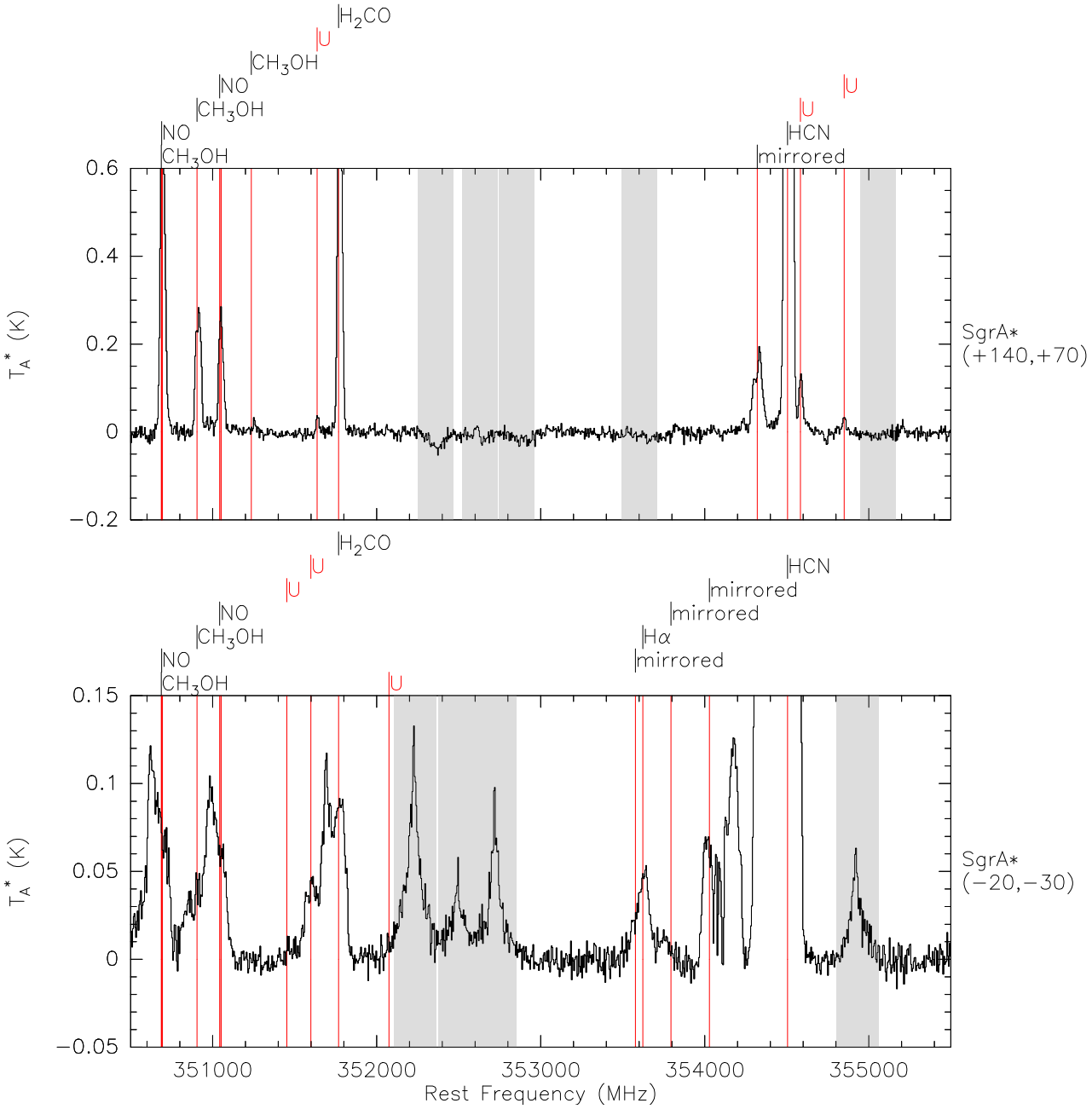

Figure 5.8.19: Reduced survey of SgrA*$(-20, -30)$ (bottom) and SgrA*$(+140, +70)$ (top), composing all subscans from 350500 MHz to 355500 MHz. Astronomical lines are marked by a vertical line that is labeled on top of each spectrum. The area 120 km s^{-1} around atmospheric lines in calibration scans is highlighted in grey. Lines that are "mirrored" from the other sideband are labeled accordingly.

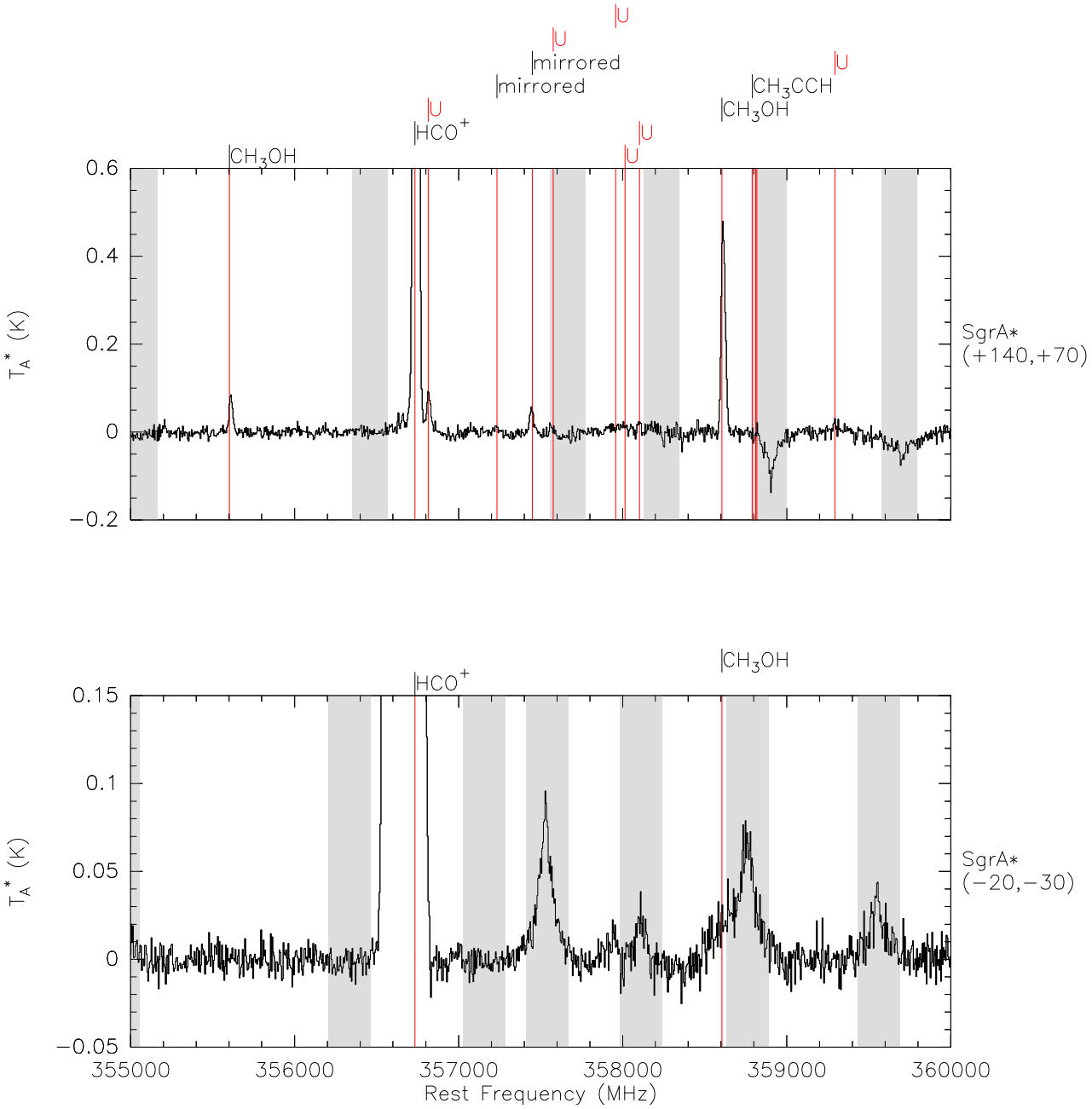

Figure 5.8.20: Reduced survey of SgrA*$(-20, -30)$ (bottom) and SgrA*$(+140, +70)$ (top), composing all subscans from 355000 MHz to 360000 MHz. Astronomical lines are marked by a vertical line that is labeled on top of each spectrum. The area 120 km s^{-1} around atmospheric lines in calibration scans is highlighted in grey. Lines that are "mirrored" from the other sideband are labeled accordingly.

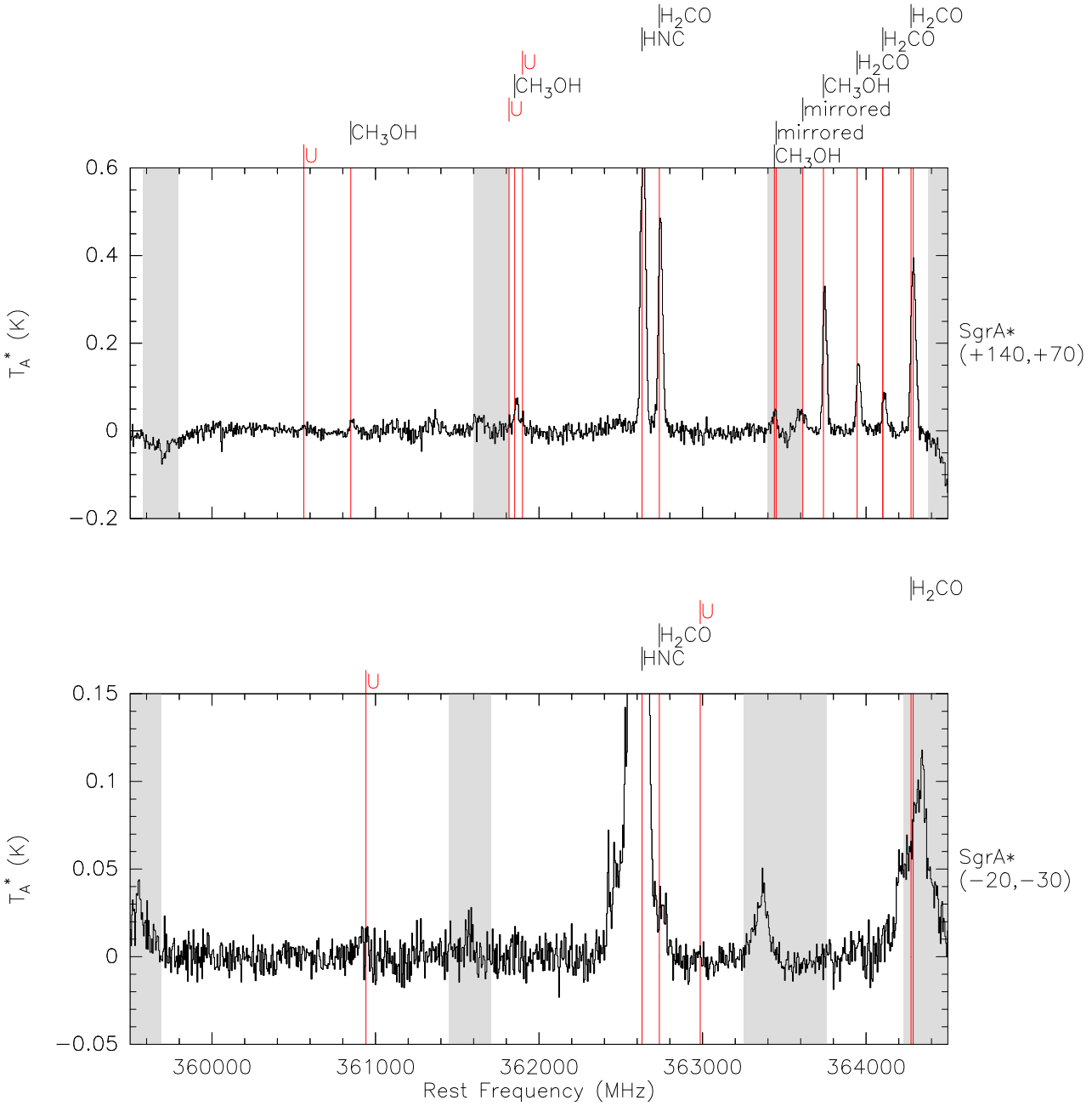

Figure 5.8.21: Reduced survey of SgrA*$(-20,-30)$ (bottom) and SgrA*$(+140,+70)$ (top), composing all subscans from 359500 MHz to 364500 MHz. Astronomical lines are marked by a vertical line that is labeled on top of each spectrum. The area 120 km s^{-1} around atmospheric lines in calibration scans is highlighted in grey. Lines that are "mirrored" from the other sideband are labeled accordingly.

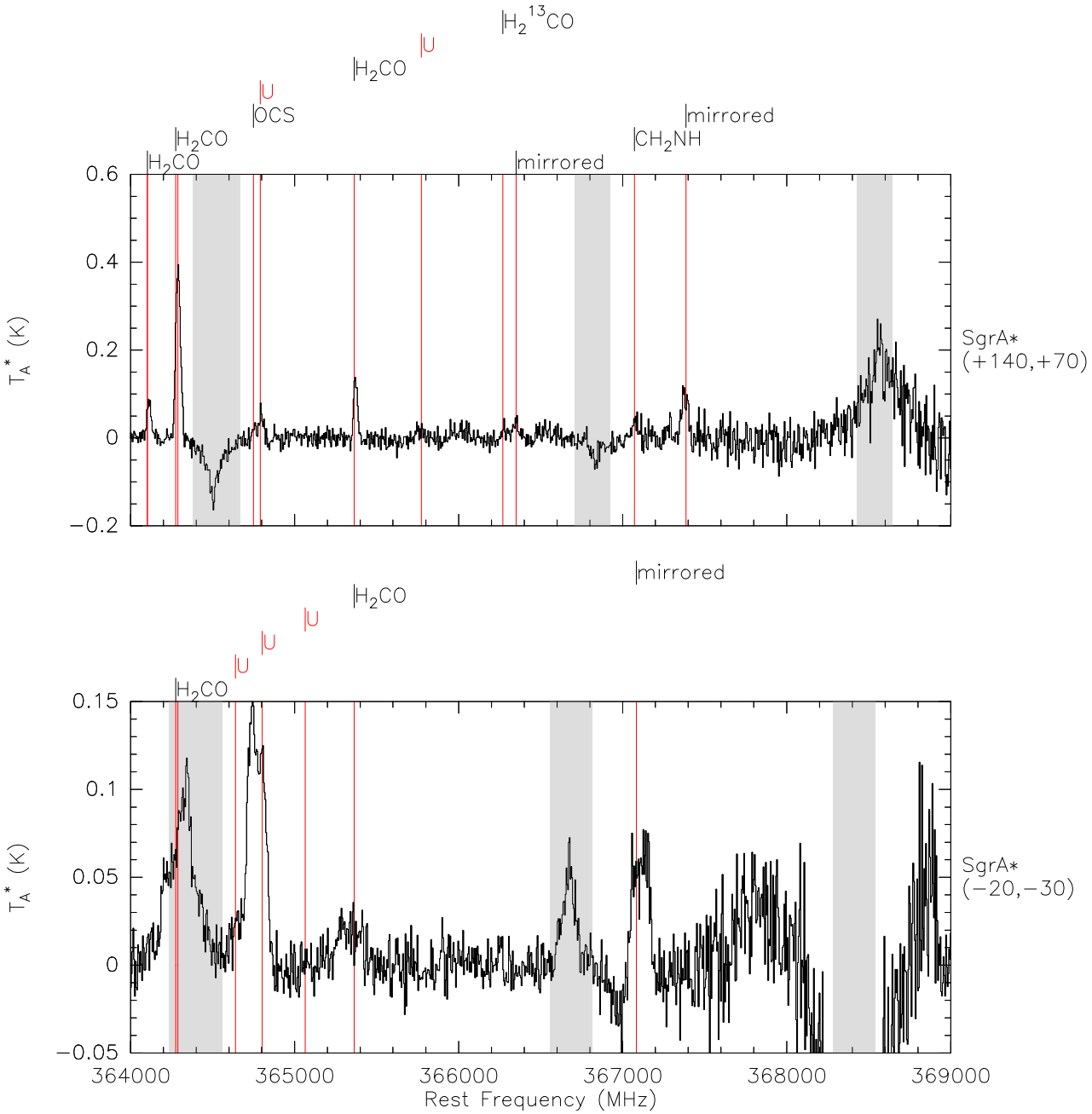

Figure 5.8.22: Reduced survey of SgrA*$(-20,-30)$ (bottom) and SgrA*$(+140,+70)$ (top), composing all subscans from 364000 MHz to 369000 MHz. Astronomical lines are marked by a vertical line that is labeled on top of each spectrum. The area 120 km s^{-1} around atmospheric lines in calibration scans is highlighted in grey. Lines that are "mirrored" from the other sideband are labeled accordingly.

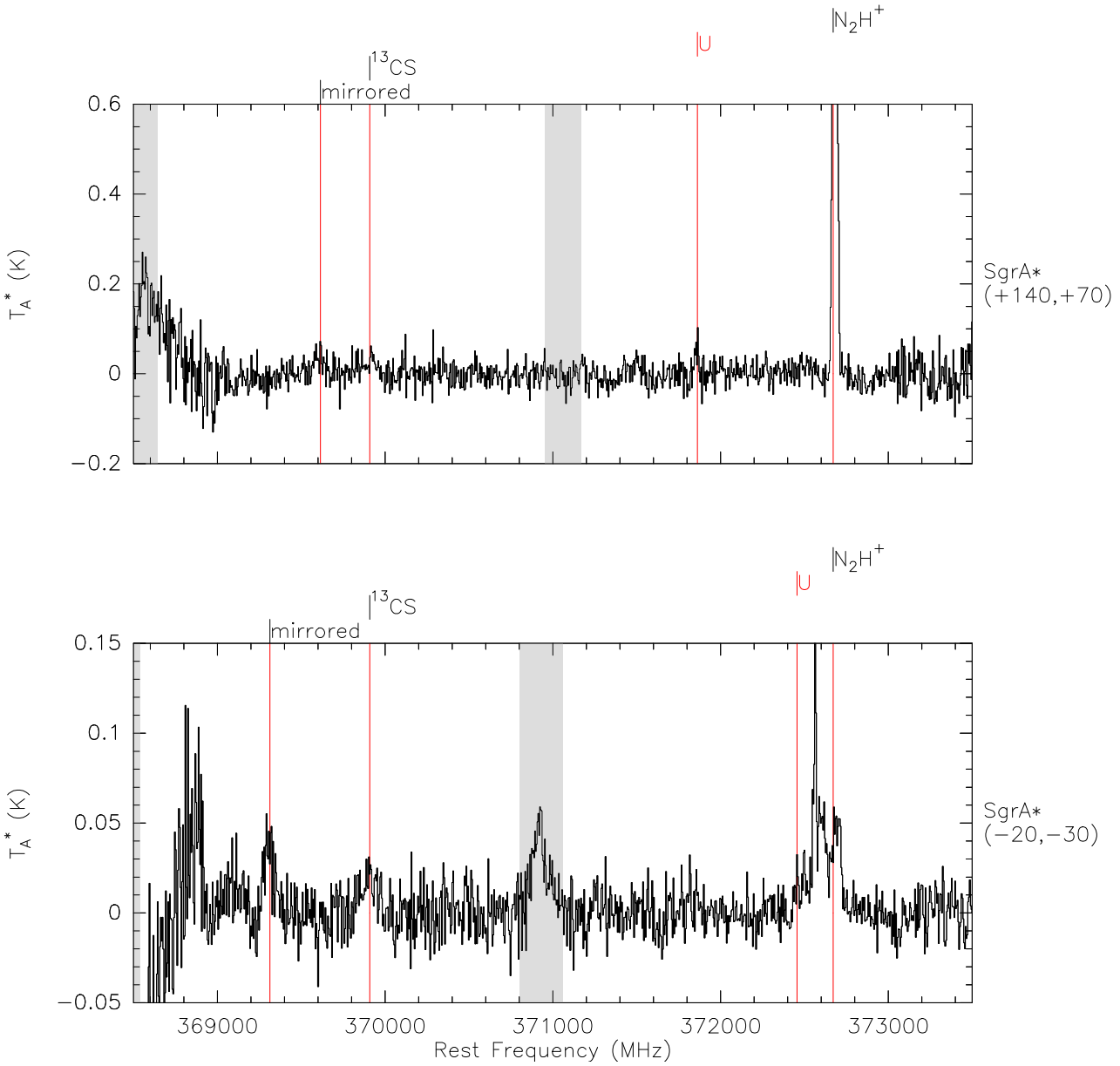

Figure 5.8.23: Reduced survey of SgrA*$(-20, -30)$ (bottom) and SgrA*$(+140, +70)$ (top), composing all subscans from 368500 MHz to 373500 MHz. Astronomical lines are marked by a vertical line that is labeled on top of each spectrum. The area 120 km s^{-1} around atmospheric lines in calibration scans is highlighted in grey. Lines that are "mirrored" from the other sideband are labeled accordingly.

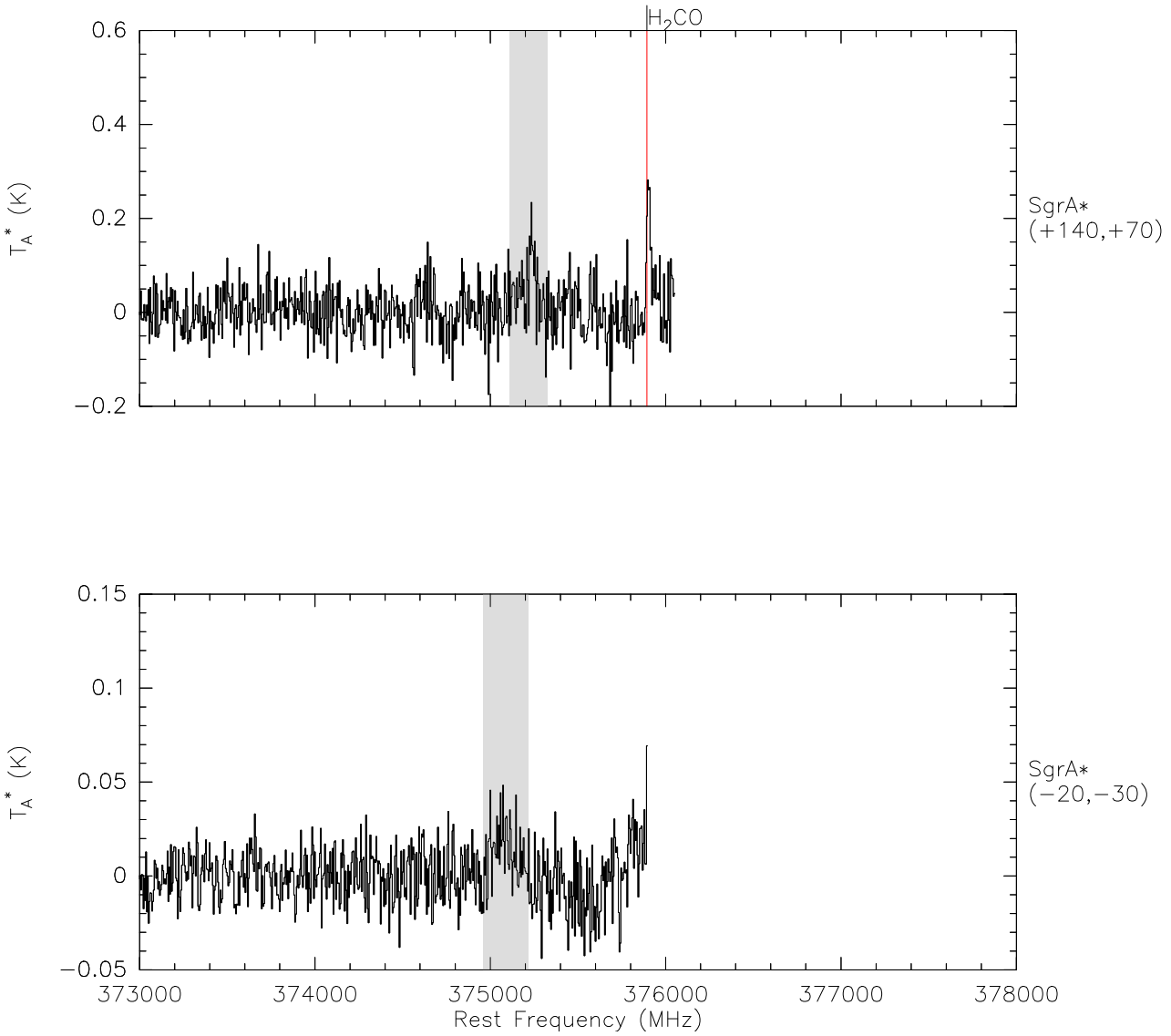

Figure 5.8.24: Reduced survey of SgrA*$(-20, -30)$ (bottom) and SgrA*$(+140, +70)$ (top), composing all subscans from 373000 MHz to 378000 MHz. Astronomical lines are marked by a vertical line that is labeled on top of each spectrum. The area 120 km s^{-1} around atmospheric lines in calibration scans is highlighted in grey. Lines that are "mirrored" from the other sideband are labeled accordingly.

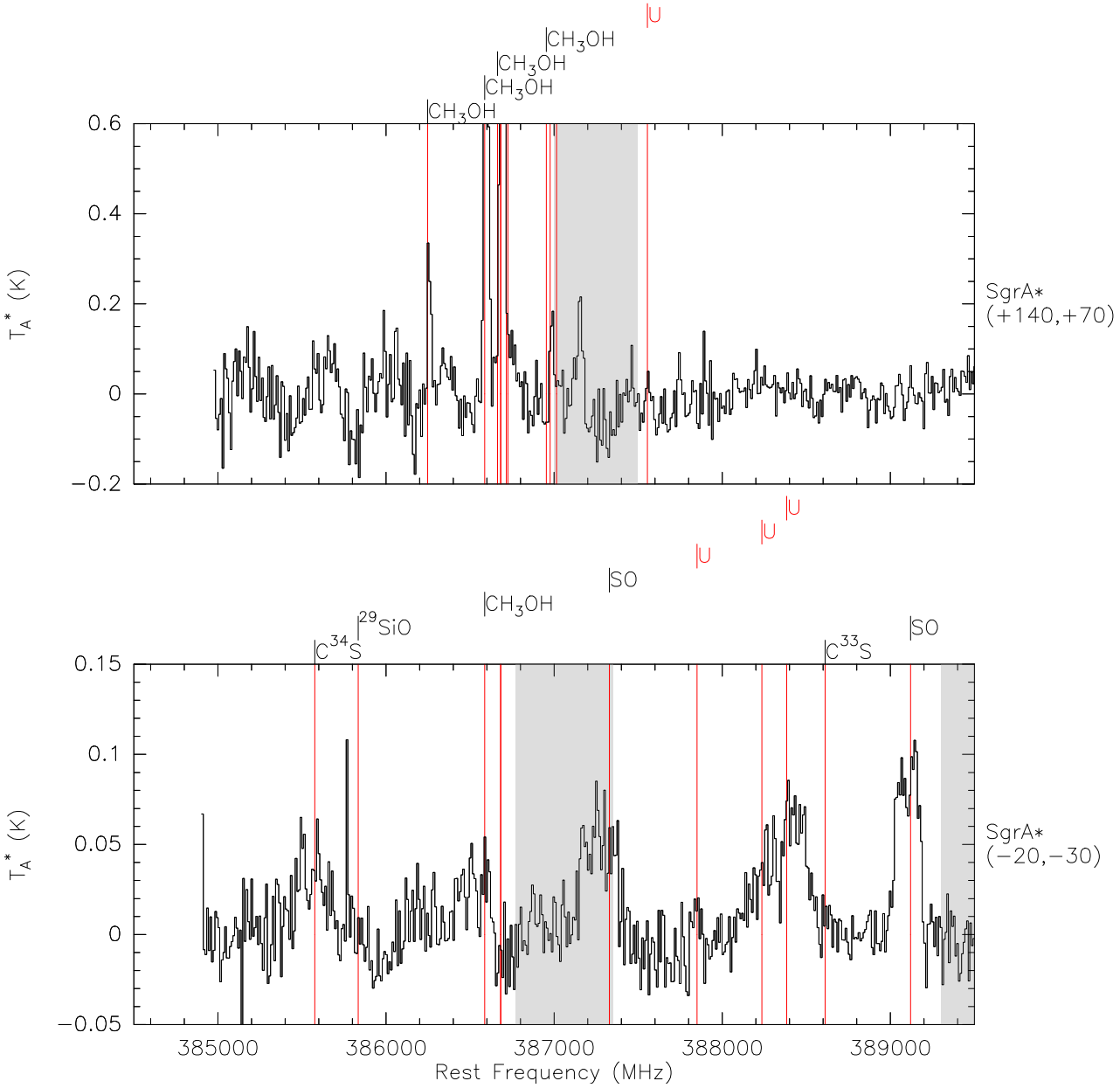

Figure 5.8.25: Reduced survey of SgrA*$(-20,-30)$ (bottom) and SgrA*$(+140,+70)$ (top), composing all subscans from 384500 MHz to 389500 MHz. Astronomical lines are marked by a vertical line that is labeled on top of each spectrum. The area 120 km s^{-1} around atmospheric lines in calibration scans is highlighted in grey. Lines that are "mirrored" from the other sideband are labeled accordingly.

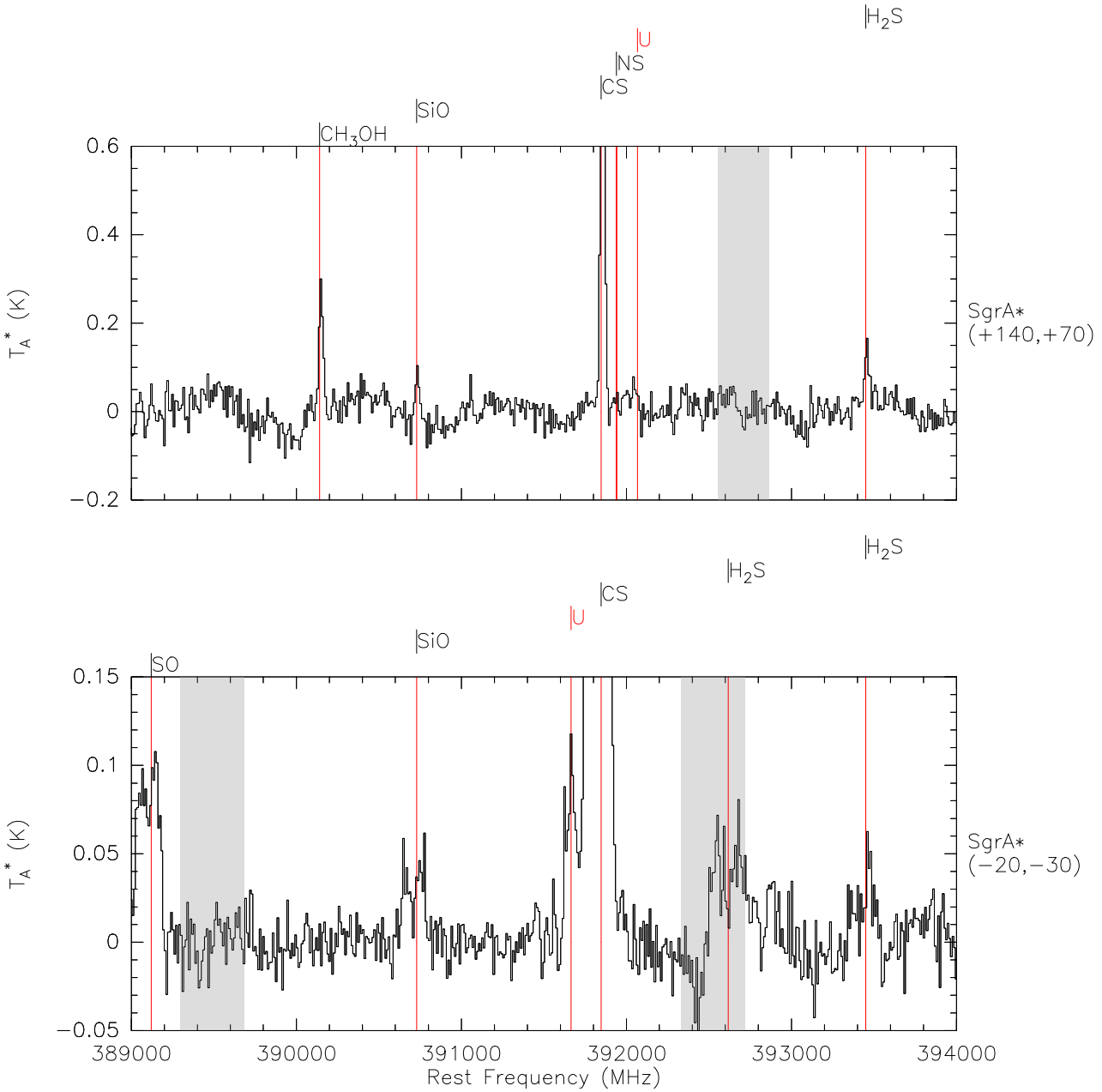

Figure 5.8.26: Reduced survey of SgrA*$(-20, -30)$ (bottom) and SgrA*$(+140, +70)$ (top), composing all subscans from 389000 MHz to 394000 MHz. Astronomical lines are marked by a vertical line that is labeled on top of each spectrum. The area 120 km s^{-1} around atmospheric lines in calibration scans is highlighted in grey. Lines that are "mirrored" from the other sideband are labeled accordingly.

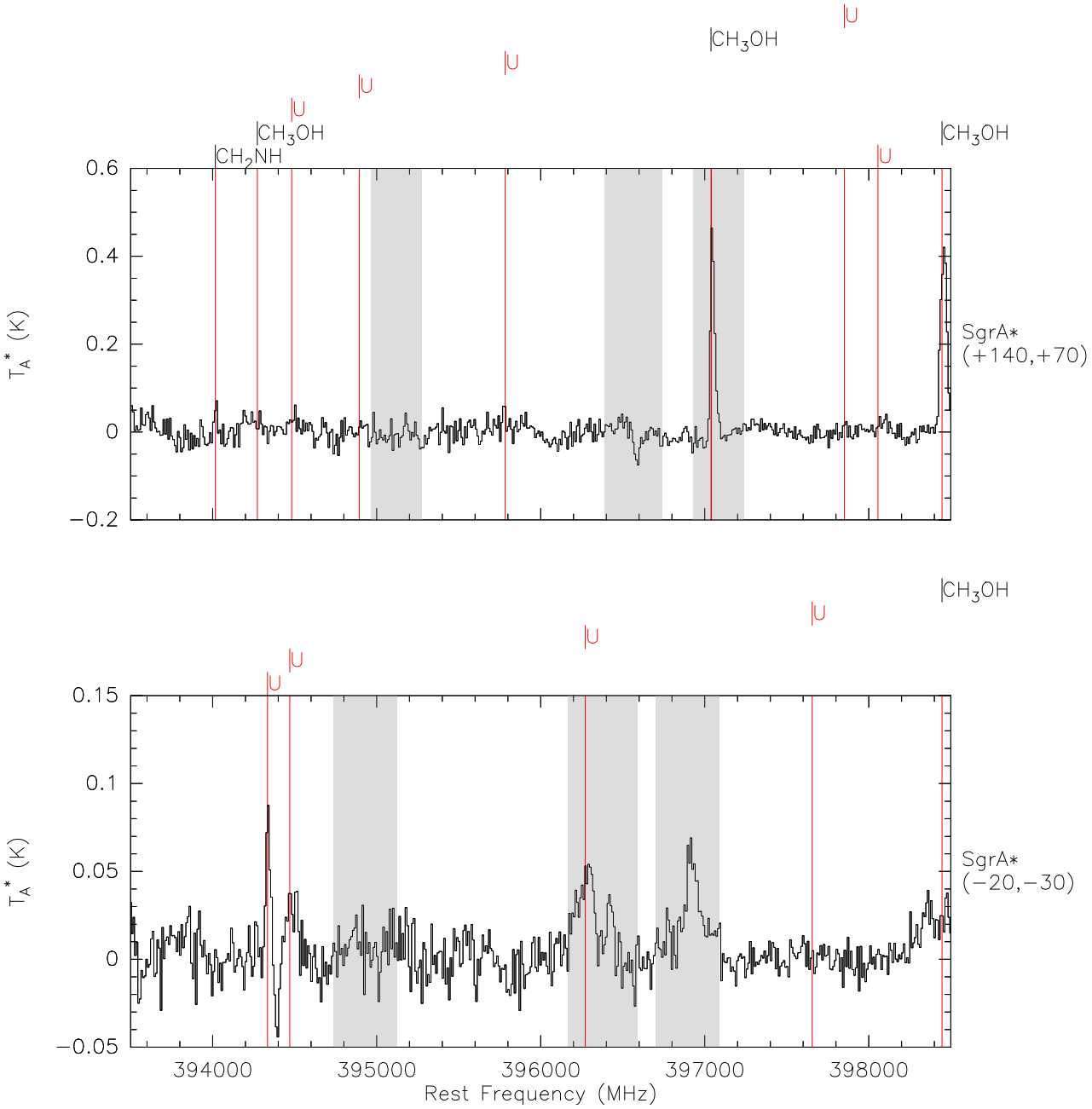

Figure 5.8.27: Reduced survey of SgrA*$(-20,-30)$ (bottom) and SgrA*$(+140,+70)$ (top), composing all subscans from 393500 MHz to 398500 MHz. Astronomical lines are marked by a vertical line that is labeled on top of each spectrum. The area 120 km s^{-1} around atmospheric lines in calibration scans is highlighted in grey. Lines that are "mirrored" from the other sideband are labeled accordingly.

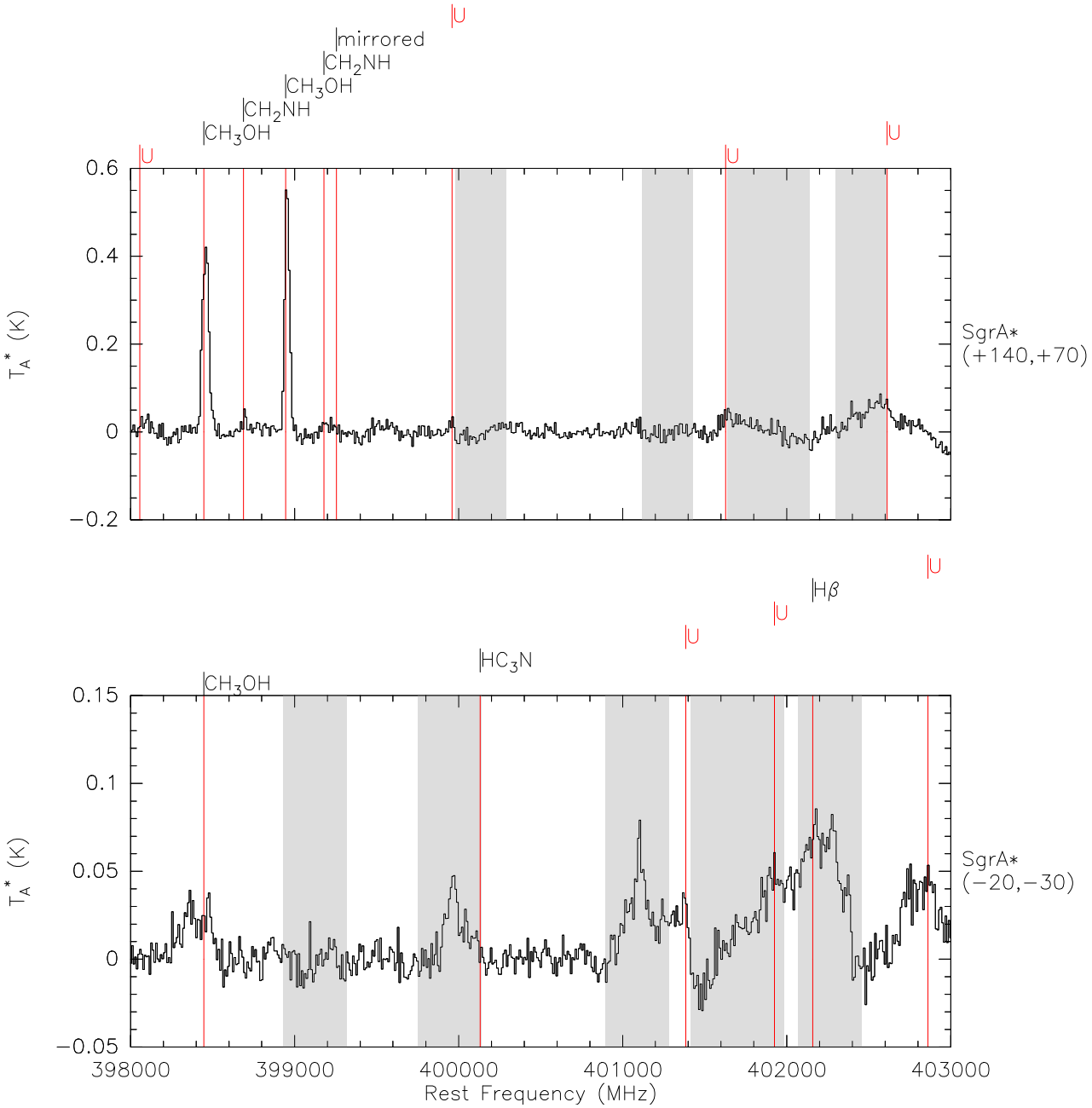

Figure 5.8.28: Reduced survey of SgrA*$(-20, -30)$ (bottom) and SgrA*$(+140, +70)$ (top), composing all subscans from 398000 MHz to 403000 MHz. Astronomical lines are marked by a vertical line that is labeled on top of each spectrum. The area 120 km s^{-1} around atmospheric lines in calibration scans is highlighted in grey. Lines that are "mirrored" from the other sideband are labeled accordingly.

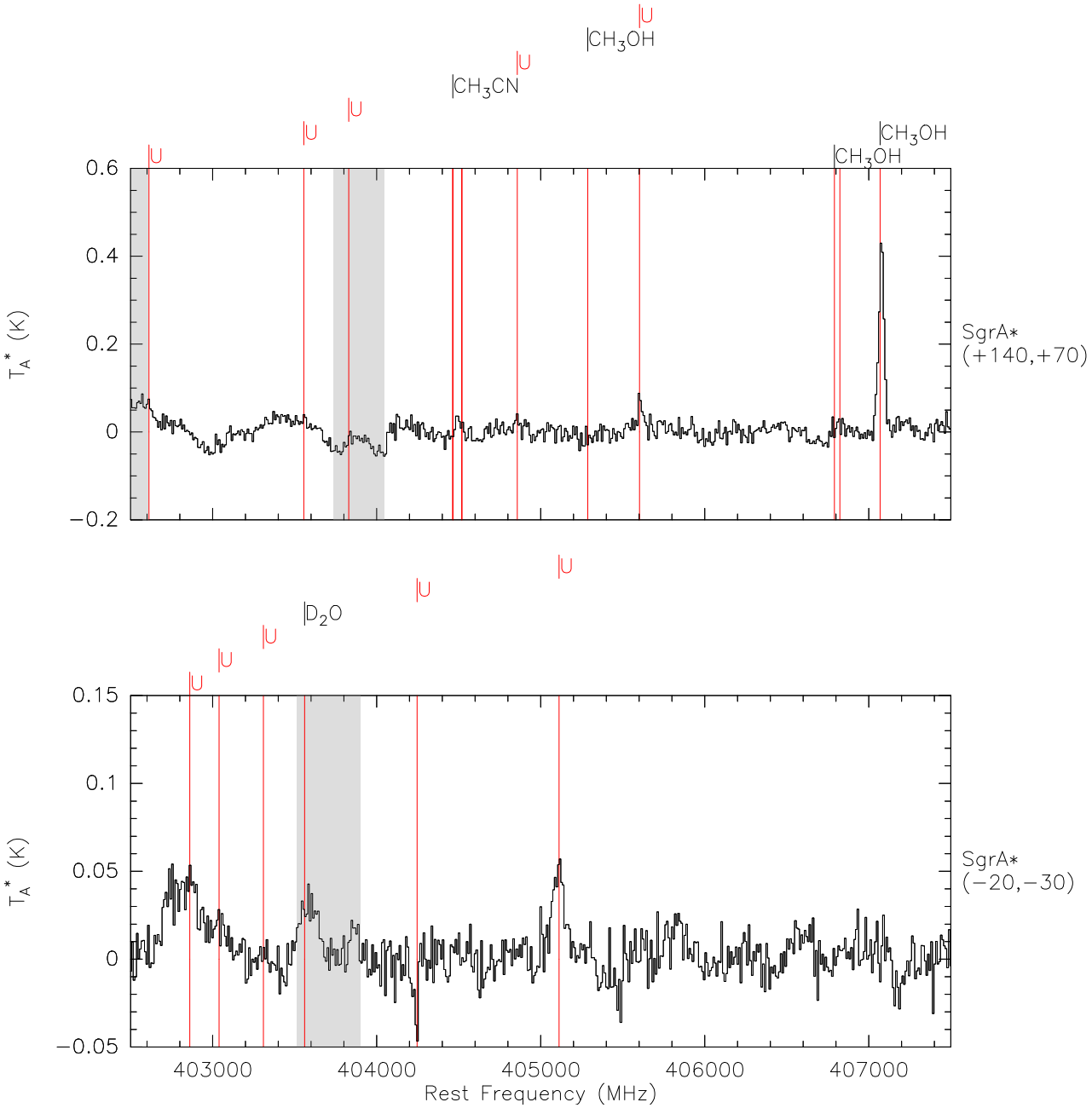

Figure 5.8.29: Reduced survey of SgrA*$(-20, -30)$ (bottom) and SgrA*$(+140, +70)$ (top), composing all subscans from 402500 MHz to 407500 MHz. Astronomical lines are marked by a vertical line that is labeled on top of each spectrum. The area 120 km s^{-1} around atmospheric lines in calibration scans is highlighted in grey. Lines that are "mirrored" from the other sideband are labeled accordingly.

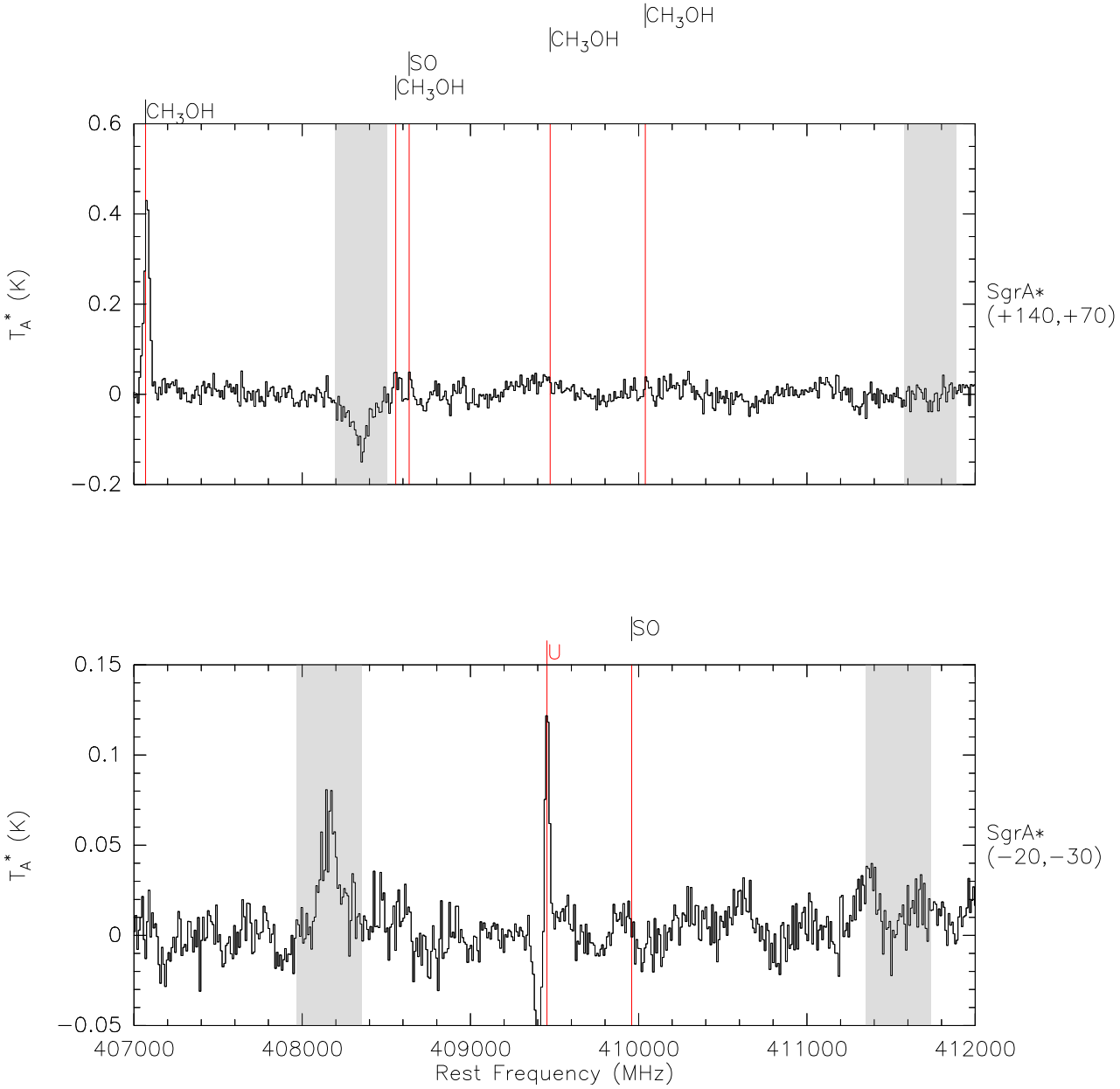

Figure 5.8.30: Reduced survey of SgrA*$(-20, -30)$ (bottom) and SgrA*$(+140, +70)$ (top), composing all subscans from 407000 MHz to 412000 MHz. Astronomical lines are marked by a vertical line that is labeled on top of each spectrum. The area 120 km s^{-1} around atmospheric lines in calibration scans is highlighted in grey. Lines that are "mirrored" from the other sideband are labeled accordingly.

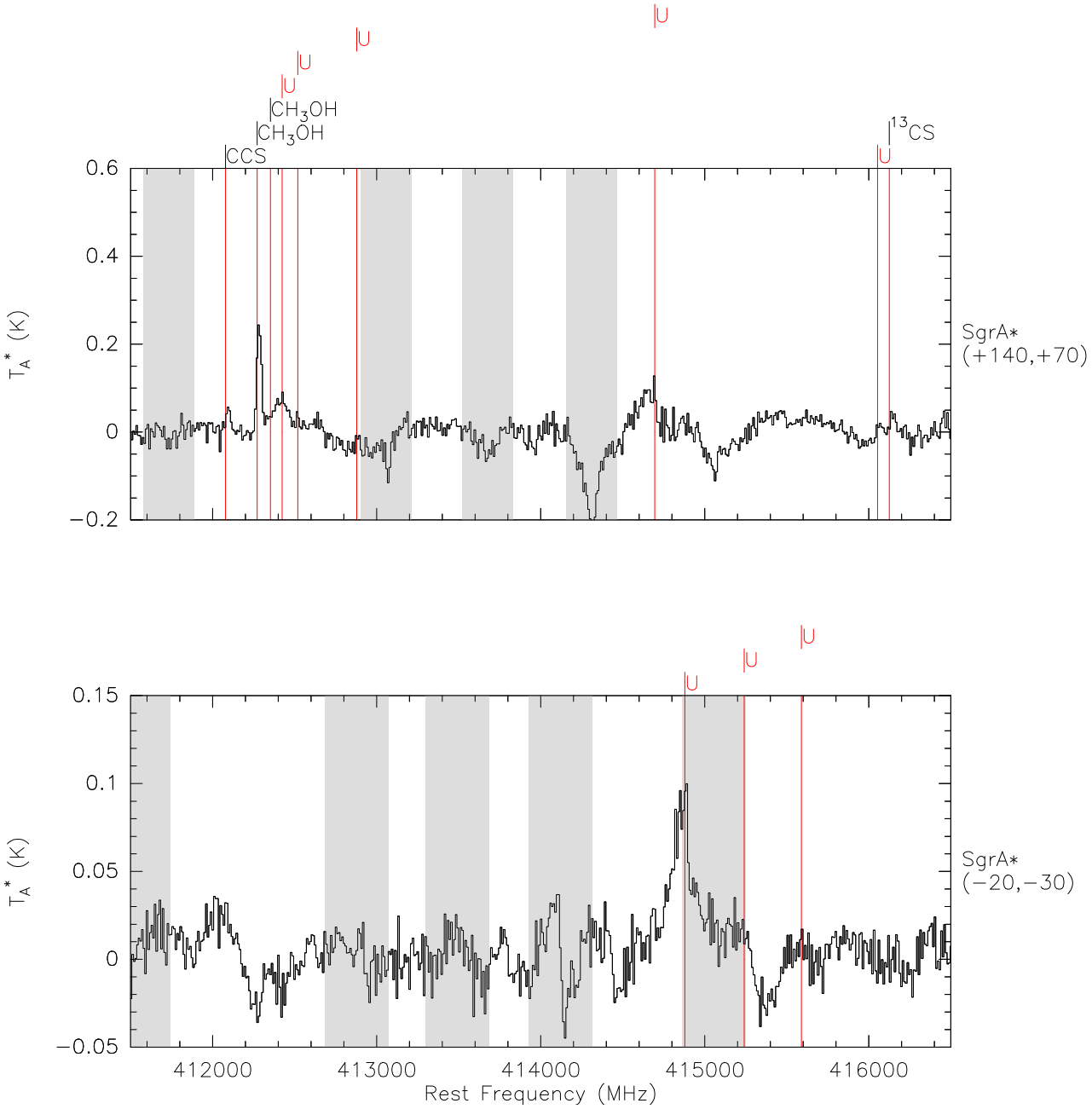

Figure 5.8.31: Reduced survey of SgrA*$(-20, -30)$ (bottom) and SgrA*$(+140, +70)$ (top), composing all subscans from 411500 MHz to 416500 MHz. Astronomical lines are marked by a vertical line that is labeled on top of each spectrum. The area 120 km s^{-1} around atmospheric lines in calibration scans is highlighted in grey. Lines that are "mirrored" from the other sideband are labeled accordingly.

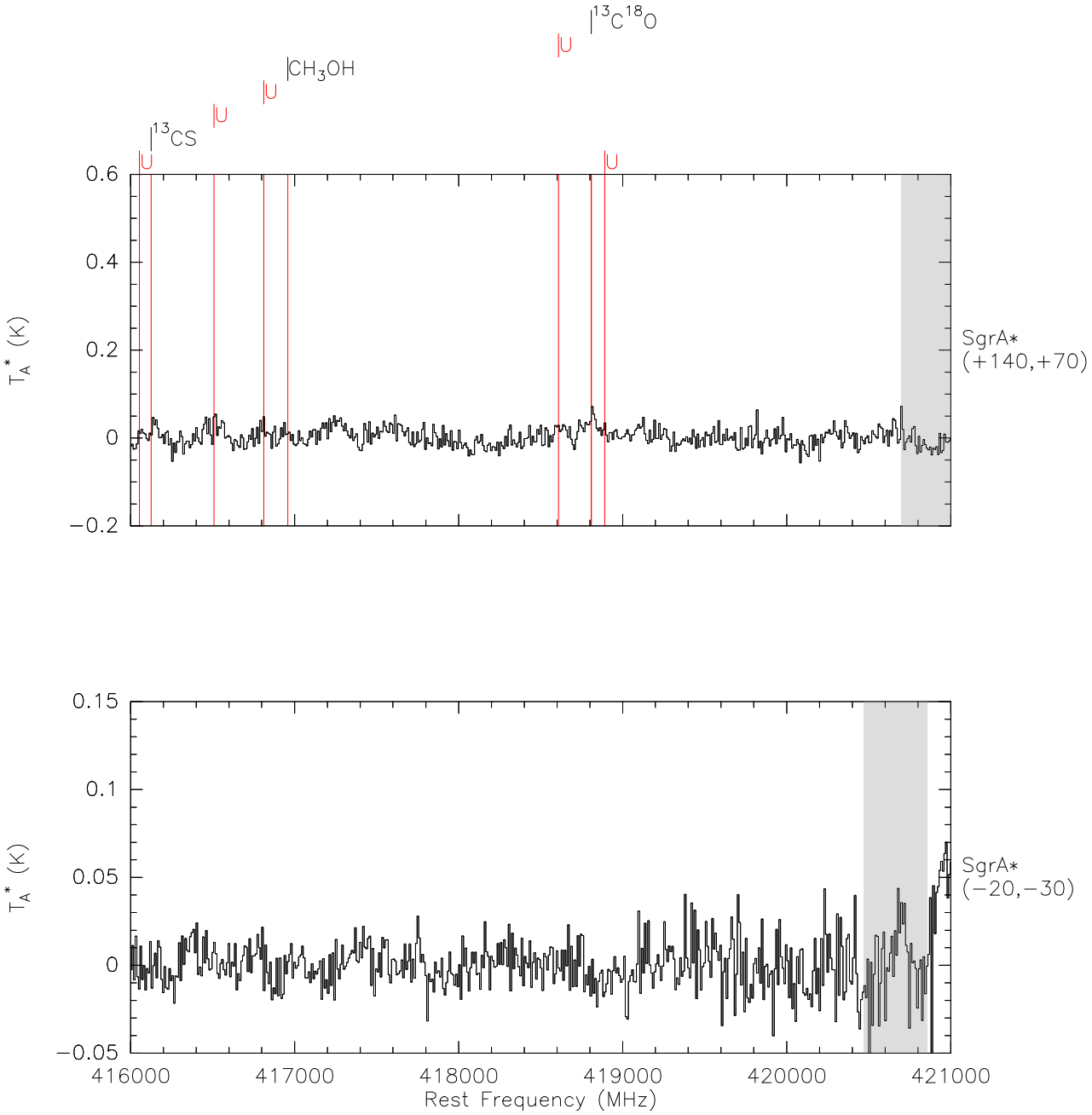

Figure 5.8.32: Reduced survey of SgrA*$(-20, -30)$ (bottom) and SgrA*$(+140, +70)$ (top), composing all subscans from 416000 MHz to 421000 MHz. Astronomical lines are marked by a vertical line that is labeled on top of each spectrum. The area 120 km s^{-1} around atmospheric lines in calibration scans is highlighted in grey. Lines that are "mirrored" from the other sideband are labeled accordingly.

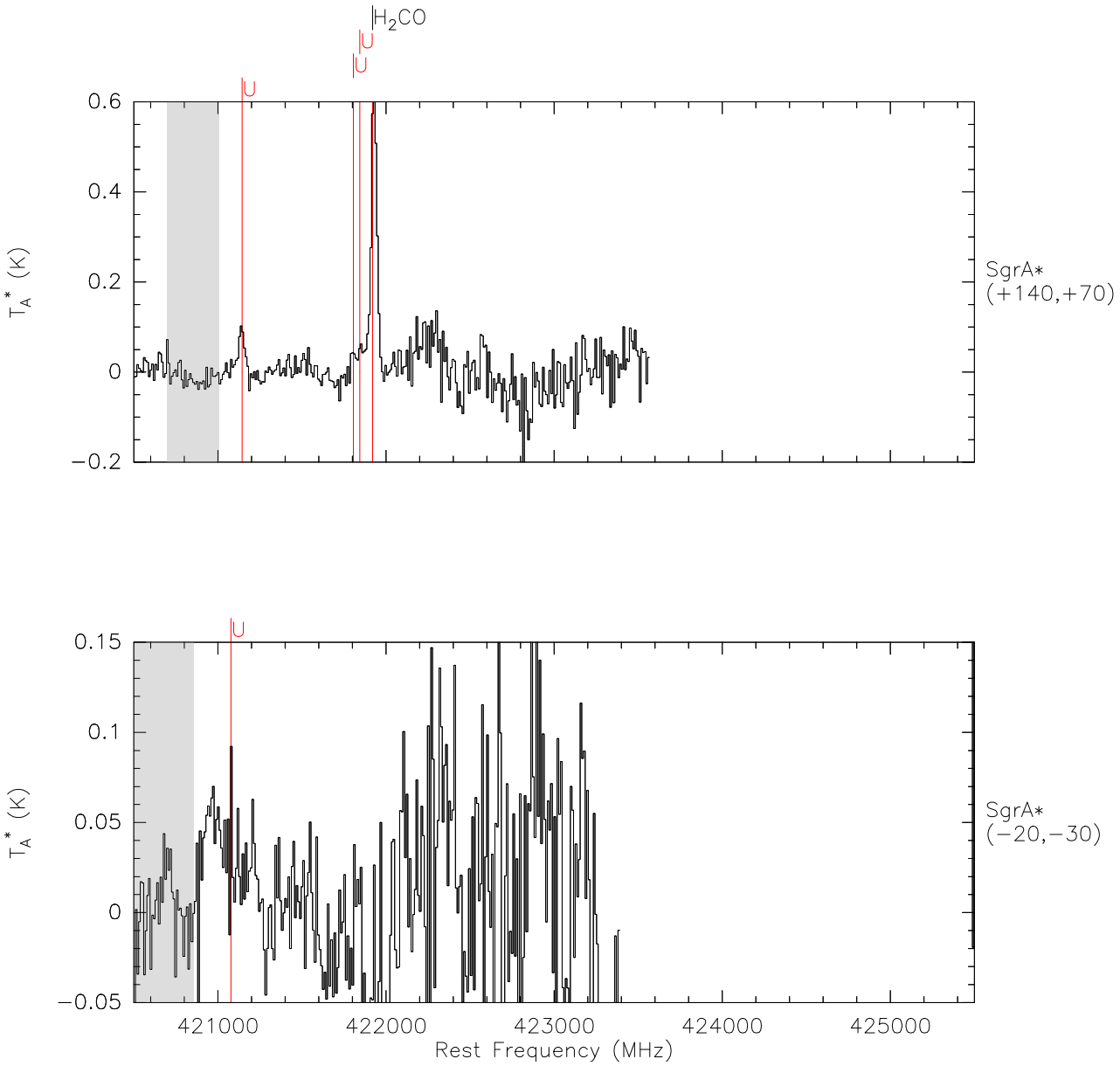

Figure 5.8.33: Reduced survey of SgrA*$(-20, -30)$ (bottom) and SgrA*$(+140, +70)$ (top), composing all subscans from 420500 MHz to 425500 MHz. Astronomical lines are marked by a vertical line that is labeled on top of each spectrum. The area 120 km s^{-1} around atmospheric lines in calibration scans is highlighted in grey. Lines that are "mirrored" from the other sideband are labeled accordingly.

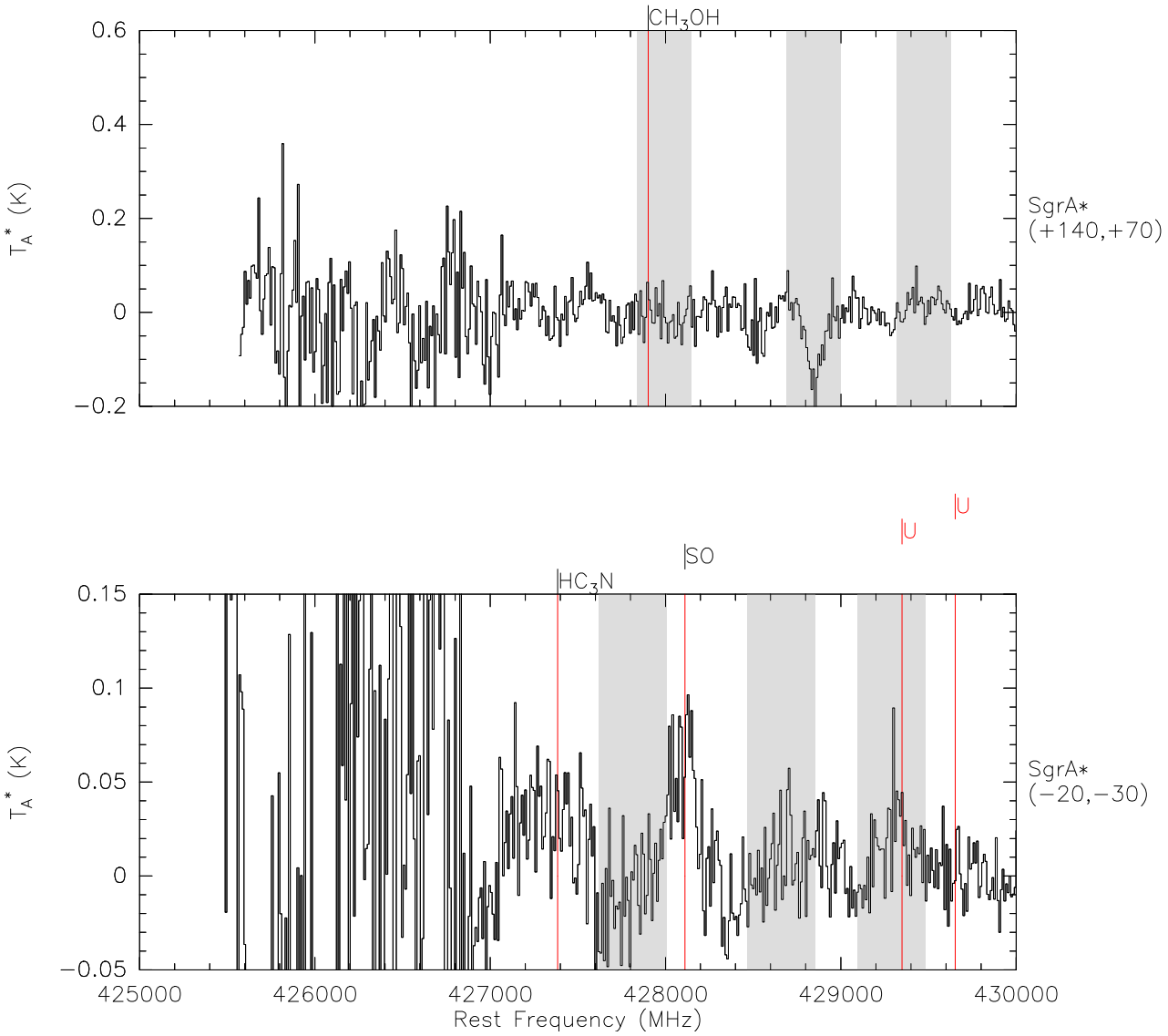

Figure 5.8.34: Reduced survey of SgrA*$(-20, -30)$ (bottom) and SgrA*$(+140, +70)$ (top), composing all subscans from 425000 MHz to 430000 MHz. Astronomical lines are marked by a vertical line that is labeled on top of each spectrum. The area 120 km s^{-1} around atmospheric lines in calibration scans is highlighted in grey. Lines that are "mirrored" from the other sideband are labeled accordingly.

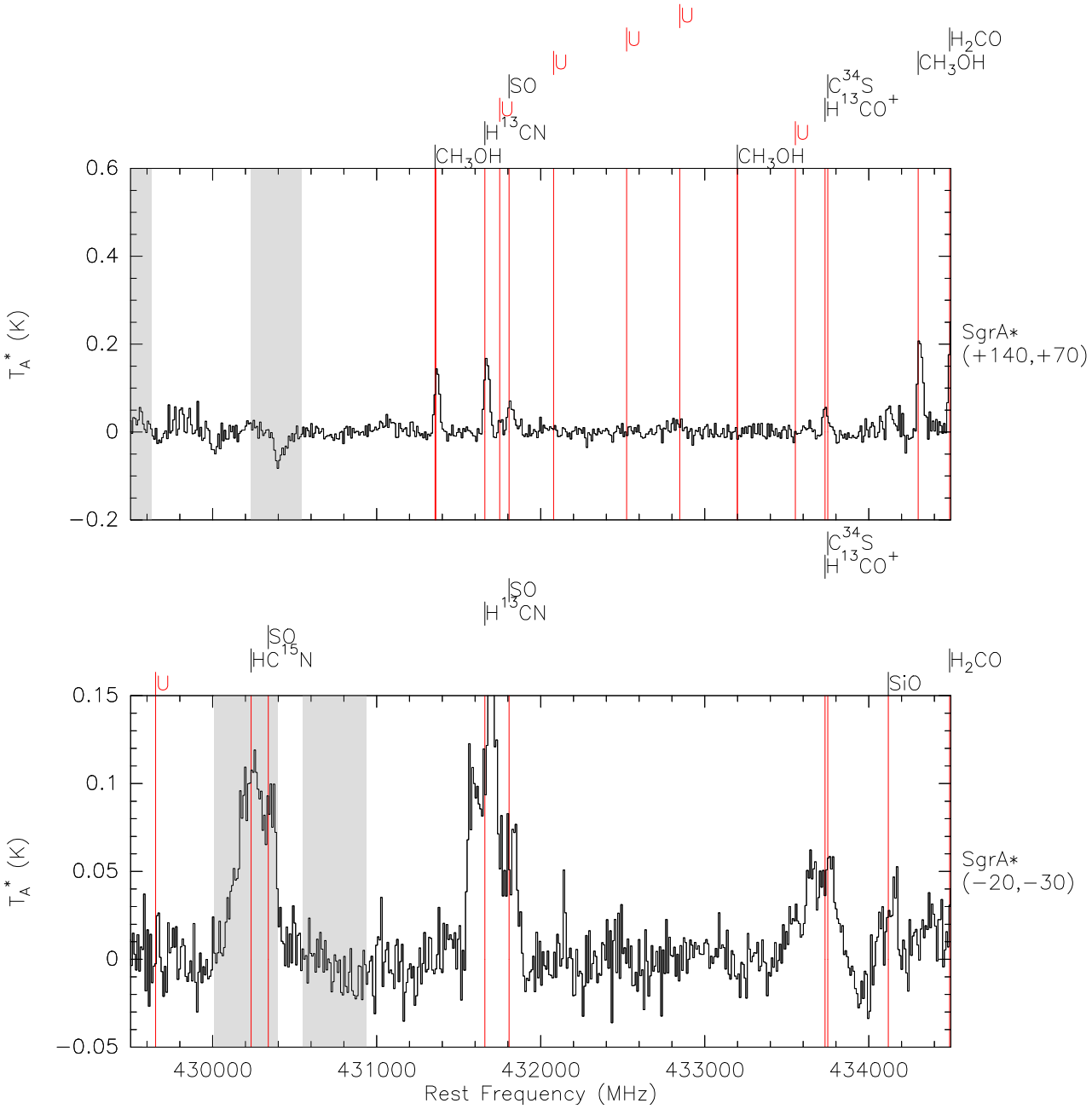

Figure 5.8.35: Reduced survey of SgrA*$(-20, -30)$ (bottom) and SgrA*$(+140, +70)$ (top), composing all subscans from 429500 MHz to 434500 MHz. Astronomical lines are marked by a vertical line that is labeled on top of each spectrum. The area 120 km s^{-1} around atmospheric lines in calibration scans is highlighted in grey. Lines that are "mirrored" from the other sideband are labeled accordingly.

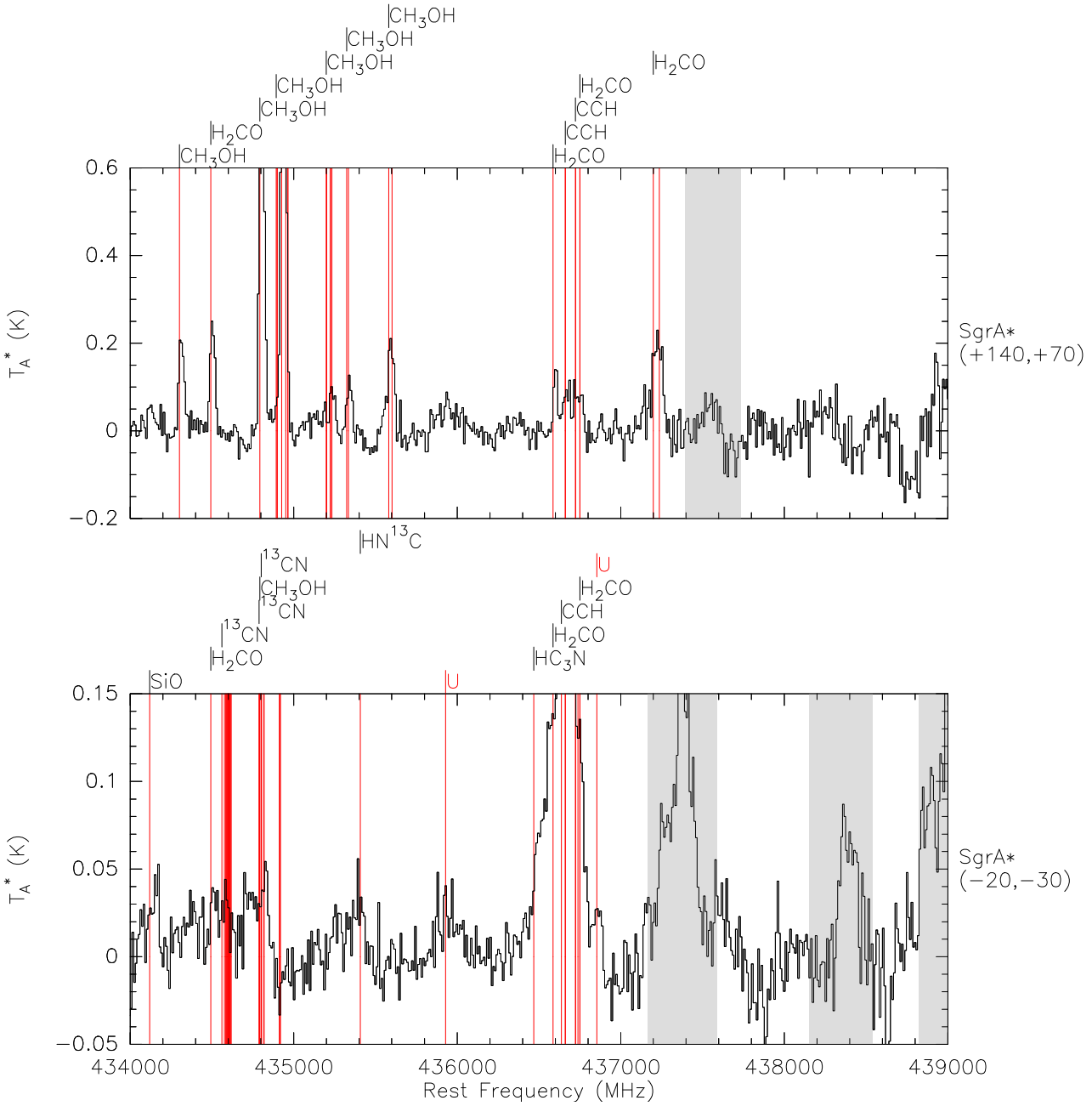

Figure 5.8.36: Reduced survey of SgrA*$(-20, -30)$ (bottom) and SgrA*$(+140, +70)$ (top), composing all subscans from 434000 MHz to 439000 MHz. Astronomical lines are marked by a vertical line that is labeled on top of each spectrum. The area 120 km s^{-1} around atmospheric lines in calibration scans is highlighted in grey. Lines that are "mirrored" from the other sideband are labeled accordingly.

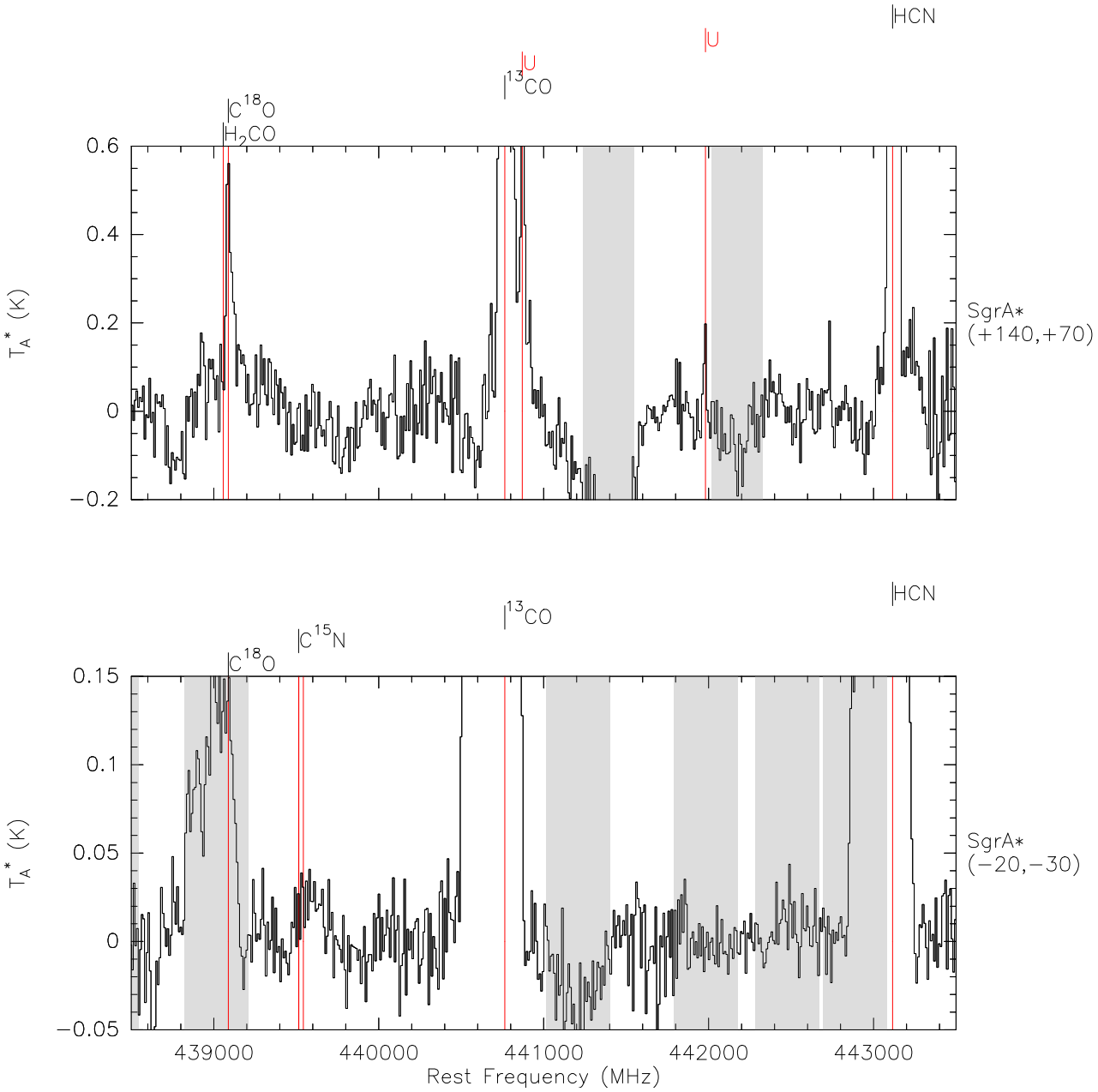

Figure 5.8.37: Reduced survey of SgrA*$(-20, -30)$ (bottom) and SgrA*$(+140, +70)$ (top), composing all subscans from 438500 MHz to 443500 MHz. Astronomical lines are marked by a vertical line that is labeled on top of each spectrum. The area 120 km s^{-1} around atmospheric lines in calibration scans is highlighted in grey. Lines that are "mirrored" from the other sideband are labeled accordingly.

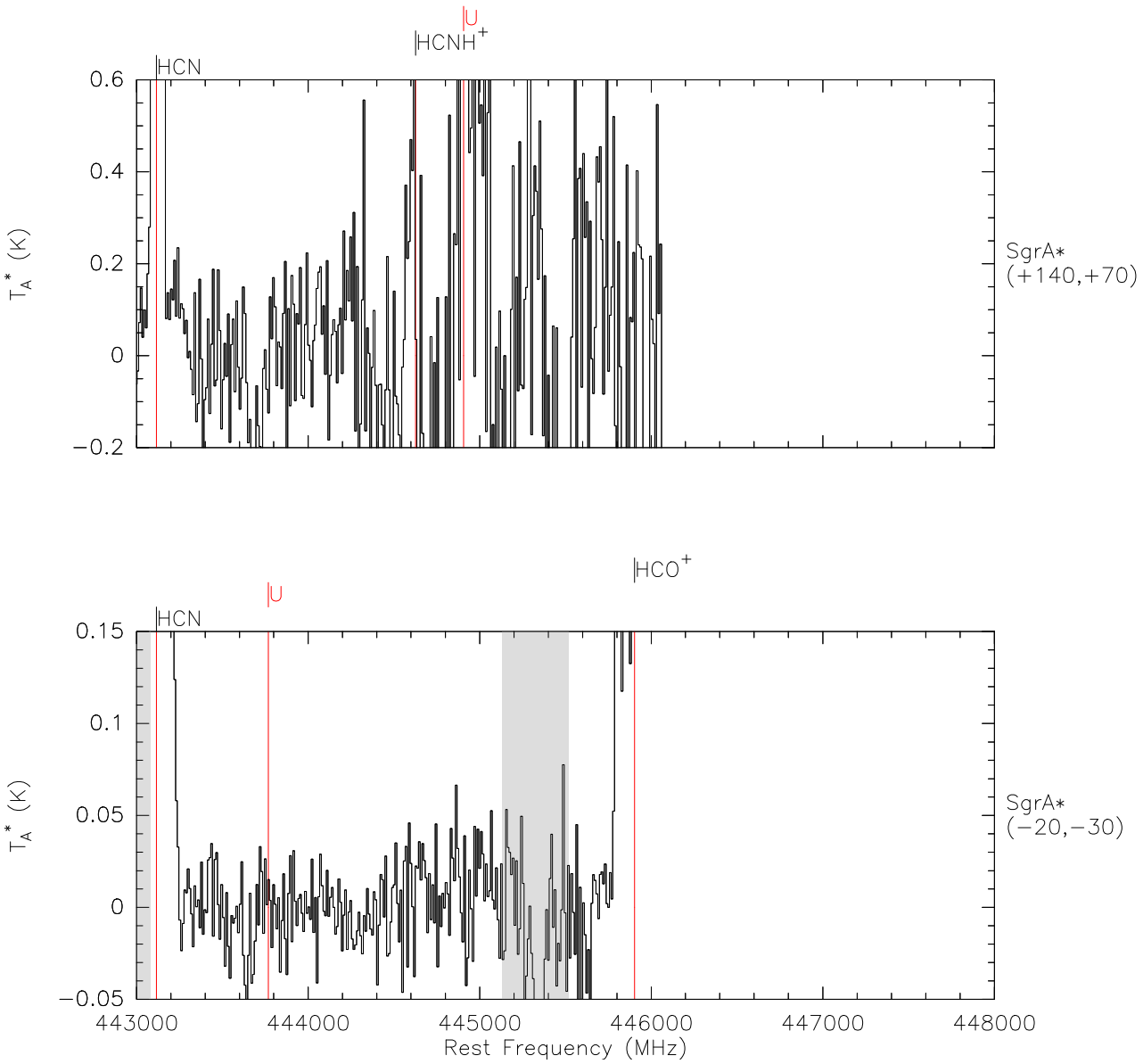

Figure 5.8.38: Reduced survey of SgrA*$(-20,-30)$ (bottom) and SgrA*$(+140,+70)$ (top), composing all subscans from 443000 MHz to 448000 MHz. Astronomical lines are marked by a vertical line that is labeled on top of each spectrum. The area 120 km s^{-1} around atmospheric lines in calibration scans is highlighted in grey. Lines that are "mirrored" from the other sideband are labeled accordingly.

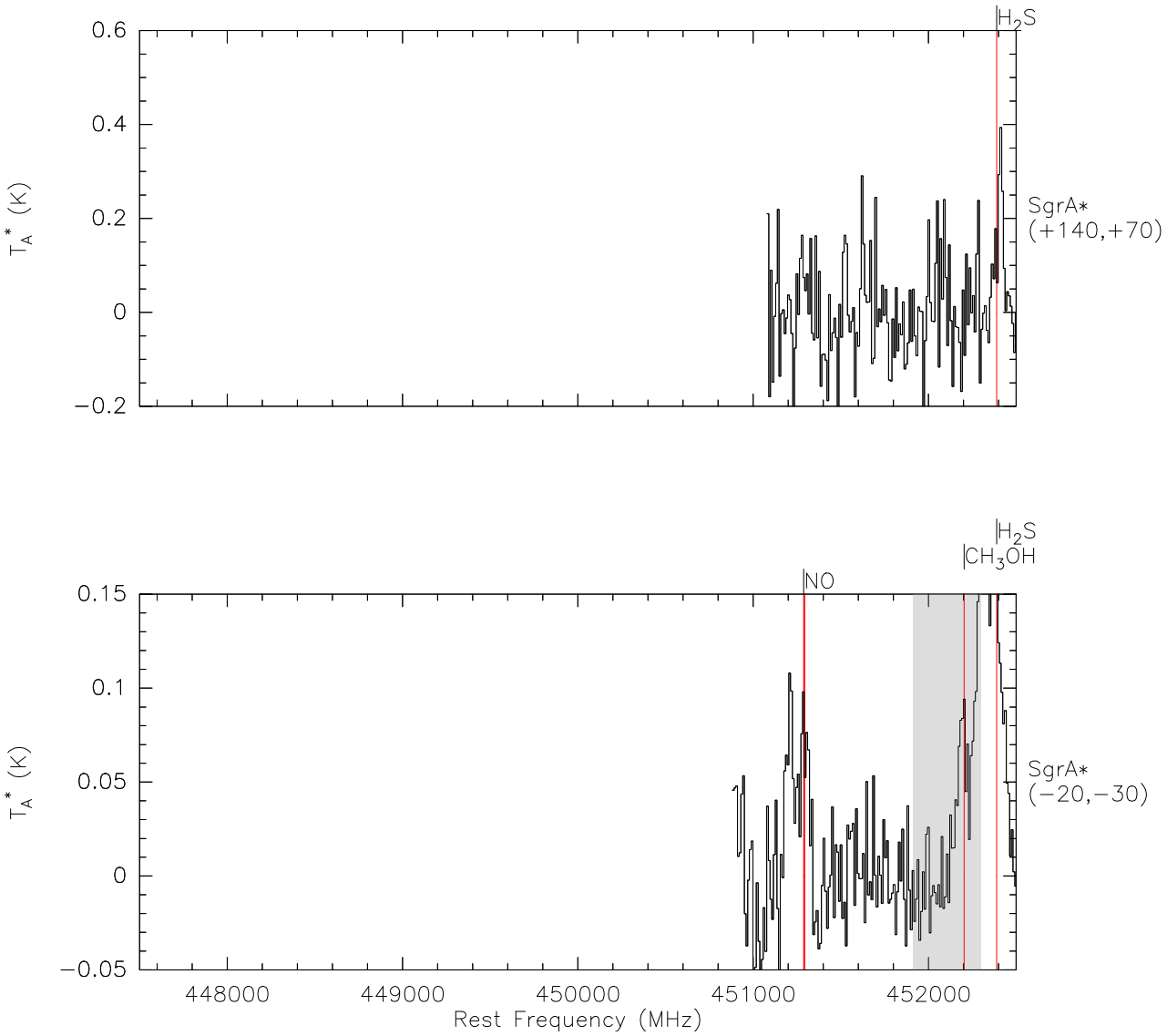

Figure 5.8.39: Reduced survey of SgrA*$(-20, -30)$ (bottom) and SgrA*$(+140, +70)$ (top), composing all subscans from 447500 MHz to 452500 MHz. Astronomical lines are marked by a vertical line that is labeled on top of each spectrum. The area 120 km s^{-1} around atmospheric lines in calibration scans is highlighted in grey. Lines that are "mirrored" from the other sideband are labeled accordingly.

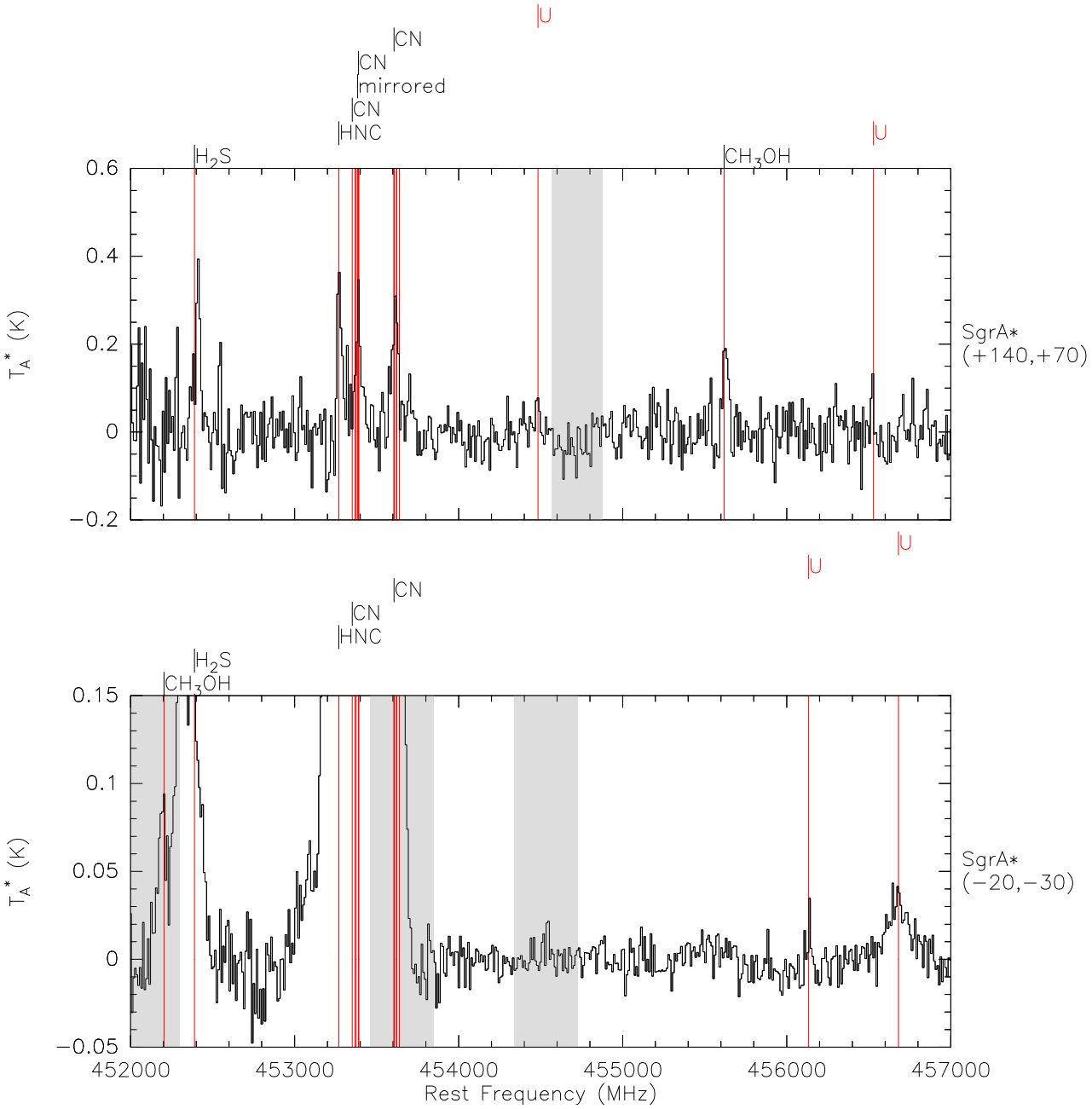

Figure 5.8.40: Reduced survey of SgrA*$(-20,-30)$ (bottom) and SgrA*$(+140,+70)$ (top), composing all subscans from 452000 MHz to 457000 MHz. Astronomical lines are marked by a vertical line that is labeled on top of each spectrum. The area 120 km s^{-1} around atmospheric lines in calibration scans is highlighted in grey. Lines that are "mirrored" from the other sideband are labeled accordingly.

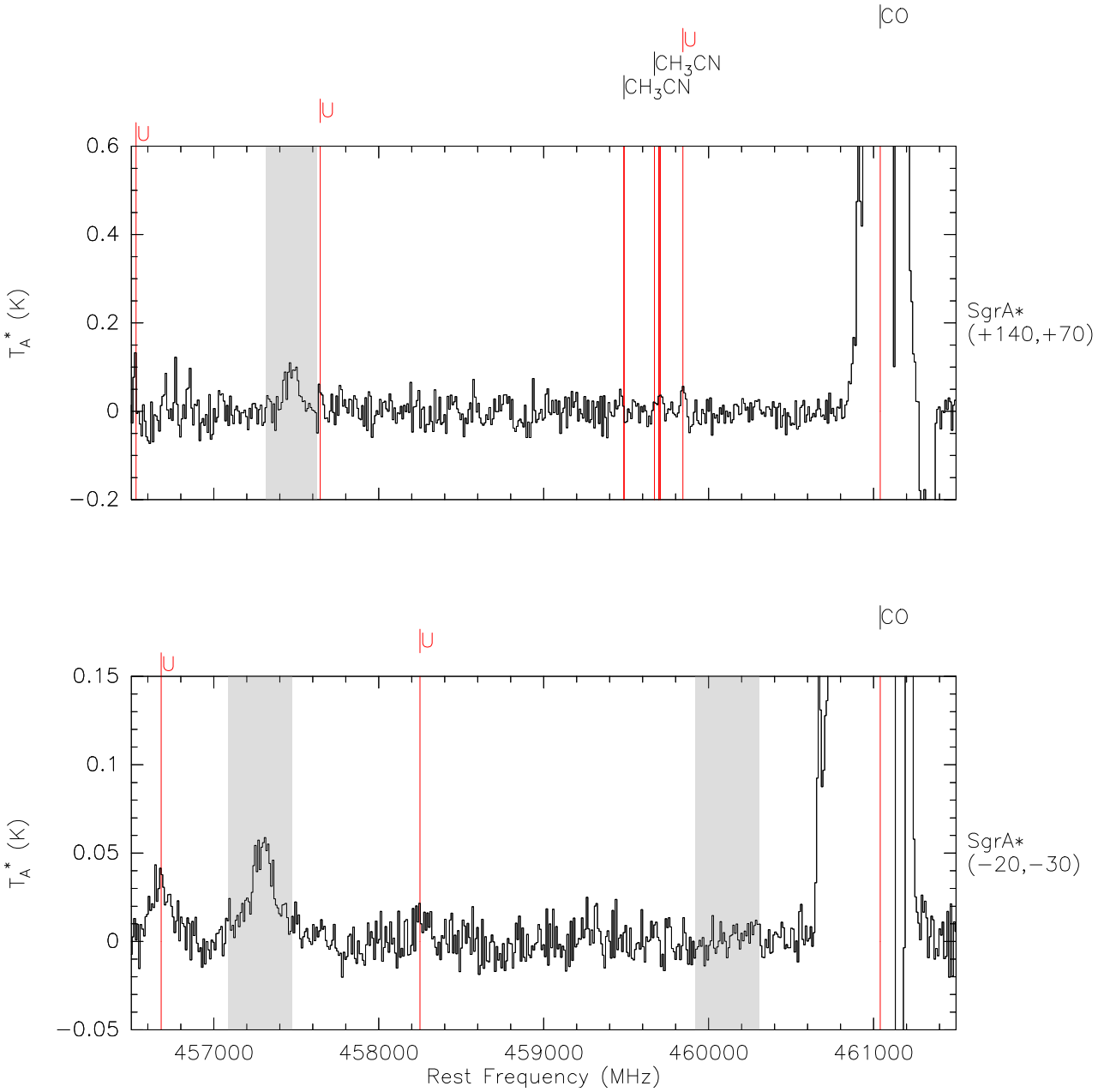

Figure 5.8.41: Reduced survey of SgrA*$(-20,-30)$ (bottom) and SgrA*$(+140,+70)$ (top), composing all subscans from 456500 MHz to 461500 MHz. Astronomical lines are marked by a vertical line that is labeled on top of each spectrum. The area 120 km s^{-1} around atmospheric lines in calibration scans is highlighted in grey. Lines that are "mirrored" from the other sideband are labeled accordingly.

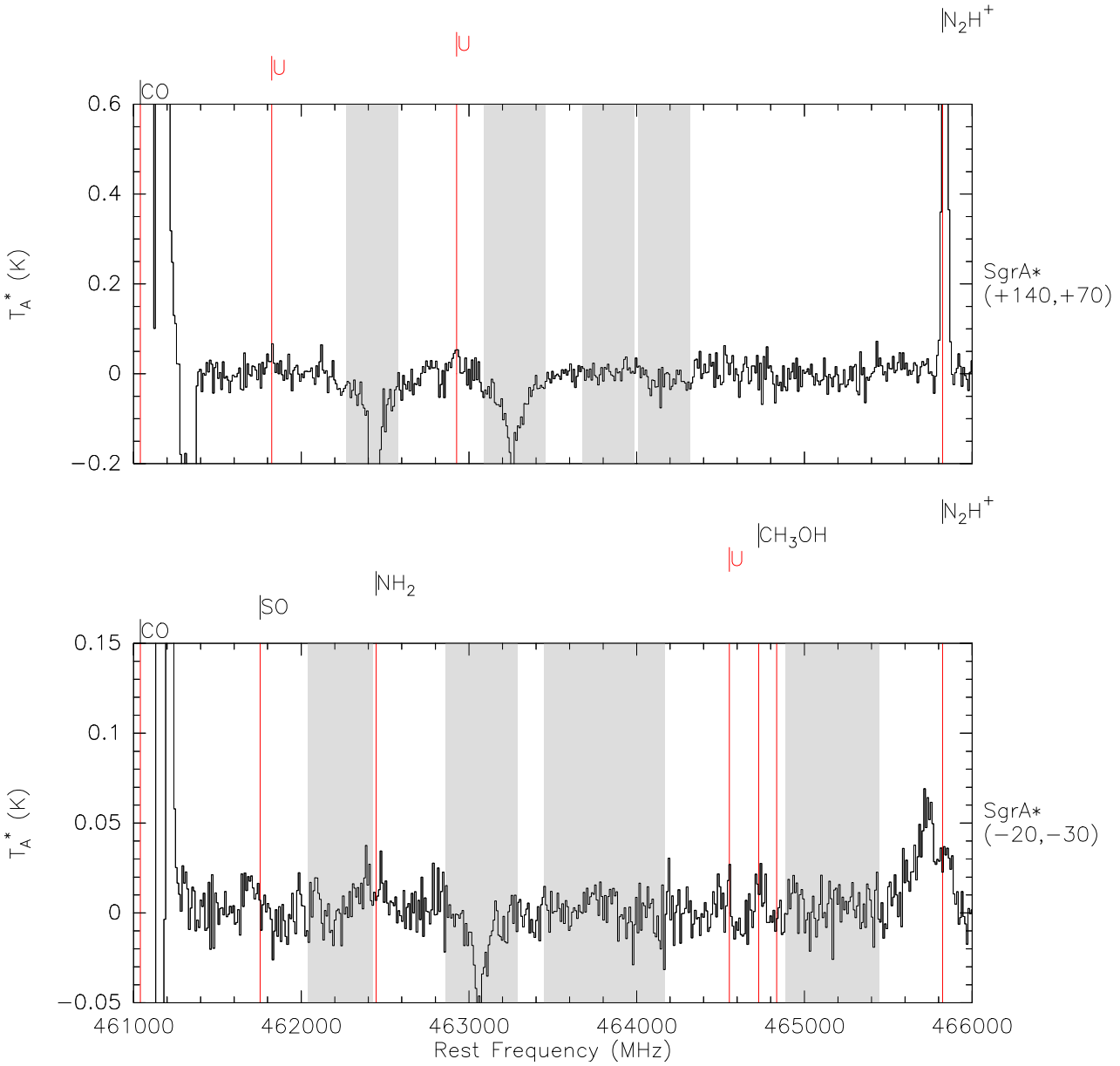

Figure 5.8.42: Reduced survey of SgrA*$(-20,-30)$ (bottom) and SgrA*$(+140,+70)$ (top), composing all subscans from 461000 MHz to 466000 MHz. Astronomical lines are marked by a vertical line that is labeled on top of each spectrum. The area 120 km s^{-1} around atmospheric lines in calibration scans is highlighted in grey. Lines that are "mirrored" from the other sideband are labeled accordingly.

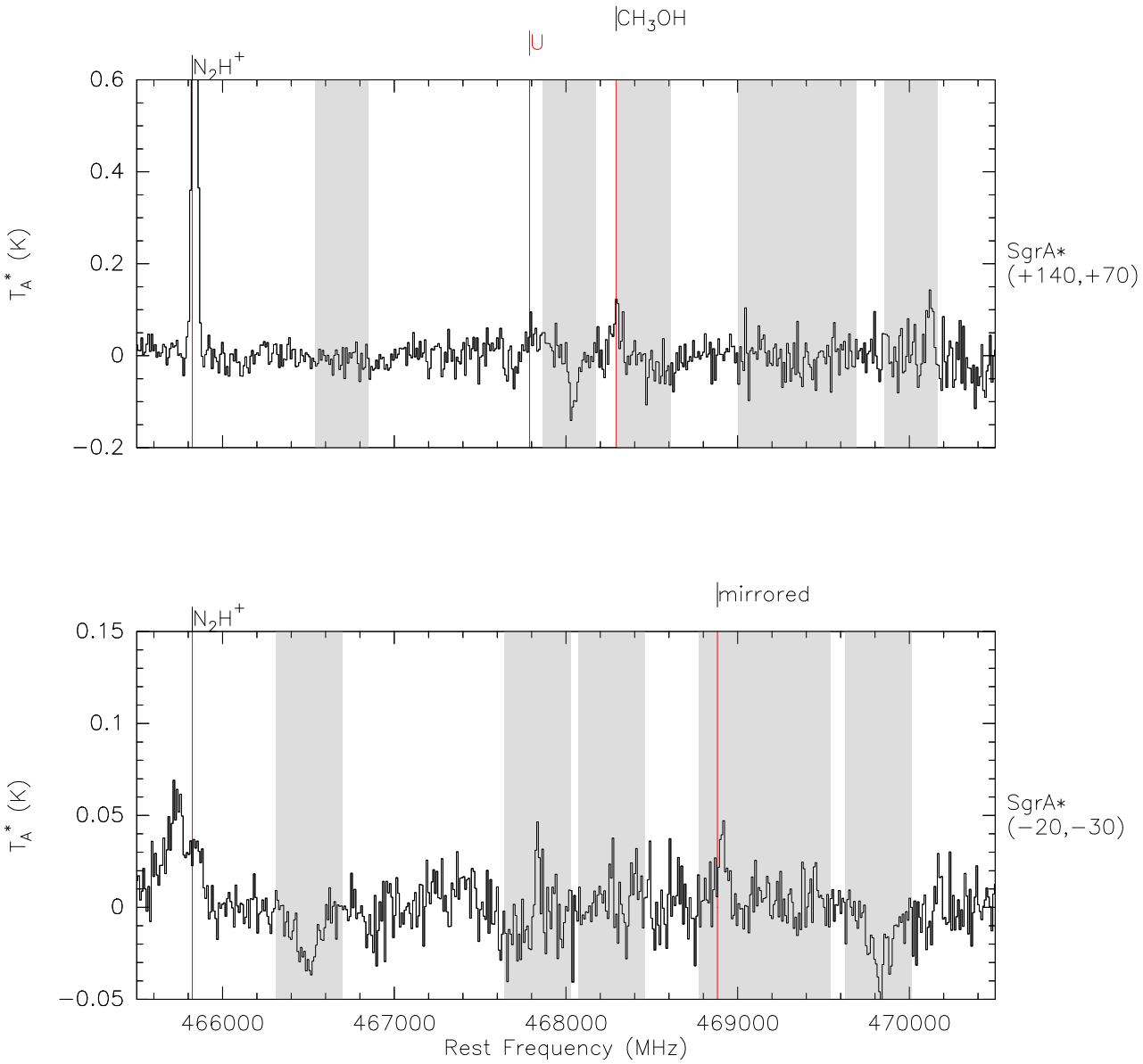

Figure 5.8.43: Reduced survey of SgrA*$(-20, -30)$ (bottom) and SgrA*$(+140, +70)$ (top), composing all subscans from 465500 MHz to 470500 MHz. Astronomical lines are marked by a vertical line that is labeled on top of each spectrum. The area 120 km s^{-1} around atmospheric lines in calibration scans is highlighted in grey. Lines that are "mirrored" from the other sideband are labeled accordingly.

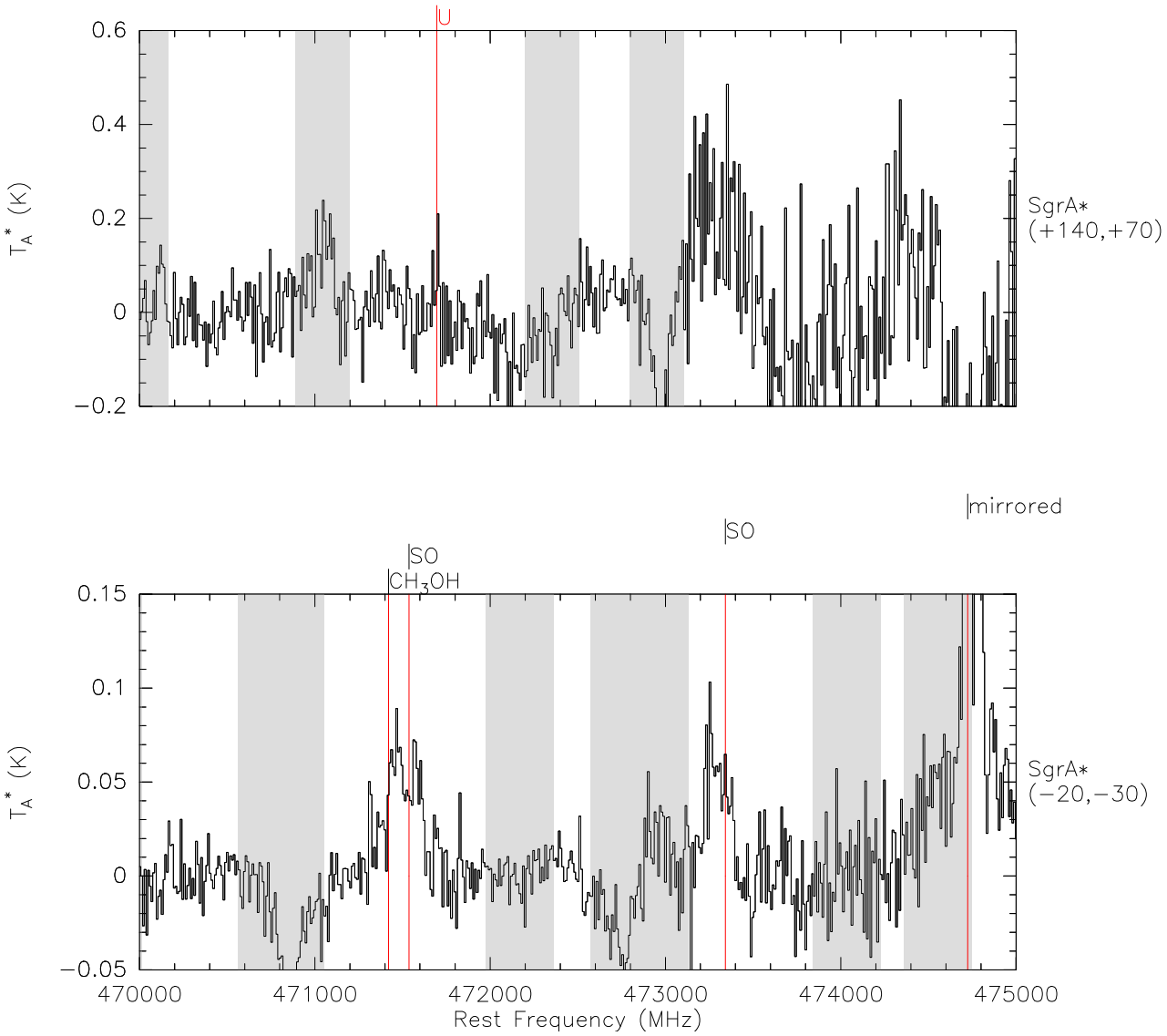

Figure 5.8.44: Reduced survey of SgrA*$(-20, -30)$ (bottom) and SgrA*$(+140, +70)$ (top), composing all subscans from 470000 MHz to 475000 MHz. Astronomical lines are marked by a vertical line that is labeled on top of each spectrum. The area 120 km s^{-1} around atmospheric lines in calibration scans is highlighted in grey. Lines that are "mirrored" from the other sideband are labeled accordingly.

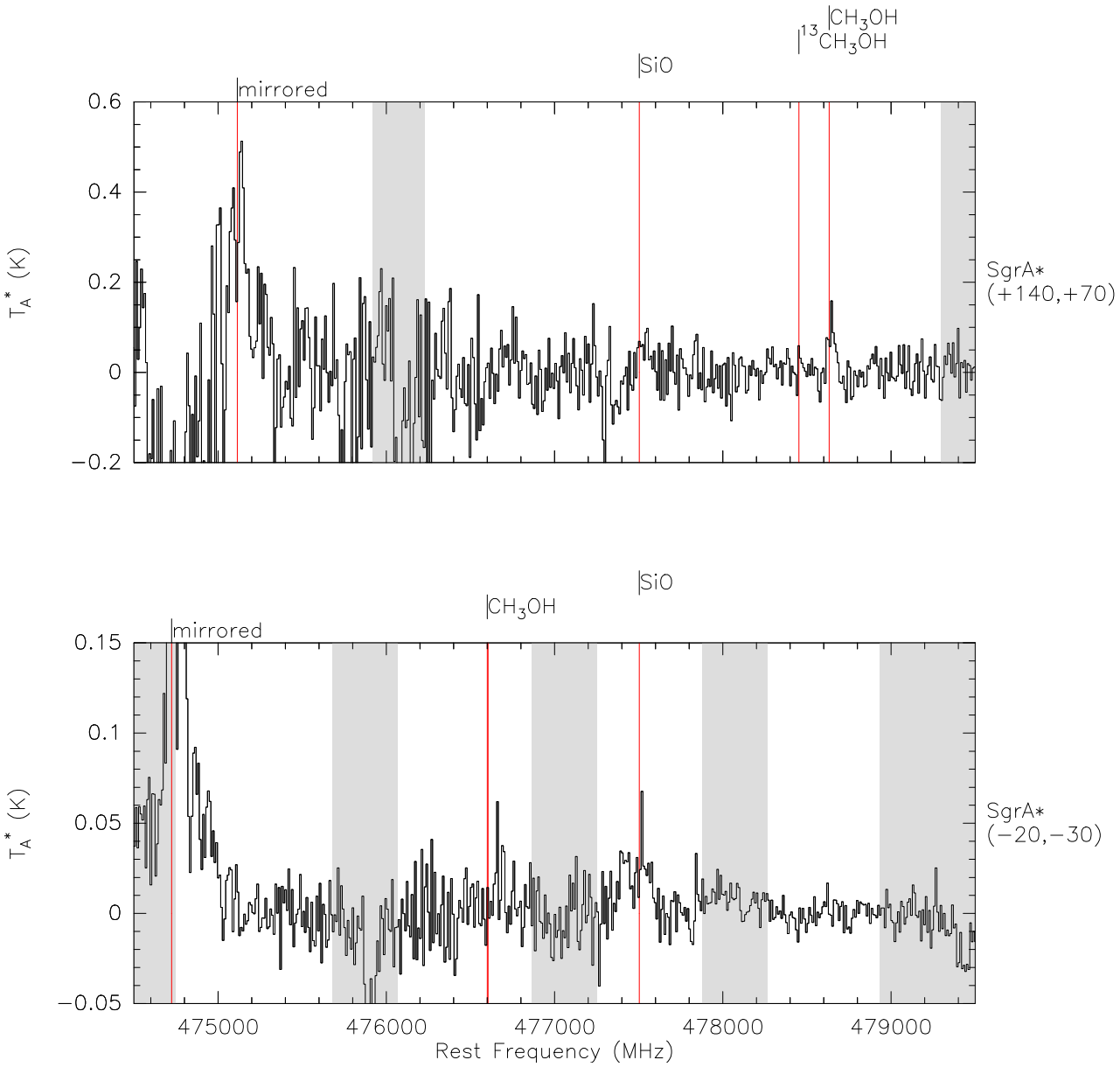

Figure 5.8.45: Reduced survey of SgrA*$(-20, -30)$ (bottom) and SgrA*$(+140, +70)$ (top), composing all subscans from 474500 MHz to 479500 MHz. Astronomical lines are marked by a vertical line that is labeled on top of each spectrum. The area 120 km s^{-1} around atmospheric lines in calibration scans is highlighted in grey. Lines that are "mirrored" from the other sideband are labeled accordingly.

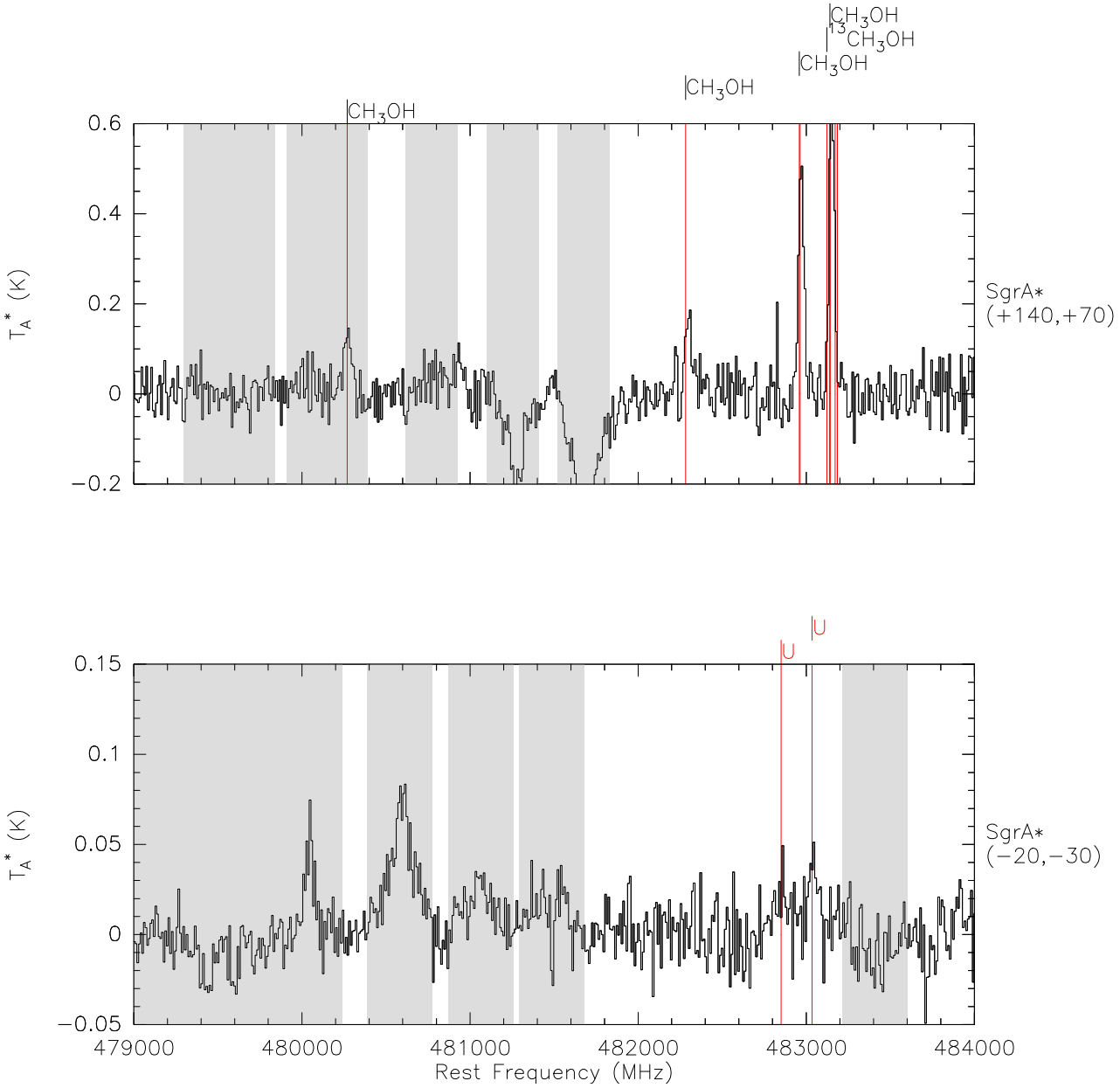

Figure 5.8.46: Reduced survey of SgrA*$(-20, -30)$ (bottom) and SgrA*$(+140, +70)$ (top), composing all subscans from 479000 MHz to 484000 MHz. Astronomical lines are marked by a vertical line that is labeled on top of each spectrum. The area 120 km s^{-1} around atmospheric lines in calibration scans is highlighted in grey. Lines that are "mirrored" from the other sideband are labeled accordingly.

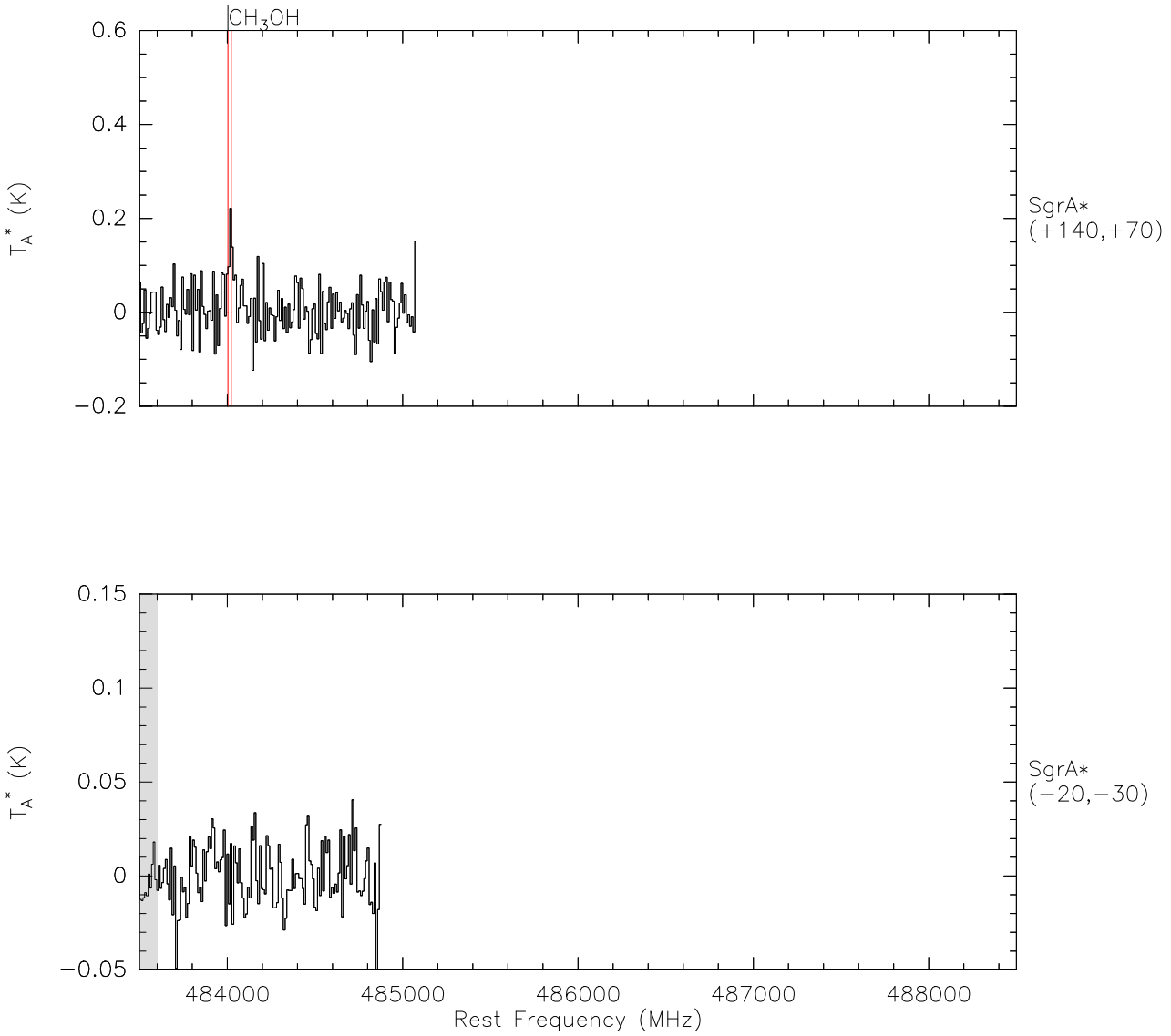

Figure 5.8.47: Reduced survey of SgrA*$(-20, -30)$ (bottom) and SgrA*$(+140, +70)$ (top), composing all subscans from 483500 MHz to 488500 MHz. Astronomical lines are marked by a vertical line that is labeled on top of each spectrum. The area 120 km s^{-1} around atmospheric lines in calibration scans is highlighted in grey. Lines that are "mirrored" from the other sideband are labeled accordingly.

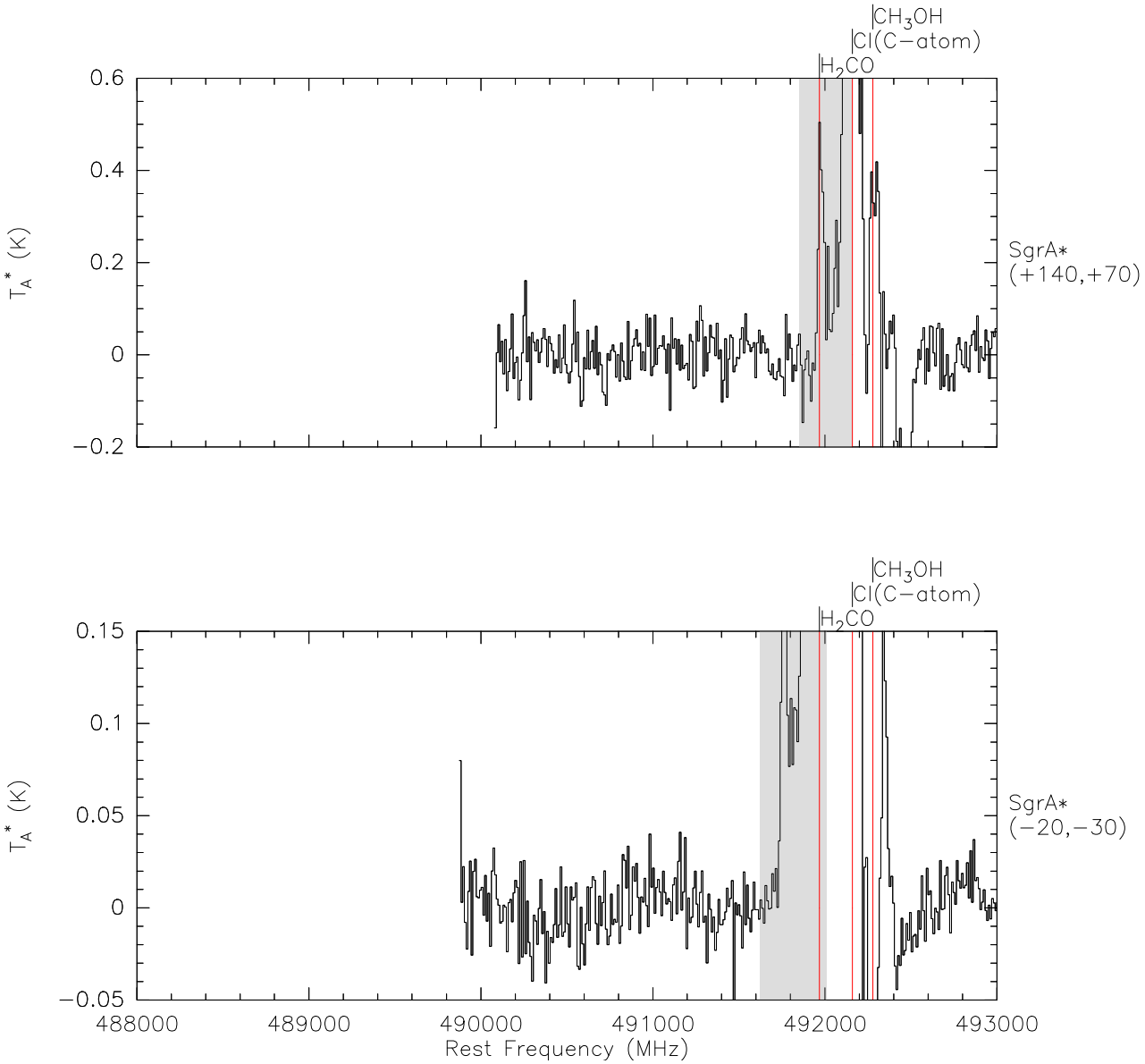

Figure 5.8.48: Reduced survey of SgrA*$(-20, -30)$ (bottom) and SgrA*$(+140, +70)$ (top), composing all subscans from 488000 MHz to 493000 MHz. Astronomical lines are marked by a vertical line that is labeled on top of each spectrum. The area 120 km s^{-1} around atmospheric lines in calibration scans is highlighted in grey. Lines that are "mirrored" from the other sideband are labeled accordingly.

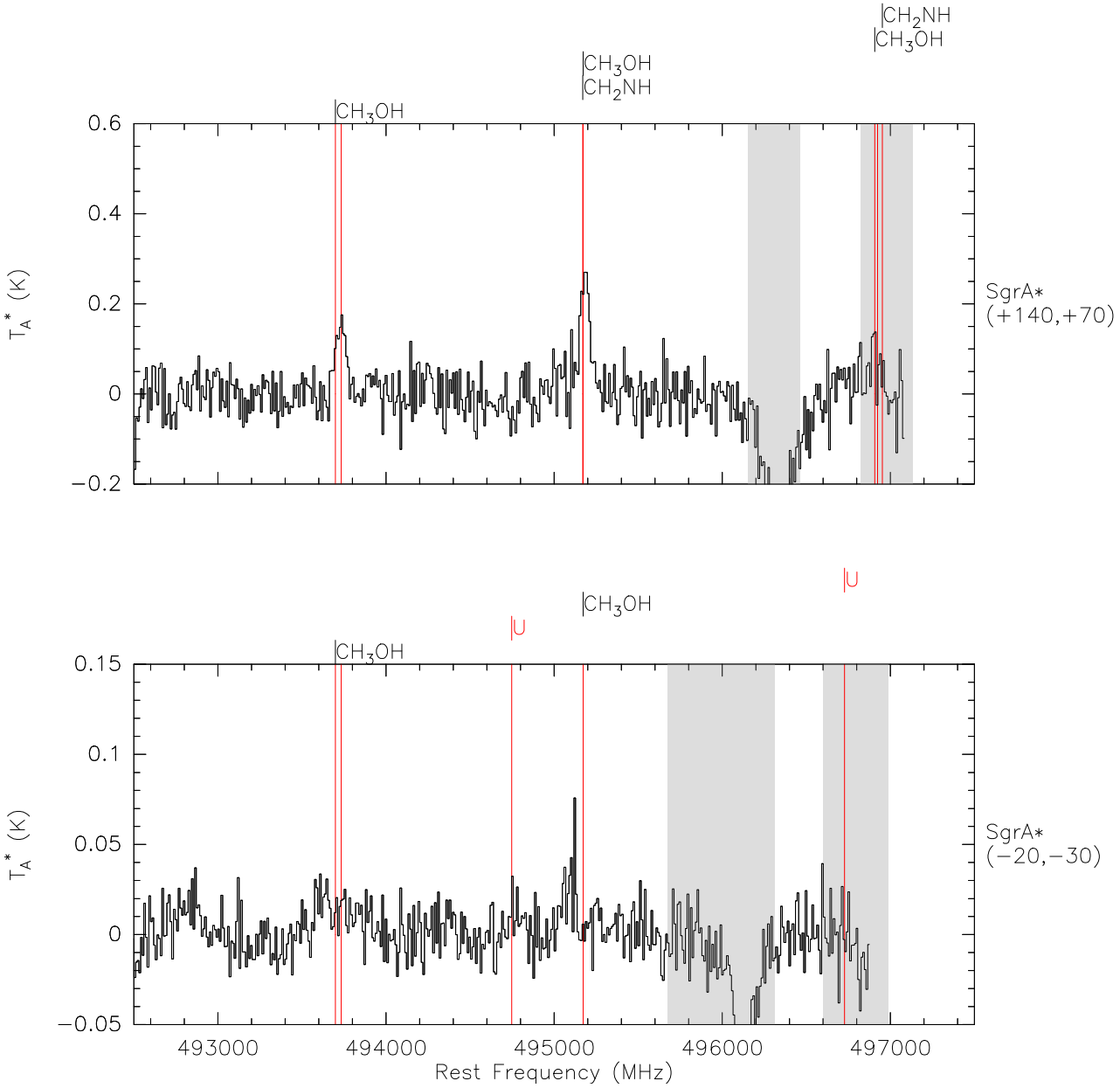

Figure 5.8.49: Reduced survey of SgrA*$(-20,-30)$ (bottom) and SgrA*$(+140,+70)$ (top), composing all subscans from 492500 MHz to 497500 MHz. Astronomical lines are marked by a vertical line that is labeled on top of each spectrum. The area 120 km s^{-1} around atmospheric lines in calibration scans is highlighted in grey. Lines that are "mirrored" from the other sideband are labeled accordingly.

5.5 Line intensity

To perform further analysis, the intensity of the identified spectral lines must be determined. Since spectra from multiple scans may cover the same line, all of them are averaged. Using **set weight sigma** weights them according to their standard deviation σ, which has been determined during baseline subtraction. The intensity is given by the main beam temperature integrated over the frequency range of the line. With respect to an extended velocity range for some species, the range is adjusted for each line individually, starting with assumptions for the line width, that are similar to those from chapter 5.3. This standard integration range was $v_\delta = [-145, +35]\,\mathrm{km\,s^{-1}}$ for SgrA*$(-20, -30)$ and $v_\delta = [+15, +75]\,\mathrm{km\,s^{-1}}$ for SgrA*$(+140, +70)$. If a line is blended with another line and can't be distinguished by frequency range, the standard range is used and the line is marked accordingly. Therefore, the intensity of lines that are marked as blended are probably exaggerated. Using (2.91) allows to calculate a standard deviation σ_{avg} of the averaged spectrum with respect to its spectral channels. An error margin for the line intensity depends on σ_{avg} and decreases with the square root of the line width (compare chapter 2.8). However, additional error of up to 10 % among different frequencies of the survey, due to uncertainties of the calibration process of single spectra, has to be added quadratically.

The integrated antenna temperature, which can be derived from the spectrum by **print area**, must be converted to the main beam brightness temperature [85, Ch. 8.2.5]:

$$T_{\mathrm{MB}} = T_{\mathrm{A}}^{*} \cdot \frac{F_{\mathrm{eff}}}{B_{\mathrm{eff}}} \tag{5.3}$$

The forward efficiency $F_{\mathrm{eff}} = 0.95$ is a fixed value for the receiver and is already considered in the spectra. The frequency dependent beam efficiency $B_{\mathrm{eff}}\,(f)$ can be calculated by Ruze's equation [43, Ch. 5.1.22]:

$$B_{\mathrm{eff}}\,(f) = B_0 \cdot e^{-\left(\frac{4\pi\sigma_{\mathrm{ant}} f}{c}\right)^2} \tag{5.4}$$

The gain of the perfect antenna B_0 and the root-mean-square (RMS) deviation σ_{ant} of the surface from a perfect parabola are derived from other APEX observations in June 2012. It was $B_0 \approx 0.752$ for FLASH-345, $B_0 \approx 0.697$ for FLASH-460, and $\sigma_{\mathrm{ant}} \approx 20\,\mu\mathrm{m}$ for both receivers. With respect to the averaged spectra, B_{eff} is calculated for each line individually. The intensity and its error margin are scaled accordingly.

Table 5.2 and table 5.3 present the results of this procedure: intensities of all identified lines including error margins. Additionally, table 5.4 presents the accumulated intensities of each species to provide an overview of their relevance in the source.

Table 5.2: Integrated intensity of the identified lines from SgrA*$(-20, -30)$.

species	f (MHz)	transition	E_L (K)	$\int T_{MB}\,dv$ (K km s^{-1})	$\Delta\int T_{MB}\,dv$ (K km s^{-1})	note
H_2CS	270522	8(1,8)-7(1,7)	59	0.83	0.02	
HNC	271981	J=3-2	13	80.02	0.01	
HC_3N	272885	J=30-29	190	2.16	0.01	
CH_3CCH	273355	16(K)-15(K),K=0,1,2,3,4,5	>98	1.15	0.01	
H_2CS	274703	8(2,7)-7(2,6)	99	2.33	0.01	
CH_3CN	275651	15(K)-14(K),K=6,7,8	>350	2.18	0.01	
CH_3CN	275849	15(K)-14(K),K=0,1,2,3,4,5	>92	2.85	0.01	
^{13}CS	277455	6-5	33	5.11	0.01	
CH_3OH	278305	9(-1,9)-8(0,8)	97	1.19	0.01	
H_2CS	278888	8(1,7)-7(1,6)	60	1.03	0.01	
N_2H^+	279512	J=3-2	13	4.97	0.02	
H_2CO	281527	4(1,4)-3(1,3)	32	27.62	0.01	
HC_3N	281977	J=31-30	203	3.03	0.01	
H	282333	H(35)β	0	1.10	0.01	
H	284251	H(28)α	0	5.59	0.01	
$C^{34}S$	289209	6-5	24	9.18	0.02	
CH_3OH	289939	6(0,6)-5(0,5)	48	6.67	0.01	1
CH_3OH	290130	6(K_a,K_c+1)-5(K_a,K_c)	>35	15.09	0.01	
CH_3CCH	290458	17(K)-16(K),K=0,1,2,3,4	>112	2.13	0.01	
H_2CO	290623	4(0,4)-3(0,3)	21	6.57	0.02	
H_2CO	291238	4(2,3)-3(2,2)	68	3.60	0.01	
H_2CO	291382	4(3,K_c+1)-3(3,K_c),K_c=0,1	>127	9.52	0.01	
H_2CO	291948	4(2,2)-3(2,1)	68	3.69	0.01	
CH_3OH	292673	6(1,5)-5(1,4)–	50	0.18	0.01	
CS	293912	6-5	35	159.45	0.01	
CH_3CN	294232	16(K)-15(K),K=0,1,2,3,4,5	>106	0.36	0.01	
SO	295356	9(10)-9(9)	106	0.73	0.02	
SO	296550	6(7)-5(6)	51	14.31	0.01	2
^{30}SiO	296576	7-6	43	13.88	0.02	2
HCS^+	298690	7-6	43	2.09	0.01	
NS	299700	J=13/2-11/2,Ω=1/2,l=e	>40	1.92	0.01	
NS	300098	J=13/2-11/2,Ω=1/2,l=f	>40	4.59	0.01	2
^{29}SiO	300120	7-6	43	4.86	0.01	2
HC_3N	300160	J=33-32	231	3.97	0.01	1
H_2CO	300837	4(1,3)-3(1,2)	33	19.66	0.01	
SO	301286	7(7)-6(6)	56	15.40	0.02	

Table 5.2 (continued): Integrated intensity of the identified lines from SgrA*$(-20, -30)$.

species	f (MHz)	transition	E_L (K)	$\int T_{MB}\,dv$ (K km s^{-1})	$\Delta\int T_{MB}\,dv$ (K km s^{-1})	note
CH_3OH	302370	3(0,3)-2(-1,2)	13	2.19	0.01	
CH_3OH	303367	1(1,0)-1(0,1)-+	2	4.36	0.01	
SiO	303927	7-6	44	15.50	0.01	
SO	304078	8(7)-7(6)	48	21.43	0.01	
CH_3OH	304208	2(1,1)-2(0,2)-+	7	5.38	0.01	
CH_3OH	305474	3(1,2)-3(0,3)-+	14	6.00	0.01	
CH_3OH	307166	4(1,3)-4(0,4)-+	23	3.18	0.02	
H	307258	H(34)β	0	1.28	0.02	
HC_3N	309250	J=34-33	245	4.88	0.01	2
CH_3OH	309290	5(1,4)-5(0,5)-+	35	5.06	0.01	2
SO	309502	2(2)-2(1)	4	0.77	0.01	
CH_3OH	310193	3(1,2)-2(0,2)	20	2.55	0.01	
CH_3OH	311853	6(1,5)-6(0,6)-+	49	3.54	0.01	
CH_3CN	312613	17(K)-16(K),K=0,1,2,3,4,5	> 120	2.77	0.01	
CH_3OH	313597	7(1,6)-6(2,4)	71	0.64	0.01	
H_2CS	313717	9(1,8)-8(1,7)	73	1.19	0.01	
CH_3OH	314860	7(1,6)-7(0,7)-+	65	3.06	0.01	
mirrored	315250	330587.96875	0	6.44	0.01	2
CH_3OH	315267	6(2,4)-5(1,4)	56	4.72	0.01	2
H	316415	H(27)α	0	4.74	0.02	
CH_3OH	318319	8(1,7)-8(0,8)-+	84	4.67	0.01	2
HC_3N	318341	J=35-34	260	4.53	0.01	2
mirrored	321249	330587.96875	0	3.52	0.01	
^{13}CS	323685	7-6	47	6.12	0.04	
^{13}CN	325938	N=3-2,J=5/2-3/2	> 16	5.06	0.02	
^{13}CN	326139	N=3-2,J=7/2-5/2	> 16	5.72	0.03	
$C^{18}O$	329331	3-2	16	41.80	0.02	
SO	329385	1(2)-0(1)	0	17.21	0.02	1
^{13}CO	330588	3-2	16	428.87	0.01	
CH_3OH	335582	7(1,7)-6(1,6)++	63	0.82	0.02	
mirrored	336033	345796.00000	0	30.34	0.01	
HC_3N	336520	J=37-36	291	1.60	0.01	2
SO	336554	10(11)-10(10)	127	1.67	0.01	2
CH_3OH	336865	12(1,11)-12(0,12)-+	181	3.35	0.01	1
$C^{17}O$	337061	J=3-2	> 16	11.08	0.01	
$C^{34}S$	337396	7-6	34	6.18	0.01	

Table 5.2 (continued): Integrated intensity of the identified lines from SgrA*$(-20, -30)$.

species	f (MHz)	transition	E_L (K)	$\int T_{MB}\,dv$ (K km s^{-1})	$\Delta\int T_{MB}\,dv$ (K km s^{-1})	note
H_2CS	338083	10(1,10)-9(1,9)	86	3.94	0.01	2
CH_3OH	338125	7(0,7)-6(0,6)	62	4.12	0.01	2
CH_3OH	338345	7(-1,7)-6(-1,6)	54	6.40	0.02	
CH_3OH	338474	7(K_a,K_c+1)-6(K_a,K_c)	>49	8.67	0.01	
CH_3OH	338641	7(K_a,K_c+1)-6(K_a,K_c)	>70	5.29	0.01	
^{30}SiO	338930	8-7	57	-0.10	0.01	
mirrored	339321	354505.50000	0	6.91	0.01	1
SO	339341	3(3)-3(2)	9	6.80	0.01	1
CN	339482	N=3-2,J=5/2-5/2	>16	17.88	0.01	
CN	340014	N=3-2,J=5/2-3/2	>16	158.02	0.01	
CN	340263	N=3-2,J=7/2-5/2	>16	165.12	0.02	
SO	340714	7(8)-6(7)	65	10.54	0.01	
$C^{13}CH$	341033	N=3-2,J=9/2-7/2,7/2-5/2	>25	-1.60	0.01	
HCS^+	341350	8-7	57	1.99	0.01	2
CH_3OH	341416	7(1,6)-6(1,5)–	64	1.65	0.01	2
CH_3OH	342730	13(1,12)-13(0,13)-+	211	32.46	0.01	1
CS	342883	7-6	49	133.14	0.01	
^{29}SiO	342981	8-7	58	65.70	0.01	1
$HC^{15}N$	344200	4-3	25	2.09	0.01	
SO	344311	8(8)-7(7)	71	13.48	0.01	
mirrored	345319	354505.50000	0	38.74	0.01	2
$H^{13}CN$	345339	J=4-3	>25	40.33	0.01	2
CO	345796	3-2	17	3674.33	0.01	
SO	346528	9(8)-8(7)	62	16.66	0.01	
$H^{13}CO^+$	346998	4-3	25	7.79	0.01	
SiO	347331	8-7	58	9.02	0.01	
$HN^{13}C$	348340	J=4-3	25	0.58	0.01	
CCH	349364	N=4-3,J=9/2-7/2,7/2-5/2	>25	61.94	0.01	
CH_3OH	350688	4(0,4)-3(-1,3)	20	16.08	0.02	2
NO	350692	J=7/2-5/2,Ω=1/2+	>19	16.08	0.02	2
CH_3OH	350905	1(1,1)-0(0,0)++	0	4.44	0.01	
NO	351048	J=7/2-5/2,Ω=1/2-	>19	13.62	0.01	
H_2CO	351769	5(1,5)-4(1,4)	46	16.61	0.01	
mirrored	353578	340247.78125	0	5.23	0.01	2
H	353623	H(26)α	0	6.32	0.01	2
mirrored	353795	340031.56250	0	1.07	0.01	

Table 5.2 (continued): Integrated intensity of the identified lines from SgrA*$(-20, -30)$.

species	f (MHz)	transition	E_L (K)	$\int T_{MB}\,dv$ (K km s^{-1})	$\Delta\int T_{MB}\,dv$ (K km s^{-1})	note
mirrored	354029	345796.00000	0	20.17	0.01	
HCN	354506	J=4-3	26	526.12	0.01	
HCO^+	356734	4-3	26	280.84	0.01	
CH_3OH	358606	4(1,3)-3(0,3)	27	3.89	0.01	
HNC	362630	J=4-3	26	44.31	0.01	
H_2CO	362736	5(0,5)-4(0,4)	35	2.60	0.02	
H_2CO	364282	5(3,K_c+1)-4(3,K_c),K_c=1,2	>141	6.65	0.02	
H_2CO	365363	5(2,3)-4(2,2)	82	4.06	0.01	
mirrored	367084	356734.21875	0	7.06	0.02	
mirrored	369313	354505.50000	0	2.59	0.03	
^{13}CS	369909	8-7	62	2.59	0.03	
N_2H^+	372672	J=4-3	27	10.41	0.02	
$C^{34}S$	385577	8-7	45	8.09	0.06	
^{29}SiO	385836	9-8	74	0.88	0.06	
CH_3OH	386635	8(K_a,K_c+1)-7(K_a,K_c)	>65	4.60	0.03	
SO	387329	9(9)-8(8)	87	10.59	0.04	
$C^{33}S$	388613	8-7	46	5.56	0.03	1
SO	389121	10(9)-9(8)	79	16.61	0.04	
SiO	390729	9-8	75	6.40	0.04	
CS	391847	8-7	66	107.44	0.02	
H_2S	392618	3(1,3)-2(2,0)	84	6.14	0.04	
H_2S	393451	2(1,1)-2(0,2)	55	4.78	0.03	
CH_3OH	398447	2(1,2)-1(0,1)++	2	5.67	0.02	
HC_3N	400132	J=44-43	413	1.26	0.02	
H	402159	H(31)β	0	12.86	0.02	
D_2O	403562	2(1,1)-2(0,2)	52	4.38	0.02	
SO	409960	5(5)-5(4)	24	0.52	0.02	
HC_3N	427386	J=47-46	472	10.35	0.07	
SO	428111	9(10)-8(9)	100	12.79	0.07	
$HC^{15}N$	430235	5-4	41	20.68	0.03	2
SO	430340	10(10)-9(9)	106	22.16	0.03	2
$H^{13}CN$	431660	J=5-4	41	16.70	0.03	
SO	431808	11(10)-10(9)	97	14.59	0.03	
$H^{13}CO^+$	433734	5-4	42	10.97	0.03	2
$C^{34}S$	433751	9-8	58	10.92	0.03	2
SiO	434120	10-9	94	2.70	0.03	

Table 5.2 (continued): Integrated intensity of the identified lines from SgrA*$(-20, -30)$.

species	f (MHz)	transition	E_L (K)	$\int T_{MB}\,dv$ (K km s^{-1})	$\Delta\int T_{MB}\,dv$ (K km s^{-1})	note
H_2CO	434493	6(0,6)-5(0,5)	52	6.54	0.03	2
^{13}CN	434590	N=4-3,J=7/2-5/2	>31	7.23	0.02	2
^{13}CN	434790	N=4-3,J=9/2-7/2	>31	6.47	0.03	2
CH_3OH	434793	9(-1,9)-8(-1,8)	89	6.36	0.03	2
^{13}CN	434861	N=4-3,J=9/2-7/2	>31	4.82	0.02	2
$HN^{13}C$	435408	J=5-4	42	4.01	0.03	
HC_3N	436469	J=48-47	492	11.47	0.03	1
H_2CO	436587	6(2,5)-5(2,4)	100	32.01	0.03	1
CCH	436688	N=5-4,J=11/2-9/2,9/2-7/2	>42	43.02	0.03	
H_2CO	436751	6(5,K_c+1)-5(5,K_c),K_c=0,1	>346	34.39	0.03	1
$C^{18}O$	439089	4-3	32	36.62	0.04	3
$C^{15}N$	439529	N=4-3,J=7/2-5/2	>32	5.03	0.04	
^{13}CO	440765	4-3	32	615.78	0.03	
HCN	443116	J=5-4	43	441.79	0.03	3
HCO^+	445903	5-4	43	21.39	0.11	
NO	451291	J=9/2-7/2,Ω=1/2-	>36	8.37	0.07	
CH_3OH	452205	13(0,13)-12(1,11)	202	15.14	0.07	1
H_2S	452390	1(1,1)-0(0,0)	0	31.53	0.04	
HNC	453270	J=5-4	44	23.70	0.05	
CN	453372	N=4-3,J=7/2-5/2	>33	118.40	0.04	
CN	453622	N=4-3,J=9/2-7/2	>33	122.15	0.05	
CO	461041	4-3	33	4630.11	0.02	
SO	461756	13(14)-13(13)	201	1.22	0.02	
NH_2	462447	1(1,0)-1(0,1),J=3/2-3/2	30	3.15	0.02	
CH_3OH	464781	9(2,7)-9(1,8)+-,...	>120	0.49	0.02	
N_2H^+	465825	J=5-4	45	9.32	0.03	
mirrored	468882	461040.78125	0	2.28	0.07	
CH_3OH	471420	7(2,5)-7(1,6)+-	80	2.76	0.04	
SO	471538	10(11)-9(10)	120	11.80	0.03	
SO	473342	11(11)-10(10)	127	10.22	0.05	
mirrored	474725	461040.78125	0	27.24	0.08	
CH_3OH	476603	5(2,3)-5(1,4)+-,...	>50	2.64	0.03	
SiO	477505	11-10	115	5.68	0.03	
H_2CO	491968	7(1,7)-6(1,6)	83	400.15	0.03	1
C	492161	3P1-3P0	0	555.94	0.02	
CH_3OH	492279	4(1,4)-3(0,3)++	14	144.18	0.03	1

Table 5.2 (continued): Integrated intensity of the identified lines from SgrA*$(-20, -30)$.

species	f (MHz)	transition	E_L (K)	$\int T_{MB}\,dv$ (K km s^{-1})	$\Delta\int T_{MB}\,dv$ (K km s^{-1})	note
CH_3OH	493716	5(3,K_c')-4(2,K_c)	> 61	4.34	0.03	
CH_3OH	495173	7(0,7)-6(-1,6)	54	2.56	0.02	

Notes: **1** blend with strong astronomical line, **2** blend with similar astronomical line, **3** possibly blend with atmospheric line

Table 5.3: Integrated intensity of the identified lines from SgrA*$(+140, +70)$.

species	f (MHz)	transition	E_L (K)	$\int T_{MB}\,dv$ (K km s^{-1})	$\Delta\int T_{MB}\,dv$ (K km s^{-1})	note
H_2CS	270522	8(1,8)-7(1,7)	59	8.63	0.03	
SO_2	271529	7(2,6)-6(1,5)	22	1.16	0.02	
CH_3OH	271933	25(1,24)-25(0,25)	762	0.49	0.03	
HNC	271981	J=3-2	13	63.12	0.02	
HC_3N	272885	J=30-29	190	3.37	0.03	
CH_3CCH	273337	16(4)-15(4)	214	0.70	0.02	
CH_3CCH	273373	16(3)-15(3)	163	2.21	0.03	
CH_3CCH	273410	16(K)-15(K),K=0,1,2	> 98	5.16	0.02	
H_2CS	274703	8(2,7)-7(2,6)	99	2.03	0.03	
$H_2{}^{13}CO$	274762	4(1,4)-3(1,3)	32	3.85	0.03	
H_2CS	274954	8(2,6)-7(2,5)	99	1.52	0.02	
CH_3CN	275881	15(K)-14(K),K=2,3	> 121	1.54	0.03	
CH_3CN	275913	15(K)-14(K),K=0,1	> 93	3.26	0.03	
^{13}CS	277455	6-5	33	2.54	0.03	
CH_3OH	278305	9(-1,9)-8(0,8)	97	17.15	0.02	
CH_3OH	278342	2(-2,1)-3(-1,3)	20	3.36	0.03	
H_2CS	278888	8(1,7)-7(1,6)	60	5.36	0.03	
N_2H^+	279512	J=3-2	13	93.20	0.02	
OCS	279685	23-22	148	4.05	0.02	
mirrored	280183	293912.09375	0	2.11	0.03	
H_2CO	281527	4(1,4)-3(1,3)	32	66.24	0.02	
CH_3OH	281957	9(-3,7)-10(-2,9)	154	1.98	0.02	1
HC_3N	281977	J=31-30	203	2.44	0.02	
SO_2	282037	6(2,4)-5(1,5)	16	1.31	0.02	
CH_3OH	282073	19(3,16)-18(4,15)–	477	0.07	0.03	
$^{13}CH_3OH$	282966	6(0,6)-5(0,5)	47	0.73	0.02	

Table 5.3 (continued): Integrated intensity of the identified lines from SgrA*$(+140, +70)$.

species	f (MHz)	transition	E_L (K)	$\int T_{MB}\,dv$ (K km s^{-1})	$\Delta\int T_{MB}\,dv$ (K km s^{-1})	note
$^{13}CH_3OH$	283079	6(-1,6)-5(-1,5)	40	4.89	0.03	
CH_3OH	283095	4(-4,1)-5(-3,3)	98	8.34	0.03	1
$^{13}CH_3OH$	283116	6(0,6)-5(0,5)++	34	5.42	0.04	
$^{13}CH_3OH$	283215	6(K_a,K_c+1)-5(K_a,K_c)	>55	0.09	0.02	
$H_2{}^{13}CO$	283442	4(0,4)-3(0,3)	20	1.13	0.02	2
$^{13}CH_3OH$	283442	2(-2,1)-3(-1,3)	19	1.14	0.02	2
$H_2{}^{13}CO$	283993	4(2,3)-3(2,2)	68	0.68	0.02	
$H_2{}^{13}CO$	284119	4(3,K_c+1)-3(3,K_c),K_c=0,1	>127	1.53	0.02	
CH_2NH	284254	2(1,2)-1(0,1)	3	2.98	0.02	
$H_2{}^{13}CO$	284632	4(2,2)-3(2,1)	68	1.58	0.03	
CH_2NH	284778	2(2,1)-3(1,2)	27	1.70	0.03	
CH_3OH	284984	26(1,25)-26(0,26)	821	0.71	0.02	
CH_3OH	285111	3(2,2)-4(1,3)–	38	1.39	0.02	
$^{13}CH_3OH$	285556	6(1,5)-5(1,4)–	49	0.12	0.02	
HNCO	285722	13(0,13)-12(0,12)	82	5.32	0.02	
CH_3OH	287671	6(1,6)-5(1,5)++	49	19.67	0.03	
CH_3OH	288077	15(7,K_c')-16(6,K_c)	>509	0.44	0.02	
$C^{34}S$	289209	6-5	24	3.80	0.03	
CH_3OH	289939	6(0,6)-5(0,5)	48	34.09	0.03	
CH_3OH	290070	6(-1,6)-5(-1,5)	40	109.06	0.03	
CH_3OH	290128	6(K_a,K_c+1)-5(K_a,K_c)	>35	147.90	0.02	
CH_3OH	290187	6(K_a,K_c+1)-5(K_a,K_c)	>73	5.41	0.02	
CH_3OH	290256	6(K_a,K_c+1)-5(K_a,K_c)	>56	13.13	0.03	
CH_3OH	290308	6(K_a,K_c+1)-5(K_a,K_c)	>57	22.15	0.03	
CH_3CCH	290433	17(K)-16(K),K=3,4	>177	1.45	0.02	
CH_3CCH	290491	17(K)-16(K),K=0,1,2	>111	3.99	0.02	
H_2CO	290623	4(0,4)-3(0,3)	21	33.61	0.04	
HC_3N	291068	J=32-31	217	1.15	0.03	
H_2CO	291238	4(2,3)-3(2,2)	68	12.76	0.02	2
CH_3OH	291241	15(1,14)-14(2,13)–	281	12.67	0.02	2
H_2CO	291382	4(3,K_c+1)-3(3,K_c),K_c=0,1	>127	30.00	0.02	
OCS	291840	24-23	161	4.01	0.02	
H_2CO	291948	4(2,2)-3(2,1)	68	13.15	0.02	
CH_3OH	292673	6(1,5)-5(1,4)–	50	24.86	0.02	
$H_2{}^{13}CO$	293127	4(1,3)-3(1,2)	33	0.81	0.03	
CH_3OH	293464	3(2,1)-4(1,4)++	38	1.17	0.03	

Table 5.3 (continued): Integrated intensity of the identified lines from SgrA*$(+140, +70)$.

species	f (MHz)	transition	E_L (K)	$\int T_{MB}\,dv$ (K km s^{-1})	$\Delta\int T_{MB}\,dv$ (K km s^{-1})	note
CS	293912	6-5	35	85.16	0.04	
CH_3CN	294161	16(5)-15(5)	> 284	-0.06	0.02	
CH_3CN	294212	16(4)-15(4)	> 220	-0.03	0.03	
CH_3CN	294266	16(K)-15(K),K=2,3	> 134	0.72	0.03	
CH_3CN	294300	16(K)-15(K),K=0,1	> 106	1.56	0.03	
SO	295356	9(10)-9(9)	106	0.22	0.03	
$HCNH^+$	296434	J=4-3	21	2.95	0.02	
SO	296550	6(7)-5(6)	51	6.10	0.03	
$^{13}CH_3OH$	297414	4(3,1)-5(2,3)	56	0.18	0.02	
CH_3OH	297823	6(4,K_c')-7(3,K_c)	> 115	0.32	0.02	
$^{13}CH_3OH$	297975	3(0,3)-2(-1,2)	12	1.32	0.02	
HCS^+	298690	7-6	43	1.65	0.02	
NS	299700	J=13/2-11/2,Ω=1/2,l=e	> 40	2.63	0.03	
mirrored	299909	310193.00000	0	1.31	0.03	
NS	300098	J=13/2-11/2,Ω=1/2,l=f	> 40	2.74	0.02	
^{29}SiO	300120	7-6	43	2.48	0.02	1
HC_3N	300160	J=33-32	231	1.06	0.02	
H_2CO	300837	4(1,3)-3(1,2)	33	49.78	0.02	
SO	301286	7(7)-6(6)	56	4.21	0.04	
CH_3OH	302370	3(0,3)-2(-1,2)	13	47.80	0.02	
CH_3OH	302913	12(0,12)-11(1,11)++	166	4.99	0.03	
CH_3OH	303367	1(1,0)-1(0,1)-+	2	22.14	0.02	
$^{13}CH_3OH$	303693	1(1,0)-1(0,1)-+	2	1.08	0.02	
SiO	303927	7-6	44	12.51	0.02	
OCS	303993	25-24	175	3.44	0.02	
SO	304078	8(7)-7(6)	48	11.13	0.04	
CH_3OH	304208	2(1,1)-2(0,2)-+	7	29.99	0.04	
H_2CS	304308	9(1,9)-8(1,8)	72	5.52	0.04	
$^{13}CH_3OH$	304494	2(1,1)-2(0,2)-+	7	1.43	0.02	
CH_3OH	305474	3(1,2)-3(0,3)-+	14	29.16	0.02	
$^{13}CH_3OH$	305699	3(1,2)-3(0,3)-+	14	2.05	0.03	
CH_2NH	306172	5(1,5)-4(1,4)	37	1.67	0.02	
CH_3OH	307166	4(1,3)-4(0,4)-+	23	25.45	0.03	
$^{13}CH_3OH$	307205	3(1,2)-2(0,2)	20	9.13	0.03	1
$^{13}CH_3OH$	307311	4(1,3)-4(0,4)-+	23	1.28	0.03	
CH_3CCH	307530	18(3)-17(3)	190	1.22	0.03	

Table 5.3 (continued): Integrated intensity of the identified lines from SgrA*$(+140, +70)$.

species	f (MHz)	transition	E_L (K)	$\int T_{MB}\,dv$ (K km s^{-1})	$\Delta\int T_{MB}\,dv$ (K km s^{-1})	note
CH_3CCH	307571	18(K)-17(K),K=0,1,2	>125	2.95	0.02	
HNCO	307694	14(0,14)-13(0,13)	96	3.47	0.02	
H_2CS	308750	9(0,9)-8(0,8)	59	2.09	0.04	
CH_3OH	308887	22(-4,19)-21(-5,16)	660	1.13	0.04	
HC_3N	309250	J=34-33	245	1.61	0.03	2
mirrored	309265	300836.62500	0	1.56	0.03	2
CH_3OH	309290	5(1,4)-5(0,5)-+	35	21.48	0.03	
$^{13}CH_3OH$	309335	5(1,4)-5(0,5)-+	34	1.03	0.03	
SO	309502	2(2)-2(1)	4	1.67	0.02	
CH_3OH	310193	3(1,2)-2(0,2)	20	29.28	0.03	
$^{13}CH_3OH$	311774	6(1,5)-6(0,6)-+	48	0.91	0.04	
CH_3OH	311853	6(1,5)-6(0,6)-+	49	18.08	0.04	
CH_3CN	312649	17(K)-16(K),K=2,3	>148	0.85	0.03	
CH_3CN	312685	17(K)-16(K),K=0,1	>120	1.12	0.03	
CH_3OH	313597	7(1,6)-6(2,4)	71	3.26	0.03	
H_2CS	313717	9(1,8)-8(1,7)	73	4.59	0.03	
$^{13}C^{18}O$	314120	J=3-2	>15	1.38	0.03	
CH_3OH	314351	10(0,10)-9(1,8)	126	1.24	0.03	
CH_3OH	314860	7(1,6)-7(0,7)-+	65	14.34	0.04	
CH_3OH	315267	6(2,4)-5(1,4)	56	19.01	0.03	
OCS	316146	26-25	190	2.64	0.04	
CCS	316618	N=7-4,J=6-5	8	1.55	0.03	2
mirrored	316630	305473.50000	0	1.55	0.03	2
CH_2NH	317405	5(0,5)-4(0,4)	31	6.47	0.03	
CH_3OH	318319	8(1,7)-8(0,8)-+	84	11.58	0.03	
CH_2NH	319631	5(2,4)-4(2,3)	62	0.14	0.06	
mirrored	321521	330587.96875	0	4.66	0.06	
mirrored	327229	342882.84375	0	4.13	0.12	
$C^{18}O$	329331	3-2	16	51.87	0.06	
SO	329385	1(2)-0(1)	0	4.18	0.07	
$^{13}CH_3OH$	330194	7(-1,7)-6(-1,6)	53	2.64	0.04	
$^{13}CH_3OH$	330253	7(0,7)-6(0,6)++	48	3.18	0.04	
$^{13}CH_3OH$	330465	7(2,5)-6(2,4)++	85	3.60	0.04	1
$^{13}CH_3OH$	330536	7(K_a,K_c+1)-6(K_a,K_c)	>70	61.73	0.04	1
^{13}CO	330588	3-2	16	376.96	0.02	
CH_3OH	330794	8(-3,6)-9(-2,8)	130	-10.13	0.04	1

Table 5.3 (continued): Integrated intensity of the identified lines from SgrA*$(+140, +70)$.

species	f (MHz)	transition	E_L (K)	$\int T_{MB}\,dv$ (K km s^{-1})	$\Delta\int T_{MB}\,dv$ (K km s^{-1})	note
CH_3OH	331502	11(1,10)-11(0,11)-+	153	3.80	0.03	
CH_2NH	332573	5(1,4)-4(1,3)	40	2.38	0.05	
$^{13}CH_3OH$	333115	7(1,6)-6(1,5)–	63	0.96	0.03	
CH_3OH	335134	2(2,1)-3(1,2)–	29	1.53	0.03	
CH_3OH	335582	7(1,7)-6(1,6)++	63	11.74	0.04	
mirrored	336318	345796.00000	0	20.27	0.02	
HC_3N	336520	J=37-36	291	0.60	0.03	2
SO	336554	10(11)-10(10)	127	0.61	0.03	2
CH_3OH	336865	12(1,11)-12(0,12)-+	181	2.23	0.03	
$C^{17}O$	337061	J=3-2	> 16	12.02	0.04	
$C^{34}S$	337396	7-6	34	2.00	0.04	
H_2CS	338083	10(1,10)-9(1,9)	86	2.74	0.04	
CH_3OH	338125	7(0,7)-6(0,6)	62	17.86	0.03	
CH_3OH	338345	7(-1,7)-6(-1,6)	54	60.54	0.03	
CH_3OH	338423	7(K_a,K_c+1)-6(K_a,K_c)	> 49	82.40	0.03	
CH_3OH	338508	7(K_a,K_c+1)-6(K_a,K_c)	> 87	1.81	0.03	
CH_3OH	338562	7(K_a,K_c+1)-6(K_a,K_c)	> 96	3.14	0.04	
CH_3OH	338628	7(K_a,K_c+1)-6(K_a,K_c)	> 70	9.12	0.04	
CH_3OH	338722	7(K_a,K_c+1)-6(K_a,K_c)	> 71	15.76	0.04	
SO	339341	3(3)-3(2)	9	0.54	0.03	
CN	339482	N=3-2,J=5/2-5/2	> 16	5.74	0.02	1
mirrored	339524	330587.96875	0	5.24	0.02	
mirrored	339610	354505.50000	0	2.58	0.03	
CN	340014	N=3-2,J=5/2-3/2	> 16	19.03	0.02	
CH_3OH	340141	2(2,0)-3(1,3)++	28	2.50	0.03	
CN	340263	N=3-2,J=7/2-5/2	> 16	20.18	0.03	
$^{13}CH_3OH$	340314	2(2,1)-3(1,2)–	28	1.48	0.05	
CH_2NH	340354	3(1,3)-2(0,2)	9	2.04	0.04	
CH_3OH	340394	16(6,K_c')-17(5,K_c)	> 493	0.13	0.04	
OCS	340449	28-27	221	0.64	0.04	
SO	340714	7(8)-6(7)	65	1.88	0.02	
HCS^+	341350	8-7	57	0.36	0.02	
CH_3OH	341416	7(1,6)-6(1,5)–	64	12.35	0.02	
CH_3CCH	341728	20(K)-19(K),K=0,1,2	> 156	2.66	0.03	
mirrored	342347	351768.65625	0	0.46	0.03	
CH_3OH	342730	13(1,12)-13(0,13)-+	211	0.86	0.03	

Table 5.3 (continued): Integrated intensity of the identified lines from SgrA*$(+140, +70)$.

species	f (MHz)	transition	E_L (K)	$\int T_{MB}\,dv$ (K km s^{-1})	$\Delta\int T_{MB}\,dv$ (K km s^{-1})	note
CS	342883	7-6	49	48.01	0.03	
H_2CS	342946	10(0,10)-9(0,9)	74	2.01	0.03	
^{29}SiO	342981	8-7	58	0.44	0.04	
$H_2{}^{13}CO$	343326	5(1,5)-4(1,4)	45	1.65	0.04	
SO	344311	8(8)-7(7)	71	2.25	0.03	
$H^{13}CN$	345340	J=4-3	25	12.74	0.03	
mirrored	345611	354505.50000	0	2.21	0.03	1
CO	345796	3-2	17	1812.49	0.01	
CH_3OH	345904	16(1,15)-15(2,14)–	316	212.27	0.03	1
CH_3OH	345919	18(-3,16)-17(-4,14)	443	94.76	0.03	1
SO	346528	9(8)-8(7)	62	5.94	0.03	
$H^{13}CO^+$	346998	4-3	25	3.64	0.03	
SiO	347331	8-7	58	5.58	0.03	
$HN^{13}C$	348340	J=4-3	25	0.98	0.03	
H_2CS	348534	10(1,9)-9(1,8)	88	2.03	0.03	
CH_3OH	349107	14(1,13)-14(0,14)-+	243	1.03	0.04	
CCH	349326	N=4-3,J=9/2-7/2	> 25	10.60	0.04	
CCH	349407	N=4-3,J=7/2-5/2	> 25	9.02	0.04	
mirrored	349706	338408.68750	0	1.90	0.03	
mirrored	349770	338344.62500	0	1.40	0.03	
CH_3OH	350688	4(0,4)-3(-1,3)	20	29.81	0.04	2
NO	350692	J=7/2-5/2,Ω=1/2+	> 19	30.10	0.04	2
CH_3OH	350905	1(1,1)-0(0,0)++	0	12.86	0.04	
NO	351048	J=7/2-5/2,Ω=1/2-	> 19	10.84	0.02	
CH_3OH	351236	9(5,5)-10(4,6)	224	0.80	0.03	
H_2CO	351769	5(1,5)-4(1,4)	46	35.36	0.03	
mirrored	354321	345796.00000	0	12.02	0.02	
HCN	354506	J=4-3	26	183.71	0.02	
CH_3OH	355603	13(0,13)-12(1,12)++	194	2.66	0.02	
HCO^+	356734	4-3	26	76.22	0.03	
mirrored	357234	342882.84375	0	0.32	0.02	
mirrored	357449	372672.46875	0	0.81	0.03	
CH_3OH	358606	4(1,3)-3(0,3)	27	16.79	0.03	
CH_3CCH	358804	21(K)-20(K),K=0,1,2	> 172	-0.66	0.03	
CH_3OH	360849	11(0,11)-10(1,9)	149	0.75	0.03	
CH_3OH	361852	8(1,7)-7(2,5)	87	2.97	0.04	

Table 5.3 (continued): Integrated intensity of the identified lines from SgrA*$(+140, +70)$.

species	f (MHz)	transition	E_L (K)	$\int T_{MB}\,dv$ (K km s^{-1})	$\Delta\int T_{MB}\,dv$ (K km s^{-1})	note
HNC	362630	J=4-3	26	28.93	0.05	
H_2CO	362736	5(0,5)-4(0,4)	35	17.99	0.05	
CH_3OH	363440	16(1,15)-16(0,16)-+	315	0.94	0.03	2
mirrored	363450	372672.46875	0	1.09	0.04	2
mirrored	363614	354505.50000	0	3.87	0.03	3
CH_3OH	363740	7(2,5)-6(1,5)	70	10.27	0.03	
H_2CO	363946	5(2,4)-4(2,3)	82	5.28	0.03	
H_2CO	364103	5(4,K_c+1)-4(4,K_c),K_c=0,1	> 223	3.15	0.05	
H_2CO	364282	5(3,K_c+1)-4(3,K_c),K_c=1,2	> 141	15.77	0.04	
OCS	364749	30-29	254	0.70	0.04	
H_2CO	365363	5(2,3)-4(2,2)	82	4.14	0.04	
$H_2{}^{13}CO$	366270	5(1,4)-4(1,3)	47	1.06	0.05	
mirrored	366351	351768.65625	0	1.82	0.05	
CH_2NH	367072	6(1,6)-5(1,5)	52	1.93	0.10	
mirrored	367386	356734.21875	0	5.41	0.10	
mirrored	369615	354505.50000	0	2.71	0.08	
^{13}CS	369909	8-7	62	2.28	0.08	
N_2H^+	372672	J=4-3	27	52.16	0.07	
H_2CO	375893	5(1,4)-4(1,3)	48	7.90	0.22	
CH_3OH	386248	8(0,8)-7(0,7)	78	9.08	0.38	
CH_3OH	386587	8(-1,8)-7(-1,7)	71	43.46	0.21	
CH_3OH	386695	8(K_a,K_c+1)-7(K_a,K_c)	> 65	73.33	0.16	
CH_3OH	386984	8(K_a,K_c+1)-7(K_a,K_c)	> 86	3.89	0.17	
CH_3OH	390141	8(1,7)-7(1,6)–	80	10.38	0.12	
SiO	390729	9-8	75	2.16	0.15	
CS	391847	8-7	66	34.80	0.10	
NS	391941	J=17/2-15/2,Ω=1/2,l=e	> 71	1.91	0.10	
H_2S	393451	2(1,1)-2(0,2)	55	6.71	0.10	
CH_2NH	394017	4(1,4)-3(0,3)	18	0.10	0.09	
CH_3OH	394273	19(-3,17)-18(-4,15)	485	0.55	0.09	
CH_3OH	397040	3(3,K_c')-2(2,K_c)	> 45	16.65	0.05	3
CH_3OH	398447	2(1,2)-1(0,1)++	2	22.52	0.05	
CH_2NH	398689	6(1,5)-5(1,4)	56	1.64	0.04	
CH_3OH	398946	5(0,5)-4(-1,4)	29	23.15	0.04	
CH_2NH	399179	8(0,8)-7(1,7)	90	0.98	0.05	
mirrored	399255	386682.03125	0	0.64	0.05	

Table 5.3 (continued): Integrated intensity of the identified lines from SgrA*$(+140, +70)$.

species	f (MHz)	transition	E_L (K)	$\int T_{MB}\,dv$ (K km s^{-1})	$\Delta\int T_{MB}\,dv$ (K km s^{-1})	note
CH_3CN	404492	22(K)-21(K),K=3,4	> 268	0.83	0.05	
CH_3OH	405288	17(-8,9)-18(-7,11)	657	-0.56	0.06	
CH_3OH	406808	12(0,12)-11(1,10),...	> 174	1.09	0.05	
CH_3OH	407070	5(1,4)-4(0,4)	36	16.94	0.10	
CH_3OH	408557	14(0,14)-13(1,13)++	224	1.25	0.13	
SO	408636	2(3)-1(0)	1	0.49	0.13	
CH_3OH	409475	16(-1,16)-15(2,13)	301	2.45	0.07	
CH_3OH	410040	9(1,8)-8(2,6)	106	1.05	0.07	
CCS	412079	N=10-7,J=9-8	20	2.02	0.07	
CH_3OH	412272	8(2,6)-7(1,6)	86	9.83	0.07	
CH_3OH	412353	25(3,22)-25(-2,24)	782	4.82	0.07	1
^{13}CS	416125	9-8	80	1.77	0.09	
CH_3OH	416959	21(7,15)-22(6,17)	765	0.65	0.07	
$^{13}C^{18}O$	418809	J=4-3	> 30	3.24	0.07	
H_2CO	421921	6(1,6)-5(1,5)	62	31.79	0.10	
CH_3OH	427902	18(-2,17)-17(3,14)	403	0.62	0.18	3
CH_3OH	431358	9(1,9)-8(1,8)++,...	> 98	5.11	0.07	
$H^{13}CN$	431660	J=5-4	41	7.30	0.05	
SO	431808	11(10)-10(9)	97	3.30	0.05	
CH_3OH	433200	12(7,K_c')-13(6,K_c)	> 405	0.19	0.05	
$H^{13}CO^+$	433734	5-4	42	2.06	0.06	2
$C^{34}S$	433751	9-8	58	2.15	0.06	2
CH_3OH	434302	9(0,9)-8(0,8)	97	8.97	0.10	
H_2CO	434493	6(0,6)-5(0,5)	52	9.83	0.08	
CH_3OH	434793	9(-1,9)-8(-1,8)	89	38.68	0.08	
CH_3OH	434929	9(K_a,K_c+1)-8(K_a,K_c)	> 84	52.56	0.06	
CH_3OH	435217	9(K_a,K_c+1)-8(K_a,K_c)	> 133	5.27	0.07	
CH_3OH	435330	9(K_a,K_c+1)-8(K_a,K_c)	> 104	4.13	0.08	
CH_3OH	435592	9(K_a,K_c+1)-8(K_a,K_c)	> 106	9.24	0.13	
H_2CO	436587	6(2,5)-5(2,4)	100	5.33	0.12	
CCH	436661	N=5-4,J=11/2-9/2	> 42	5.66	0.12	
CCH	436723	N=5-4,J=9/2-7/2	> 42	3.65	0.16	
H_2CO	436751	6(5,K_c+1)-5(5,K_c),K_c=0,1	> 346	2.41	0.14	
H_2CO	437218	6(3,K_c+1)-5(3,K_c),K_c=2,3	> 158	16.48	0.15	
H_2CO	439058	6(2,4)-5(2,3)	100	21.88	0.26	1
$C^{18}O$	439089	4-3	32	27.86	0.26	

Table 5.3 (continued): Integrated intensity of the identified lines from SgrA*$(+140, +70)$.

species	f (MHz)	transition	E_L (K)	$\int T_{MB}\,dv$ (K km s^{-1})	$\Delta \int T_{MB}\,dv$ (K km s^{-1})	note
^{13}CO	440765	4-3	32	342.34	0.13	
HCN	443116	J=5-4	43	178.22	0.59	
HCNH$^+$	444627	J=6-5	53	3.97	2.02	
H_2S	452390	1(1,1)-0(0,0)	0	14.63	0.58	
HNC	453270	J=5-4	44	12.48	0.23	
CN	453364	N=4-3,J=7/2-5/2	>33	15.03	0.20	2
mirrored	453384	440765.15625	0	13.32	0.23	2
CN	453391	N=4-3,J=7/2-5/2	>33	12.91	0.22	2
CN	453622	N=4-3,J=9/2-7/2	>33	15.40	0.21	
CH_3OH	455618	6(1,5)-5(0,5)	48	7.12	0.17	
CH_3CN	459487	25(5)-24(5)	>443	0.78	0.11	
CH_3CN	459689	25(K)-24(K),K=0,1,2	>265	0.92	0.13	
CO	461041	4-3	33	1858.15	0.04	
N_2H^+	465825	J=5-4	45	50.25	0.13	
CH_3OH	468294	8(2,6)-8(1,7)+-	99	5.58	0.11	
mirrored	475115	461040.78125	0	41.08	0.43	
SiO	477505	11-10	115	4.17	0.22	
$^{13}CH_3OH$	478454	5(2,3)-5(1,4)+-	49	1.25	0.15	
CH_3OH	478633	4(2,2)-4(1,3)+-	38	3.92	0.15	
CH_3OH	480269	3(2,1)-3(1,2)+-	29	7.48	0.14	3
CH_3OH	482282	10(0,10)-9(0,9)	117	7.56	0.25	
CH_3OH	482961	10(-1,10)-9(-1,9),...	>110	20.47	0.17	
$^{13}CH_3OH$	483124	2(2,0)-2(1,1)+-	21	24.37	0.17	2
CH_3OH	483163	10(K_a,K_c+1)-9(K_a,K_c)	>105	26.57	0.14	2
CH_3OH	484014	2(2,1)-2(1,2)-+,...	>22	8.35	0.22	
H_2CO	491968	7(1,7)-6(1,6)	83	19.52	0.17	1
C	492161	3P1-3P0	0	402.31	0.07	3
CH_3OH	492279	4(1,4)-3(0,3)++	14	18.98	0.17	1
CH_3OH	493716	5(3,K_c')-4(2,K_c)	>61	10.92	0.14	
CH_2NH	495171	6(1,6)-5(0,5)	46	16.50	0.18	2
CH_3OH	495173	7(0,7)-6(-1,6)	54	16.68	0.18	2
CH_3OH	496916	14(0,14)-13(1,12),...	>232	6.84	0.25	3
CH_2NH	496953	4(3,2)-5(2,3)	78	2.12	0.27	3

Notes: **1** blend with strong astronomical line, **2** blend with similar astronomical line, **3** possibly blend with atmospheric line

Table 5.4: Identified species from each source with the number of lines and the total intensity of each species.

species	SgrA*$(-20,-30)$ lines	SgrA*$(-20,-30)$ $\int \mathrm{T_{MB}}\,\mathrm{d}v$ $(\mathrm{K\,km\,s^{-1}})$	SgrA*$(+140,+70)$ lines	SgrA*$(+140,+70)$ $\int \mathrm{T_{MB}}\,\mathrm{d}v$ $(\mathrm{K\,km\,s^{-1}})$
H	(1+) 5	(6.32+) 25.57	0	0.00
C	1	555.94	1	402.31
CH_3CCH	2	3.28	9	19.68
CCH	2	104.97	4	28.94
$C^{13}CH$	1	−1.60	0	0.00
HCO^+	2	302.23	1	76.22
$H^{13}CO^+$	(1+) 1	(10.97+) 7.79	(1+) 1	(2.06+) 3.64
D_2O	1	4.38	0	0.00
H_2CO	(4+) 10	(473.10+) 100.59	(3+) 17	(54.17+) 348.19
$H_2{}^{13}CO$	0	0.00	(1+) 7	(1.13+) 11.16
CH_3OH	(12+) 25	(244.47+) 99.92	(12+) 90	(417.71+) 1392.92
$^{13}CH_3OH$	0	0.00	(5+) 18	(99.97+) 30.04
CO	2	8304.44	2	3670.64
$C^{17}O$	1	11.08	1	12.02
$C^{18}O$	2	78.42	2	79.73
^{13}CO	2	1044.66	2	719.30
$^{13}C^{18}O$	0	0.00	2	4.62
HCS^+	(1+) 1	(1.99+) 2.09	2	2.00
H_2S	3	42.46	2	21.34
H_2CS	(1+) 4	(3.94+) 5.38	10	36.51
CS	3	400.02	3	167.96
$C^{34}S$	(1+) 3	(10.92+) 23.45	(1+) 2	(2.15+) 5.79
^{13}CS	3	13.83	3	6.58
CCS	0	0.00	(1+) 1	(1.55+) 2.02
SO	(5+) 15	(62.14+) 157.34	(1+) 12	(0.61+) 41.92
SO_2	0	0.00	2	2.47
OCS	0	0.00	6	15.48
N_2H^+	3	24.69	3	195.62
NH_2	1	3.15	0	0.00
HNC	3	148.02	3	104.53
$HN^{13}C$	2	4.59	1	0.98
HCN	2	967.91	2	361.93
$HC^{15}N$	(1+) 1	(20.68+) 2.09	0	0.00
$H^{13}CN$	(1+) 1	(40.33+) 16.70	2	20.04

Table 5.4 (continued): Identified species from each source with the number of lines and the overall intensity of each species.

species	SgrA*$(-20,-30)$ lines	$\int \mathbf{T_{MB}}\,\mathbf{d}v$ $(\mathrm{K\,km\,s^{-1}})$	SgrA*$(+140,+70)$ lines	$\int \mathbf{T_{MB}}\,\mathbf{d}v$ $(\mathrm{K\,km\,s^{-1}})$
$HCNH^+$	0	0.00	2	6.91
HC_3N	(5+) 4	(26.45+) 16.79	(2+) 4	(2.21+) 8.02
CN	5	581.57	(3+) 3	(33.68+) 54.61
$C^{15}N$	1	5.03	0	0.00
^{13}CN	(3+) 2	(18.52+) 10.78	0	0.00
CH_2NH	0	0.00	(1+) 12	(16.50+) 24.14
CH_3CN	4	8.16	11	11.50
NS	(1+) 1	(4.59+) 1.92	3	7.29
NO	(1+) 2	(16.08+) 21.99	(1+) 1	(30.10+) 10.84
HNCO	0	0.00	2	8.79
SiO	5	39.30	4	24.43
^{29}SiO	(2+) 1	(70.57+) 0.88	(1+) 1	(2.48+) 0.44
^{30}SiO	(1+) 1	(13.88+) $-$ 0.10	0	0.00

Notes: numbers in brackets refer to lines, blend with another astronomical line. They are marked with note 1 or note 2 in table 5.2 and table 5.3

5.6 Physical properties

To evaluate properties of the source, such as its temperature or the column density of certain species, a relation between those parameters and the line intensity in the spectrum must be established. Scaled by the Planck constant h, the energy levels E_l, E_u of the lower and upper state of the transition define the transition frequency f_ul [85, Ch. 11.1]:

$$f_\mathrm{ul} = \frac{E_\mathrm{u} - E_\mathrm{l}}{h} \qquad h \approx 6.626 \cdot 10^{-34}\,\mathrm{J\,s} \tag{5.5}$$

The dipole moment μ of the species, the line strength S_ul, and the statistical weight g_u of the upper transition state define the dipole moment μ_ul of the transition. Together with the transition frequency

and the speed of light c, these parameters yield the Einstein coefficient A_{ul}, which measures the probability of the transition [81, 85]:

$$\begin{aligned} A_{\mathrm{ul}} &= \frac{64\pi^4}{3hc^3} \cdot f_{\mathrm{ul}}^3 \cdot |\mu_{\mathrm{ul}}|^2 = \frac{64\pi^4}{3hc^3} \cdot f_{\mathrm{ul}}^3 \cdot \frac{\mu^2 S_{\mathrm{ul}}}{g_{\mathrm{u}}} \\ c &= 299\,792\,458\,\mathrm{m\,s^{-1}} \end{aligned} \tag{5.6}$$

In general, A_{ul} increases strongly into the sub-mm region, since it depends on f_{ul} to the power of three. To transform units correctly note that $1\,\mathrm{D}^2 = 1 \cdot 10^{-49}\,\mathrm{J\,m^3}$ [85, Ch. 14.8].

Now consider the column density N_u of the particles of a certain species that is excited to the upper state of a certain transition. Dependent on the parameters from (5.5) and (5.6), with the Boltzmann constant k, and properties of the observation conditions, the integrated intensity $\int T_{\mathrm{MB}}\,\mathrm{d}v$ of the respective line yields N_{u} [30, Ch. 2.1]:

$$\begin{aligned} N_{\mathrm{u}} &= \frac{8\pi k f_{\mathrm{ul}}^2}{hc^3 A_{\mathrm{ul}}} \cdot \int T_{\mathrm{MB}}\,\mathrm{d}v \cdot \frac{\Delta\Omega_{\mathrm{a}}}{\Delta\Omega_{\mathrm{s}}} \cdot \frac{\tau}{1 - e^{-\tau}} \\ k &\approx 1.381 \cdot 10^{-23}\,\mathrm{J\,K^{-1}} \end{aligned} \tag{5.7}$$

Assuming the solid angle $\Delta\Omega_{\mathrm{s}}$ of the source fills the solid angle $\Delta\Omega_{\mathrm{a}}$ of the antenna, and the source is optically thin ($\tau \ll 1$), simplifies (5.7) [30, Ch. 2.2]:

$$N_{\mathrm{u}} = \frac{8\pi k f_{\mathrm{ul}}^2}{hc^3 A_{\mathrm{ul}}} \cdot \int T_{\mathrm{MB}}\,\mathrm{d}v \tag{5.8}$$

Assuming local thermodynamic equilibrium (LTE), the population N_j of the excited states j of a species follows the Boltzmann distribution for a common rotation temperature T_{rot}:

$$N_j = N_0 \cdot g_j e^{-\frac{E_j}{kT_{\mathrm{rot}}}} \tag{5.9}$$

With the knowledge of the column densities of certain transitions from (5.8), (5.9) yields a relation between universal parameters of the species in the source: a basic column density N_0 of the species, and the common excitation temperature T_{rot} of the source. The logarithmic form allows analysis by a population diagram, which is also known as rotation diagram or "Boltzmann plot":

$$\begin{aligned} \ln\left(\frac{N_{\mathrm{u}}}{g_{\mathrm{u}}}\right) &= \ln\left(\frac{8\pi k f_{\mathrm{ul}}^2}{hc^3 A_{\mathrm{ul}} g_{\mathrm{u}}} \cdot \int T_{\mathrm{MB}}\,\mathrm{d}v\right) \\ &= \ln\left(\frac{3k}{8\pi^3 f_{\mathrm{ul}} \mu^2 S_{\mathrm{ul}}} \cdot \int T_{\mathrm{MB}}\,\mathrm{d}v\right) \\ &= \ln N_0 - \frac{E_{\mathrm{u}}}{kT_{\mathrm{rot}}} \end{aligned} \tag{5.10}$$

In a population diagram, the relative column density $\frac{N_{\mathrm{u}}}{g_{\mathrm{u}}}$ of the upper state is plotted against the energy level $\frac{E_{\mathrm{u}}}{k}$ of that state. A multiple of transitions of the same species may be fit by a straight line

Table 5.5: Parameters that are derived from population diagrams of chosen species.

source (offset)	species	T_{rot} (K)		N_{tot} (10^{12} cm^{-2})		v_{LSR} (km s^{-1})		Δv (km s^{-1})	
$(+140, +70)$	CH_3CCH	127.6	± 16.1	311.2	± 78.0	44.8	± 0.5	21.5	± 0.5
$(+140, +70)$	CH_3CN	126.2	± 21.7	2.3	± 0.8	43.4	± 0.8	20.5	± 0.8
$(+140, +70)$	CH_3OH	11.1	± 0.1	74337.1	± 2603.0	43.7	< 0.1	24.1	< 0.1
$(+140, +70)$	H_2CO	89.5	± 0.6	338.6	± 5.1	43.5	< 0.1	25.0	± 0.1
$(-20, -30)$	H_2CO	146.0	± 8.6	182.9	± 19.6	-42.4	± 1.6	121.7	± 1.9

with a slope that depends on the rotation temperature if LTE conditions are met. The basic column density N_0 depends on the axis intercept in the population diagram. With N_0 and T given, the total column density N_{tot} can be derived from the partition function $Z(T)$ of the species [85, Ch. 14.8]:

$$\begin{aligned} N_{\mathrm{tot}} &= \sum_j N_j = N_0 \cdot \sum_j g_j e^{-\frac{E_j}{kT_{\mathrm{rot}}}} \\ &= N_0 \cdot Z(T_{\mathrm{rot}}) \end{aligned} \tag{5.11}$$

Figures 5.9.1 to 5.9.15 show multiplets of CH_3OH, H_2CO, CH_3CCH, and CH_3CN, which are found to be good tracers for physical conditions, such as temperature or density [61, 3, 34]. Each multiplet spans a limited frequency range and contains similar transitions with the same total angular momentum quantum number J. Note that the transitions of H_2CO can be distinguished by "ortho" and "para" type, which are to some degree independent from each other. All spectra that cover the respective frequency range are averaged and rescaled to main beam temperature T_{MB}. Spectral lines from other species or from the atmosphere are masked by **set mask** to allow a multicomponent gauss fit over the strongest transitions of the multiplet, using **method gauss** and **minimize**. Aside from the integrated intensity of each line, the spectral fit calculates a common velocity shift $v_0 = v_{\mathrm{LSR}}$ and an common line width Δv and error margins for all values. Each population diagram plots the natural logarithm of the relative column density of the upper transition state $\ln \frac{N_{\mathrm{u}}}{g_{\mathrm{u}}}$ against its energy level $\frac{E_{\mathrm{u}}}{k}$ in K. N_{u} is derived from the spectral fit, using (5.8). The fit through the data points in the population diagram yields the rotation temperature T_{rot} and the total column density N_{tot} along with their error margins. The survey of SgrA*$(-20, -30)$ provides very broad lines that exceed the distance between the lines of most multiplets. Therefore, population diagrams of CH_3OH, CH_3CCH, and CH_3CN are not feasible for that source.

Table 5.5 summarizes the findings from population diagrams. Although the shape of the broad lines from SgrA*$(-20, -30)$ is not gaussian, the gaussian fit of the H_2CO yields a reasonable result. The fit indicates an FWHM of ~ 120 km s^{-1} around a peak velocity between -40 km s^{-1} and -50 km s^{-1}. This is slightly lower than expected from observations of the even broader CO line at the very same position [83, Fig. 2]. It is, however, within the range of peak velocities between -

30 km s^{-1} and -150 km s^{-1}, which are found by HNC in the southern lobe of the CND [32, Fig. 2]. The gaussian fit for all analyzed multiplets from SgrA*$(+140, +70)$ yields consistent results: we observe a velocity of $\sim$ 44 km s^{-1} with an FWHM of $\sim$ 24 km s^{-1}, which is close to the rough value of 50 km s^{-1}, that is found in the literature for the cloud [14, Ch. 2].

The findings for the temperature in SgrA*$(+140, +70)$, however, differ significantly between the species. From CH_3CCH and CH_3CN we find temperatures in the range from 108 K to 146 K, with the exception of two multiplets with high error margins. A weighted average consistently yields $T_{\mathrm{rot}} \approx 127$ K for both these species. The rotation temperature from the H_2CO multiplets is somewhat lower but still close to 100 K. From CH_3OH we find significantly lower $T_{\mathrm{rot}} \approx 11$ K, but with little variation among the multiplets of the species.

Additionally, the column densities of CH_3OH distinguish it from the other species. The population diagrams of CH_3CCH, CH_3CN, and H_2CO yield column densities that consistently vary only by a factor of ~ 3 with a tendency of falling column density towards higher frequency. The column densities of CH_3OH, however, increase with frequency by a factor of ~ 30.

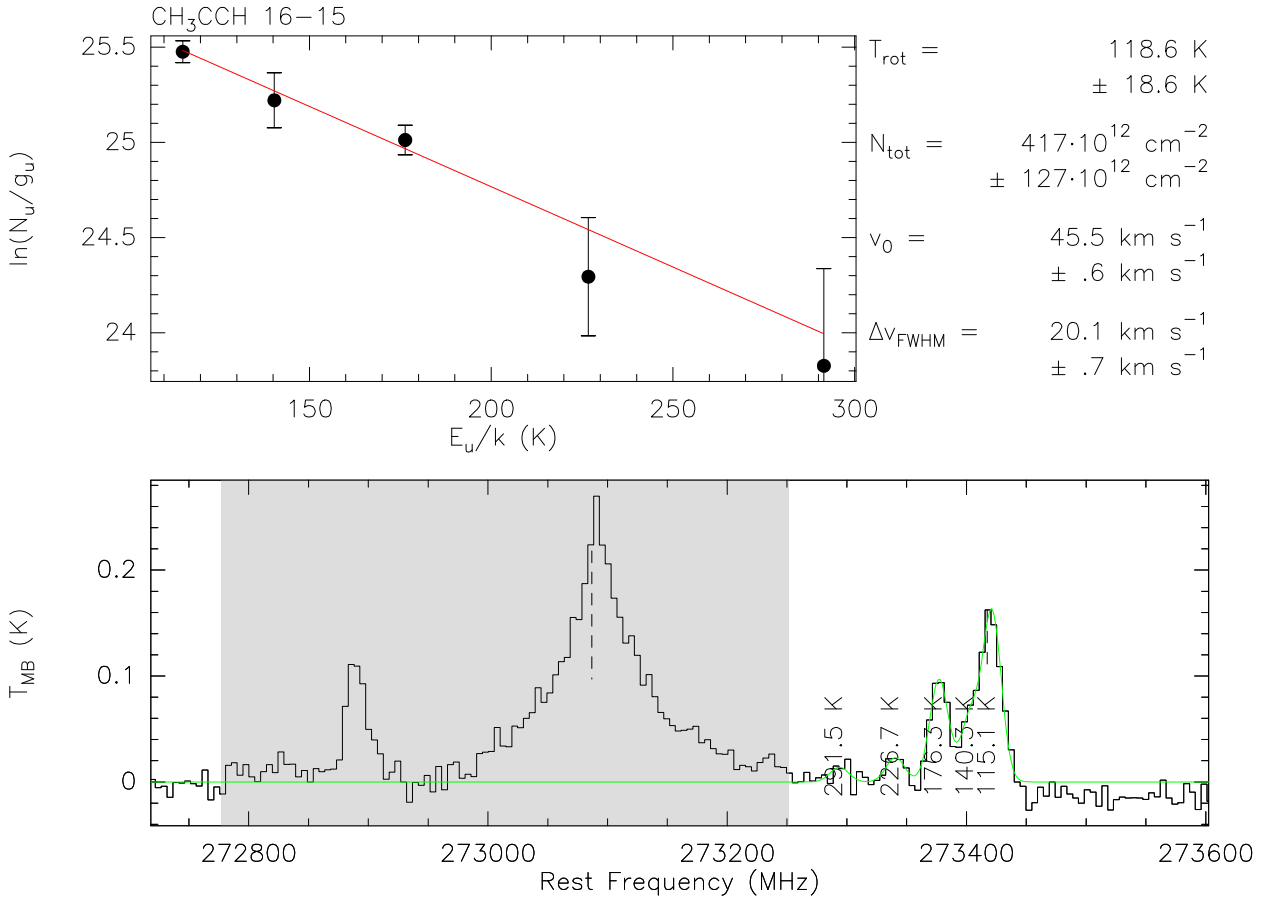

Figure 5.9.1: Spectrum (bottom) of a multiplet of CH_3CCH with transitions J=16-15 from the reduced survey of SgrA*$(+140, +70)$ and its population diagram (top). The spectrum includes a fit over the strongest transitions and masked spectral lines from other species that are highlighted in grey.

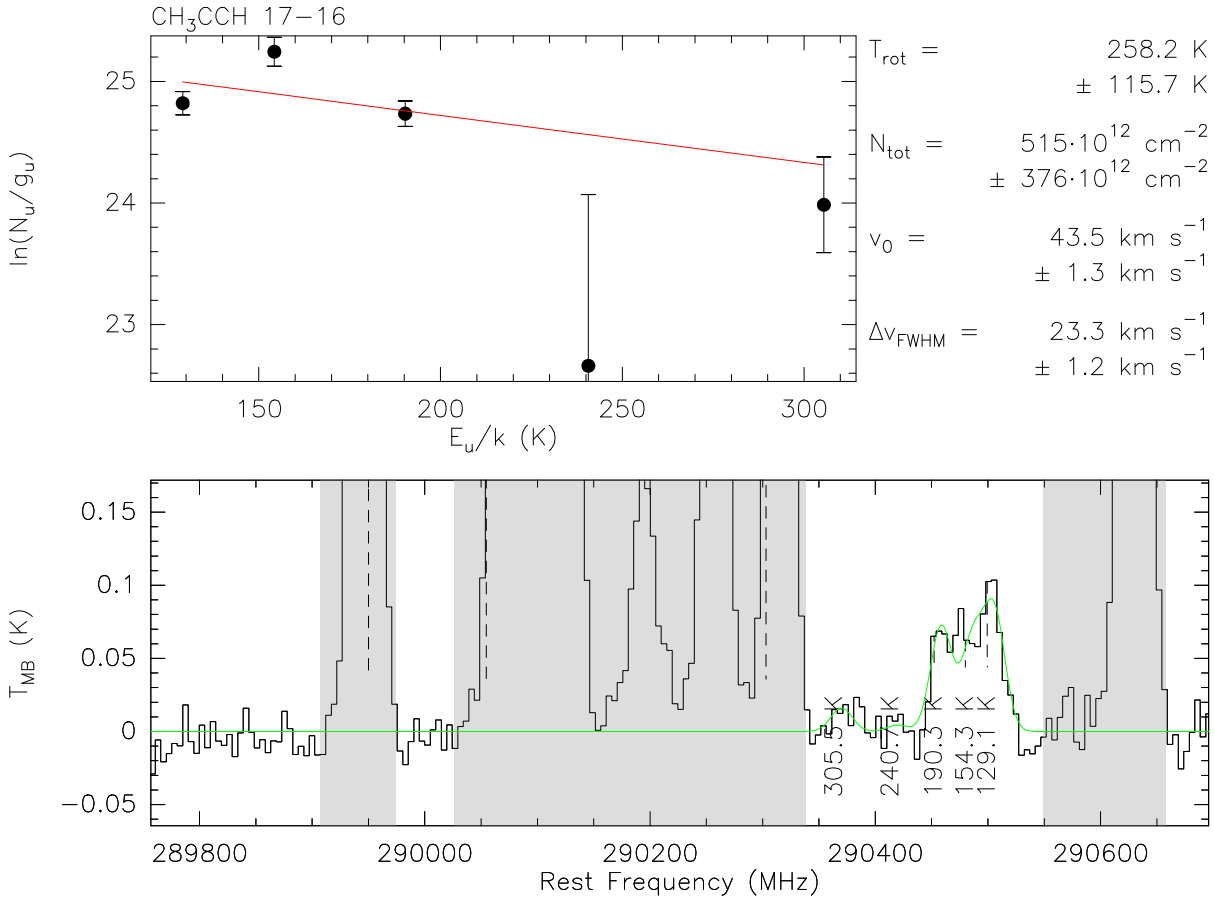

Figure 5.9.2: Spectrum (bottom) of a multiplet of CH_3CCH with transitions J=17-16 from the reduced survey of SgrA*$(+140, +70)$ and its population diagram (top). The spectrum includes a fit over the strongest transitions and masked spectral lines from other species that are highlighted in grey.

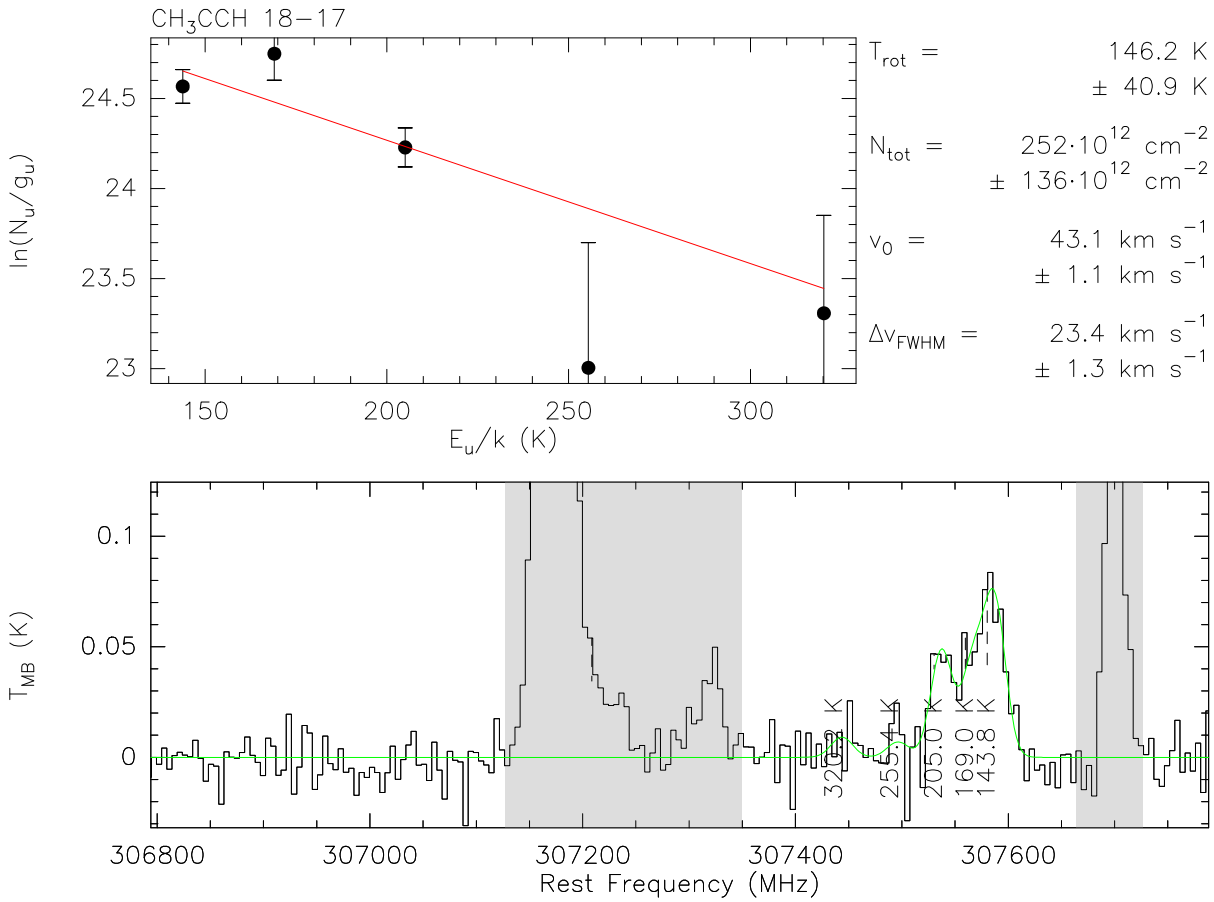

Figure 5.9.3: Spectrum (bottom) of a multiplet of CH_3CCH with transitions J=18-17 from the reduced survey of SgrA*$(+140, +70)$ and its population diagram (top). The spectrum includes a fit over the strongest transitions and masked spectral lines from other species that are highlighted in grey.

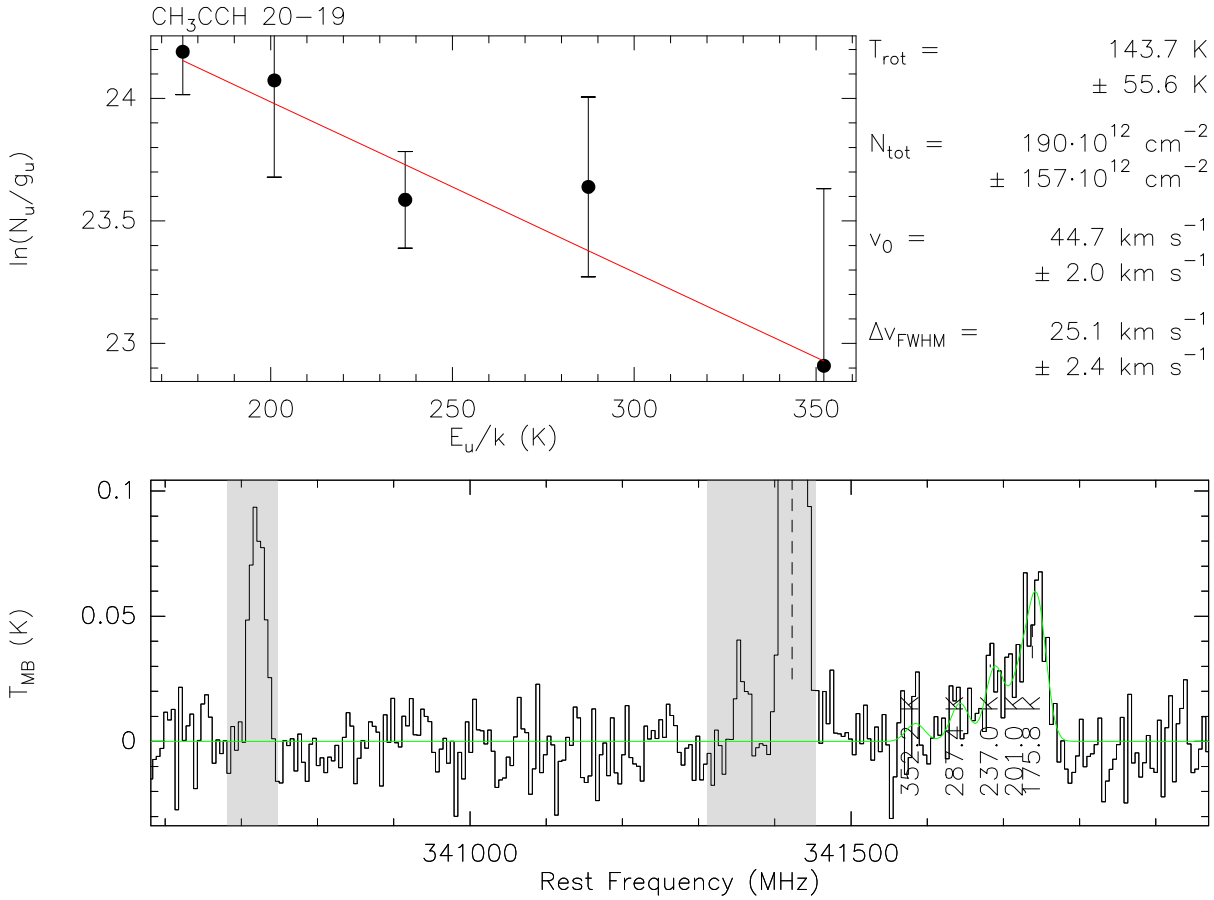

Figure 5.9.4: Spectrum (bottom) of a multiplet of CH_3CCH with transitions J=20-19 from the reduced survey of SgrA*$(+140, +70)$ and its population diagram (top). The spectrum includes a fit over the strongest transitions and masked spectral lines from other species that are highlighted in grey.

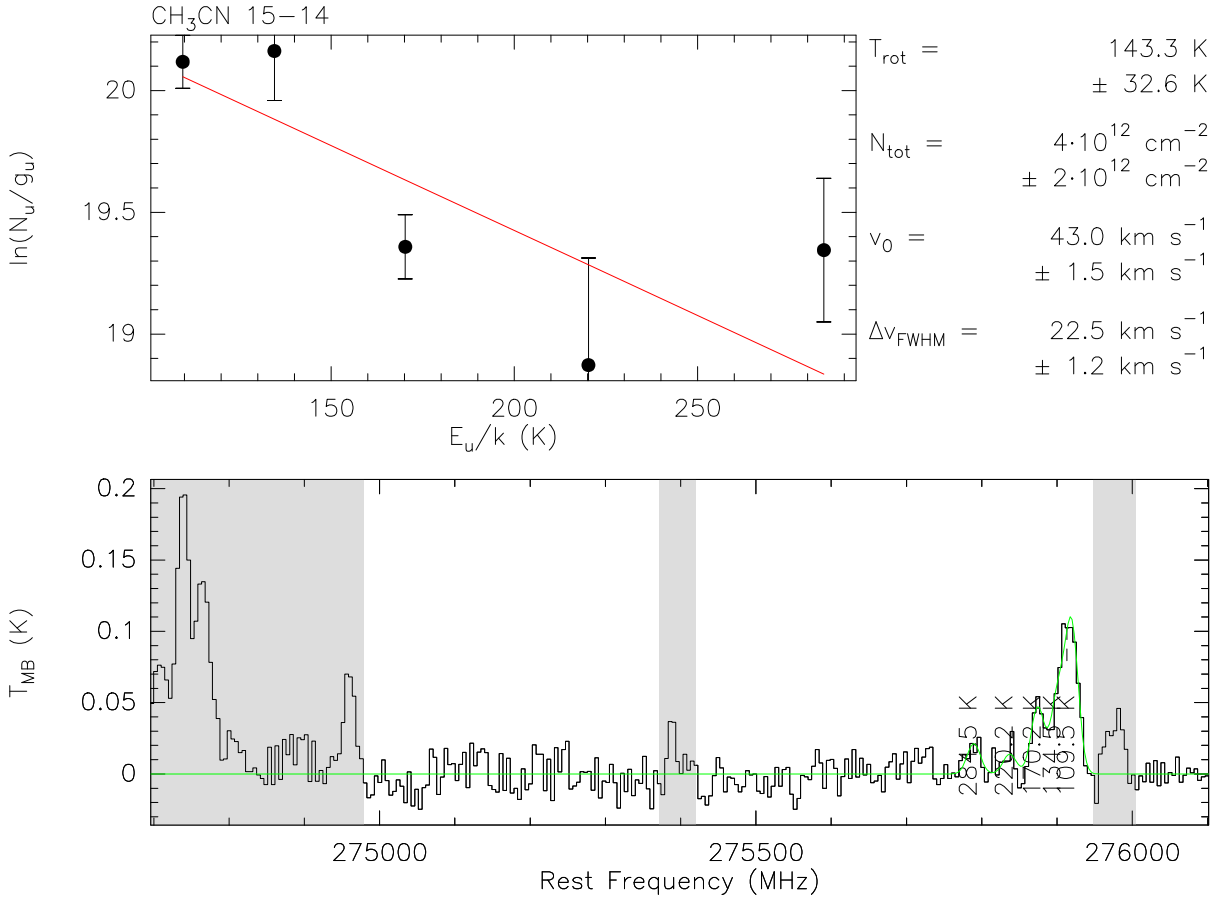

Figure 5.9.5: Spectrum (bottom) of a multiplet of CH_3CN with transitions J=15-14 from the reduced survey of SgrA*$(+140, +70)$ and its population diagram (top). The spectrum includes a fit over the strongest transitions and masked spectral lines from other species that are highlighted in grey.

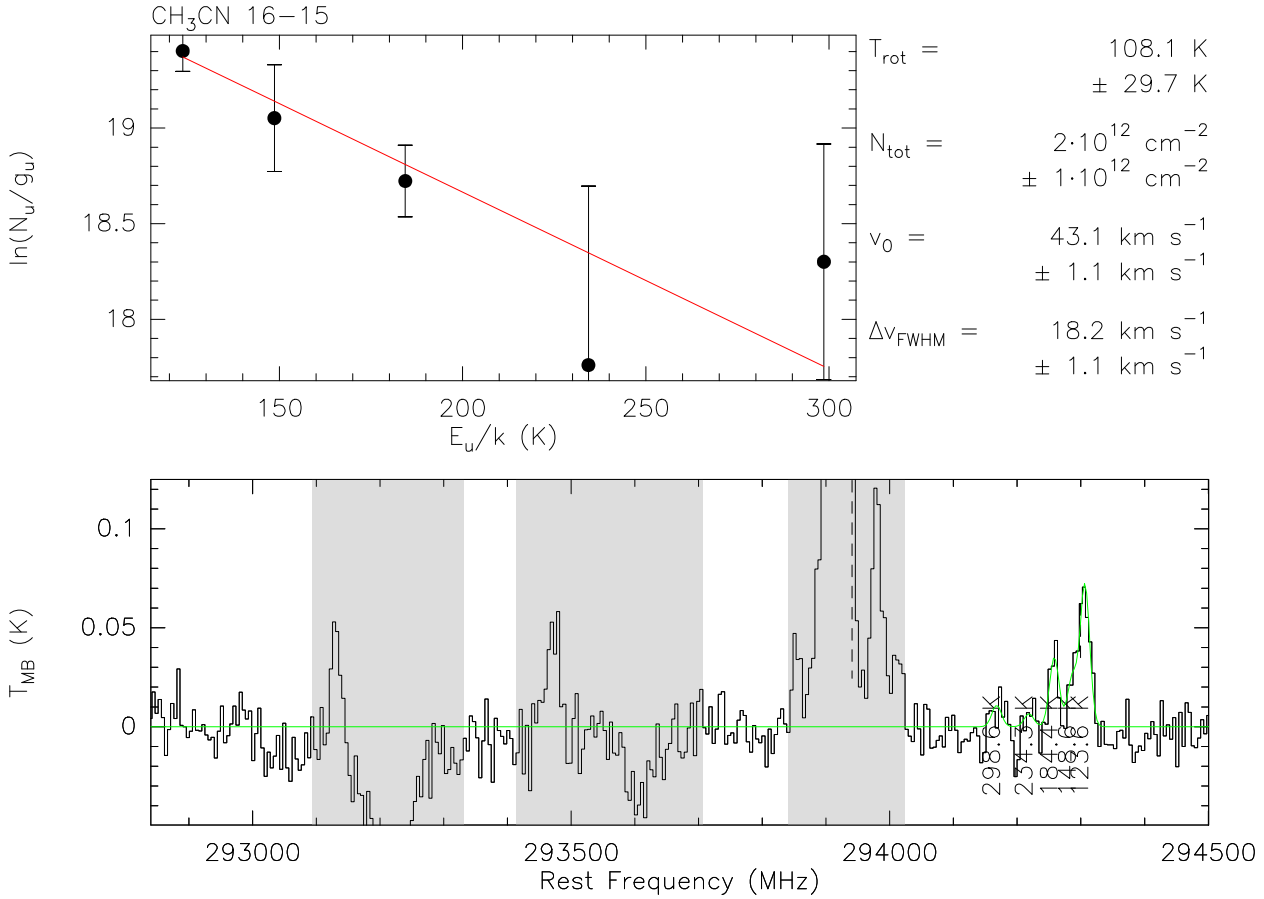

Figure 5.9.6: Spectrum (bottom) of a multiplet of CH_3CN with transitions J=16-15 from the reduced survey of SgrA*$(+140, +70)$ and its population diagram (top). The spectrum includes a fit over the strongest transitions and masked spectral lines from other species that are highlighted in grey.

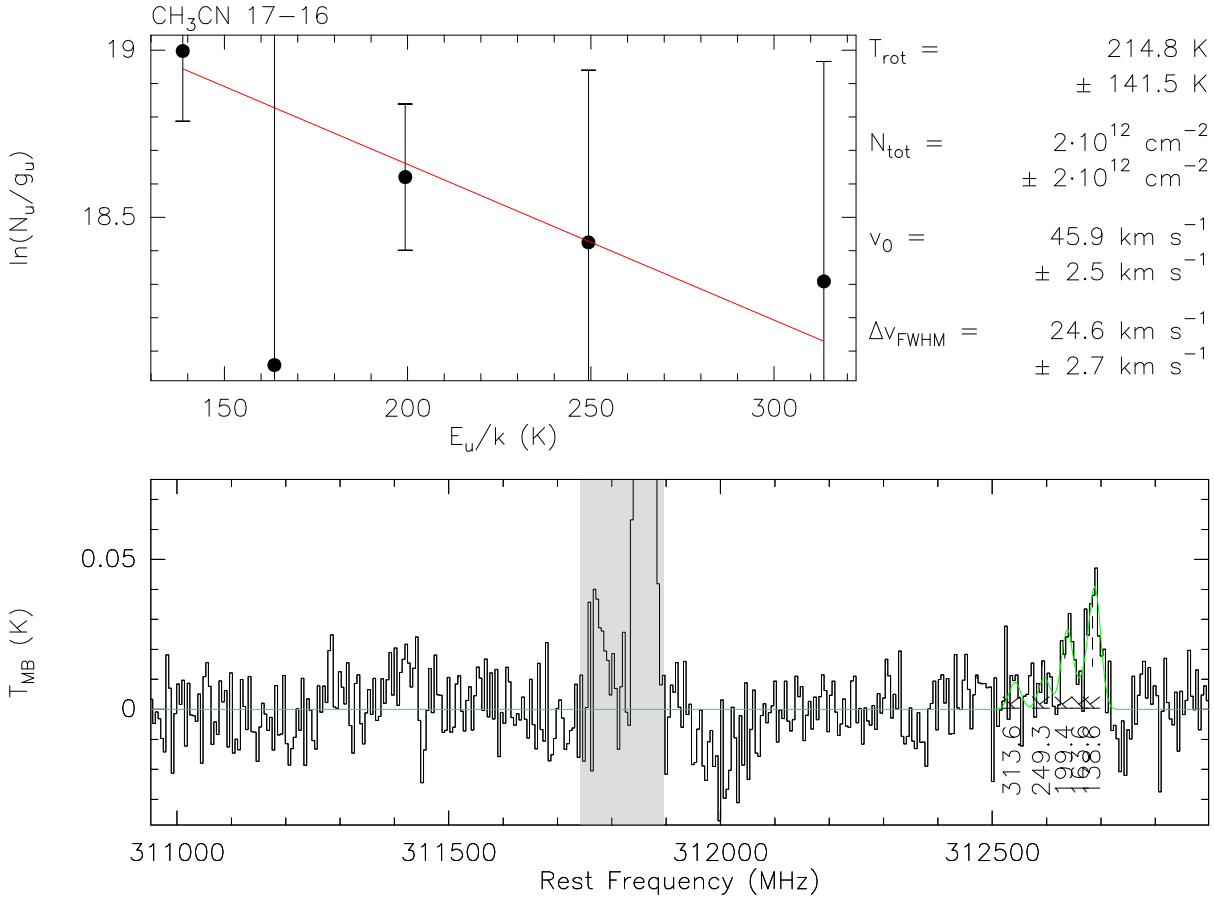

Figure 5.9.7: Spectrum (bottom) of a multiplet of CH_3CN with transitions J=17-16 from the reduced survey of SgrA*$(+140, +70)$ and its population diagram (top). The spectrum includes a fit over the strongest transitions and masked spectral lines from other species that are highlighted in grey.

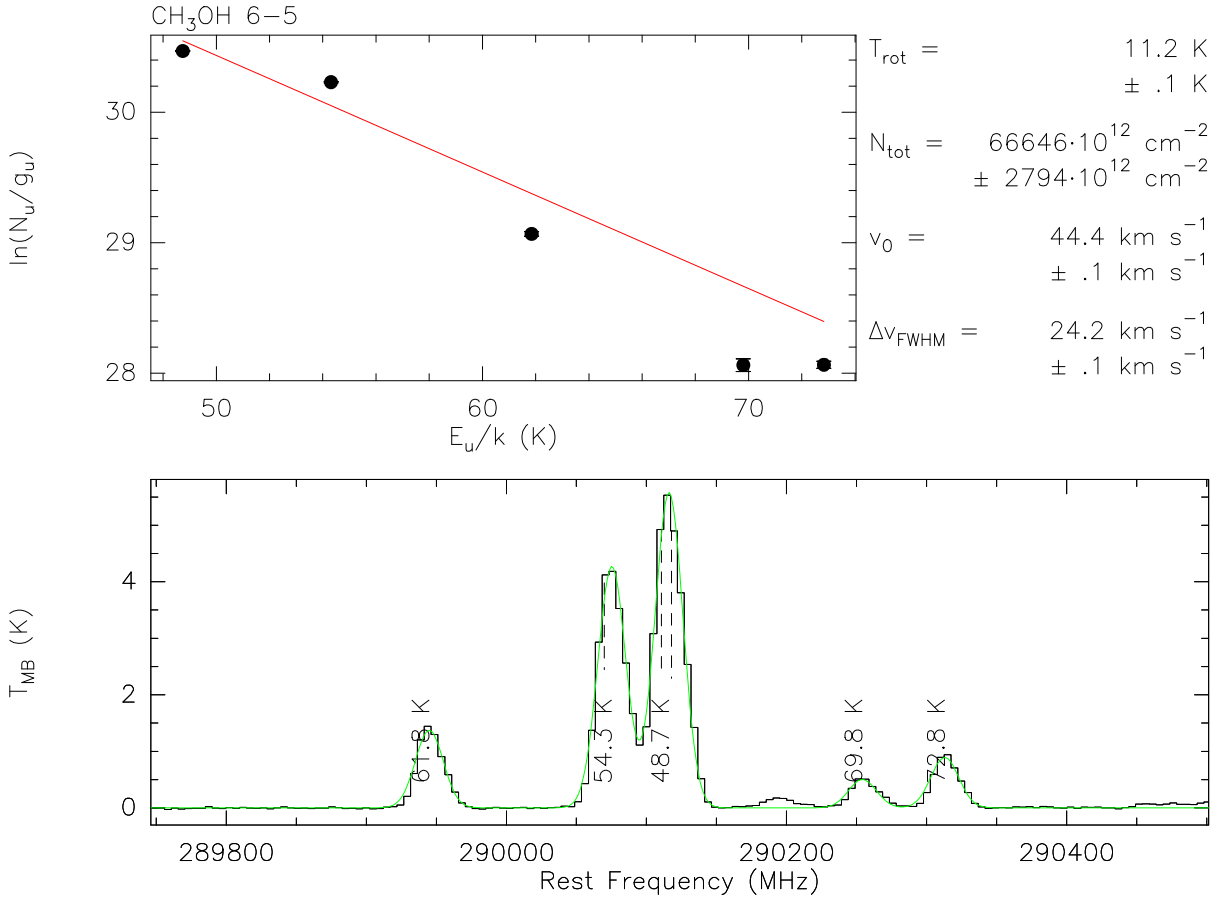

Figure 5.9.8: Spectrum (bottom) of a multiplet of CH_3OH with transitions J=6-5 from the reduced survey of SgrA*$(+140, +70)$ and its population diagram (top). The spectrum includes a fit over the strongest transitions and masked spectral lines from other species that are highlighted in grey.

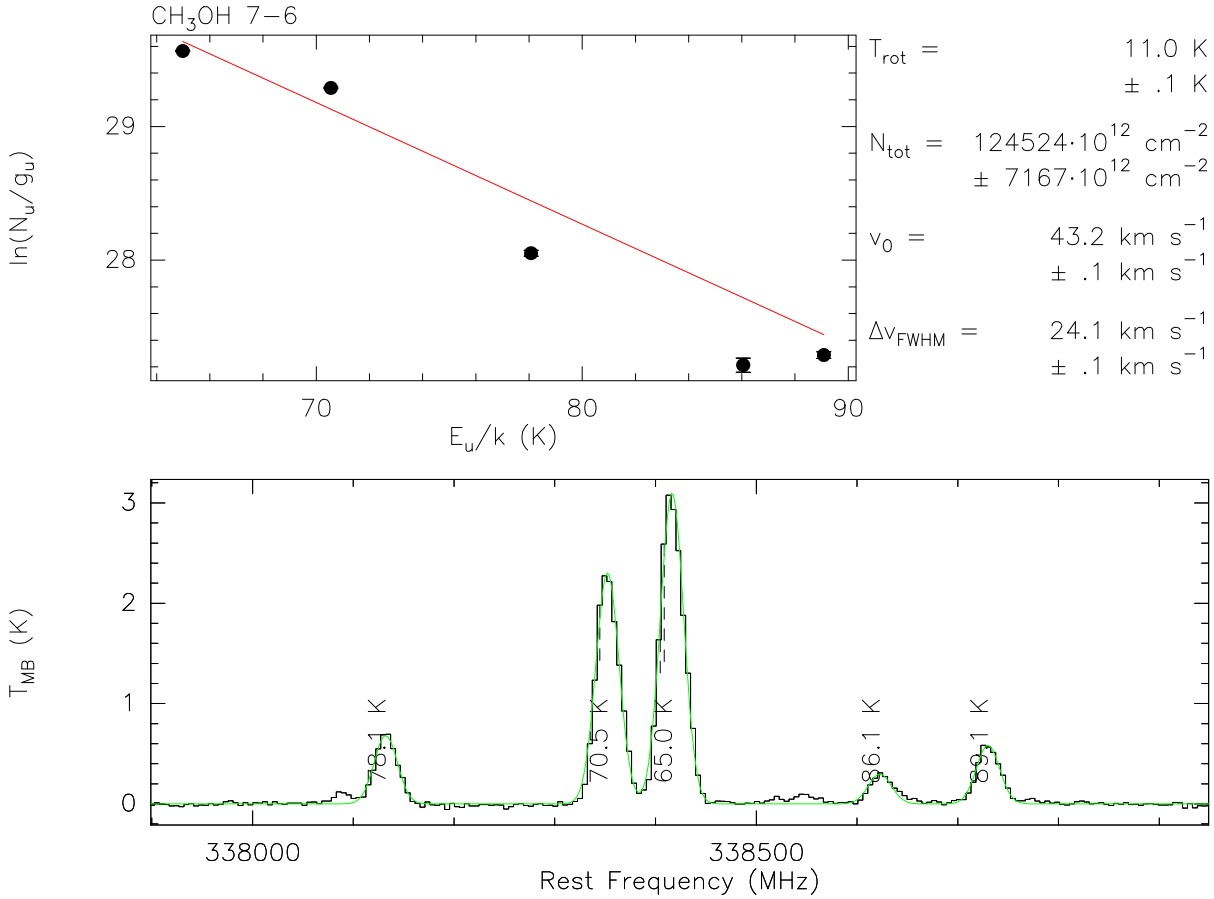

Figure 5.9.9: Spectrum (bottom) of a multiplet of CH_3OH with transitions J=7-6 from the reduced survey of SgrA*$(+140, +70)$ and its population diagram (top). The spectrum includes a fit over the strongest transitions and masked spectral lines from other species that are highlighted in grey.

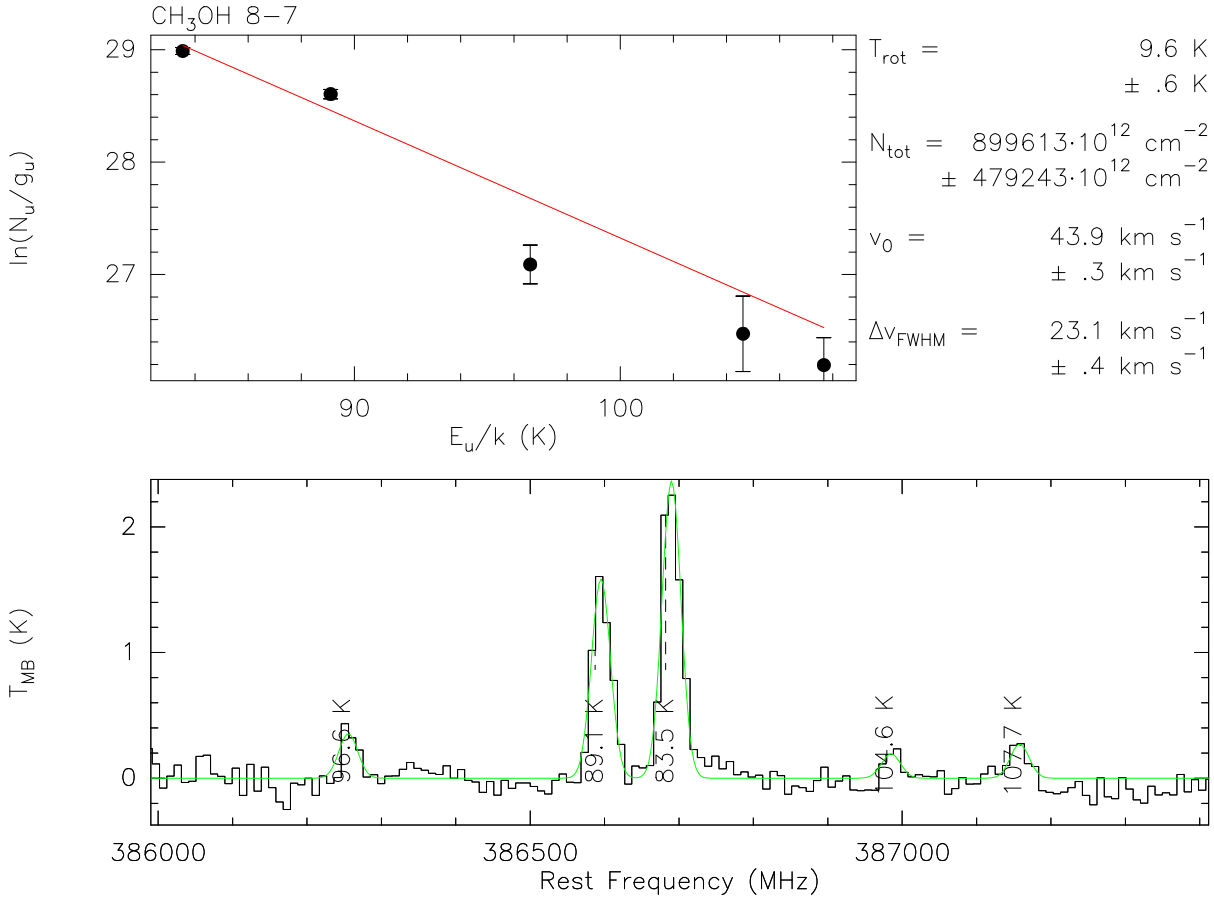

Figure 5.9.10: Spectrum (bottom) of a multiplet of CH_3OH with transitions J=8-7 from the reduced survey of SgrA*$(+140, +70)$ and its population diagram (top). The spectrum includes a fit over the strongest transitions and masked spectral lines from other species that are highlighted in grey.

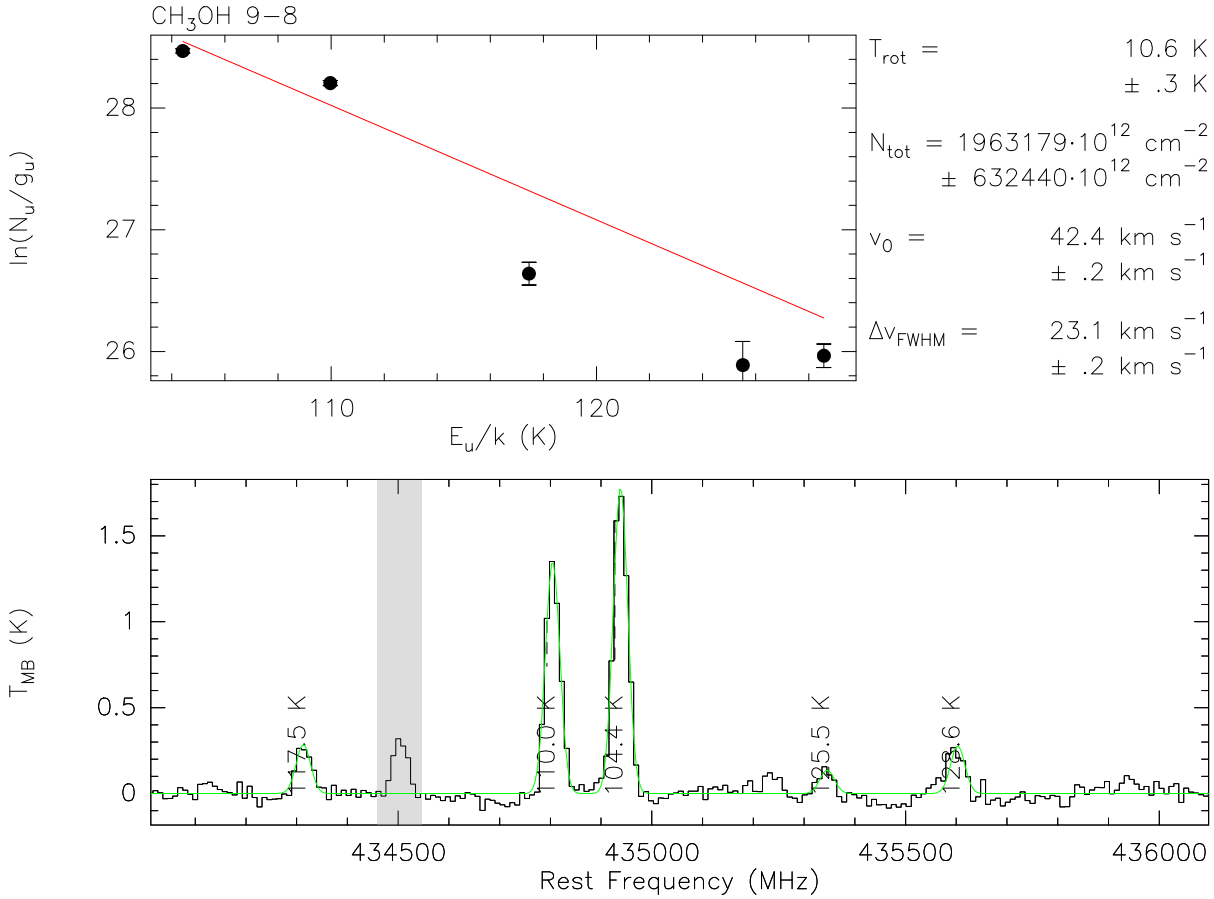

Figure 5.9.11: Spectrum (bottom) of a multiplet of CH_3OH with transitions J=9-8 from the reduced survey of SgrA*$(+140, +70)$ and its population diagram (top). The spectrum includes a fit over the strongest transitions and masked spectral lines from other species that are highlighted in grey.

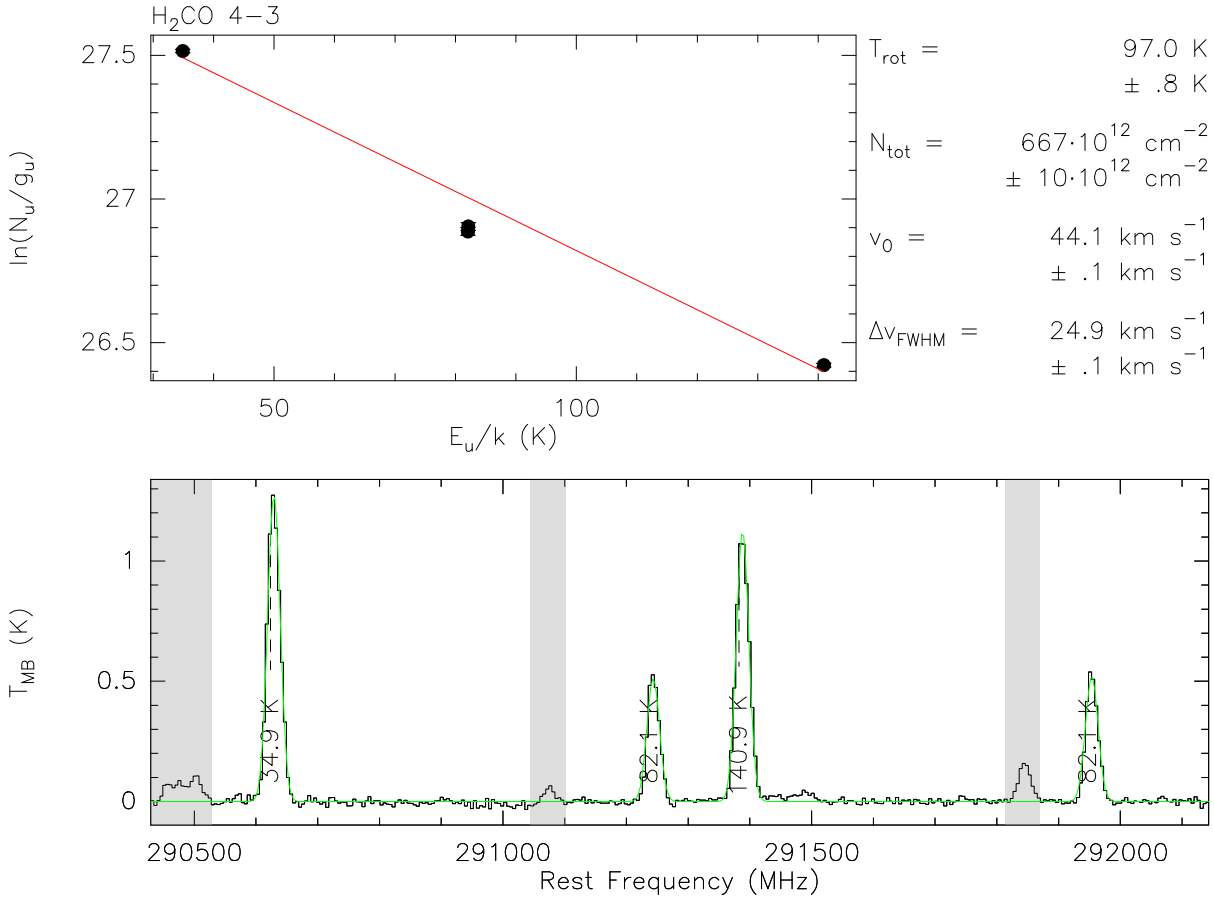

Figure 5.9.12: Spectrum (bottom) of a multiplet of H_2CO with transitions J=4-3 from the reduced survey of SgrA*$(+140, +70)$ and its population diagram (top). The spectrum includes a fit over the strongest transitions and masked spectral lines from other species that are highlighted in grey.

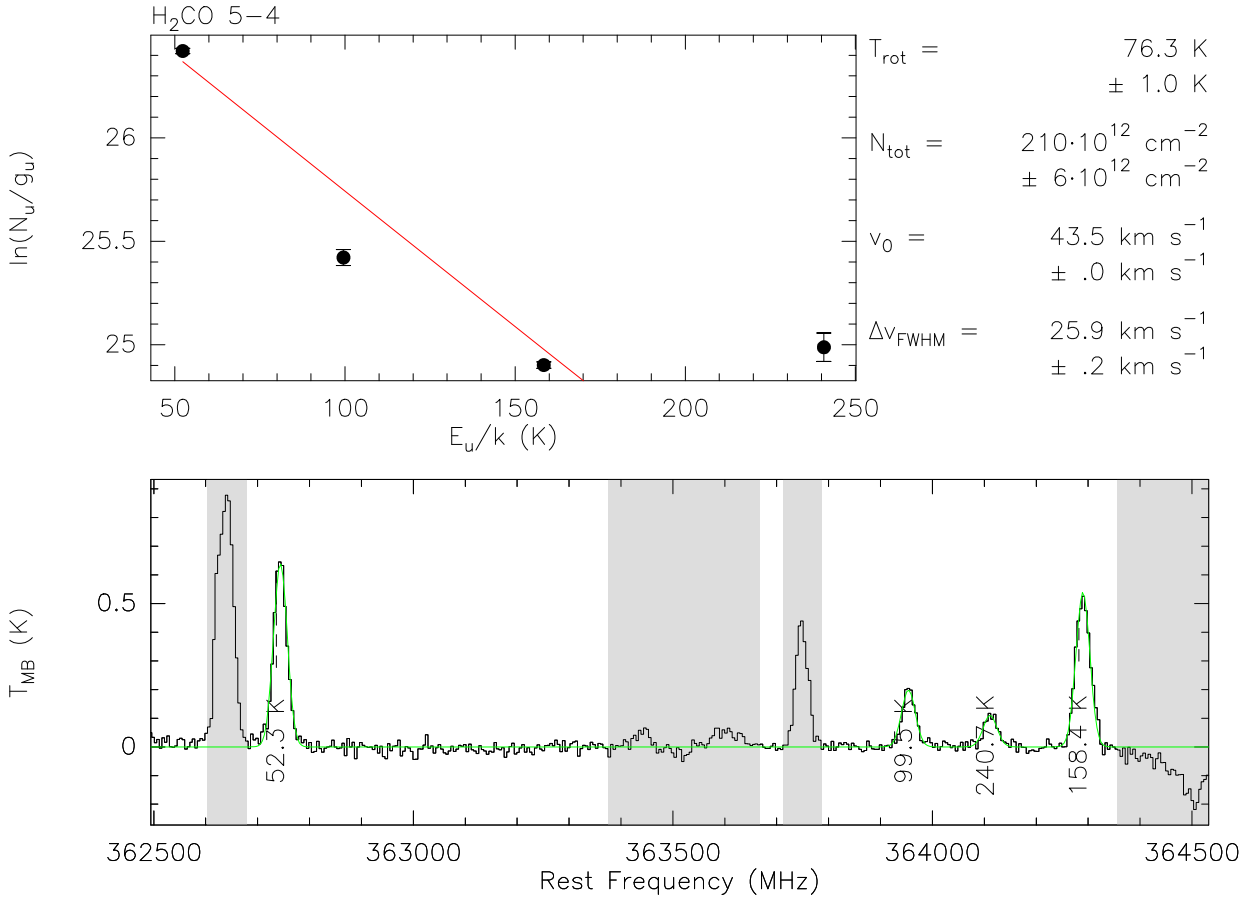

Figure 5.9.13: Spectrum (bottom) of a multiplet of H_2CO with transitions J=5-4 from the reduced survey of SgrA*$(+140, +70)$ and its population diagram (top). The spectrum includes a fit over the strongest transitions and masked spectral lines from other species that are highlighted in grey.

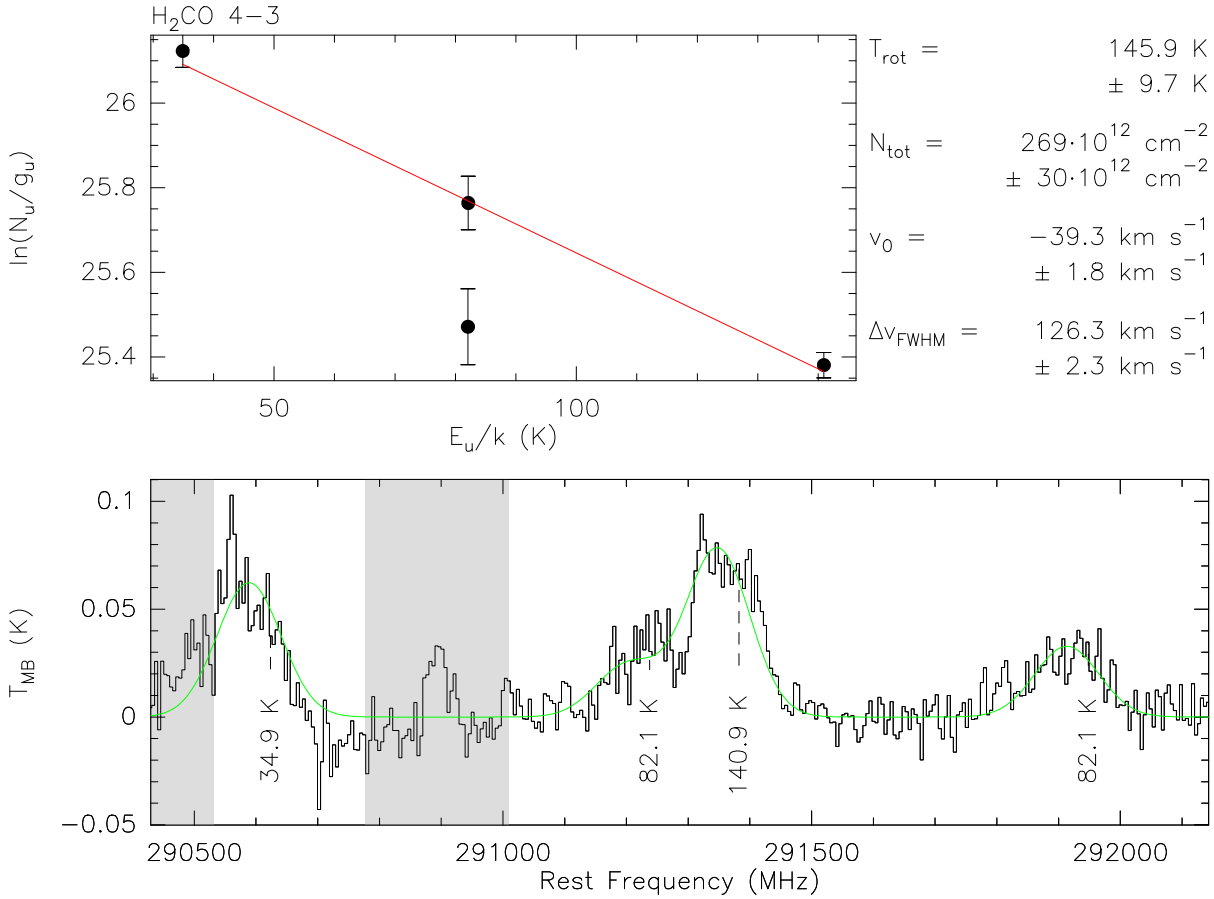

Figure 5.9.14: Spectrum (bottom) of a multiplet of H_2CO with transitions J=4-3 from the reduced survey of SgrA*$(-20, -30)$ and its population diagram (top). The spectrum includes a fit over the strongest transitions and masked spectral lines from other species that are highlighted in grey.

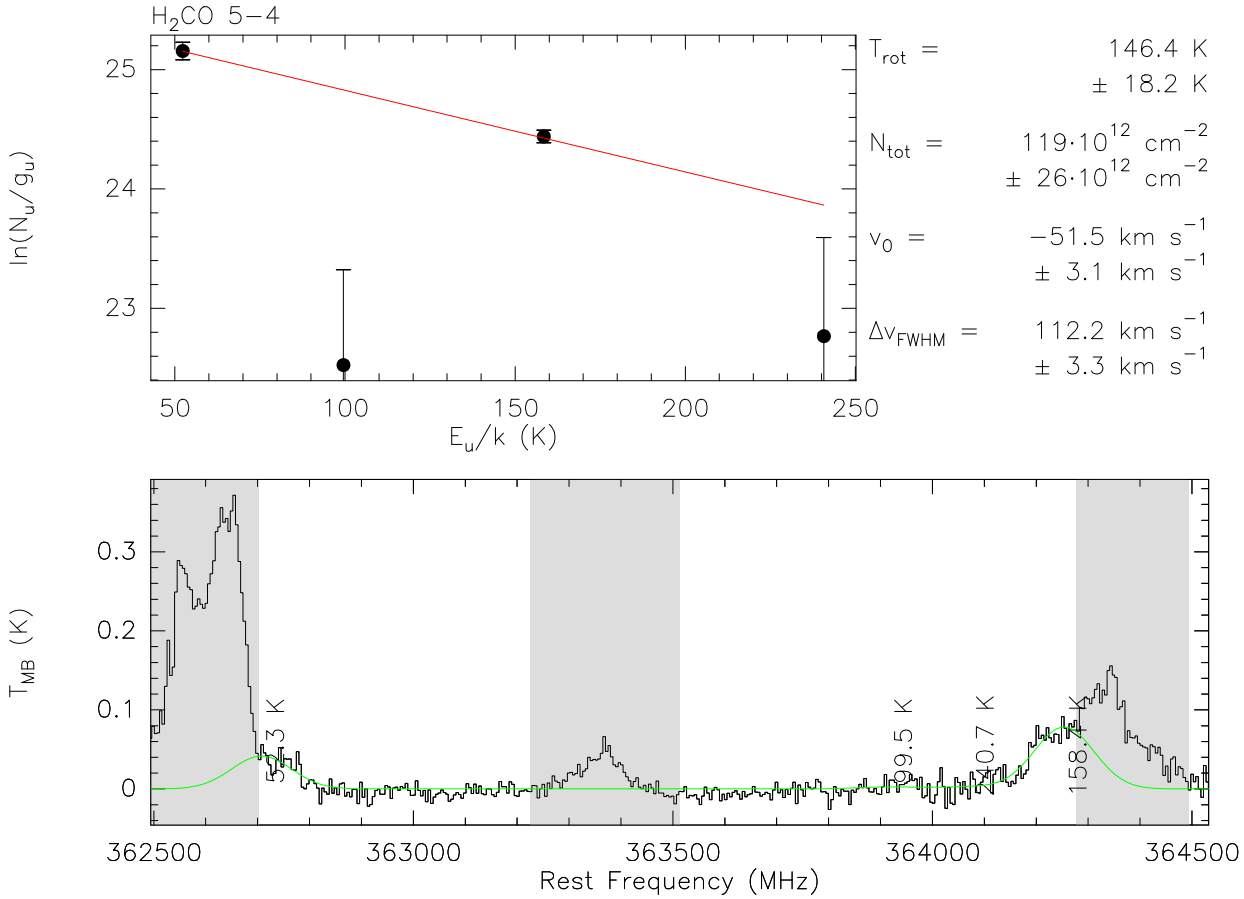

Figure 5.9.15: Spectrum (bottom) of a multiplet of H_2CO with transitions J=5-4 from the reduced survey of SgrA*$(-20, -30)$ and its population diagram (top). The spectrum includes a fit over the strongest transitions and masked spectral lines from other species that are highlighted in grey.

5.7 Density

Consistent with the results from CH_3CCH, CH_3CN, and partly H_2CO, previous observations of the $50\,\mathrm{km\,s^{-1}}$ cloud M-0.02-0.07 indicate a temperature of 100 K [34] or more [3, Ch. 4.3]. To explain the lower rotation temperature of CH_3OH and partly H_2CO, we can assume the requirements of (5.10), such as LTE, to be violated. The density of hydrogen $n(H_2)$ in the molecular cloud is a measure for the amount of potential collision partners of a molecule. Since collisions yield excitation, some excited states may be underpopulated if $n(H_2)$ is below a critical value n_{crit}, which depends on the ratio between Einstein coefficients A_{ul} and collision probabilities γ_{ul}. For a system with two states this yields [57, Ch. 2.1.4]:

$$n_{\mathrm{crit}} = \frac{A_{\mathrm{ul}}}{\gamma_{\mathrm{ul}}} \tag{5.12}$$

Such subthermal states do not follow the Boltzmann distribution from (5.9) and no LTE is attained. Since CH_3CCH is a symmetric top molecule, the excited states of a multiplet with equal quantum numbers J are affected similarly [10, Ch. 3.1]. The same is true for CH_3CN. Thus, the temperature T_{rot} that is derived from these population diagrams can be assumed to be a good estimate of the actual kinetic temperature T_{kin} of the cloud. For CH_3OH, however, higher excited states are underpopulated. Here, the fact that $n(H_2) < n_{\mathrm{crit}}$ causes $T_{\mathrm{rot}} < T_{\mathrm{kin}}$. Due to H_2CO's small asymmetry, the population diagrams of this molecule still allow a reasonable estimation of the temperature, although it slightly depends on the density [64, Ch. 4.1]. Since the ortho-to-para ratio of H_2CO is to some degree uncertain, only para-H_2CO transitions will be reconsidered along with CH_3OH.

Making assumptions for T_{kin}, $n(H_2)$, and N_{tot}, the RADEX software allows to calculate the population of each excited state under non-LTE conditions [95]. From the population diagrams of CH_3CCH and CH_3CN we can assume a common temperature $T_{\mathrm{kin}} = T_{\mathrm{rot}} \approx 130\,\mathrm{K}$. Adjusting the density $n(H_2)$ varies the relationship between the transitions of each multiplet and N_{tot} allows to adjust the average level of each multiplet. Assuming a common density, aside from the common temperature, $n \approx 2 \cdot 10^6\,\mathrm{cm^{-3}}$ yields the best fit for all multiplets of CH_3OH and H_2CO. The column densities need to be slightly varied around $N \approx 1 \cdot 10^{15}\,\mathrm{cm^{-2}}$ for CH_3OH and around $N \approx 8 \cdot 10^{13}\,\mathrm{cm^{-2}}$ for H_2CO. Figures 5.10.1 to 5.10.3 display the population diagrams from chapter 5.6, to which the populations from RADEX were added. Each parameter is varied independently to demonstrate the impact.

Consistent with the column densities that are found in chapter 5.6, the column densities of CH_3OH now decrease by a factor of ~ 4 with increasing frequency. According to (5.12) and (5.6), n_{crit} scales with A_{ul}, which scales with f_{ul}. Thus, the degree of subthermalization tends to increase with the frequency of the transitions and an even lower physical density could explain decreasing column densities. Figures 5.10.4 to 5.10.6 display another set of parameters, completed with slight variations: $n \approx 5 \cdot 10^4\,\mathrm{cm^{-3}}$ and $N \approx 3 \cdot 10^{15}\,\mathrm{cm^{-2}}$ fits for the transitions with lower energy levels in all multiplets of CH_3OH. The same is true with a common column density of $N \approx 8 \cdot 10^{14}\,\mathrm{cm^{-2}}$ for H_2CO. However, these parameters cannot explain the relation between the transitions of each multiplet: the populations of transitions with higher energy levels are extremely underestimated. To

Table 5.6: Physical parameters of possible components in the beam of SgrA*$(+140, +70)$.

component	$\mathbf{T_{rot}}$ (K)	$\mathbf{N_{tot,CH_3OH}}$ ($10^{12}\,\mathrm{cm}^{-2}$)	$\mathbf{N_{tot,H_2CO}}$ ($10^{12}\,\mathrm{cm}^{-2}$)	$\mathbf{n}\,(\mathrm{H}_2)$ ($10^{4}\,\mathrm{cm}^{-3}$)
A	130	$700 - 2800$	$40 - 80$	200
B_1	130	3200	800	5
B_2	130	$400 - 1600$	$40 - 80$	500

achieve consistency with the measured data points, requires a second component in the molecular cloud with a higher density than originally assumed. $n \approx 5 \cdot 10^6\,\mathrm{cm}^{-3}$ fits the higher energy transitions of each CH_3OH multiplet, such as shown in figures 5.10.7 to 5.10.9. However, no common column density fits for all multiplets: it needs to be decreased with increasing frequency again. Thus, both assumptions require varying column densities.

A possible explanation for column densities that vary with frequency is the beam filling factor. It depends on the relation between the solid angle of the source and of the antenna, and is part of (5.7). Since the size of the beam decreases with frequency, the beam filling factor of a compact source with a constant solid angle increases. However, we observe an opposite effect. An explanation for a beam filling factor that decreases with frequency would be a source at the border of the beam. Therefore, we can assume a region with increased column density that is increasingly missed by the beam, since it narrows with increasing frequency.

Thus, two models, which are summarized in table 5.6, can be distinguished. First, there may be one single component A with a physical density of $n \approx 2 \cdot 10^6\,\mathrm{cm}^{-3}$. However, the abundance of the analyzed molecules, increases to the edge of the beam, such that their average column density over the beam varies by a factor of ~ 4. Secondly, there may be two components. The thinner component B_1 extends over the beam and has a physical density of $n \approx 5 \cdot 10^4\,\mathrm{cm}^{-3}$ and a uniform column density. The denser component B_2 achieves $n \approx 5 \cdot 10^6\,\mathrm{cm}^{-3}$ and the analyzed molecules are concentrated at the edge of the beam to vary their average column density by a factor of ~ 4 again.

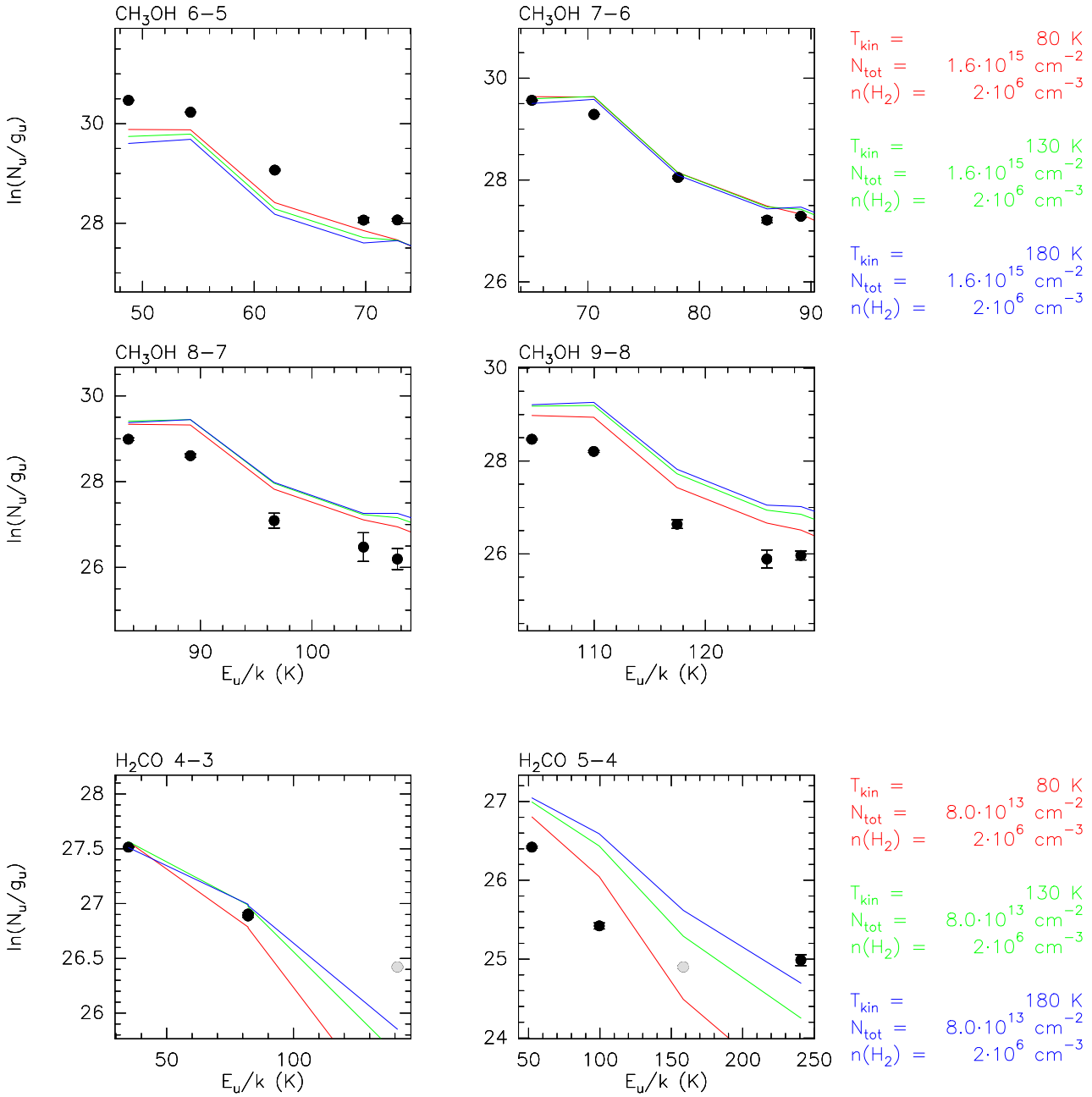

Figure 5.10.1: Upper level population versus upper level energy, calculated by RADEX, using an average density $n\,(\mathrm{H_2})$ and varying temperature T_{kin} to fit the population diagrams of CH_3OH (top) and H_2CO (bottom). The parameters of each RADEX calculation T_{kin}, N_{tot}, and $n\,(\mathrm{H_2})$ are listed in the color of the plot. Data points of ortho-H_2CO transitions are grey, due to an uncertain population ratio.

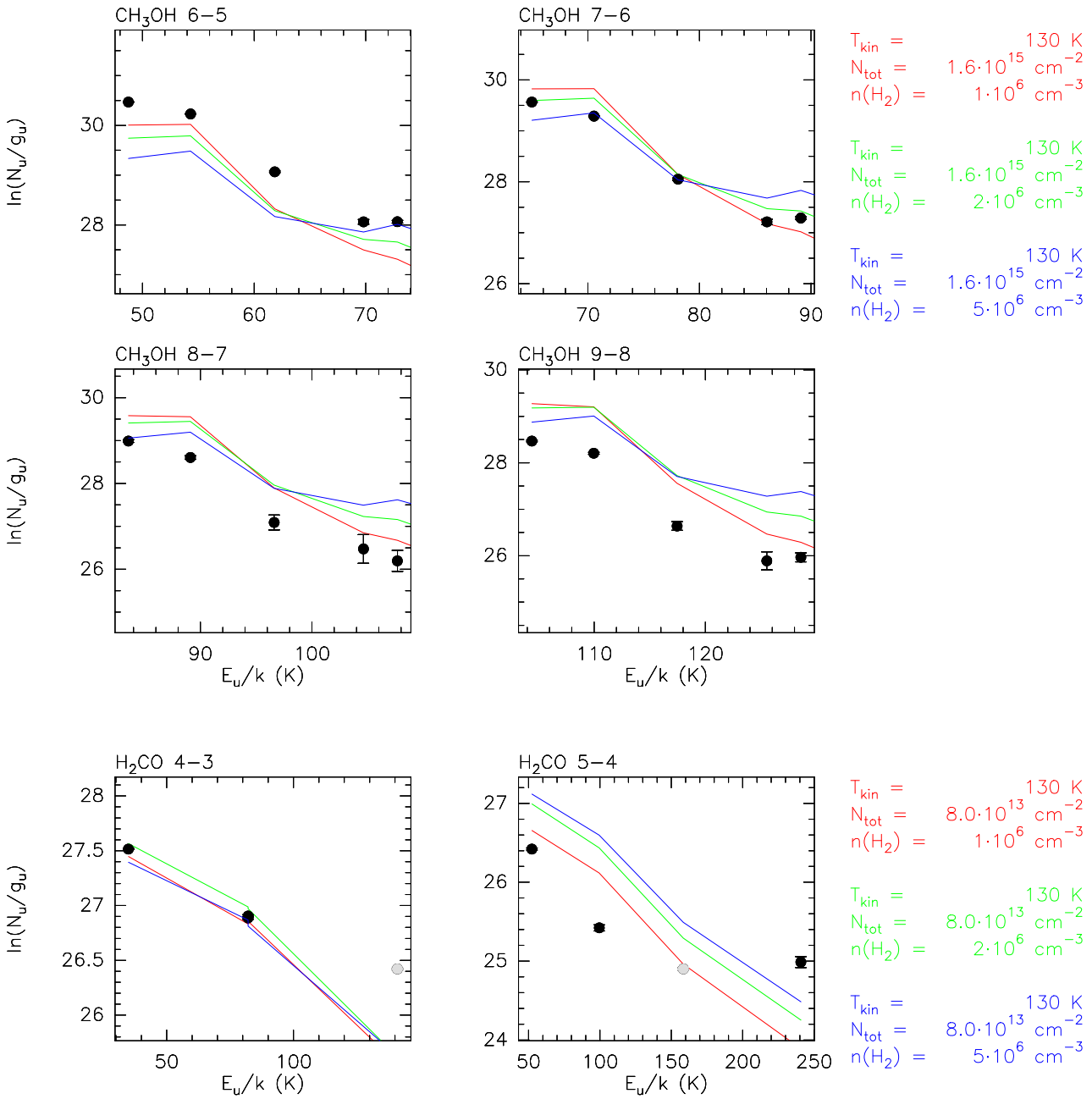

Figure 5.10.2: Upper level population versus upper level energy, calculated by RADEX, using an average density $n\,(\mathrm{H_2})$ and varying density $n\,(\mathrm{H_2})$ to fit the population diagrams of CH_3OH (top) and H_2CO (bottom). The parameters of each RADEX calculation T_{kin}, N_{tot}, and $n\,(\mathrm{H_2})$ are listed in the color of the plot. Data points of ortho-H_2CO transitions are grey, due to an uncertain population ratio.

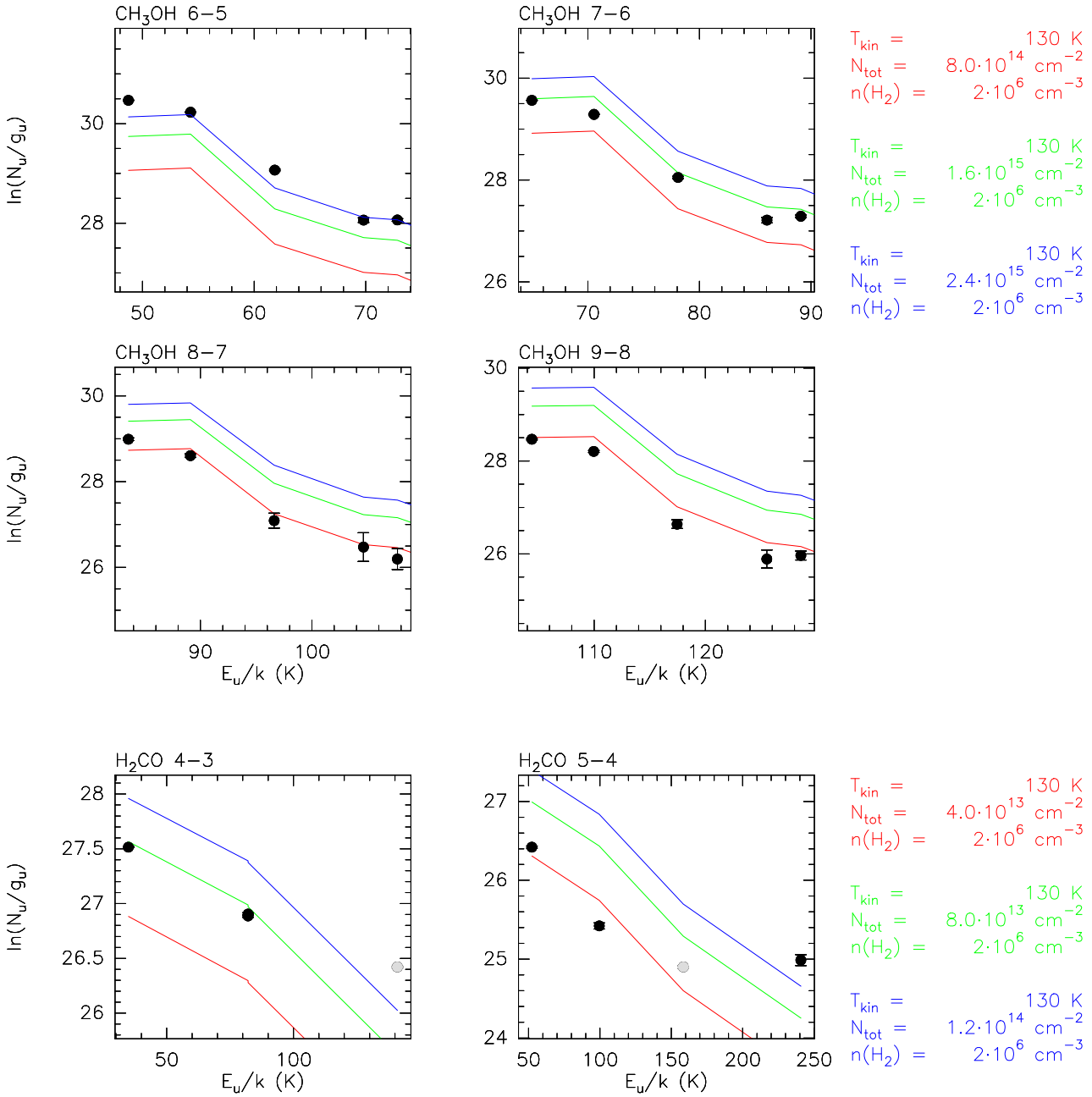

Figure 5.10.3: Upper level population versus upper level energy, calculated by RADEX, using an average density $n\,(\mathrm{H_2})$ and varying column density N_{tot} to fit the population diagrams of CH_3OH (top) and H_2CO (bottom). The parameters of each RADEX calculation T_{kin}, N_{tot}, and $n\,(\mathrm{H_2})$ are listed in the color of the plot. Data points of ortho-H_2CO transitions are grey, due to an uncertain population ratio.

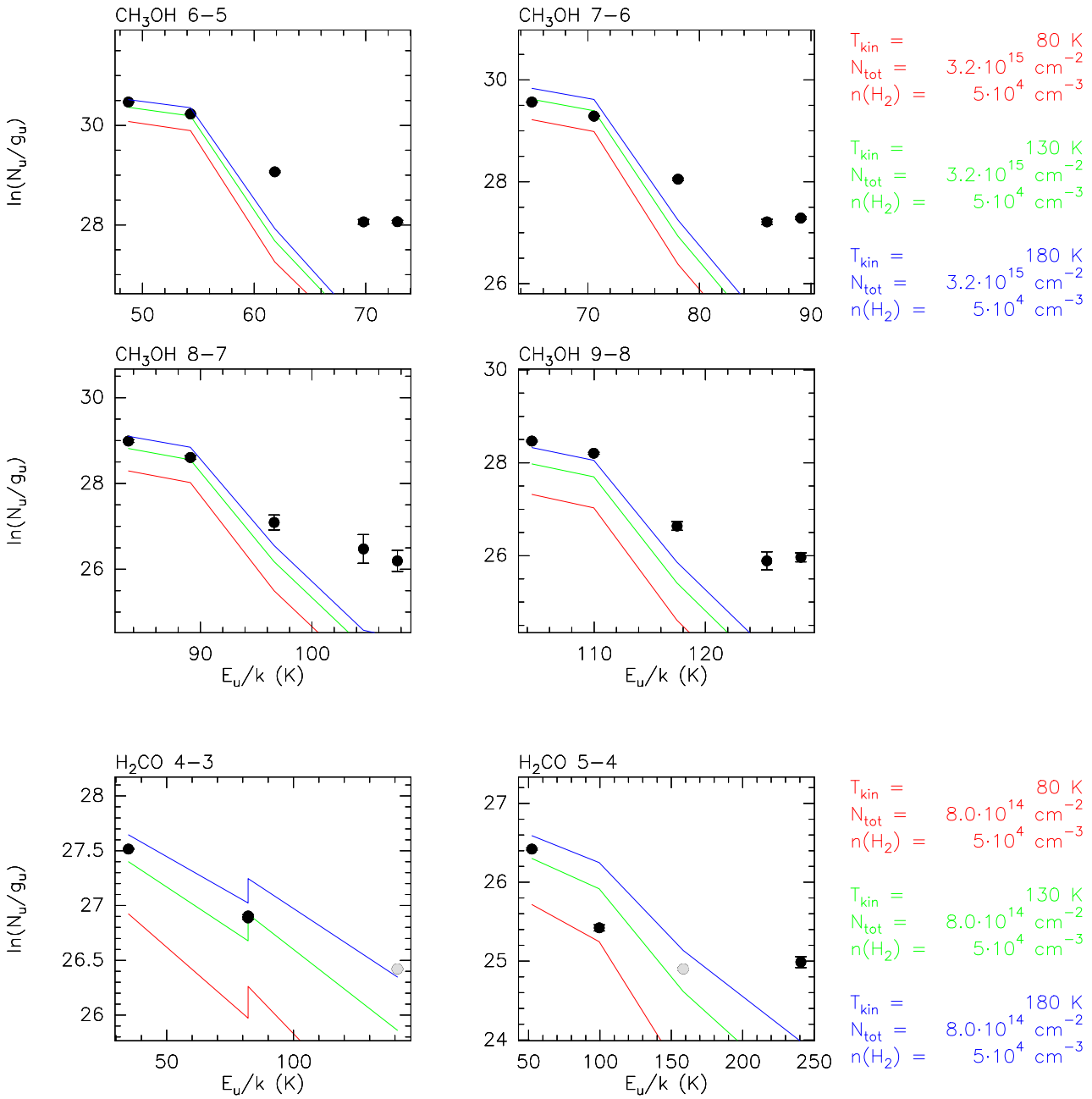

Figure 5.10.4: Upper level population versus upper level energy, calculated by RADEX, using a low density $n\,(\mathrm{H_2})$ and varying temperature T_{kin} to fit the population diagrams of CH_3OH (top) and H_2CO (bottom). The parameters of each RADEX calculation T_{kin}, N_{tot}, and $n\,(\mathrm{H_2})$ are listed in the color of the plot. Data points of ortho-H_2CO transitions are grey, due to an uncertain population ratio.

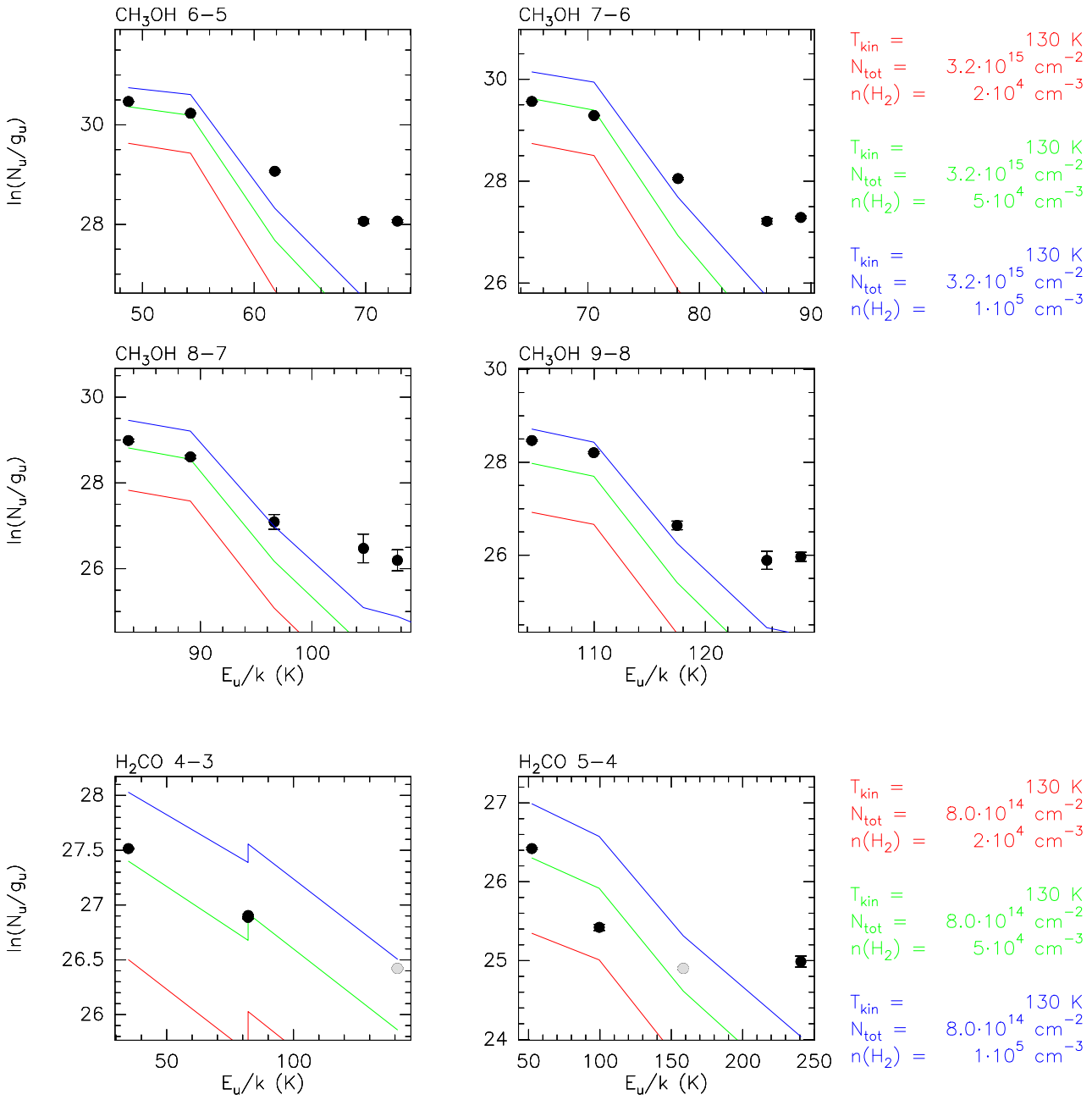

Figure 5.10.5: Upper level population versus upper level energy, calculated by RADEX, using a low density $n\,(\mathrm{H}_2)$ and varying density $n\,(\mathrm{H}_2)$ to fit the population diagrams of CH_3OH (top) and H_2CO (bottom). The parameters of each RADEX calculation T_{kin}, N_{tot}, and $n\,(\mathrm{H}_2)$ are listed in the color of the plot. Data points of ortho-H_2CO transitions are grey, due to an uncertain population ratio.

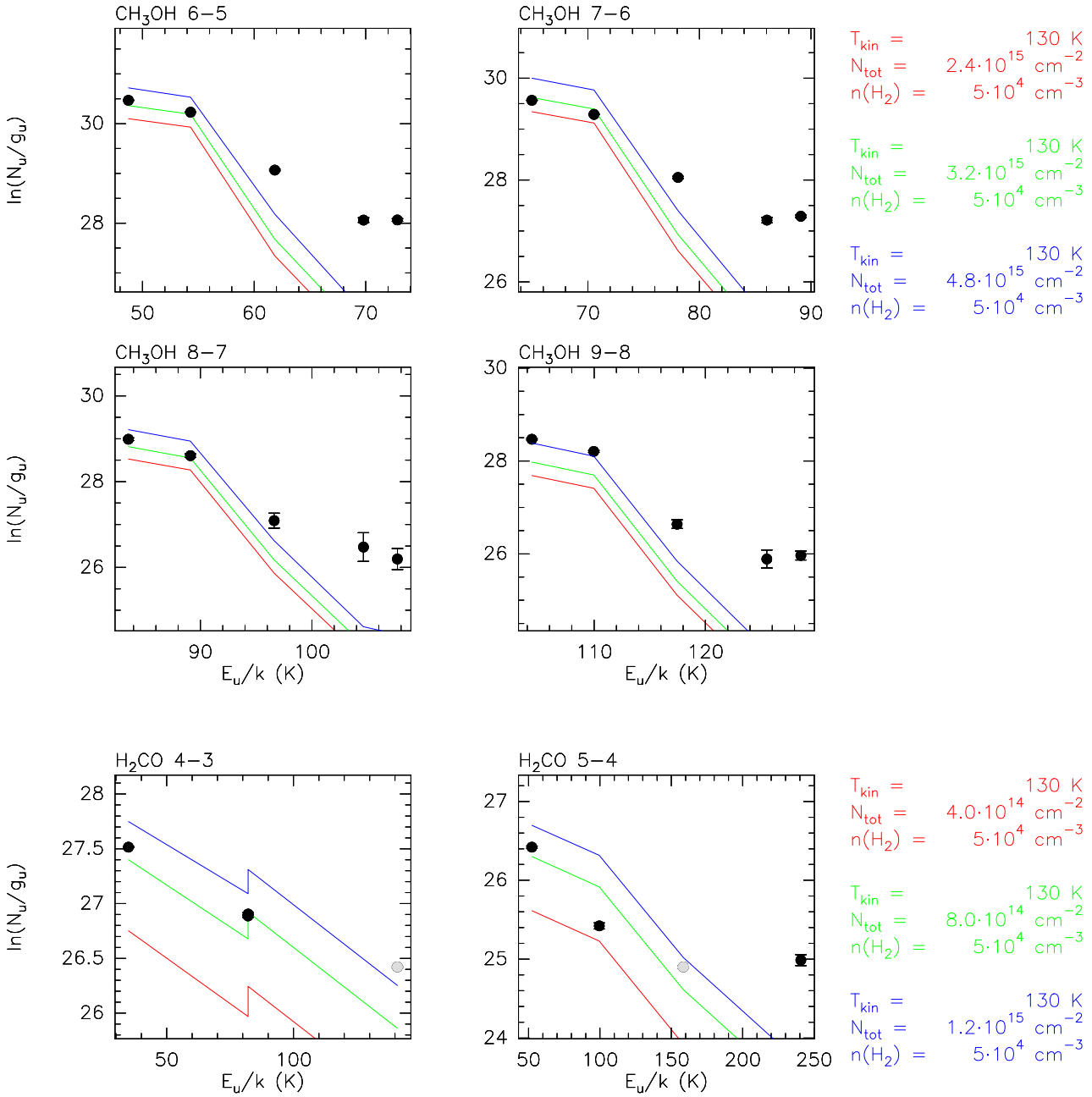

Figure 5.10.6: Upper level population versus upper level energy, calculated by RADEX, using a low density $n\,(\mathrm{H_2})$ and varying column density N_{tot} to fit the population diagrams of CH_3OH (top) and H_2CO (bottom). The parameters of each RADEX calculation T_{kin}, N_{tot}, and $n\,(\mathrm{H_2})$ are listed in the color of the plot. Data points of ortho-H_2CO transitions are grey, due to an uncertain population ratio.

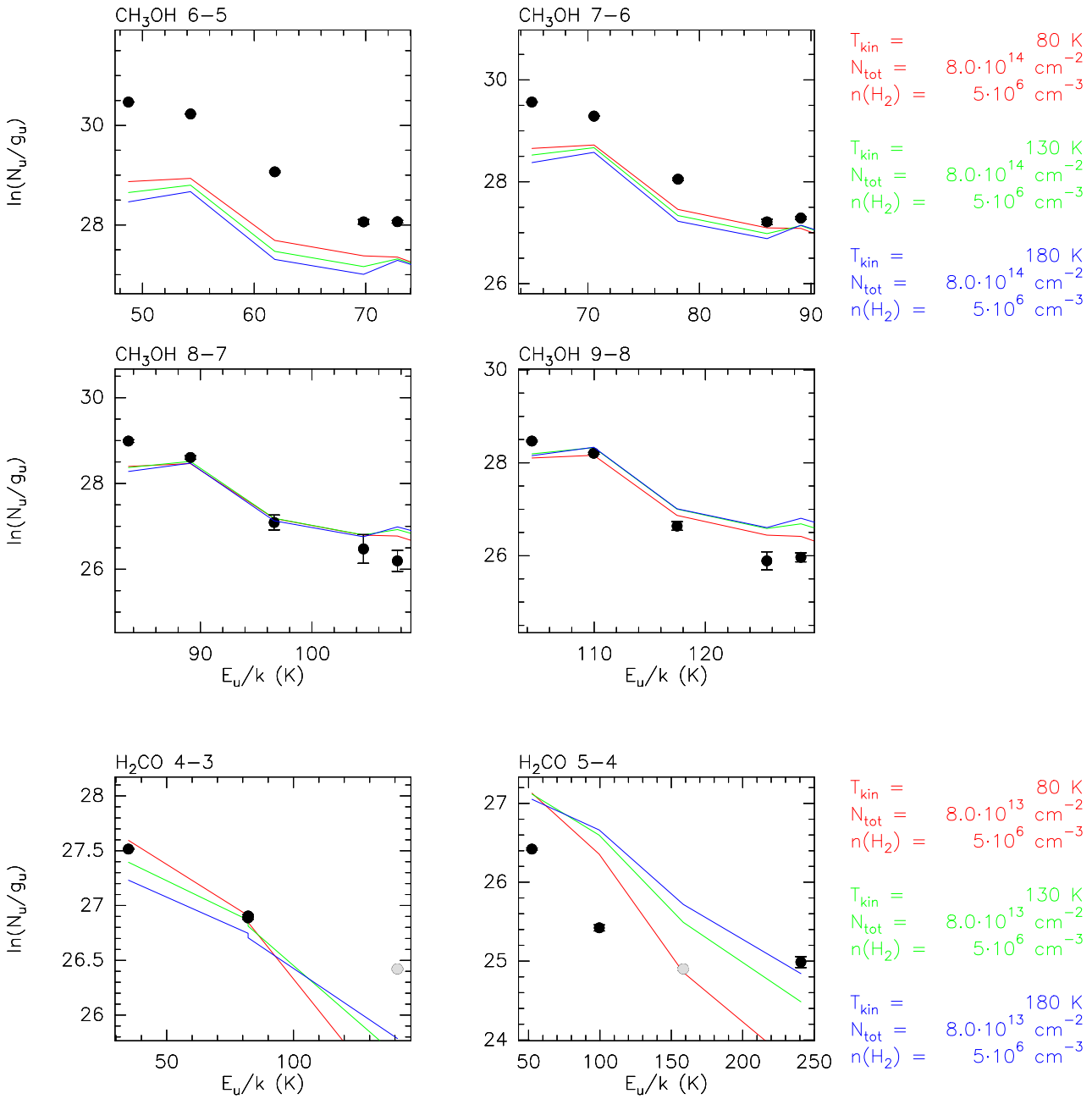

Figure 5.10.7: Upper level population versus upper level energy, calculated by RADEX, using a higher density $n\,(\mathrm{H_2})$ and varying temperature T_{kin} to fit the population diagrams of CH_3OH (top) and H_2CO (bottom). The parameters of each RADEX calculation T_{kin}, N_{tot}, and $n\,(\mathrm{H_2})$ are listed in the color of the plot. Data points of ortho-H_2CO transitions are grey, due to an uncertain population ratio.

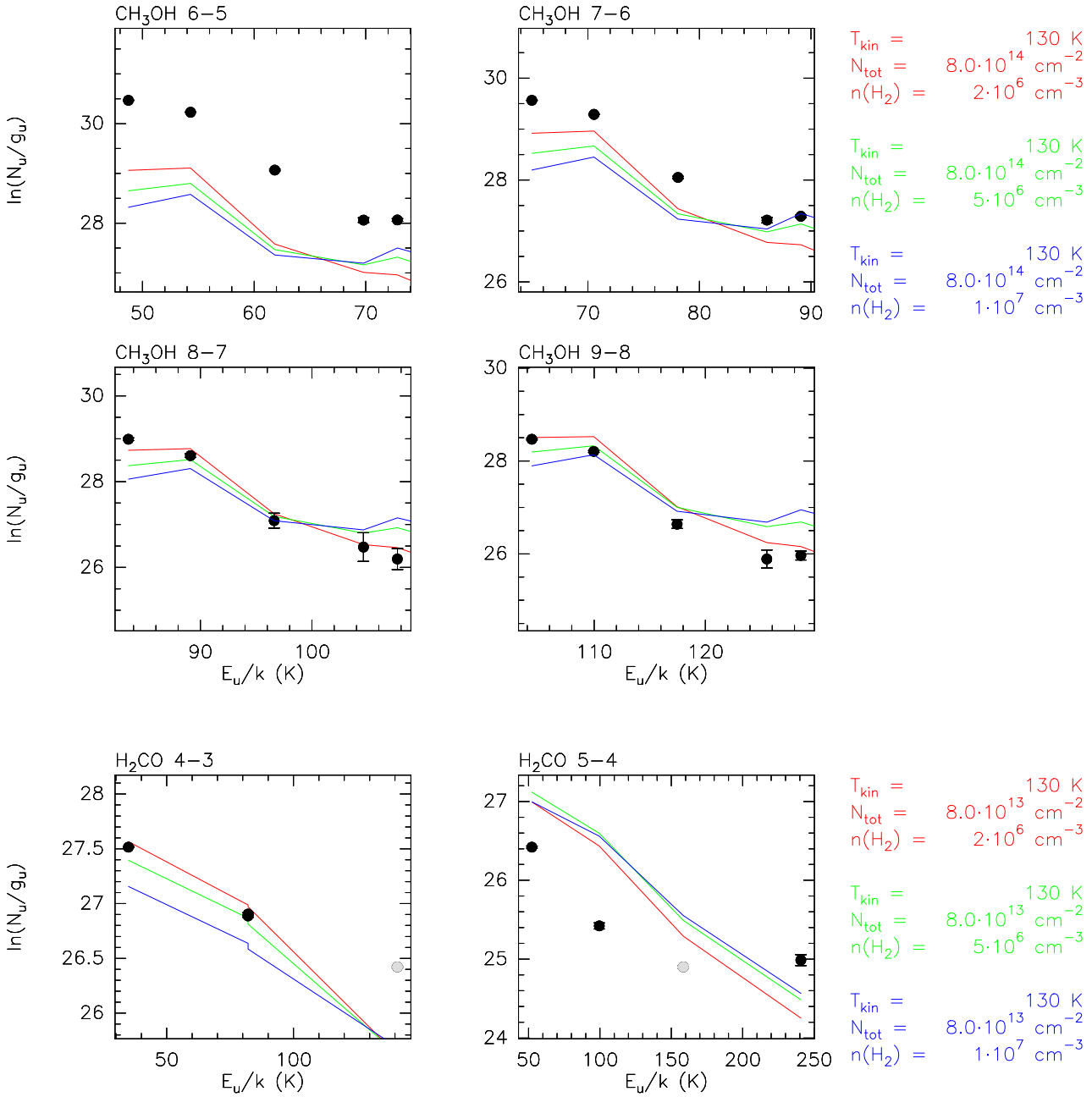

Figure 5.10.8: Upper level population versus upper level energy, calculated by RADEX, using a higher density $n\,(\mathrm{H_2})$ and varying density $n\,(\mathrm{H_2})$ to fit the population diagrams of CH_3OH (top) and H_2CO (bottom). The parameters of each RADEX calculation T_{kin}, N_{tot}, and $n\,(\mathrm{H_2})$ are listed in the color of the plot. Data points of ortho-H_2CO transitions are grey, due to an uncertain population ratio.

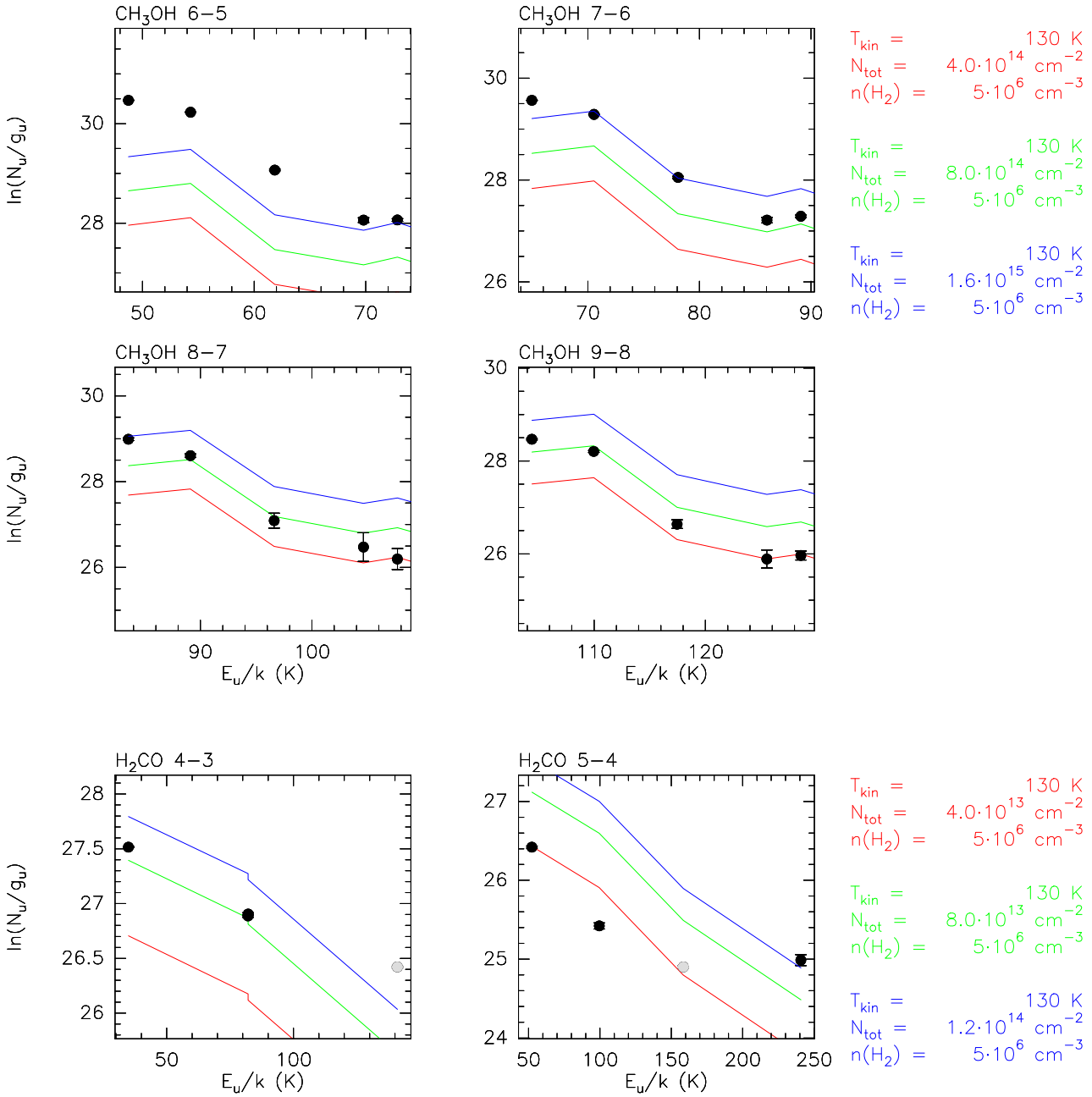

Figure 5.10.9: Upper level population versus upper level energy, calculated by RADEX, using a higher density $n\,(\mathrm{H_2})$ and varying column density N_{tot} to fit the population diagrams of CH_3OH (top) and H_2CO (bottom). The parameters of each RADEX calculation T_{kin}, N_{tot}, and $n\,(\mathrm{H_2})$ are listed in the color of the plot. Data points of ortho-H_2CO transitions are grey, due to an uncertain population ratio.

5.8 Discussion

As mentioned in chapter 5.1, the position of SgrA*$(+140, +70)$ was originally chosen as the peak of SiO emission in SgrA [65, Fig. 3]. With respect to the high abundance of this molecular tracer, the position was intended as a template for shocks [23, Ch. 7.2]. Figure 5.1 displays the position at the border of the SNR of SgrA-East with a gradient in 6 cm emission. The SNR SgrA-East and the 50 km s^{-1} GMC M-0.02-0.07 meet here, connected by a molecular ridge, which was originally considered a part of the 50 km s^{-1} cloud [24, Fig. 4]. However, mm and sub-mm continuum observations derived that the expanding shell of SgrA-East compresses the molecular cloud, which yields a shell with increased density in the region [67, Ch. 3.3]. To have an overview of the region, we overplot our position with the dust and molecular emission in the area. From the APEX Telescope Large Area Survey of the Galaxy (ATLASGAL) we can see the emission from dust, measured at 870 µm [88] by the Large APEX BOlometer CAmera (LABOCA) at the APEX telescope. For the molecular emission, we plot the emission of the CO and ^{13}CO molecules using the Carbon Heterodyne Array of the

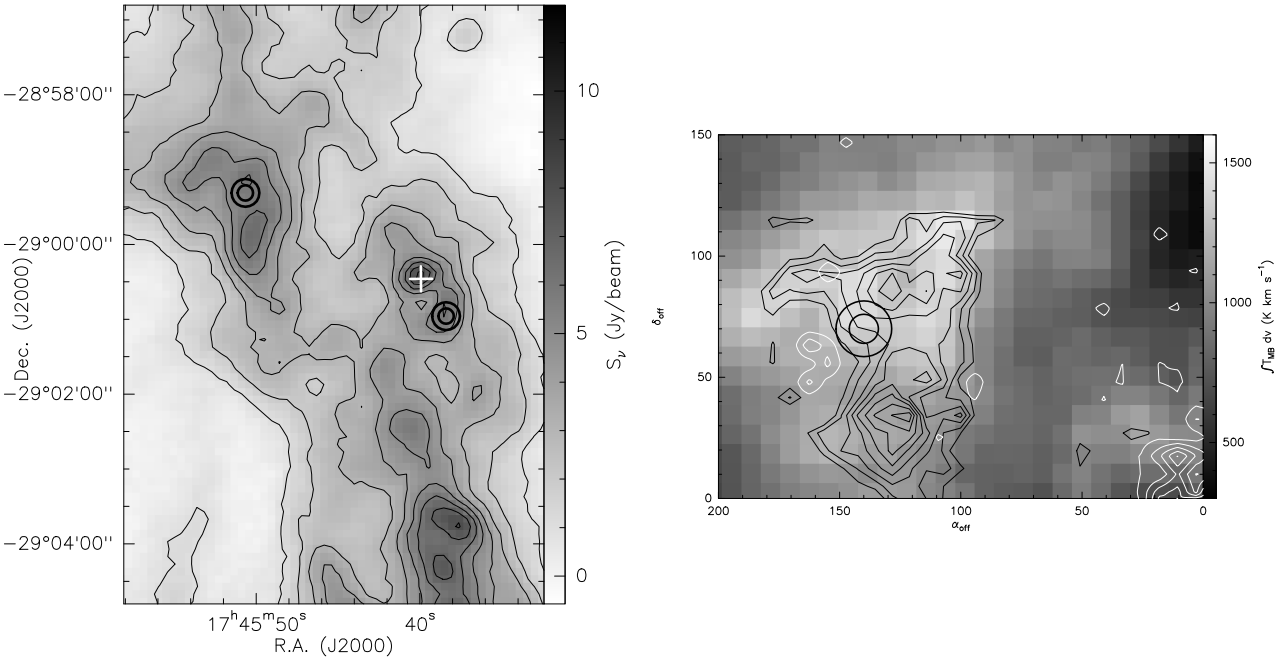

Figure 5.11: Maps of SgrA with high angular resolution. The left image zooms into a map of dust, which is derived from continuum emission at 870 µm with a beam size of $\sim 19''$ [88]. The right image shows the northeastern part of SgrA* in CO 6-5 (background), in ^{13}CO 6-5 (black contours), and in Paschen-α lines (white contours) [82, 19]. It is centered to SgrA* at the lower right corner and has an angular resolution of $\sim 9''$ for the CO lines. The white cross marks the position of SgrA*. The black circles mark the sources from chapter 5.1 and display the beam size between $\sim 23''$ and $\sim 12''$.

MPIfR (CHAMP) at the APEX telescope [82]. The map from ATLASGAL in figure 5.11 indicate a rather uniform dust emission. However, emission from ^{13}CO has a significant gradient over the beam. All in all, it is reasonable to assume a clumpy environment around the source, which supports the assumption of strong gradients of column density or of multiple components with different density.

Observations of CS emission lines around 300 GHz were used for a detailed analysis of the conditions in M-0.02-0.07 and its interaction with SgrA-East [89]. Assuming an average temperature of 70 K, the analysis found a peak density in the molecular ridge of $\sim 1.5 \cdot 10^6\,\mathrm{cm}^{-3}$ and an average density of $\sim 3 \cdot 10^4\,\mathrm{cm}^{-3}$ [89, Ch. 3]. This gradient is consistent with our assumptions for two components from table 5.6 if the ridge is located at the edge of our beam and the rest of the cloud fills the beam at any frequency. However, the absolute densities are by a factor 2 to 3 below our assumptions. The density we assumed for a single component is consistent with the findings from CS. This model would require, that only the molecular ridge is in the scope of our beam with an extreme gradient to lower column densities in the beam's center.

In the map of the CS lines we also find a velocity gradient over the whole cloud with a peak at $v_{\mathrm{LSR}} \approx 45\,\mathrm{km\,s}^{-1}$. Consistent with our findings from table 5.5, the angular position of the peak velocity coincides well with SgrA*$(+140, +70)$ [89, Fig. 3]. Previous observations of M-0.02-0.07 at frequencies around 200 GHz derived velocities of $\sim 46\,\mathrm{km\,s}^{-1}$ for CH_3OH and between $45\,\mathrm{km\,s}^{-1}$ and $53\,\mathrm{km\,s}^{-1}$ for other organic molecules [84, Tab. 3]. The width of the lines varied between $12\,\mathrm{km\,s}^{-1}$ and $27\,\mathrm{km\,s}^{-1}$, with constant $21\,\mathrm{km\,s}^{-1}$ for CH_3OH. The analysis of CH_3CN and NH_3 at mm and cm wavelengths in M-0.02-0.07 yielded velocities between $45\,\mathrm{km\,s}^{-1}$ and $48\,\mathrm{km\,s}^{-1}$ and line widths between $23\,\mathrm{km\,s}^{-1}$ and $25\,\mathrm{km\,s}^{-1}$ [34]. Since all these velocities are consistent with the results from table 5.5, there is no indication that our survey observed a different independent component. With respect to a velocity gradient, slight variations can, however, be explained by slightly different angular positions.

The aforementioned analysis of CH_3CN and NH_3 found temperatures higher than 100 K in the same molecular cloud [34]. Angular positions close to ours derived temperatures of $T_{\mathrm{rot}} \approx 109\,\mathrm{K}$ from NH_3 and $T_{\mathrm{ex,K}} \approx 100\,\mathrm{K}$ from CH_3CN. The peak temperature $T_{\mathrm{rot}} \approx 114\,\mathrm{K}$ was found from NH_3 southeast of the cloud center. Still, the value is slightly below our finding of $T_{\mathrm{kin}} \approx 130\,\mathrm{K}$. A more recent analysis of NH_3 lines at 23 GHz to 25 GHz derived two temperature components in the molecular gas of SgrA [37, Ch. 5.1]. Different transitions of the species yield a temperature of only $T \approx 21\,\mathrm{K}$ and a lower temperature limit $T_{\mathrm{kin}} > 90\,\mathrm{K}$ for the $50\,\mathrm{km\,s}^{-1}$ GMC. Two components with 15 K and 200 K were modeled to explain the difference in the presence of LTE. To assure LTE a physical density $n\,(\mathrm{H}_2) > 10^5\,\mathrm{cm}^{-3}$ is assumed, which would be consistent with our upper density assumptions. However, we observed different temperatures from different species, particularly CH_3OH, not between different transitions of the same species. Transfered to our measurements, this model would require different molecular abundances in a hot and a cold component. Figure 5.10.8 displays that CH_3OH is still significantly affected by varying densities up to $n\,(\mathrm{H}_2) > 10^7\,\mathrm{cm}^{-3}$, which indicates an even higher critical density n_{crit}. Therefore it seems more reasonable to the author to assume non-LTE conditions to explain the lower temperature found by population diagrams

of CH_3OH in table 5.5. Consistent with our results, a recent analysis of H_2CO lines also found temperatures well above 100 K at certain positions of the SgrA complex. In fact, the highest temperature in the survey $T_{\rm kin} > 250\,{\rm K}$ has been found at SgrA*$(+135, +90)$, which is the position that is closest to our source SgrA*$(+140, +70)$.

We can conclude that the temperature of $T_{\rm kin} \approx 130\,{\rm K}$ that was found for SgrA*$(+140, +70)$ is somewhat higher than previous temperature estimations at the position [34], but consistent with recent findings in the SgrA complex. Due to very broad lines, SgrA*$(-20, -30)$ yields population diagrams that are affected by blends between the lines. Of course this implies an increased uncertainty of the results from the two remaining population diagrams of H_2CO in figures 5.9.14 and 5.9.14. However, both indicate a temperature $T_{\rm rot} \approx 146\,{\rm K}$, which is also well above 100 K. Therefore, we can safely assume a temperature of $T_{\rm kin} \approx 130\,{\rm K}$ at SgrA*$(+140, +70)$ and possibly higher at SgrA*$(-20, -30)$.

Further on, an increased density of $n\,({\rm H_2}) > 2 \cdot 10^6\,{\rm cm^{-3}}$ can be expected at least at the edge of our beam, which probably coincides with a part of the molecular ridge. This is somewhat denser than previous assumptions, that have been found from the analysis of spectral lines at lower frequencies with lower critical densities [89]. Compared to space averaged densities of a few $10^4\,{\rm cm^{-3}}$, it is orders of magnitude more dense [24, Tab. 2]. A single component, such as listed in table 5.6, can be explained by an extended component that fills the beam with a uniform density of $2 \cdot 10^6\,{\rm cm^{-3}}$, but shaped, such that column density significantly varies over the beam. A second explanation is an isolated component of that density at the edge of the beam and no significant emission in the center of the beam. With respect to these explanations, the presence of two components seems more likely to the author. The thinner could be part of the molecular cloud M-0.02-0.07 and uniformly fills the beam. The denser concentrates at the edge of the beam as part of the molecular ridge. According to table 5.6, both components would be a factor of 2-3 more dense than found from less excited CS lines [89].

Chapter 6

Conclusion and Further Work

Based on concepts and algorithms that were optimized for the design of a fast Fourier transform spectrometer (FFTS), this thesis presented two spectral line surveys of the Galactic Center (GC) and analyzed the physical properties of the observed sources.

Chapter 2 gave an overview of the basic principles behind the operation of a spectrometer. The thesis explained, in particular, the mathematical properties of the fast Fourier transform (FFT), the benefit of integration, the concept of windows and weighted overlap-add (WOLA) to limit leakage, and the effects of interleaving.

In chapter 3, different astronomical applications of spectrometers were described, and their requirements were evaluated. Besides the main application of wideband spectroscopy, the demands of high resolution spectroscopy, of an incoherent pulsar search, and of a readout for microwave kinetic inductance detectors (MKIDs) were specified.

After defining the components of an FFTS and their purpose, the technical requirements of each component were described, and algorithms or implementations were discussed accordingly in chapter 4. Concepts were developed to partition algorithms between the field-programmable gate array (FPGA) and the personal computer (PC). These concepts led to simple, hardware-efficient components inside the FPGA, that allow to measure and correct errors from high-speed data capture or from interleaving of multiple analog-to-digital converters (ADCs). To achieve both, high bandwidth and high spectral resolution, parallel and pipelined algorithms were combined. The hardware utilization and the flexibility of different such FFT architectures were compared, dependent on the significance of either bandwidth or resolution. Control mechanisms were developed and implemented to function in different time frames, dependent on the application. As an example for successful high-speed operation, the recent detection of a millisecond pulsar was presented. With respect to new applications with varied requirements, future work may reconsider previously disregarded concepts, algorithms or implementations, e.g. to improve memory occupation or bit accuracy under new conditions.

As an application for the high-resolution wideband spectrometer, that was developed using the presented concepts, two unbiased spectral line surveys in the Galactic Center region were performed. Chapter 5 presents data from the two sources in the Sagittarius A (SgrA) complex that were observed:

SgrA*$(-20, -30)$ in the southern part of the circumnuclear disk (CND) around the supermassive black hole (SMBH) of SgrA*, and SgrA*$(+140, +70)$ in a shock region between the supernova remnant (SNR) of SgrA-East and the giant molecular cloud (GMC) M-0.02-0.07, which are connected by a molecular ridge of higher density. Each survey contains hundreds of spectral lines, that provide information about the respective source. A large fraction of the lines was identified, and marked in the spectra of each survey to compare both sources. The intensity of each line was calculated and listed accordingly. As good molecular tracers of physical properties, such as the temperature, CH_3OH, H_2CO, CH_3CCH, and CH_3CN were chosen and analyzed by gaussian fits and by population diagrams. Common velocities, which are close to values from previous analysis, were found for each source. With respect to broad, blended lines from SgrA*$(-20, -30)$, that add uncertainty, further analysis concentrated on SgrA*$(+140, +70)$. Since particularly the analysis of CH_3OH derived temperatures that were inconsistent to the other findings, the absence of local thermodynamic equilibrium (LTE) was assumed, as well as a kinetic temperature of $T_{\mathrm{kin}} \approx 130\,\mathrm{K}$, which was derived from the other species. These assumptions led to two models about the nature of the source: First, one component, which has a physical density of $n\,(\mathrm{H_2}) \approx 2 \cdot 10^6\,\mathrm{cm^{-3}}$, and which is concentrated at the edge of the beam of the telescope, was assumed. The second model assumes two components with different densities. The thinner component, with $n\,(\mathrm{H_2}) \approx 5 \cdot 10^4\,\mathrm{cm^{-3}}$, is uniformly distributed and may reflect the GMC of M-0.02-0.07. The thicker component, with $n\,(\mathrm{H_2}) \approx 5 \cdot 10^6\,\mathrm{cm^{-3}}$, again concentrates at the edge of our beam and may reflect a clumped part of the molecular ridge.

The second model is preferred by the author, since it is more consistent with previous results and reflects a more probable spatial arrangement in a dense environment. A more precise analysis of the region demands a map of densities with high angular resolution. Interferometric observations using the Atacama Large Millimeter/submillimeter Array (ALMA) could provide such data. However, the present survey already provides a legacy of data. Further work could eventually access additional information, e.g. by utilizing the full spectral resolution, by combining data over the full spectral range, or by analyzing so far unidentified lines. With defined values for temperature and density, the column densities of other species can be derived and the chemical composition of the sources in this thesis can be compared to each other and to other sources, such as the well studied Orion KL [87]. This may help to identify typical conditions and heating mechanisms in molecular clouds and lead to a better understanding of galactic nuclei in general.

Bibliography

[1] A-MKID - a large incoherent camera for APEX. http://www3.mpifr-bonn.mpg.de/div/submmtech/bolometer/A-MKID/a-mkidmain.html.

[2] The Atacama Large Millimeter/submillimeter Array (ALMA). http://www.almaobservatory.org.

[3] Y. Ao, C. Henkel, K. M. Menten, M. A. Requena-Torres, T. Stanke, R. Mauersberger, S. Aalto, S. Muehle, and J. Mangum. The thermal state of molecular clouds in the Galactic center: evidence for non-photon-driven heating. *Astronomy & Astrophysics*, 2012.

[4] The Atacama Pathfinder EXperiment (APEX). http://www.apex-telescope.org.

[5] P. Aufmuth, R. Gilmozzi, D. Lemke, J. E. Trümper, D. Müller, G. Mann, M. H. Soffel, K. Wilhelm, R. Staubert, K. Zuber, et al. *Instruments and Methods*. Number Bd. 4 in Landolt-Börnstein: Numerical Data and Functional Relationships in Science and Technology - New Series / Astronomy and Astrophysics. Springer, 2010.

[6] E. D. Barr, L. Guillemot, D. J. Champion, M. Kramer, R. P. Eatough, K. J. Lee, J. P. W. Verbiest, C. G. Bassa, F. Camilo, Ö. Çelik, I. Cognard, E. C. Ferrara, P. C. C. Freire, G. H. Janssen, S. Johnston, M. Keith, A. G. Lyne, P. F. Michelson, P. M. S. Parkinson, S. M. Ransom, P. S. Ray, B. W. Stappers, and K. S. Wood. Pulsar searches of fermi unassociated sources with the Effelsberg telescope. *Monthly Notices of the Royal Astronomical Society*, page 410, dec 2012.

[7] J. J. A. Baselmans, S. J. C. Yates, P. de Korte, H. Hoevers, R. Barends, J. N. Hovenier, J. R. Gao, and T. M. Klapwijk. Development of high-Q superconducting resonators for use as kinetic inductance detectors. *Advances in Space Research*, 40(5):708–713, 2007.

[8] Jochem Baselmans. Kinetic inductance detectors. *Journal of Low Temperature Physics*, 167:292–304, 2012.

[9] A. O. Benz, P. C. Grigis, V. Hungerbühler, H. Meyer, C. Monstein, B. Stuber, and D. Zardet. A broadband FFT spectrometer for radio and millimeter astronomy. *Astronomy & Astrophysics*, 442(2):767–773, sep 2005.

[10] E. A. Bergin, P. F. Goldsmith, R. L. Snell, and H. Ungerechts. CH3C2H as a temperature probe in dense giant molecular cloud cores. *The Astrophysical Journal*, 431:674–688, aug 1994.

[11] E. A. Bergin, T. G. Phillips, C. Comito, N. R. Crockett, D. C. Lis, P. Schilke, S. Wang, T. A. Bell, G. A. Blake, B. Bumble, E. Caux, S. Cabrit, C. Ceccarelli, J. Cernicharo, F. Daniel, Th. de Graauw, M.-L. Dubernet, M. Emprechtinger, P. Encrenaz, E. Falgarone, M. Gerin, T. F. Giesen, J. R. Goicoechea, P. F. Goldsmith, H. Gupta, P. Hartogh, F. P. Helmich, E. Herbst, C. Joblin, D. Johnstone, J. H. Kawamura, W. D. Langer, W. B. Latter, S. D. Lord, S. Maret, P. G. Martin, G. J. Melnick, K. M. Menten, P. Morris, H. S. P. Müller, J. A. Murphy, D. A. Neufeld, V. Ossenkopf, L. Pagani, J. C. Pearson, M. Pérault, R. Plume, P. Roelfsema, S.-L. Qin, M. Salez, S. Schlemmer, J. Stutzki, A. G. G. M. Tielens, N. Trappe, F. F. S. van der Tak, C. Vastel, H. W. Yorke, S. Yu, and J. Zmuidzinas. Herschel observations of EXtra-Ordinary Sources (HEXOS): The present and future of spectral surveys with Herschel/HIFI. *Astronomy & Astrophysics*, 521:L20, 2010.

[12] S. Boyd. Multitone signals with low crest factor. *Circuits and Systems, IEEE Transactions on*, 33(10):1018–1022, oct 1986.

[13] E. Oran Brigham. *FFT Schnelle Fourier-Transformation*. Einführung in die Nachrichtentechnik. Oldenbourg, Munich, 1982.

[14] R. L. Brown and H. S. Liszt. Sagittarius A and its environment. *Annual Review of Astronomy and Astrophysics*, 22(1):223–265, 1984.

[15] P. Caselli, P. C. Myers, and P. Thaddeus. Radio-astronomical spectroscopy of the hyperfine structure of N 2H +. *The Astrophysical Journal*, 455:L77, dec 1995.

[16] CHAMP+: The Carbon Heterodyne Array of the MPIfR. http://www3.mpifr-bonn.mpg.de/div/submmtech/heterodyne/champplus/champmain.html.

[17] James W. Cooley and John W. Tukey. An algorithm for the machine calculation of complex Fourier series. *Mathematics of Computation*, 19(90):297–301, 1965.

[18] Peter K. Day, Henry G. LeDuc, Benjamin A. Mazin, Anastasios Vayonakis, and Jonas Zmuidzinas. A broadband superconducting detector suitable for use in large arrays. *Nature*, 425(6960):817–821, oct 23, 2003.

[19] H. Dong, Q. D. Wang, A. Cotera, S. Stolovy, M. R. Morris, J. Mauerhan, E. A. Mills, G. Schneider, D. Calzetti, and C. Lang. Hubble Space Telescope Paschen α survey of the Galactic Center: data reduction and products. *Monthly Notices of the Royal Astronomical Society*, 417:114–135, oct 2011.

[20] e2v semiconductors, http://www.e2v.com. *EV10AQ190A Low power QUAD 10-bit 1.25 Gsps ADC Operating up to 5 Gsps*, 1070a-bdc edition, oct 2011.

[21] R. P. Eatough, M. Kramer, B. Klein, R. Karuppusamy, D. J. Champion, P. C. C. Freire, N. Wex, and K. Liu. Can we see pulsars around Sgr A*? - the latest searches with the Effelsberg telescope. *ArXiv e-prints*, oct 2012.

[22] Effelsberg telescope at Max Planck Institut für Radioastronomie (MPIfR). http://www.mpifr-bonn.mpg.de/effelsberg/.

[23] Rebeca Aladro Fernández. *Circumnuclear activity in galaxies and its influence on the physics and chemistry of the surrounding molecular gas*. PhD thesis, Universidad de Granada, 2011.

[24] K. Ferrière. Interstellar gas within 10 pc of Sagittarius A*. *Astronomy & Astrophysics*, 540:A50, 2012.

[25] FLASH First Light APEX Submillimeter Heterodyne receiver. http://www3.mpifr-bonn.mpg.de/div/submmtech/heterodyne/flash/flashmain.html.

[26] L. Flöer, B. Winkel, and J. Kerp. RFI mitigation for the Effelsberg Bonn HI Survey (EBHIS. In *RFI Mitigation Workshop*, 2010.

[27] Roberto G. García, Olivier Gentaza, Maryse Baldinoa, and Marc Torresa. An 8 GHz digital spectrometer for millimeter-wave astronomy. In Wayne S. Holland and Jonas Zmuidzinas, editors, *Millimeter, Submillimeter, and Far-Infrared Detectors and Instrumentation for Astronomy VI*, volume 8452. SPIE, 2012.

[28] Reinhard Genzel, Frank Eisenhauer, and Stefan Gillessen. The galactic center massive black hole and nuclear star cluster. *Reviews of Modern Physics*, 82:3121–3195, Dec 2010.

[29] GILDAS. http://www.iram.fr/IRAMFR/GILDAS/.

[30] Paul F. Goldsmith and William D. Langer. Population diagram analysis of molecular line emission. *The Astrophysical Journal*, 517(1):209, 1999.

[31] The German REceiver for Astronomy at Terahertz frequencies (GREAT). http://www3.mpifr-bonn.mpg.de/div/submmtech/great.html.

[32] R. Güsten, R. Genzel, M. C. H. Wright, D. T. Jaffe, J. Stutzki, and A. I. Harris. Aperture synthesis observations of the circumnuclear ring in the Galactic center. *The Astrophysical Journal*, 318:124–138, jul 1987.

[33] R. Güsten, L.-Å. Nyman, P. Schilke, K. Menten, C. Cesarsky, and R. Booth. The Atacama Pathfinder EXperiment (APEX) - a new submillimeter facility for southern skies. *Astronomy & Astrophysics*, 454(2):L13–L16, 2006.

[34] R. Güsten, C. M. Walmsley, H. Ungerechts, and E. Churchwell. Temperature determinations in molecular clouds of the galactic center. *Astronomy & Astrophysics*, 142:381–387, jan 1985.

[35] F. J. Harris. On the use of windows for harmonic analysis with the discrete Fourier transform. *Proceedings of the IEEE*, 66(1):51–83, jan 1978.

[36] G. Heinzel, A. Rüdiger, and R. Schilling. Spectrum and spectral density estimation by the discrete Fourier transform (DFT), including a comprehensive list of window functions and some new flat-top windows . *Max Plank Institute*, pages 1–84, feb 15, 2002.

[37] Robeson M. Herrnstein and Paul T. P. Ho. The nature of the molecular environment within 5 parsecs of the galactic center. *The Astrophysical Journal*, 620(1):287, 2005.

[38] S. Heyminck, U. U. Graf, R. Güsten, J. Stutzki, H. W. Hübers, and P. Hartogh. GREAT: the SOFIA high-frequency heterodyne instrument. *Astronomy & Astrophysics*, 542:L1, 2012.

[39] S. Heyminck, C. Kasemann, R. Güsten, G. de Lange, and U. U. Graf. The first-light APEX submillimeter heterodyne instrument FLASH. *Astronomy & Astrophysics*, 454(2):L21–L24, 2006.

[40] Stefan Hochgürtel and Bernd Klein. Space-efficient FPGA-implementations of FFTs in high-speed applications. In Lennart Lindh, editor, *Proceedings of the 5th FPGAworld Conference, Stockholm, Sweden*, pages 26–31, http://urn.kb.se/resolve?urn=urn:nbn:se:hj:diva-6563, sep 11, 2008. Jönköping University.

[41] IEEE standard for floating-point arithmetic. IEEE Std 754-2008, aug 29, 2008.

[42] Institut de RadioAstronomie Millimétrique (IRAM). http://www.iram-institute.org.

[43] IRAM, http://www.iram.fr/IRAMFR/GILDAS/. *CLASS Continuum and Line Analysis Single-dish Software*, 1.1 edition, nov 21, 2006.

[44] K. Isaak, A. Harris, and J. Zmuidzinas. WASP: A Wideband analogue Autocorrelation SPectrometer. In *American Astronomical Society Meeting Abstracts #191*, volume 30 of *Bulletin of the American Astronomical Society*, page 756, jan 1998.

[45] Preston A. Jackson, Cy P. Chan, Jonathan E. Scalera, Charles M. Rader, and M. Michael Vai. A systolic FFT architecture for real time FPGA systems. In *Proceedings of the Eighth Annual High Performance Embedded Computing (HPEC) Workshops*, sep 2004.

[46] P. A. Jones, M. G. Burton, M. R. Cunningham, M. A. Requena-Torres, K. M. Menten, P. Schilke, A. Belloche, S. Leurini, J. Martín-Pintado, J. Ott, and A. J. Walsh. Spectral imaging of the central molecular zone in multiple 3-mm molecular lines. *Monthly Notices of the Royal Astronomical Society*, 419(4):2961–2986, 2012.

[47] P. M. W. Kalberla and U. Haud. Global properties of the HI high velocity sky. *Astronomy & Astrophysics*, 455(2):481–498, 2006.

[48] C. Kasemann, R. Güsten, S. Heyminck, B. Klein, T. Klein, S. D. Philipp, A. Korn, G. Schneider, A. Henseler, A. Baryshev, and T. M. Klapwijk. CHAMP+: a powerful array receiver for APEX. In Jonas Zmuidzinas, Wayne S. Holland, Stafford Withington, and William D. Duncan, editors, *Millimeter and Submillimeter Detectors and Instrumentation for Astronomy III*, volume 6275, page 62750N. SPIE, 2006.

[49] J. Kerp, B. Winkel, N. Ben Bekhti, L. Flöer, and P. M. W. Kalberla. The Effelsberg Bonn H I Survey (EBHIS). *Astronomische Nachrichten*, 332:637, jul 2011.

[50] Walt Kester. *Taking the Mystery out of the Infamous Formula, "SNR=6.02N + 1.76dB," and Why You Should Care*. Analog Devices, http://www.analog.com/static/imported-files/tutorials/MT-001.pdf, rev.a, 10/08 edition, oct 2008.

[51] Walt Kester. *Understand SINAD, ENOB, SNR, THD, THD + N, and SFDR so You Don't Get Lost in the Noise Floor*. Analog Devices, http://www.analog.com/static/imported-files/tutorials/MT-003.pdf, rev.a edition, oct 2008.

[52] B. Klein, S. Hochgürtel, I. Krämer, A. Bell, K. Meyer, and R. Güsten. High-resolution wideband fast Fourier transform spectrometers. *Astronomy & Astrophysics*, 542:L3, 2012.

[53] Bernd Klein. *Die Suche nach hochdispergierten Radio-Pulsaren in Richtung des Galaktischen Zentrums*. Dissertation, Bonn, Universität, 2005. urn:nbn:de:hbz:5N-05369.

[54] Bernd Klein, Ingo Krämer, Stefan Hochgürtel, Rolf Güsten, Andreas Bell, Klaus Meyer, and Vitaly Chetik. The next generation of fast fourier transform spectrometer. In *19th International Symposium on Space Terahertz Technology*, 2008.

[55] Bernd Klein, Sabine D. Philipp, Rolf Güsten, Ingo Krämer, and Dorothea Samtleben. A new generation of spectrometers for radio astronomy: fast Fourier transform spectrometer. In Jonas Zmuidzinas, Wayne S. Holland, Stafford Withington, and William D. Duncan, editors, *Millimeter and Submillimeter Detectors and Instrumentation for Astronomy III*, volume 6275, page 627511. SPIE, 2006.

[56] Chryssa Kouveliotou, J. Ventura, and E. P. J. van den Heuvel. *The Neutron Star-Black Hole Connection*. NATO science series: Mathematical and physical sciences. Kluwer Academic Publishers, 2001.

[57] M. R. Krumholz. Star formation in molecular clouds. In E. Telles, R. Dupke, and D. Lazzaro, editors, *American Institute of Physics Conference Series*, volume 1386 of *American Institute of Physics Conference Series*, pages 9–57, sep 2011.

[58] Naoki Kurosawa, Haruo Kobayashi, Kaoru Maruyama, Hidetake Sugawara, and Kensuke Kobayashi. Explicit analysis of channel mismatch effects in time-interleaved ADC systems. *IEEE Transactions on Circuits and Systems I: Fundamental Theory and Applications*, 48(3):261–271, mar 2001.

[59] T. N. LaRosa, N. E. Kassim, T. J. W. Lazio, and S. D. Hyman. A wide-field 90 centimeter VLA image of the Galactic center region. *The Astronomical Journal*, 119:207–240, jan 2000.

[60] S. Leurini, R. Rolffs, S. Thorwirth, B. Parise, P. Schilke, C. Comito, F. Wyrowski, R. Güsten, P. Bergman, K. M. Menten, and L.-Å. Nyman. APEX 1 mm line survey of the orion bar. *Astronomy & Astrophysics*, 454(2):L47–L50, 2006.

[61] S. Leurini, P. Schilke, F. Wyrowski, and K. M. Menten. Methanol as a diagnostic tool of interstellar clouds. ii. modelling high-mass protostellar objects. *Astronomy & Astrophysics*, 466:215–228, apr 2007.

[62] Mark Looney. Advanced digital post-processing techniques enhance performance in time-interleaved ADC systems. *Analog Dialogue*, 37(3):5–9, aug 2003.

[63] D. R. Lorimer and Kramer M. *Handbook of Pulsar Astronomy*. Cambridge Observing Handbooks for Research Astronomers. Cambridge University Press, 2004.

[64] J. G. Mangum and A. Wootten. Formaldehyde as a probe of physical conditions in dense molecular clouds. *The Astrophysical Journal Supplement Series*, 89:123–153, nov 1993.

[65] J. Martín-Pintado, P. de Vicente, A. Fuente, and P. Planesas. SiO emission from the Galactic Center molecular clouds. In R. Gredel, editor, *The Galactic Center*, volume 102 of *Astronomical Society of the Pacific Conference Series*, page 47, 1996.

[66] Craig Marven and Gillian Ewers. *A simple approach to digital signal processing*. Texas Instruments, 1993.

[67] P. G. Mezger, R. Zylka, C. J. Salter, J. E. Wink, R. Chini, E. Kreysa, and R. Tuffs. Continuum observations of Sgr A at mm/submm wavelengths. *Astronomy & Astrophysics*, 209:337–348, jan 1989.

[68] A. Monfardini, A. Benoit, A. Bideaud, L. Swenson, A. Cruciani, P. Camus, C. Hoffmann, F. X. Désert, S. Doyle, P. Ade, P. Mauskopf, C. Tucker, M. Roesch, S. Leclercq, K. F. Schuster, A. Endo, A. Baryshev, J. J. A. Baselmans, L. Ferrari, S. J. C Yates, O. Bourrion, J. Macias-Perez, C. Vescovi, M. Calvo, and C. Giordano. A dual-band millimeter-wave kinetic inductance camera for the IRAM 30 m telescope. *The Astrophysical Journal Supplement Series*, 194(2):24, 2011.

[69] Ryan M. Monroe. Wideband spectroscopy: The design and implementation of a 3 GHz, 2048 channel digital spectrometer. Technical report, NASA Undergraduate Student Research Program, http://usrp.usra.edu/technicalPapers/jpl/MonroeSep11.pdf, sep 30, 2011.

[70] Maria Montero-Castaño, Robeson M. Herrnstein, and Paul T. P. Ho. Gas infall towards Sgr A* from the clumpy circumnuclear disk. *The Astrophysical Journal*, 695:1477–1494, apr 2009.

[71] D. C. Montgomery and G. C. Runger. *Applied Statistics and Probability for Engineers*. John Wiley & Sons, 2010.

[72] Mark Morris and Eugene Serabyn. The galactic center environment. *Annual Review of Astronomy and Astrophysics*, 34(1):645–701, 1996.

[73] Holger S. P. Müller, Frank Schlöder, Jürgen Stutzki, and Gisbert Winnewisser. The cologne database for molecular spectroscopy, CDMS: a useful tool for astronomers and spectroscopists. *Journal of Molecular Structure*, 742(1–3):215–227, 2005.

[74] National Instruments Corporation, http://www.ni.com/pdf/manuals/370192c.pdf. *LabVIEW Analysis Concepts*, march 2004 edition, mar 2004.

[75] National Instruments Corporation, http://zone.ni.com/devzone/cda/tut/p/id/4278. *The Fundamentals of FFT-Based Signal Analysis and Measurement in LabVIEW and LabWindows/CVIs*, jun 8, 2009 edition, jun 2009.

[76] National Semiconductor, http://www.ti.com/product/adc083000#doctype2. *ADC083000 8-Bit, 3 GSPS, High Performance, Low Power A/D Converter*, rev. n edition, jul 2009.

[77] A. Nuttall. Some windows with very good sidelobe behavior. *Acoustics, Speech and Signal Processing, IEEE Transactions on*, 29(1):84–91, feb 1981.

[78] M. Olbrich, V. Mittenzwei, O. Siebertz, F. Schmülling, and R. Schieder. A 3 GHz instantaneous bandwidth acousto-optical spectrometer with 1 MHz resolution. In A. Karpov, editor, *Eighteenth International Symposium on Space Terahertz Technology*, page 231, 2007.

[79] B. Parise, A. Belloche, F. Du, R. Güsten, and K. M. Menten. Extended emission of D2H+ in a prestellar core. *Astronomy & Astrophysics*, 526:A31, 2011.

[80] A. Parsons. The symmetric group in data permutation, with applications to high-bandwidth pipelined FFT architectures. *Signal Processing Letters, IEEE*, 16(6):477–480, jun 2009.

[81] H. M. Pickett, R. L. Poynter, E. A. Cohen, M. L. Delitsky, J. C. Pearson, and H. S. P. Möller. Submillimeter, millimeter, and microwave spectral line catalog. *Journal of Quantitative Spectroscopy and Radiative Transfer*, 60(5):883–890, 1998.

[82] M. A. Requena-Torres. in preparation.

[83] M. A. Requena-Torres, R. Güsten, A. Weiß, A. I. Harris, J. Martín-Pintado, J. Stutzki, B. Klein, S. Heyminck, and C. Risacher. GREAT confirms transient nature of the circumnuclear disk. *Astronomy & Astrophysics*, 542:L21, 2012.

[84] M. A. Requena-Torres, J. Martín-Pintado, S. Martín, and M. R. Morris. The Galactic center: The largest oxygen-bearing organic molecule repository. *The Astrophysical Journal*, 672:352–360, jan 2008.

[85] K. Rohlfs and T. L. Wilson. *Tools of radio astronomy*. Astronomy and astrophysics library. Springer, 1996.

[86] Ahmed Saeed, M. Elbably, G. Abdelfadeel, and M. I. Eladawy. Efficient FPGA implementation of FFT/IFFT processor. *International Journal of Circuits, Systems and Signal Processing*, 3(3):103–110, 2009.

[87] P. Schilke, T. D. Groesbeck, G. A. Blake, and T. G. Phillips. A line survey of orion kl from 325 to 360 ghz. *The Astrophysical Journal Supplement Series*, 108(1):301, 1997.

[88] F. Schuller, K. M. Menten, Y. Contreras, F. Wyrowski, P. Schilke, L. Bronfman, T. Henning, C. M. Walmsley, H. Beuther, S. Bontemps, R. Cesaroni, L. Deharveng, G. Garay, F. Herpin, B. Lefloch, H. Linz, D. Mardones, V. Minier, S. Molinari, F. Motte, L.-Å. Nyman, V. Reveret, C. Risacher, D. Russeil, N. Schneider, L. Testi, T. Troost, T. Vasyunina, M. Wienen, A. Zavagno, A. Kovacs, E. Kreysa, G. Siringo, and A. Weiß. ATLASGAL - the APEX telescope large area survey of the galaxy at 870 μm. *Astronomy & Astrophysics*, 504(2):415–427, 2009.

[89] E. Serabyn, J. H. Lacy, and J. M. Achtermann. The compression of the M-0.02-0.07 molecular cloud by the Sagittarius A east shell source. *The Astrophysical Journal*, 395:166–173, aug 1992.

[90] The Stratospheric Observatory For Infrared Astronomy (SOFIA). http://www.sofia.usra.edu.

[91] splatalogue database for astronomical spectroscopy. http://www.splatalogue.net.

[92] S. Stanko, B. Klein, and J. Kerp. A field programmable gate array spectrometer for radio astronomy. *Astronomy & Astrophysics*, 436(1):391–395, 2005.

[93] Samuel D. Stearns. *Digitale Verarbeitung analoger Signale*. Grundlagen der Schaltungstechnik. Oldenbourg, Munich, 1979.

[94] Norbert K. Stuhrmann. Implementation and evaluation of weighted-overlap-add techniques for FPGA-based FFT spectrometers. Master's thesis, Bonn, Universität, 2007.

[95] F. F. S. van der Tak, J. H. Black, F. L. Schöier, D. J. Jansen, and E. F. van Dishoeck. A computer program for fast non-LTE analysis of interstellar line spectra. *Astronomy & Astrophysics*, 468(2):627–635, 2007.

[96] G. Villanueva and P. Hartogh. The high resolution chirp transform spectrometer for the SOFIA-GREAT instrument. *Experimental Astronomy*, 18:77–91, 2004. 10.1007/s10686-005-9004-3.

[97] W. H. T. Vlemmings, R. M. Torres, and R. Dodson. Zeeman splitting of 6.7 GHz methanol masers. *Astronomy & Astrophysics*, 529:A95, 2011.

[98] Christian Vogel. A signal processing view on time-interleaved ADCs. In Arthur H. M. Roermund, Herman Casier, and Michiel Steyaert, editors, *Analog Circuit Design*, pages 61–78. Springer Netherlands, 2010.

[99] S. Weinreb. A digital spectral analysis technique and its application to radio astronomy. Technical Report 412, Massachusetts Institute of Technology, Research Laboratory of Electronics, http://hdl.handle.net/1721.1/4413, 1963.

[100] S. Weinreb, A. H. Barret, M. L. Meeks, and J. C. Henry. Radio observations of OH in the interstellar medium. *Nature*, 200(4909):829–831, nov 30, 1963. 10.1038/200829a0.

[101] P. Welch. The use of fast Fourier transform for the estimation of power spectra: A method based on time averaging over short, modified periodograms. *Audio and Electroacoustics, IEEE Transactions on*, 15(2):70–73, jun 1967.

[102] T. L. Wilson and R. T. Rood. Abundances in the interstellar medium. *Annual Review of Astronomy and Astrophysics*, 32:191–226, 1994.

[103] A. Wootten and A. R. Thompson. The Atacama Large Millimeter/submillimeter Array. *Proceedings of the IEEE*, 97(8):1463 –1471, aug 2009.

[104] Xilinx. Xilinx®: What is an FPGA? Field Programmable Gate Array (FPGA). http://www.xilinx.com/training/fpga/fpga-field-programmable-gate-array.htm.

[105] Xilinx, http://www.xilinx.com/support/documentation/user_guides/ug070.pdf. *Virtex-4 FPGA User Guide UG070*, v2.6 edition, dec 1, 2008.

[106] Xilinx, http://www.xilinx.com/support/documentation/data_sheets/ds302.pdf. *Virtex-4 FPGA Data Sheet: DC and Switching Characteristics DS302*, v3.7 edition, sep 9, 2009.

[107] Xilinx, http://www.xilinx.com/support/documentation/user_guides/ug361.pdf. *Virtex-6 FPGA SelectIO Resources User Guide UG361*, v1.3 edition, aug 16, 2010.

[108] Xilinx, http://www.xilinx.com/support/documentation/sw_manuals/xilinx13_3/ise_tutorial_ug695.pdf. *ISE In-Depth Tutorial UG695*, v13.3 edition, oct 19, 2011.

[109] Xilinx, http://www.xilinx.com/support/documentation/user_guides/ug363.pdf. *Virtex-6 FPGA Memory Resources User Guide UG363*, v1.6 edition, apr 22, 2011.

[110] Xilinx, http://www.xilinx.com/support/documentation/ip_documentation/ds808_xfft.pdf. *LogiCORE IP Fast Fourier Transform v8.0 DS808*, v1.2 edition, jul 25, 2012.

[111] Xilinx, http://www.xilinx.com/support/documentation/user_guides/ug362.pdf. *Virtex-6 FPGA Clocking Resources User Guide UG362*, v2.1 edition, may 7, 2012.

[112] Xilinx, http://www.xilinx.com/support/documentation/data_sheets/ds152.pdf. *Virtex-6 FPGA Data Sheet: DC and Switching Characteristics DS152*, v3.4 edition, jan 12, 2012.

[113] S. J. C. Yates, A. M. Baryshev, J. J. A. Baselmans, B. Klein, and R. Güsten. Fast fourier transform spectrometer readout for large arrays of microwave kinetic inductance detectors. *Applied Physics Letters*, 95(4):042504–042504–3, jul 2009.

[114] F. Yusef-Zadeh and M. Morris. Structural details of the Sagittarius A complex - evidence for a large-scale poloidal magnetic field in the Galactic center region. *The Astrophysical Journal*, 320:545–561, sep 1987.